AN ANALYTICAL STUDY OF THE CONE PENETRATION TEST

by

Cee-Ing Teh

A Thesis Submitted for the Degree of

Doctor of Philosophy

at the

University of Oxford

Hertford College

Trinity Term, 1987

ACKNOWLEDGEMENT

First and foremost, I like to thank Dr Guy Houlsby who has been an extremely able and conscientious supervisor of my work. His guidance and thoughtful suggestions have been invaluable throughout the course of this study. His advice and comments during the preparation of this thesis are also very much appreciated.

I am indebted to Dr Harvey Burd for the many helpful discussions on the various aspects of large displacement finite element analysis, and for the use of his frontal solving routine. I am grateful to Professor Cesar Sagaseta of the University of Cantabria, Santander, who provided me with detailed explanations of his solutions to the cavity expansion and cone tip problems referred to in this thesis. I must also thank my friend Tack Weng who painstakingly proof read the final draft of this thesis.

It is a privilege to be a member of the Oxford University Soil Mechanics Group under the able leadership of Professor Peter Wroth. The friendly atmosphere he engenders in the group has made it a particularly stimulating place to work in. And to all fellow members in the group who have contributed in various ways towards this work, I would like to express my thanks.

I am particularly grateful to Kuok Foundation, Malaysia, for the scholarship and the generous financial support, without which all these would not have been possible. Above everything else, it is the kindness of everyone at the Foundation that I shall always remember.

Last but not the least, I would like to express my sincere gratitude to my parents, brothers and sisters for their continuing support and encouragement, and to Meei Fang whose love and understanding have been a constant source of motivation.

ABSTRACT

An Analytical Study of the Cone Penetration Test

Teh, Cee Ing
Hertford College, University of Oxford

A Thesis Submitted for the Degree of Doctor of Philosophy
Trinity Term, 1987

The quasi-static penetration of a cone penetrometer into clay can be formulated as a steady state problem by considering a steady flow of soil past a stationary cone. The soil velocities are estimated from the flow field of an inviscid fluid, and the incompressibility condition is achieved by adopting a stream function formulation. Emphasis is placed on obtaining an accurate velocity estimate and this is accomplished by a solution of the Navier-Stokes equations.

The strain rates are evaluated from the flow field using a finite difference scheme. The clay is modelled as a homogeneous incompressible elastic-perfectly plastic material and the soil stresses are computed by integrating along streamlines from some initial stress state in the upstream region. These stresses do not in general obey the equilibrium equations, although one of the two equations can be satisfied by an appropriate choice of the mean stress. Several attempts have been made to use the remaining equilibrium equation to obtain an improved velocity estimate and three plausible iterative methods are detailed in this thesis.

In a second study, a series of finite element calculations on the cone penetration problem is performed. In modelling the penetration process, the cone is introduced in a pre-formed hole and some initial stresses assumed in the soil, incremental displacements are then applied to the cone until a failure condition is reached. Although the equilibrium condition is satisfied very closely in the finite element calculations, it is extremely difficult to achieve a steady state solution.

In a third series of computations, the stresses evaluated by the strain path method are used as the starting condition for the finite element analysis. This is believed to give the most realistic solution of the cone penetration problem because both the steady state and equilibrium conditions are approximately satisfied. Numerically derived cone factors are presented and these are found to depend on the rigidity index of the soil and the in situ stresses.

The pore pressure distribution in the soil around the penetrometer is estimated using Henkel's empirical equation. The dissipation analysis is based on Terzaghi's uncoupled consolidation theory. The governing equation is formulated in the Alternating-Direction-Implicit finite difference scheme. This formulation is unconditionally stable and variable time steps are used to optimise the solution procedure. The dissipation curves are found to be significantly affected by the rigidity index of the soil and a dimensionless time factor is proposed to account for this effect.

CONTENTS

CHAPTER 1 INTRODUCTION AND LITERATURE REVIEW

1.1	Introduction	1.1
1.2	Literature Review	1.2
1.2.1	Historical Development of the Cone Penetrometer	1.2
1.2.2	Application of Cone Penetration Test Data	1.4
1.2.3	Theories on Cone Penetration Test in Clay	1.7
1.3	Strain Path Analysis of the Cone Penetration Test	1.17

CHAPTER 2 STRAIN PATH METHOD

2.1	Introduction	2.1
2.2	Application of the Strain Path Method	2.1
2.2.1	Velocity Field	2.3
2.2.2	Stress Strain Relationship	2.3
2.3	Simple Pile Problem	2.4
2.3.1	Formulation	2.4
2.3.2	Geometry of a Simple Pile	2.6
2.4	Undrained Simple Pile Penetration into Clay	2.7
2.4.1	Stress and Strain Due to Simple Pile Penetration	2.9
2.4.2	Strain Paths	2.11
2.4.3	Stress Paths	2.13

Appendix 2A Calculation of Strain Path due to Simple Pile Penetration

CHAPTER 3 FLOW FIELD COMPUTATION

3.1	Introduction	3.1
3.2	Mathematical Formulation	3.2
3.3	Numerical Solution Method	3.5
3.3.1	Choice of Finite Difference Mesh	3.5
3.3.2	Overall Solution Procedure	3.6
3.3.3	The Vorticity Transport Equation	3.7
3.3.4	Finite Difference Representation	3.8
3.3.5	Stream Function Equation	3.10
3.4	Boundary Conditions	3.13
3.4.1	Boundary Conditions for ψ	3.13
3.4.2	Boundary Conditions for ζ	3.14
3.5	Verification of Computer Program	3.16
3.5.1	Steady Flow in a Circular Conduit with a Sudden Expansion	3.17
3.5.2	Steady Flow in a Circular Conduit with a Sudden Contraction	3.19
3.5.3	Steady Flow around a Circular Disc	3.21

Appendix 3A Derivation of Finite Difference Equations 3.24

CHAPTER 4 COMPUTATIONS OF STRESS AND STRAIN

4.1	Introduction	4.1
4.2	Flow Solution	4.1
4.3	Strain Computations	4.2
4.3.1	Determination of Streamline Profile	4.3
4.3.2	Strain Rates Definitions	4.5
4.3.3	Integration of Stress-Strain Equations	4.7
4.4	Stress Computations	4.8
4.4.1	Constitutive Relationship for Clay	4.9

4.4.2 von Mises Plasticity 4.11
4.4.3 Deviatoric Stress Update Calculations 4.12
4.4.4 Stress Interpolations 4.13
4.5 Calculations of the Octahedral Normal Stress 4.15
4.5.1 Integration along Radial Grid Lines 4.16
4.5.2 Integration along Axial Grid Lines 4.17
4.5.3 Solution of the Poisson Equation for Mean Pressure 4.18
4.6 Deviatoric Stresses 4.20
4.7 Mean Pressure Solution 4.22

CHAPTER 5 EQUILIBRIUM CONSIDERATIONS

5.1 Introduction 5.1
5.2 Estimating the Errors in the Stress Solution 5.1
5.3 Equilibrium Correction Methods 5.3
5.3.1 Newton-Raphson Correction Scheme 5.3
5.3.2 Pseudo-Dynamic Correction Scheme 5.7
5.3.3 Finite Element Correction Method 5.12
5.4 Summary 5.14

CHAPTER 6 STRESS AND STRAIN IN THE SOIL DUE TO CONE PENETRATION

6.1 Introduction 6.1
6.2 Effect of Cone Geometry 6.1
6.3 Stress and Strain around a 10° Cone Penetrometer 6.6
6.4 Stress and Strain around a Standard 60° Cone Penetrometer 6.11
6.5 Failure Zone due to Cone Penetration 6.18
6.6 Tip Resistance 6.21
6.6.1 Effect of rigidity index on Tip Resistance 6.22
6.7 Effect of Anisotropic Initial Stresses 6.24
6.8 Cone Factor as Evaluated by the Strain Path Method 6.29
6.9 Summary 6.30

CHAPTER 7 FORMULATION OF FINITE ELEMENT ANALYSIS

7.1 Specific Considerations for the Finite Element Formulation 7.1
7.2 Description of Kinematics 7.1
7.3 Objective Stress Rate 7.3
7.4 Incompressibility 7.4
7.5 Formulation of Finite Element Equations 7.6
7.5.1 Element Stiffness Matrix 7.7
7.6 Constitutive Relationship 7.12
7.7 Strain Rate Calculations 7.13
7.8 Stress Update Calculations 7.14
7.8.1 Elastic Behaviour Including Jaumann Terms 7.14
7.8.2 von Mises Plasticity Including Jaumann Terms 7.16
7.8.3 Calculation of Yield Surface Intersection 7.16
7.8.4 Yield Surface Correction 7.17
7.9 Solution Scheme 7.18
7.10 Calculations of Consistent Nodal Forces 7.21
7.10.1 Body Forces 7.21
7.10.2 Distributed Boundary Tractions 7.22

Appendix 7A Finite Element Equations for a 15-node Triangular Element 7.24

CHAPTER 8 FINITE ELEMENT ANALYSIS OF THE CONE PENETRATION TEST

8.1	Verification of Finite Element Formulation	8.1
8.1.1	Expansion of a Thick-Walled Cylinder	8.1
8.1.2	Cylindrical Cavity Expansion in an Infinite Medium	8.3
8.1.3	Collapse Load Analysis of a Rough Rigid Circular Footing	8.5
8.2	Finite Element Modelling of the Cone Penetration Process	8.8
8.3	Effect of Poisson's Ratio	8.10
8.4	Stress Changes due to Cone Penetration	8.12
8.5	Effect of Rigidity Index on the Cone Resistance	8.18
8.6	Effect of In Situ Stress State	8.19
8.7	Strain Path-Finite Element Analysis	8.21
8.7.1	Effect of Anisotropic Initial Stresses	8.24
8.7.2	Variation of N_k with I_r	8.25
8.8	Summary	8.27

CHAPTER 9 DISSIPATION ANALYSIS

9.1	Introduction	9.1
9.2	Consolidation Theories	9.1
9.3	Mathemaical Formulation	9.3
9.4	Boundary Conditions	9.7
9.5	Factors Affecting Pore Pressure Dissipation	9.7
9.6	Initial Pore Pressure Distribution	9.9
9.7	Pore Pressure Dissipation around a Cone Penetrometer	9.11
9.8	Results of Dissipation Analysis	9.15
9.8.1	Effect of Anisotropic Consolidation Characteristics	9.18
9.8.2	Effect of Rigidity Index on the Rate of Dissipation	9.21
9.8.3	Interpretation of Dissipation Test Data from CPT	9.24
9.9	Pore Pressure Correction for Cone Resistance	9.29
9.10	Location of Piezometric Element	9.31

CHAPTER 10 CONCLUDING REMARKS

10.1	Summary and Remarks	10.1
10.2	Future Research	10.6

REFERENCES

Chapter 1

Introduction and Literature Review

1.1 Introduction

The cone penetrometer (CPT) has undergone tremendous development in recent years as an in-situ site investigation tool. From its primitive form which was first used by the Swedish Railway to correlate pile end bearing resistance in sand, it has evolved into a highly sophisticated instrument suitable for use in most types of soil. The use of a penetrometer with pore pressure measurement for soil profiling is unsurpassed by any other modern instrument, as it is capable of providing a continuous measurement over the whole depth of penetration. The simplicity of the test procedure and the high repeatability of the test data has made it increasingly popular, especially in off-shore works.

The advance in equipment design, however, is not matched by the progress in interpretation techniques. At the present moment, a rigorous quantitative interpretation of CPT data is still not available. Correlations between test data and soil properties still rely very heavily on empirical relationships. Thus, it is not surprising that the main application of the CPT in site investigation is for soil profiling.

Due to the complexity of soil behaviour and the complicated boundary conditions in the cone penetration problem, it is highly improbable that a unique analytical solution to the problem can be found. However, theories assist in providing a better understanding of the problem despite the inevitable simplifications and idealizations. When the problem is properly formulated, a theoretical approach helps to shed light on the significance of the various parameters and aids in the selection of the appropriate form of correlation equations.

1.2 Literature Review

In this section, a review of the development of the cone penetrometer as a site investigation device, and the existing theories on cone penetration will be presented. The relevance and limitations of these theories will be critically reviewed so that a rational approach may be adopted in the present study.

1.2.1 Historical Development of the Cone Penetrometer

The earliest recorded use of the cone in the form of a static sounding probe in soil investigation can be attributed to the Swedish State Railway around 1917 (Terzaghi and Peck, 1967). By the 1930s, the standard cone penetrometer shape with a 60° cone angle and 10 cm^2 base area had emerged in Holland. These probes were developed by the Delft Soil Mechanics Laboratory (Delft, 1936) and the Dutch Department of Public Works.

In the early cone designs, the tip and sounding tubes were advanced separately and clogging of the probe was a considerable problem. This led to a number of modifications which improved the performance of the cone. However, another major problem remained. This concerned the failure of the total friction on the sounding tubes to scale directly to the skin friction on driven piles. In an attempt to improve the correlation between the measured friction on the penetrometer and the skin friction on driven piles, Begemann (1953) developed a penetrometer which measured the skin friction with the aid of a friction sleeve. This represented the first attempt to measure the localised friction on the penetrometer.

By the 1960s, strain gauges were added to the tip to measure the tip resistance electrically instead of mechanically. By 1970, Fugro B.V. had

developed an electric cone capable of measuring the tip resistance and the sleeve friction continuously during penetration (De Ruiter, 1971). Perhaps the most significant development in penetrometer design is the incorporation of pore pressure measuring elements into the probe. The evolution began with the development of a piezometer probe by Torstensson (1975). This instrument was used for measuring pore pressure only and could not provide any measurement of tip resistance or skin friction. Around the same period, a pore pressure probe of the same shape as the standard cone penetrometer was developed at the Norwegian Geotechnical Institute. This pore pressure probe was used to measure both the pore pressure during penetration and its subsequent dissipation. The results from this probe were used in conjunction with standard cone penetration tests (Janbu & Senneset, 1974). Although the usefulness of simultaneous pore pressure and tip resistance measurement was realised much earlier (Schmertmann, 1974), it was not until the 1980s that a research penetrometer capable of measuring the tip resistance and pore pressure was developed (Zuidberg et al., 1982).

As the use of the cone penetrometer becomes more widespread, it is

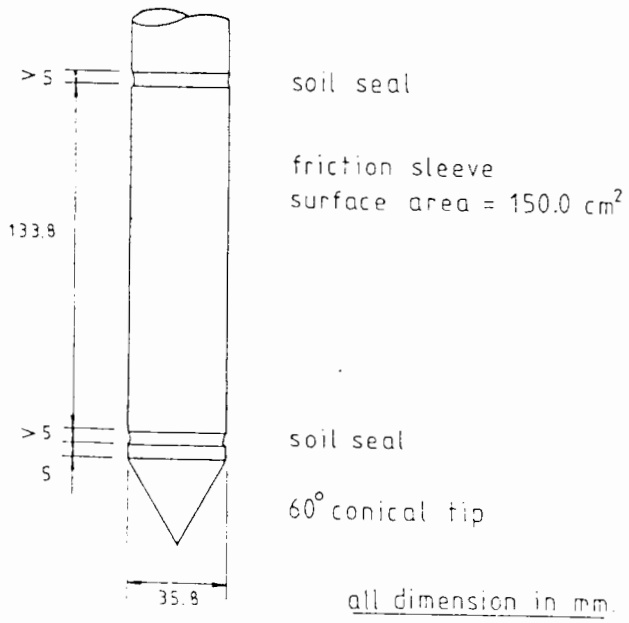

Figure 1.1: Standard Cone Penetrometer Geometry

important that a standard cone design is adopted. Since the available interpretation techniques are mostly empirical in nature, standardization will help in the building up of a data base which can be used to validate and improve these empirical relationships. Significant steps toward standardising the penetrometer design were taken in the late 1970s (ASTM-D-3441, 1979; ISSMFE, 1977). The standardised cone penetrometer has a 60^{o} conical tip and a 10 cm^2 cross-sectional area with a 150 cm^2 friction sleeve (Figure 1.1).

1.2.2 Application of Cone Penetration Test Data

Most early cone penetration testings were concerned with the determination of the end bearing of driven piles (e.g. Plantema, 1948). The addition of a friction sleeve enabled a prediction of the soil type to be made (Begemann, 1965). With the advent of the electric friction cone, this soil type classification technique was further refined by Sanglerat (1972) and Schmertmann (1975). The latter, based on the accumulated experience in a wide range of soils, produced a chart (Figure 1.2) which classified soil according to the measured tip resistance, q_c, and friction ratio, f_s/q_c (in %). More recently, the use of the excess pore pressure and tip resistance to determine soil type has also been proposed (Jones & Rust, 1982).

The measurement of pore pressure during cone penetration has significantly improved the sensitivity of the test data to changes in soil stratigraphy. The excellent response of measured data to variation in soil type is illustrated in Figure 1.3 (after Zuidberg et al., 1982), which shows the output from an actual penetration test. With this device, even thin laminated structures in the order of a few millimeters can be detected. This characteristic has contributed to the status of the piezocone as an outstanding tool for determining soil stratification.

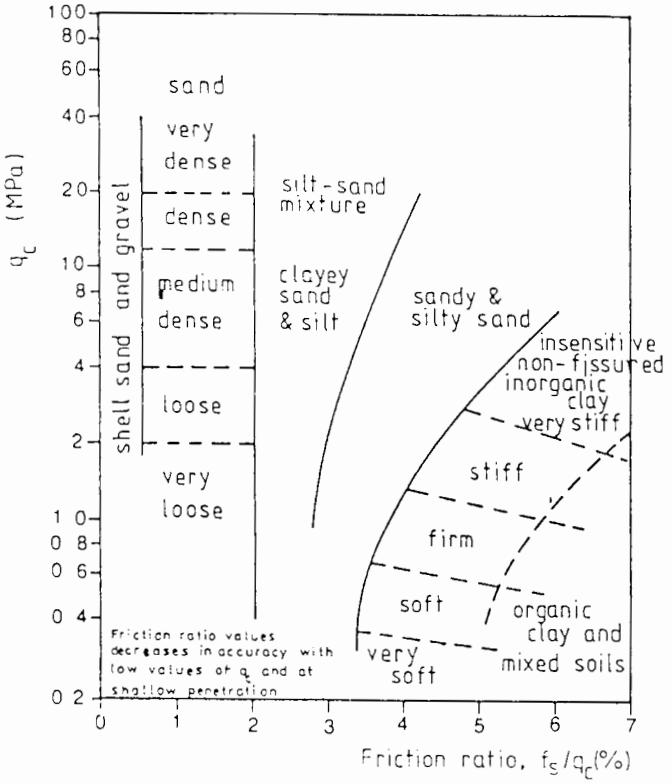

Figure 1.2 Schmertmann's Soil Type Chart

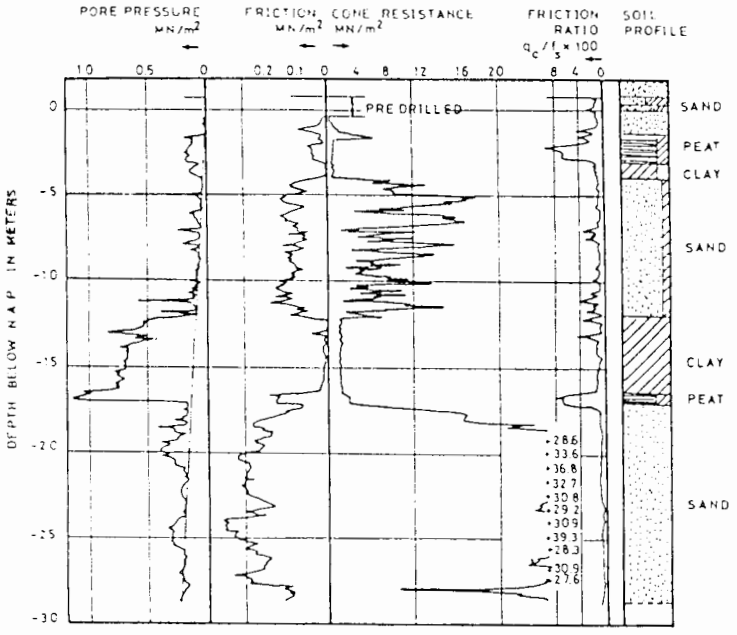

Figure 1.3 Output from a Piezocone Penetration Test

(after Zuidberg et al., 1982)

Apart from such qualitative correlations, the possibility of using measured cone resistance and pore pressure to correlate soil strength has also been suggested (Begemann, 1965; Tavenas et al., 1982). These applications have become more important as a result of increased off-shore activities where undisturbed soil samples are extremely difficult and expensive to obtain. However, such correlations give rise to a large scatter (Figure 1.4) and although part of this may be due to the errors in the tests used to determine undrained shear strength, it is equally likely that the correlation relationship used is inadequate.

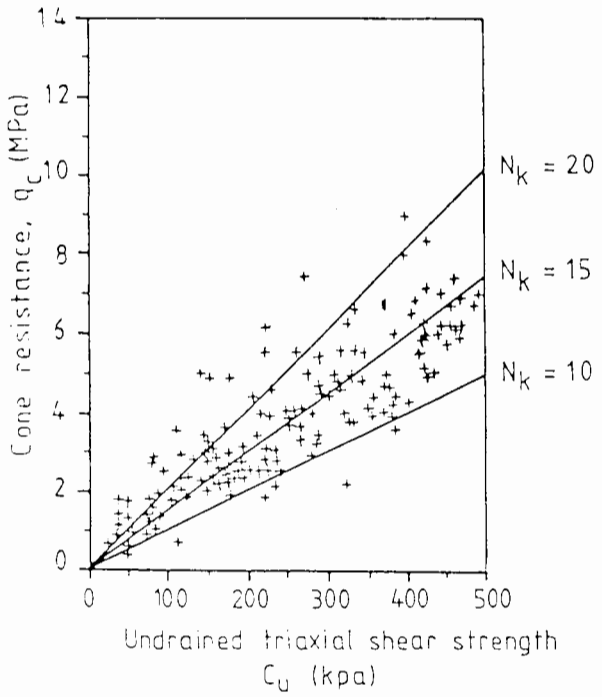

Figure 1.4 Correlation Between q_c and c_u (after Toolan et al., 1980)

The possibility of using the measured pore pressure to determine the overconsolidation ratio (OCR) has also been suggested by some authors (Baligh et al., 1981; Lacasse et al., 1981). The empirical relationships proposed are often based on some ratio of pore pressure to tip resistance. Several expressions have been used but the B_q factor proposed by Senneset et al. (1982) is becoming increasingly popular.

$$B_q = \frac{\Delta u}{q_c - \sigma_{vo}} \qquad (1.1)$$

Lunne & Lacasse (1982) reported good correlation of this ratio with OCR.

In addition, it has been suggested that the excess pore pressure dissipation after stopping the penetration process can be used to obtain an estimate of the consolidation parameters. Levadoux & Baligh (1986) conducted a dissipation analysis around the cone penetrometer based on an initial pore pressure distribution evaluated by the strain path method. The theoretical dissipation curves were then used to derive an estimate of the consolidation coefficient of Boston Blue clay. It was reported that the values of c_h determined by this method was comparable to those obtained from other field or laboratory tests.

More recently, many new applications of the cone penetrometer have also been suggested. These generally require the use of specially designed penetrometers. Tringale & Mitchell (1982) reported the use of an acoustic cone to gather information on soil types and profile conditions. Other possibilities include the determination of the deformation modulus of soil using a seismic cone (Campanella et al., 1985), and the relative density of soil using a penetro-gammadensimeter (Ledoux et al., 1982). Although most of these instruments are still at an early development stage, the potential for practical applications seems promising.

1.2.3 Theories on Cone Penetration Test in Clay

The theories which have been proposed for the cone penetration problem in clay can broadly be divided into three main categories. They are:

1. Bearing capacity theories (Meyerhof, 1961; Janbu & Senneset, 1974;

Durgunoglu & Mitchell, 1975)

2. Cavity expansion theories (Ladanyi, 1963; Vesic, 1972)

3. The strain path method (Levadoux & Baligh, 1980; Baligh, 1985)

The first two groups of theories will be reviewed in this chapter. A separate, more in depth treatment of the strain path method is presented in Chapter 2.

A. Bearing Capacity Theory

The bearing capacity theory in foundation analysis is based on the plasticity approach as developed by Prandtl (1921). The success of this theory in predicting the bearing capacity of shallow foundations is widely acknowledged. A number of attempts have been made to extend this approach to deep foundation problems, and an analogous bearing capacity equation is obtained for undrained analysis:

$$q_c = N_k c_u + \gamma z \qquad (1.2)$$

c_u = undrained shear strength

γz = total overburden pressure

The extension of the bearing capacity approach to penetrometer analysis required the assumption of a failure mechanism. Some of the mechanisms which have been proposed for cohesive-frictional materials are shown in Figure 1.5. Meyerhof (1961) adopted a failure mechanism as shown in Figure 1.5a, in which the effect of embedment depth was replaced by a surcharge pressure acting on the level of the cone base. A value of 9.3 was obtained for the N_k factor. Begemann (1965), on the other hand, assumed a system of circular sliding planes and obtained an N_k factor of 14.0 from a similar analysis.

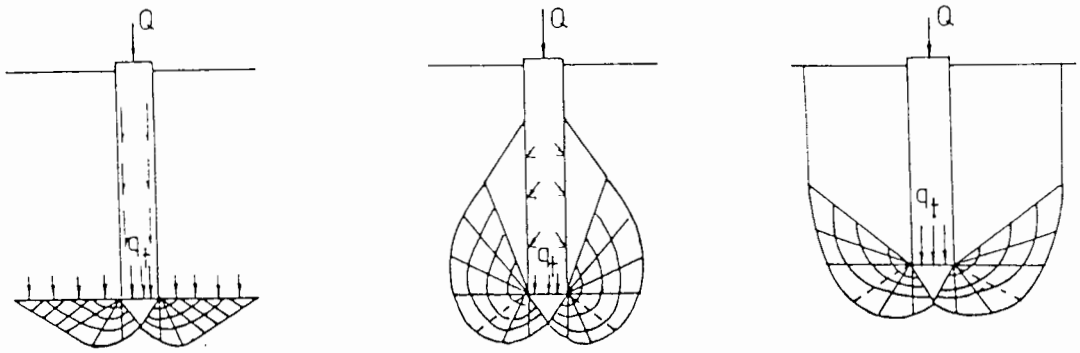

Meyerhof (1961) | Nowatzki & Karafiath (1972) | Mitchell & Durgunoglu (1973)

Figure 1.5 Proposed Failure Mechanisms.

De Beer (1974) studied a plane strain problem in which a 90° wedge was pushed into soil ahead of a flat ended penetrometer. The failure surfaces were assumed to be semi-circular and centred at the corner of the base. The slip lines were assumed to begin at the tip and extended tangentially to the shaft from the other end of the semi-circular arc. A shape factor of 1.2 was then applied to convert this plane strain solution to axial symmetry. By this process, an N_k factor of 9.94 was obtained. Durgunoglu & Mitchell (1974) solved the problem of the wedge based on a different set of failure surfaces. The plane strain solution was then modified by shape factors derived from Hansen's equation (1970). The proposed relationship is of the form:

$$q_c = \xi_c N_c c_u + \xi_q N_q B\gamma z \qquad (1.3)$$

where: ξ_c and ξ_q are shape factors

B is the penetrometer diameter

All the analyses which have been reviewed so far were based on a plane strain model. It is clear that the failure mechanisms which are relevant to a plane strain problems cannot be extended directly to an axially symmetric

problem. The use of shape factors to convert the plane strain solution to axisymmetry may have met with some success in shallow foundations, but the straightforward extension of this procedure to deep penetration can at best be described as dubious. It is also doubtful that the effect of embedment can be adequately modelled by simulating it by a surcharge pressure. In addition, the boundary conditions used in the analysis are not exactly equivalent to those in the real problem, and the solution obtained cannot be considered to be representative.

In an attempt to overcome the shortcomings of a plane strain analysis, Koumoto & Kaku (1982) performed a 3-dimensional analysis of a cone penetrometer buried deep in the soil. The problem was formulated in axisymmetry and the governing equations were solved with the well established method of characteristics. For a 60^{o} rough cone, they obtained an N_k factor of 9.8 by assuming a vertical stress free surface behind the cone. This boundary condition is not strictly representative of the real problem and the solution can only be considered as approximate.

Koumoto & Kaku have also carried out laboratory and field tests with a penetrometer in which the cone has a diameter greater than that of the shaft. The experimental data were reported to agree reasonably well with the predicted N_k factor. Muromachi (1974) performed a series of penetration tests into clay and obtained an average N_k factor of 10.0. This result was in close agreement with the analytical value obtained by Koumoto & Kaku. The good agreement in this case was not entirely unexpected and could be attributed to the peculiar shape of the penetrometer with an enlarged conical tip. During the penetration of such a probe, a void is formed behind the cone shoulder by the passage of the enlarged tip. The presence of a free surface near the tip created a situation where the slip line theory could

give a reasonable solution. However, this solution no longer holds true when the diameter of the shaft and the cone is the same.

This argument found support in a series of self-boring plate load tests performed by Kay & Parry (1982) in a well-investigated site in Cambridgeshire, U.K.. The average bearing capacity factor from these plate test was about 9.0. In contrast, the N_k factor from adjacent CPTs averaged about 20. Although the rate of loading in the plate tests was lower than the cone penetration rate, this in itself could not explain the large discrepancy in the two factors. It is more likely that the deformation mechanisms associated with a flush penetrometer and the plate test (or a cone penetrometer with an enlarged tip) are fundamentally different.

Different results have also been obtained theoretically when the actual standard penetrometer geometry is included in the analysis. Houlsby & Wroth (1982) analysed a penetrometer with a flush shaft using the method of characteristics. The N_k factor computed using this approach was found to increase indefinitely with depth. This trend was caused by the need of the slip lines to extend all the way to the ground level, the nearest free surface in the problem. This slip line pattern is due to the rigid plastic model assumed for the soil. It has been suggested that if the elastic response is included, a different failure mechanism would result and a cut-off value for N_k could be obtained when the depth exceeded a certain limit. Unfortunately, this cannot be directly verified because the method of characteristics is not applicable for an elasto-plastic material model.

From the above review, it may be concluded that the bearing capacity theory is not adequate for deep penetration analysis. One of the major difficulty with this approach stems from the rigid-plastic soil model assumed in the theory. In addition, most of the analyses were based on failure

mechanisms which are not compatible with the boundary conditions. Therefore, although the correlation equation based on the bearing capacity approach is attractively simple, the N_k factor derived from such analysis is not strictly applicable.

B. Cavity Expansion Theory

The problem of the expansion of a cavity in an ideally plastic infinite medium has been treated by several authors (Bishop et al., 1945; Hill, 1950), and Vesic (1972) suggested that this can be used to approximate the soil deformation during deep penetration. The first attempts to apply spherical cavity expansion theory to deep bearing capacity problems were those of Meyerhof (1951) and Skempton (1951). The relationship proposed was of the form:

$$N_k = \frac{4}{3}\left[1 + \ln\left(\frac{E}{3c_u}\right)\right] + 1 \qquad (1.4)$$

where E is a representative Young's modulus. Meyerhof suggested that E could be obtained from the initial tangent to the stress-strain curve from triaxial tests. Skempton, on the other hand, proposed that E should be obtained from the tangent of the line through the origin and the 50% failure stress on the stress-strain curve. These recommendations immediately revealed the difficulty of choosing the appropriate value for E. The two proposed procedures are actually inexact attempts to derive a shear modulus of soil from conventional laboratory tests.

Ladanyi (1963) showed that the strain field around an expanding cavity is independent of soil properties and is uniquely determined by the geometry of the problem. He suggested that if the strain path of the soil around the cavity can be reproduced in a suitable laboratory test, then the soil

stresses could be determined. Based on this procedure, Ladanyi proposed a bearing capacity factor in the form of:

$$N_k = (\sigma_p - p'_m)/c_u + 1 \qquad (1.5)$$

where p'_m = initial mean effective stress

σ_p = cavity pressure

This expression gives a typical N_k value of 9. The addition of 1 in the expression was supposed to compensate for the effect of cohesion on the vertical normal stress. This, however, has been questioned by De Beer (1977).

A more general solution of the cavity expansion problem in a Mohr-Coulomb material was presented by Vesic (1972). In particular, the limit pressure for the expansion of a spherical cavity in an incompressible frictionless material subjected to an isotropic effective stress q was shown to be:

$$\sigma_p = F_c c_u + q \qquad (1.6)$$

where:

$$F_c = \frac{4}{3}\left[\ln\left(\frac{G}{c_u}\right) + 1\right] \qquad (1.7)$$

and G = shear modulus of soil

Equation (1.6) is analogous to the bearing capacity equation and F_c is comparable to N_k. For the typical range of $\frac{G}{c_u}$, the value of F_c is between 5.5 and 9.0.

Correlation with experimental data suggested that cavity expansion theory tends to underestimate the N_k factor. Al-Aykati (1977) conducted a

series of penetrometer model tests in clay and found that a better correlation between the experimental data and the theoretical prediction could be obtained if the cone factor is defined as:

$$N_k = 1.42\ F_c \tag{1.8}$$

Baligh (1975) and Baligh & Vivatrat (1979), also working from cavity expansion theory, suggested that the bearing capacity equation should be re-defined as:

$$q_c = N_h c_u + \sigma_{ho} \tag{1.9}$$

where: σ_{ho} = in-situ horizontal stress

Based on this equation, a range of N_h of 16 ± 2 was obtained for soil with the typical values of rigidity index, I_r. Equation (1.9) has been used by Lacasse & Lunne (1982) to interpret field data and good correlation with experimental results was obtained.

In addition, cavity expansion theory has also been used as a theoretical basis for deriving empirical correlations between the excess pore pressure and undrained shear strength. Vesic (1972) adopted Henkel's empirical pore pressure equation and obtained the following expression for the excess pore pressure at the cavity wall:

$$\Delta u = \left[4\ln(I_r)^{1/3} + 0.943\alpha_f\right]c_u \quad \text{- spherical cavity} \tag{1.10}$$

and

$$\Delta u = \left[2\ln(I_r)^{1/2} + 0.817\alpha_f\right]c_u \quad \text{- cylindrical cavity} \tag{1.11}$$

where: α_f = Henkel's pore pressure parameter at failure

It has generally been accepted that cylindrical cavity expansion solution is relevant for predicting the pore pressure around the shaft and spherical cavity expansion is appropriate for the tip of a penetrometer. Roy et al. (1981) compared the prediction based on Equations (1.10) and (1.11) with the results obtained from jacked pile tests. A good fit of the experimental data at the tip level was achieved by using the cylindrical cavity expansion solution. A similar trend has also been observed by Tavenas et al. (1982) who suggested that cylindrical rather than spherical cavity expansion provides a better description of soil behaviour around the penetrometer tip. These proposals appear to raise doubt about the accepted convention that spherical cavity expansion is the suitable model for the pile tip.

Butterfield & Bannerjee (1970) presented a solution for the expansion of a cylindrical cavity in a von Mises material. The maximum pore pressure on the cavity wall was found to lie between 4 and 6.5. Although there was a mathematical error in the analysis, the analytical result was reported to agree with published field data by Lo & Stermac (1965) and Koizumi & Ito (1967). Randolph & Wroth (1979) have also analysed the cavity expansion problem using an elastic-perfectly plastic soil model. The maximum excess pore pressure at the cavity wall was found to be:

$$\Delta u = c_u \ln(I_r) \qquad (1.12)$$

This result was supported by a finite element analysis by Carter et al. (1979) using a Cam-Clay model. Similar results have also been presented by Battaglio et al. (1981) who compared the cavity expansion prediction with pore pressure measured by the Torstensson probe. Good agreement was obtained using cylindrical cavity expansion and values of rigidity index derived from K_o consolidated direct simple shear tests.

More recently, Sagaseta (1984) investigated the general problem of the expansion of a cylindrical cavity with friction on the cavity wall in an anisotropic soil. For the special case of zero friction and isotropic soil state, the solution is equivalent to the expressions derived by Gibson & Anderson (1969).

From the above review, it may be stated that the application of cavity expansion theory for the prediction of soil strength from measured cone resistance has met with limited success. Cavity expansion theory generally under-predicts the cone factor, N_k. Correlation between Δu and c_u is hampered by the ambiguity in the choice of the cavity type which should be used. Several authors (Tavenas et al., 1982; Baligh, 1986) have discussed the inadequacy of this approach. Among the criticisms raised was that the actual shape of the penetrometer cannot be modelled by cavity expansions. A more significant problem, however, is the over-simplication in modelling the cone penetration process by a one dimensional analysis. The strain paths of soil during cone penetration are very complicated and cannot be reproduced by cavity expansion. Thus, cavity expansion theories, no matter how generalised and refined, will not give an accurate description of the stress state around a cone. The limitation of this theory is apparent in the poor correlation between the predicted results and experimental data.

C. Other Theories

A major development of Ladanyi's concept of stress calculation based on a unique strain field was given by Levadoux & Baligh (1980). The principles of this new development is encapsulated in an approximate analytical procedure called the strain path method. Using this approach, the quasi-static penetration process is modelled as a steady flow of soil past a stationary penetrometer. Soil strains are estimated from an approximate

velocity field and the stresses in the soil around the penetrometer are evaluated by integrating the strain paths of the soil elements. A detailed discussion of the numerical procedures involved is included in Chapter 2 because the principles of this approximate method form the basis of the analytical studies performed in this thesis.

Apart from the theoretical approaches described above, the conventional finite element method has also been used to solve the cone penetration problems. De Borst & Vermeer (1984) analysed the case of a penetrometer placed in a pre-bored hole. Incremental displacement controlled finite element analysis was carried out until a limit state was reached. For this purpose, the limit state was defined as the condition when the load on the penetrometer did not change with further increase in the cone displacement. It was assumed that the states of stress and strain around the cone at limit state are similar to those which exist in a steady state penetration process. For a penetrometer with a rough surface, an N_k value of 10.2 was obtained.

De Borst (1982) also suggests that for normally consolidated clay, soil stiffness does not influence the cone factor, N_k. This finding is at variance with the trend suggested by cavity expansion theory. No explanation to this apparent discrepancy was given and further study is necessary to verify this tentative suggestion.

1.3 Strain Path Analysis of the Cone Penetration Test

In this thesis, the quasi-static penetration of a penetrometer is analysed by the strain path method. When the soil mass is assumed to be infinite (e.g. in deep penetration), the penetration process can be modelled by a steady flow of soil past a stationary penetrometer. The basic principles of the solution procedure are outlined in Chapter 2. The

application of the method is illustrated with a simple pile problem. The velocities of the soil elements are estimated from the flow field of an ideal fluid. Although only the inviscid flow solution was used in this thesis, provision has been made for the possibility of using a viscous flow field for estimating the soil velocities. The numerical algorithm for solving the fluid flow problem is presented in Chapter 3.

Chapter 4 deals with the detailed implementation of the strain path method for stress calculations using a finite difference formulation. Since the velocity field is only approximate, the computed stresses are inexact. Various attempts were made to use the approximate stress field to improve the initial velocity estimate. Three different methods have been tried and the details of the correction procedures are described in Chapter 5. The stresses computed from the strain path method are presented in Chapter 6.

In order to assess the acceptability of the strain path solution, an independent numerical study has also been carried out. This was based on a large strain finite element analysis of the cone penetration problem. The soil was modelled by 15-node cubic strain triangular elements since this has been shown to be the lowest order element which is suitable for limit load calculations. The detailed formulation of the finite element analysis is presented in Chapter 7. The accuracy of the finite element program was checked by using it to solve some test problems with known solutions. Extensive comparisons were made between the strain path and finite element solutions and these are presented in Chapter 8.

The dissipation of excess pore pressure around a cone penetrometer was investigated using Terzaghi-Rendulic three dimensional consolidation theory. The governing equation was formulated in finite difference form using the Alternating-Direction-Implicit (A.D.I.) method. The initial pore pressure

distribution in the soil was evaluated using Henkel's empirical pore pressure equation. This is considered to be justified because a comprehensive pore pressure model for soil is not currently available. Parametric studies of the various factors which influenced dissipation have also been included. The details of these dissipation analyses are presented in Chapter 9.

Chapter 2

Strain Path Method

2.1 Introduction

Experimental observations of deep penetration problems (Rourk, 1961; Vesic, 1963; Szechy, 1968) indicate that soil deformations due to the penetration of piles and penetrometers are similar even though the properties of the soils may be very different. This led Baligh (1985) to speculate that deep steady penetration problems in soil are basically strain-controlled and that the associated deformations are not sensitive to material behaviour. He also argued that, due to the severe kinematic constraints that exist in deep foundation problems, soil deformations can be estimated with a reasonable degree of accuracy from kinematic considerations alone. This led to a new approximate method of analysis which was called the strain path method.

In this chapter, the essential features of the strain path method in undrained, deep steady penetration analysis are described. The application of the method is illustrated with the analysis of a "simple pile" problem.

2.2 Application of Strain Path Method

The quasi-static penetration of a cone penetrometer into a homogeneous soil is a steady state problem. For an observer moving with the penetrometer, the deformation pattern in the soil does not vary with time. Accordingly, by changing the reference co-ordinate system, the penetration process can be modelled by a steady flow of soil past a stationary penetrometer. With respect to this reference system, the paths of the soil particles are defined by streamlines.

A complete solution to the deep penetration problem consists of the determination of the states of stress and strain in the soil. In the strain

path method, this solution is achieved by the following procedure for an undrained total stress analysis:

(1) The initial total stresses and, if necessary, the hydrostatic pore pressure in the soil are estimated.

(2) An approximate velocity field for the soil around the penetrometer is obtained based on some simplifying assumptions. This velocity estimate must be consistent with the boundary conditions of the problem.

(3) The strain rates in the soil are evaluated by differentiating the velocities with respect to the fixed spatial co-ordinate system.

(4) The strain paths of soil elements are calculated by integrating the strain rates along streamlines.

(5) By adopting an appropriate constitutive soil model, the deviatoric stresses which correspond to a given strain path are computed.

(6) The total mean pressure is evaluated from one of the two equilibrium equations (or some linear combination of the two equations). At this stage only one of the two equilibrium equations can be satisfied.

(7) The error in the stress solution is computed by examining the remaining equilibrium equation. If the margin of error is unacceptable, the initial deviatoric stresses are used in a corrective scheme to obtain an improved estimate for the velocity field.

(8) If the effective stresses are required, the excess pore pressure in the soil are estimated by using an appropriate model.

2.2.1 Velocity Field

Most of the existing experimental approaches to the deformation studies of deep penetration consist of visual records of deformation pattern by means of some photographic techniques (Rourk, 1961; Randolph et al., 1979). Recently, more advanced experiments using X-ray equipment (Randolph, 1979) and the photo-elasticity method (Allersma, 1982) have also been attempted. While these measurements are suitable for determining the deformation and the velocity field around the penetrometer, they are not suitable for stress computation (Levadoux & Baligh, 1980). The main objection concerns the inherent errors in such measurements, which are compounded by the process of differentiation to obtain the strain in soil. The stress solution based on these strain values therefore contains an intolerable margin of error.

In the strain path method, soil strains are evaluated from a velocity field estimated on the basis of kinematic considerations alone. As a first approximation, it has been suggested that this velocity field can be derived from the flow solution of an inviscid, incompressible fluid.

2.2.2 Stress Strain Relationship

The strain paths of soil due to cone penetration are very complex, involving very large strain rates and strains. It is as yet not possible to duplicate such complicated strain paths in the laboratory. In a theoretical study, however, the stress-strain behaviour is usually modelled by a suitable

constitutive relationship. In steady penetration, soil stresses are evaluated by integrating the constitutive equations along streamlines. This process can then be repeated along as many streamlines as is necessary to obtain sufficient detail of the stress field around the penetrometer.

2.3 Simple Pile Solution

The flow of an incompressible, inviscid fluid around a regular body of revolution (Rankine-body) is a well-researched problem in Fluid Mechanics. Such problems are usually solved by superimposing a suitable distribution of sources and sinks in a uniform flow. The stream function formulation has proved to be particularly convenient since many complicated flow patterns can be obtained by superimposing the stream functions of the individual sources and sinks. In steady flow. this formulation has the added advantage that lines of constant stream function also represent particle paths.

The application of the strain path method will be illustrated in the following sections with a simple example. The problem consists of a single source in a uniform flow and the solid body of revolution generated is termed a "simple pile" by Baligh (1986a).

2.3.1 Formulation

The flow field around a simple pile is axially symmetric, and it is convenient to adopt a cylindrical co-ordinate system. The velocity components v_r and v_z in the directions of the co-ordinates axes (r,z) respectively are defined as:

$$v_r = \frac{1}{r}\frac{\partial \psi}{\partial z} \; ; \qquad v_z = -\frac{1}{r}\frac{\partial \psi}{\partial r} \tag{2.1}$$

The stream function at a point P with coordinate (r,z), due to a point source at the origin is:

$$\psi_s = \frac{Q}{4\pi} \cos\phi \tag{2.2}$$

where: $$\phi = \tan^{-1}(\frac{r}{z}) \tag{2.3}$$

$$Q = \text{Source strength (volume/time)} \tag{2.4}$$

The stream function of a uniform flow with velocity V_o in the positive z direction is:

$$\psi_u = -\frac{r^2}{2} V_o \tag{2.5}$$

By the principle of superposition, the stream function of a flow system consisting of a point source in a uniform flow is given by:

$$\psi = \frac{Q}{4\pi} \cos\phi - \frac{r^2}{2} V_o \tag{2.6}$$

Substituting equation (2.6) into (2.1), we obtained:

$$v_r = \frac{Q}{4\pi\rho^2} \sin\phi \; ; \qquad v_z = V_o + \frac{Q}{4\pi\rho^2} \cos\phi \tag{2.7}$$

Far ahead of the pile tip, $z \to -\infty$ and $\phi \to 180^\circ$, the stream function at a point located at a radial distance r_o from the axis is given by:

$$\psi = -\frac{Q}{4\pi} - \frac{V_o r_o^2}{2} \tag{2.8}$$

Substituting equation (2.8) into (2.6), the equation of the streamline in the simple pile problem is found to be:

$$r^2 = r_o^2 + \frac{1}{2} R^2(1 + \cos\phi) \tag{2.9}$$

where: $$R = \left[\frac{Q}{\pi V_o}\right]^{1/2} \tag{2.10}$$

2.3.2 Geometry of a Simple Pile

In an axisymmetric problem, the flux, q, enclosed by any stream tube (i.e. the body of revolution generated by a streamline) at radius r is given by the equation:

$$q = \int_0^r v_z \, 2\pi r dr \tag{2.11}$$

By definition, the flux enclosed within the simple pile boundary must be equal to Q, the strength of the point source. Substituting Q and v_z into equation (2.11), the profile of the simple pile is given by:

$$r_p^2 = \frac{1}{2} R^2(1 + \cos\phi) \tag{2.12}$$

where r_p is the radius of the simple pile and ϕ is the polar angle as shown in Figure 2.1.

The tip of the simple pile is defined as the point along the axis at which the vertical velocity component vanishes. This is found to be located at:

$$z = -\frac{R}{2} \tag{2.13}$$

The radius of a simple pile increases asymtoptically to a value R as z approaches infinity. For all practical purposes, however, it can be considered to be equal to R when the distance from the tip is greater than 4R.

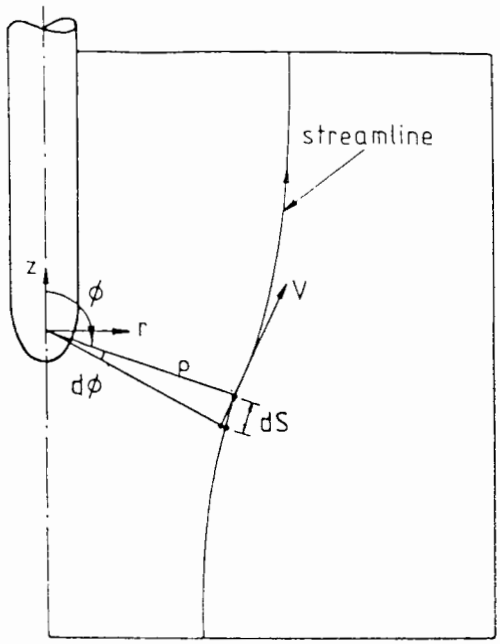

Figure 2.1 Simple Pile Problem: Definition Sketch

2.4 Undrained Simple Pile Penetration into Clay

The strain path approach assumed that soil deformation caused by simple pile penetration can be approximated by the flow field of an inviscid fluid. Therefore, the stream function solution described in the previous section can be used to compute the strains in the soil. The geometry of the problem is illustrated in Figure 2.1 where, for the sake of clarity, the streamline profile has been exaggerated. In the present analysis, soil deformation is described by a natural strain measure which is defined as:

$$\varepsilon_{ij} = \int_0^t \dot{\varepsilon}_{ij}\, dt + \varepsilon_o \qquad (2.14)$$

where $\dot{\varepsilon}_{ij}$ is the strain rate tensor. The in-situ strain, ε_o, can be considered to be zero without loss of generality. The strain rate components are evaluated from the gradients of the velocity as:

$$\dot{\varepsilon}_{rr} = \frac{\partial v_r}{\partial r} = \frac{V_o R^2}{4\rho^3}(\cos^2\phi - 2\sin^2\phi) \tag{2.15}$$

$$\dot{\varepsilon}_{zz} = \frac{\partial v_z}{\partial z} = \frac{V_o R^2}{4\rho^3}(\sin^2\phi - 2\cos^2\phi) \tag{2.16}$$

$$\dot{\varepsilon}_{\theta\theta} = \frac{v_r}{r} = \frac{V_o R^2}{4\rho^3} \tag{2.17}$$

$$\dot{\varepsilon}_{rz} = \frac{1}{2}\left(\frac{\partial v_r}{\partial z} + \frac{\partial v_z}{\partial r}\right) = \frac{V_o R}{4\rho^3}(-\sin 2\phi) \tag{2.18}$$

Substituting these strain rate expressions into equation (2.14), it is possible to express the strain integral as a function of ϕ only (Appendix 2A). Evaluating this integral with the relevant boundary conditions gives the following analytical solutions for strains:

$$\varepsilon_{rr} = F_1(\phi) + (1 - \tfrac{3}{2}B^2)F_2(\phi) \tag{2.19}$$

$$\varepsilon_{zz} = -F_1(\phi) - \tfrac{1}{2}(1 - 3B^2)F_2(\phi) \tag{2.20}$$

$$\varepsilon_{\theta\theta} = -\frac{1}{2}F_2(\phi) \tag{2.21}$$

$$\varepsilon_{rz} = -\frac{3}{2}\left[(2B^2 - 1)\left(\frac{\pi-\phi}{2}\right) + B\sin\phi - \frac{\sin 2\phi}{4} - 2B(B^2 - 1)^{0.5}\tan^{-1}\left(\left(\frac{B+1}{B-1}\right)^{0.5}\cot\left(\frac{\phi}{2}\right)\right)\right] \tag{2.22}$$

where:

$$F_1(\phi) = 3(1 + \cos\phi)\left[\left(\frac{r_o}{R}\right)^2 + \frac{3}{4} - \frac{\cos\phi}{4}\right] \tag{2.23}$$

$$F_2(\phi) = \ln\left(1 + \frac{1}{2}\left(\frac{r_o}{R}\right)^2(1 + \cos\phi)\right) \tag{2.24}$$

$$B = 2\left(\frac{r_o}{R}\right)^2 + 1 \qquad (2.25)$$

For the case when $\frac{r_o}{R}$ is very large, these expressions reduce to the approximate solutions derived by Baligh (1985).

Once the strain path of a soil element has been evaluated, the corresponding stress path can be calculated using a suitable soil model. For the sake of clarity a simple and yet relevant constitutive model has been selected and the soil was modelled as an elastic-perfectly plastic material obeying the von Mises yield criterion. For this constitutive model, closed form expressions which relate the stress increments to strain increments along a straight strain path exist (Booker, 1984). These expressions are only applicable when the rotation rates are zero. Since the simple pile problem is based on an irrotational flow system, these could be used to compute the stress changes.

The strain path due to simple pile penetration is not straight, so the stress calculation must proceed incrementally by approximating the strain path by small straight line sections. Beginning at a point far ahead of the pile tip, the strain increments experienced by a soil element as it traversed a small distance along the streamline is evaluated using equations (2.19) to (2.22). The corresponding stress increment is computed using the analytical stress update equations. When this calculation is carried out along the entire length of the streamline, the complete stress path of soil due to simple pile penetration is obtained.

2.4.1 Stress and Strain Due to Simple Pile Penetration

The stress paths and strain paths in the soil due to simple pile penetration are believed to be representative of deep penetration problem in

general. The analytical solutions afforded by this simple problem may help to shed light on the important features of soil behaviour during deep penetration. With this objective in mind, the strain and stress changes due to simple pile penetration are analysed in some detail.

In an axisymmetric problem, the stress tensor is completely defined by the four non-zero components σ_{rr}, σ_{zz}, $\sigma_{\theta\theta}$ and τ_{rz}. It is possible to represent the deviatoric terms of the stress tensor graphically by expressing it in terms of three deviatoric stresses (Baligh, 1986a) which are defined as:

$$S_1 = \sigma_{zz} - \frac{1}{2}(\sigma_{rr} - \sigma_{\theta\theta}) \tag{2.26}$$

$$S_2 = \frac{\sqrt{3}}{2}(\sigma_{rr} - \sigma_{\theta\theta}) \tag{2.27}$$

$$S_3 = \sqrt{3}\ \tau_{rz} \tag{2.28}$$

In the stress space defined by three mutually orthogonal axes S_1, S_2 and S_3, the distance from a stress point to the origin is proportional to the second stress invariants, I_2:

$$I_2 = \frac{\sqrt{2}}{3}\left(S_1^2 + S_2^2 + S_3^2\right)^{0.5} \tag{2.29}$$

In addition, three deviatoric strain components can be defined such that the stress-strain behaviour in the elastic range is described by:

$$E_i = \frac{S_i}{3G} \qquad i=1,\ 2,\ 3 \tag{2.30}$$

where:

$$E_1 = \varepsilon_{zz} \tag{2.31}$$

$$E_2 = \frac{1}{\sqrt{3}}(\varepsilon_{rr} - \varepsilon_{\theta\theta}) \tag{2.32}$$

$$E_3 = \frac{2}{\sqrt{3}}\ \gamma_{rz} \tag{2.33}$$

It should be noted that E_1 represents the strain mode in a triaxial compression test; E_2 corresponds to the strain mode in a pressuremeter test and E_3 is similar to the strain mode in a direct shear test. The soil strains as represented in equations (2.31) to (2.33) can similarly be mapped onto a strain space described by three orthogonal axes, E_i. In this strain space, the locus of successive strain states denotes the strain path. The distance from a point in this strain space to the origin is proportional to the octahedral shear strain, γ_{oct}:

$$\gamma_{oct} = \frac{1}{\sqrt{2}}\left[E_1^2 + E_2^2 + E_3^2\right]^{1/2} \qquad (2.34)$$

This octahedral shear strain is a good measure of the level of straining to which a soil element has been subjected.

2.4.2 Strain Paths

A graphical representation of the strain history of soil due to simple pile penetration can be achieved by plotting the projections of the strain path on three planes normal to the E_i axes. Figure 2.2 shows the strain paths in the far field of a simple pile. Significant strain reversals in the E_1 and the E_3 components are observed. These strain reversals may have an important effect on soil behaviour and should be taken into consideration in the selection of a constitutive relationship. The E_2 component increases monotonically to reach a final value which is comparable to the solution predicted by the cavity expansion theory.

The strain paths of three soil elements in the near field of a simple pile are illustrated in Figure 2.3. Close to the pile, the deviatoric E_1 and E_3 components again show significant strain reversals. The shaded region indicates the range of soil strain normally encountered in conventional

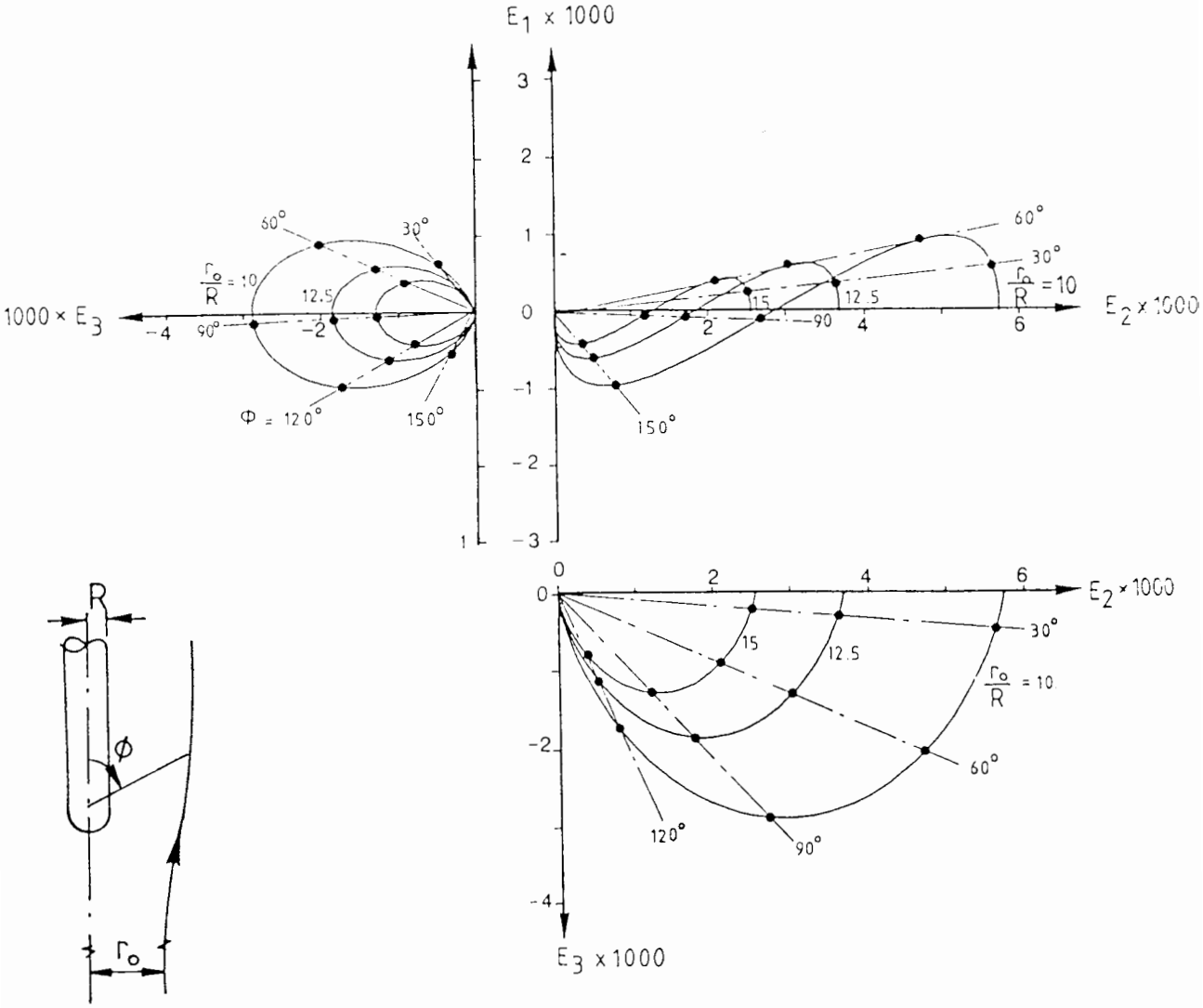

Figure 2.2 Simple Pile Problem: Far Field Strain Paths

laboratory tests. The magnitudes of soil strains due to simple pile penetration are found to be much greater than those obtained in standard laboratory tests.

Far behind the pile tip, E_1 and E_3 are no longer zero (as in the far field) but have finite values. These results should be compared with the cylindrical cavity expansion solution which, being a one dimensional analysis, necessarily shows that E_1 and E_3 are zero. The present analysis, which incorporate the two-dimensional nature of penetration process, can be considered to give a more realistic solution for the strain paths.

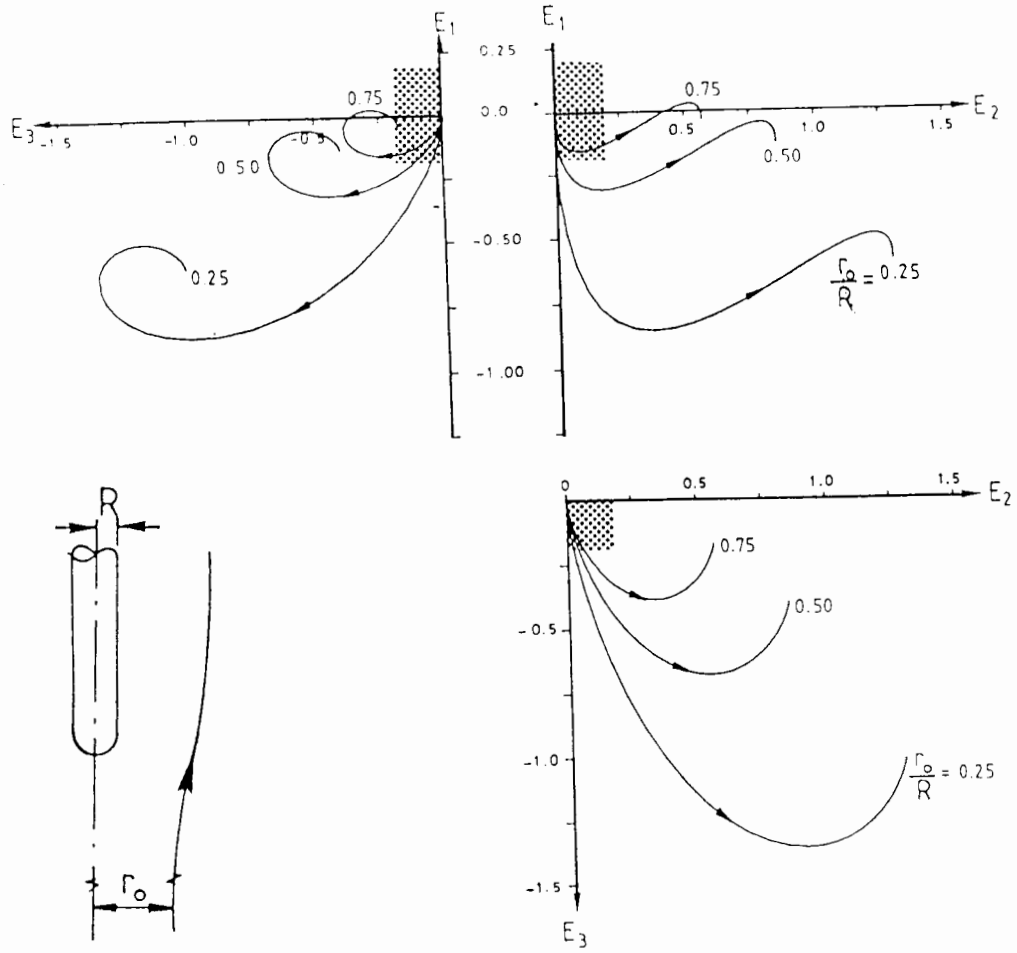

Figure 2.3: Simple Pile Problem - Near Field Strain Paths

2.4.3 Stress paths

In the far field (where the soil stresses are elastic) the deviatoric stress components, S_i, are directly proportional to the deviatoric strain components, E_i, as indicated by equation (2.30). In a stress space defined by three mutually orthogonal axes, S_i, the stress path has the same shape as the strain path. Therefore, by a suitable change of scales of the axes, the curves in Figure 2.3 also represent the stress paths in the far field. The stress deviators, S_i, are found to decay approximately in proportion to $(\frac{R}{r_o})^2$, where r_o is the initial location of the soil element from the axis of penetration. The deviatoric stresses do not increase monotonically but show stress reversals, and important changes in soil stresses occur on a

horizontal plane $\frac{R}{2}$ above the pile tip. On this level, S_1 vanishes, S_3 reaches its maximum value and S_2 reaches half its maximum value. Far behind the pile tip, both S_1 and S_3 tend to zero while S_2 reaches a maximum value.

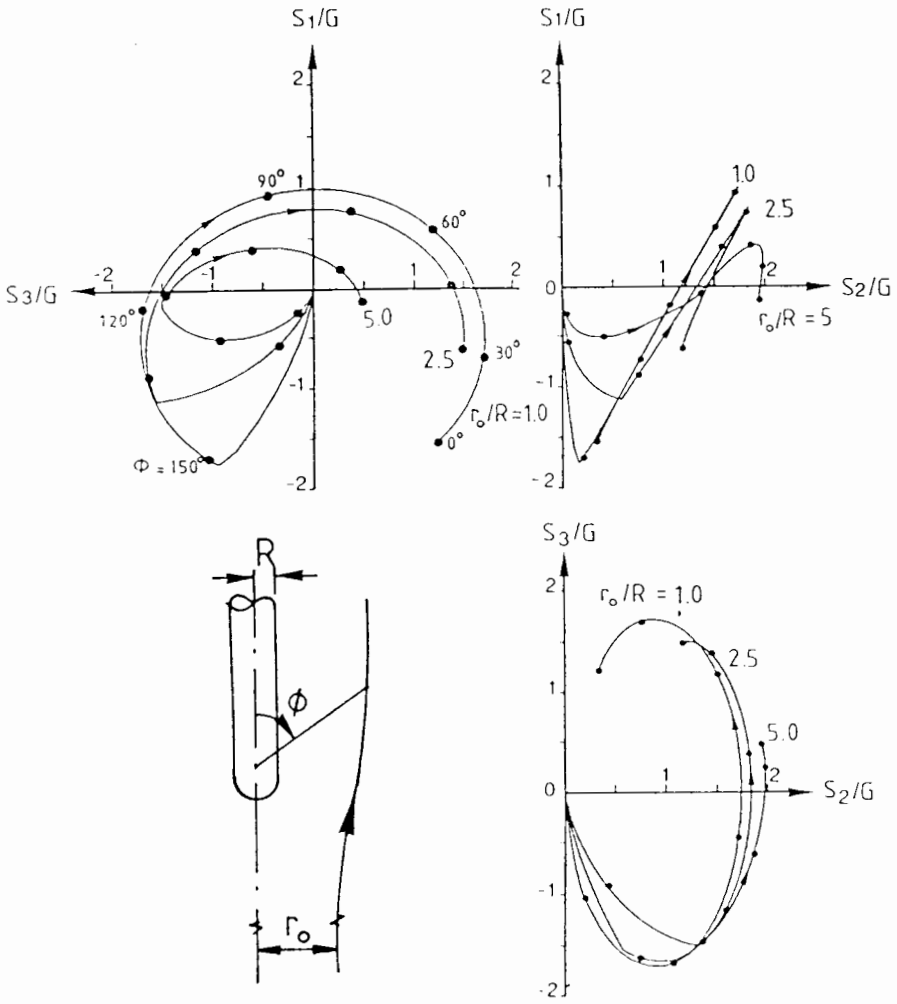

Figure 2.4 Simple Pile Problem: Near Field Stress Paths

For a soil with a rigidity index of 100, the stress paths of three soil elements initially located close to the axis of the pile are shown in Figure 2.4. These are significantly different from the far field stress paths (Figure 2.3). Unlike the stresses in the elastic region, even the S_2 component exhibits large stress reversal. Furthermore, the S_1 and S_3 components do not vanish far behind the pile tip. This result is different

from the cylindrical cavity expansion solution which predicts that S_1 and S_3 are zero.

In addition, the solution very close to the pile (Figure 2.5) also differs from that obtained by Baligh (1986a) who adopted a similar consititutive relationship for soil. Baligh's solution shows that S_3 is zero far behind the tip, while a finite, non-zero S_3 is obtained in the present analysis. The discrepancy between the two results may be caused by the different approaches used in the stress calculations. Baligh's solution ignored the initial elastic response whereas the full range of soil behaviour including elasticity is included in the present calculation.

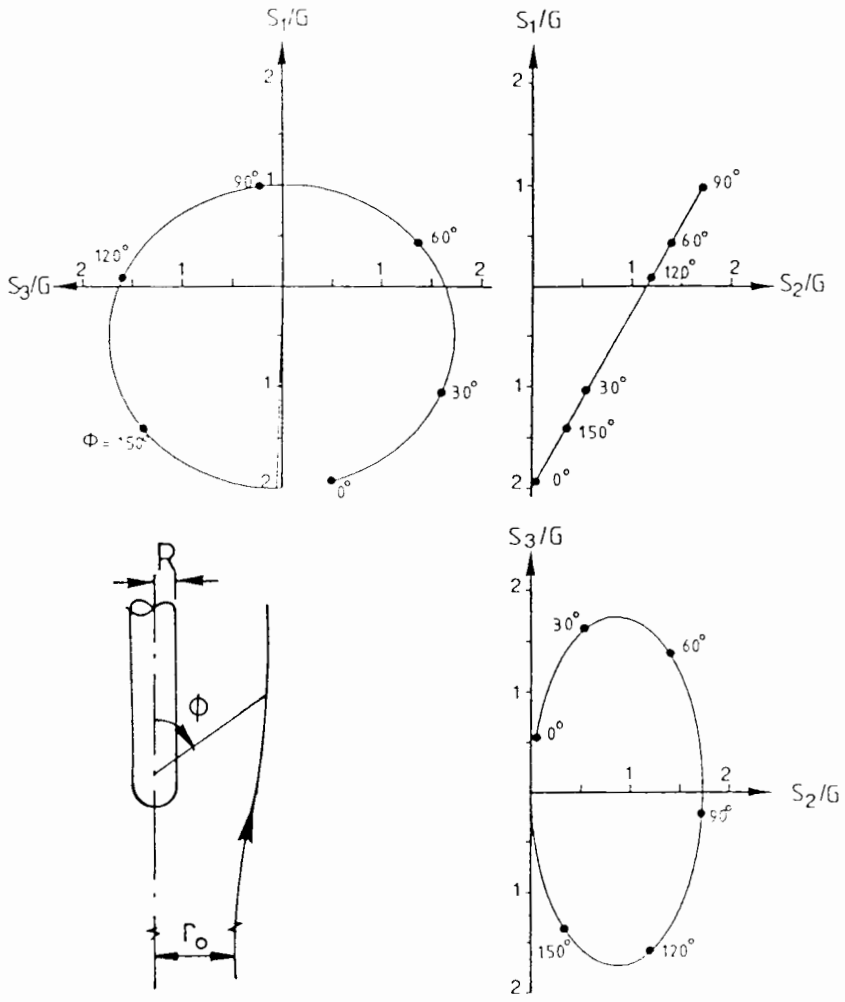

Figure 2.5 Simple Pile Problem - Stress Path of Soil Element at $\frac{r_o}{R} = 0.001$

In the far field where $\frac{r_o}{R}$ is very large, the analytical solutions for strains can be reduced to the approximate expressions derived by Baligh. It has been shown that the soil stresses which correspond to this approximate strain field satisfy the equilibrium equations (Baligh, 1986b) and can thus be considered to be exact. However, the stresses in the near field do not satisfy the equilibrium equations completely and hence are only approximate. Nevertheless, the analysis of a simple pile problem has revealed some important features of deep undrained penetrations which cannot be obtained by other simplified analytical methods. The strain path method can be considered to be superior to the cavity expansion approach because it takes into account the two-dimensional nature of the penetration process.

Appendix 2: Calculation of Strain Path Due to Simple Pile Penetration

The natural strain measure of soil can be expressed in terms of the strain rates as:

$$\varepsilon_{ij} = \int_0^t \dot{\varepsilon}_{ij} dt = \int_0^S \dot{\varepsilon}_{ij} \frac{dS}{V} \qquad (2A.1)$$

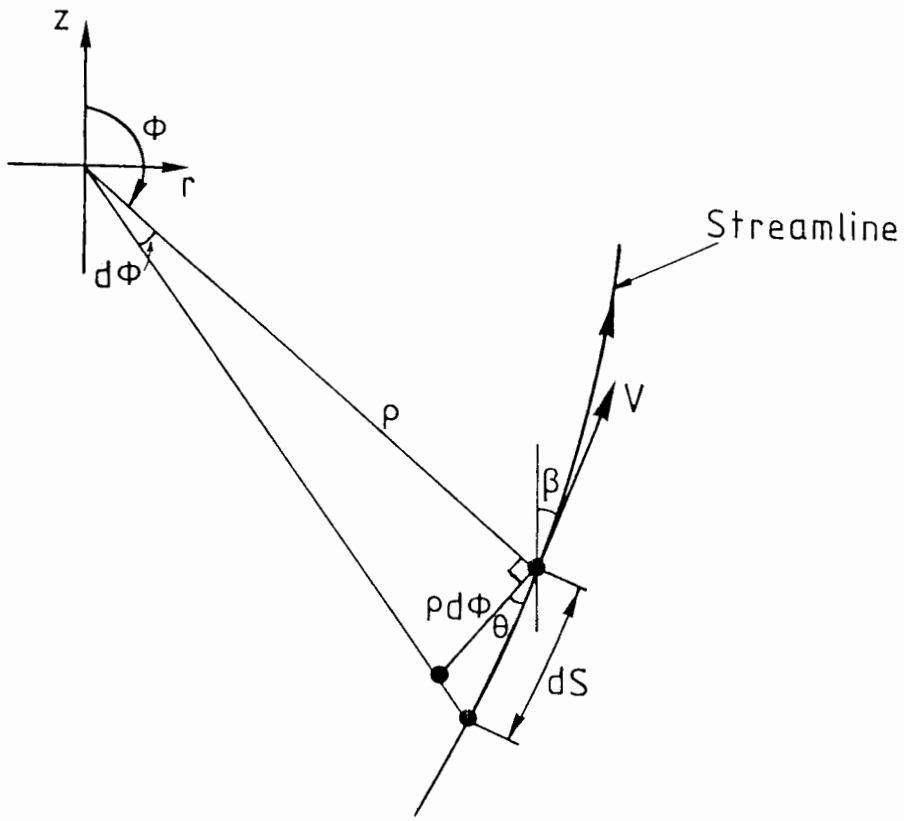

Figure 2A.1 Simple Pile Problem - Determination of Strain Paths

From Figure 2A.1, an infinitesimal arc length along the streamline is given by:

$$dS = \frac{\rho d\phi}{\sin(\phi-\beta)} \qquad (2A.2)$$

The denominator in equation (2A.2) can be expanded using standard trigonometric identities. The sine and cosine of the angle β can be expressed in terms of the velocity components which results in:

$$\frac{dS}{\dot{V}} = \frac{\rho d\phi}{(v_z \sin\phi - v_r \cos\phi)} \tag{2A.3}$$

Therefore,

$$\varepsilon_{ij} = \int_{\pi}^{\phi} \dot{\varepsilon}_{ij} \frac{\rho d\phi}{(v_z \sin\phi - v_r \cos\phi)} \tag{2A.4}$$

Since $\dot{\varepsilon}_{ij}$, v_r and v_z are functions of ϕ only, Equation (2A.4) is a function of ϕ and thus can be evaluated by direct integration.

Chapter 3

Flow Field Computation

3.1 Introduction

The successful application of the strain path method hinges on the assumption that the deformation field of soil during deep undrained penetration can be estimated from the kinematic constraints alone. In this thesis, the flow field of an inviscid fluid is used as a first approximation for the soil velocities. This assumption is essential as a direct determination of soil deformation is virtually impossible.

The computation of the flow field around the cone penetrometer is by no means a trivial problem. Levadoux & Baligh (1980) has attempted to simulate the flow by the method of superimposing a combination of sources and sinks in a uniform flow field. It is difficult to simulate the geometry of the penetrometer exactly by such a method. Some modifications to the profile of the cone are necessary in order to avoid numerical instability and to ensure convergence of the solution procedure. Levadoux & Baligh achieved this by replacing the sharp corners in the cone geometry by circular arcs. One important effect of this idealization was that the resulting solutions underestimated the amount of deformation in the soil around the cone.

In this thesis, the actual shape of the penetrometer will be incorporated in the analysis and provision is made for viscous flow computations. Thus, the superposition method would not be applicable and a numerical method was used instead. The formulation of the flow problem and the solution procedure adopted are described in this chapter. The numerical procedure was tested with some simple flow problems and comparisons were made with published results.

3.2 Mathematical Formulation

The flow around a cone penetrometer is an axisymmetric problem since there is no variation in the circumferential direction. A cylindrical co-ordinate system has thus been adopted (Figure 3.1) and the problem is formulated in an Eulerian reference frame.

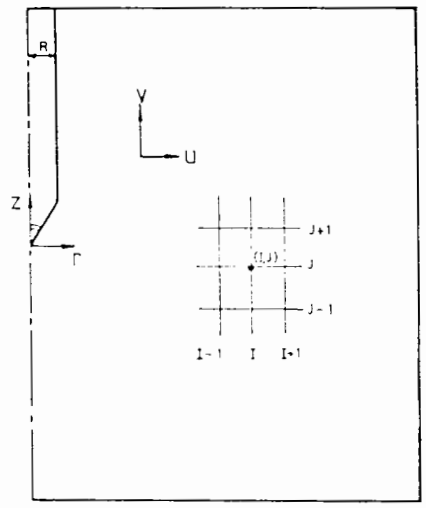

Figure 3.1: Flow around a Cone Penetrometer - Definition Sketch

In the flow computation, the fluid is assumed to be Newtonian. The inviscid solution is obtained as a special case by using a large Reynolds number and the appropriate boundary conditions. In an axisymmetric flow, the governing equations are the relevant form of the Navier-Stokes equations (Batchelor, 1967):

$$\frac{\partial \bar{v}_r}{\partial \bar{t}} + v_r \frac{\partial \bar{v}_r}{\partial \bar{r}} + v_z \frac{\partial \bar{v}_r}{\partial \bar{z}} = -\frac{1}{\bar{\rho}} \frac{\partial \bar{p}}{\partial \bar{r}} + \nu \left(\frac{\partial^2 \bar{v}_r}{\partial \bar{r}^2} + \frac{\partial^2 \bar{v}_r}{\partial \bar{z}^2} + \frac{1}{r} \frac{\partial \bar{v}_r}{\partial \bar{r}} - \frac{\bar{v}_r}{\bar{r}^2} \right) \qquad (3.1)$$

$$\frac{\partial \bar{v}_z}{\partial \bar{t}} + \bar{v}_r \frac{\partial \bar{v}_z}{\partial \bar{r}} + \bar{v}_z \frac{\partial \bar{v}_z}{\partial \bar{z}} = -\frac{1}{\bar{\rho}} \frac{\partial \bar{p}}{\partial \bar{z}} + \nu \left(\frac{\partial^2 \bar{v}_z}{\partial \bar{r}^2} + \frac{\partial^2 \bar{v}_z}{\partial \bar{z}^2} + \frac{1}{\bar{r}} \frac{\partial \bar{v}_z}{\partial \bar{r}} \right) \qquad (3.2)$$

and the continuity equation:

$$\frac{\partial \bar{v}_r}{\partial \bar{r}} + \frac{\partial \bar{v}_z}{\partial \bar{z}} + \frac{\bar{v}_r}{\bar{r}} = 0 \tag{3.3}$$

where $\bar{v}_r$ and $\bar{v}_z$ are the velocity components in the $\bar{r}$ and $\bar{z}$ directions respectively, $\bar{p}$ is the pressure, $\bar{\rho}$ is the fluid density and $\bar{\nu}$ the kinematic viscosity. The bar indicates that these quantities are dimensioned and they can be normalised as follows:

$$(r, z) = \frac{(\bar{r}, \bar{z})}{\bar{R}} \tag{3.4}$$

$$(v_r, v_z) = \frac{(\bar{v}_r, \bar{v}_z)}{\bar{V}_o} \tag{3.5}$$

$$p = \frac{\bar{p}}{\bar{\rho}\,\bar{V}_o^2} \tag{3.6}$$

$$t = \frac{\bar{V}_o \bar{t}}{\bar{R}} \tag{3.7}$$

where $\bar{V}_o$ is the velocity of the uniform flow and $\bar{R}$ the cone radius. Substituting these normalised quantities into equations (3.1) and (3.2), we obtain:

$$\frac{\partial v_r}{\partial t} + v_r \frac{\partial v_r}{\partial r} + v_z \frac{\partial v_r}{\partial z} = -\frac{\partial p}{\partial r} + \frac{1}{Re}\left(\frac{\partial^2 v_r}{\partial r^2} + \frac{\partial^2 v_r}{\partial z^2} + \frac{1}{r}\frac{\partial v_r}{\partial r} - \frac{v_r}{r^2}\right) \tag{3.8}$$

$$\frac{\partial v_z}{\partial t} + v_r \frac{\partial v_z}{\partial r} + v_z \frac{\partial v_z}{\partial z} = -\frac{\partial p}{\partial z} + \frac{1}{Re}\left(\frac{\partial^2 v_z}{\partial r^2} + \frac{\partial^2 v_z}{\partial z^2} + \frac{1}{r}\frac{\partial v_z}{\partial r}\right) \tag{3.9}$$

where Re, the Reynolds number of the flow is defined as:

$$Re = \frac{\bar{V}_o \bar{R}}{\bar{\nu}} \tag{3.10}$$

If the vorticity is defined in the usual way by:

$$\zeta = \frac{\partial v_r}{\partial z} - \frac{\partial v_z}{\partial r} \tag{3.11}$$

and the pressure, p, is eliminated by differentiating (3.8) with respect to z and (3.9) with respect to r and subtracting, then we obtain:

$$\frac{\partial \zeta}{\partial t} = -\left[v_r \frac{\partial \zeta}{\partial r} + v_z \frac{\partial \zeta}{\partial z} - \frac{v_r \zeta}{r}\right] + \frac{1}{Re}\left[\frac{\partial^2 \zeta}{\partial r^2} + \frac{1}{r}\frac{\partial \zeta}{\partial r} + \frac{\partial^2 \zeta}{\partial z^2} - \frac{\zeta}{r^2}\right] \tag{3.12}$$

Equation (3.12) is usually referred to as the vorticity transport equation. In addition, if we define a stream function, ψ, such that

$$v_r = -\frac{1}{r}\frac{\partial \psi}{\partial z} \tag{3.13}$$

$$v_z = \frac{1}{r}\frac{\partial \psi}{\partial r} \tag{3.14}$$

then the continuity equation is automatically satisfied. Substituting for v_r and v_z in equation (3.11) and using the definitions in (3.13) and (3.14) gives:

$$\frac{\partial^2 \psi}{\partial r^2} + \frac{\partial^2 \psi}{\partial z^2} + \frac{1}{r}\frac{\partial \psi}{\partial r} = -r\zeta \tag{3.15}$$

which is a Poisson equation with ζ as the source term.

The flow field is governed by (3.12) and (3.15) in terms of the two flow parameters (ψ, ζ) and a set of relevant boundary conditions. The solution to such a set of equations is in fact primarily governed by the

boundary conditions. A discussion of the appropriate boundary conditions pertaining to this problem will be presented in a later section.

3.3 Numerical Solution Method

The governing equations (3.12) and (3.15) can be solved by using a numerical procedure such as the finite difference method. The particular forms of finite difference expressions which have been used to represent the partial differential equations are described in this section. The overall solution algorithm adopted will also be detailed.

3.3.1 Choice of Finite Difference Mesh

In order to obtain a meaningful solution, it is essential that the numerical procedure is able to model the various aspects of the problem as accurately as possible. In particular, the computation must take into account the infinite extent of the fluid medium associated with the original problem. This requirement demands that the boundaries in the computation mesh are set at a sufficiently large distance away from the cone. In addition, a fine mesh should be used in regions where high gradients of ψ and ζ are expected in order to ensure that a reasonable degree of accuracy is achieved. In view of the limited computer storage available, these two requirements cannot be accomodated at the same time with a uniform mesh. To overcome this problem, a non-uniform mesh has been adopted (Figure 3.2).

In the vicinity of the penetrometer, a fine mesh with small grid interval is adopted. Further away from the cone, the grid spacing gradually increases in size. Whilst this mesh may not be the optimum one possible, the use of non-uniform grid size is unavoidable if the analysis is not to fall prey to excessive computer storage and time requirements.

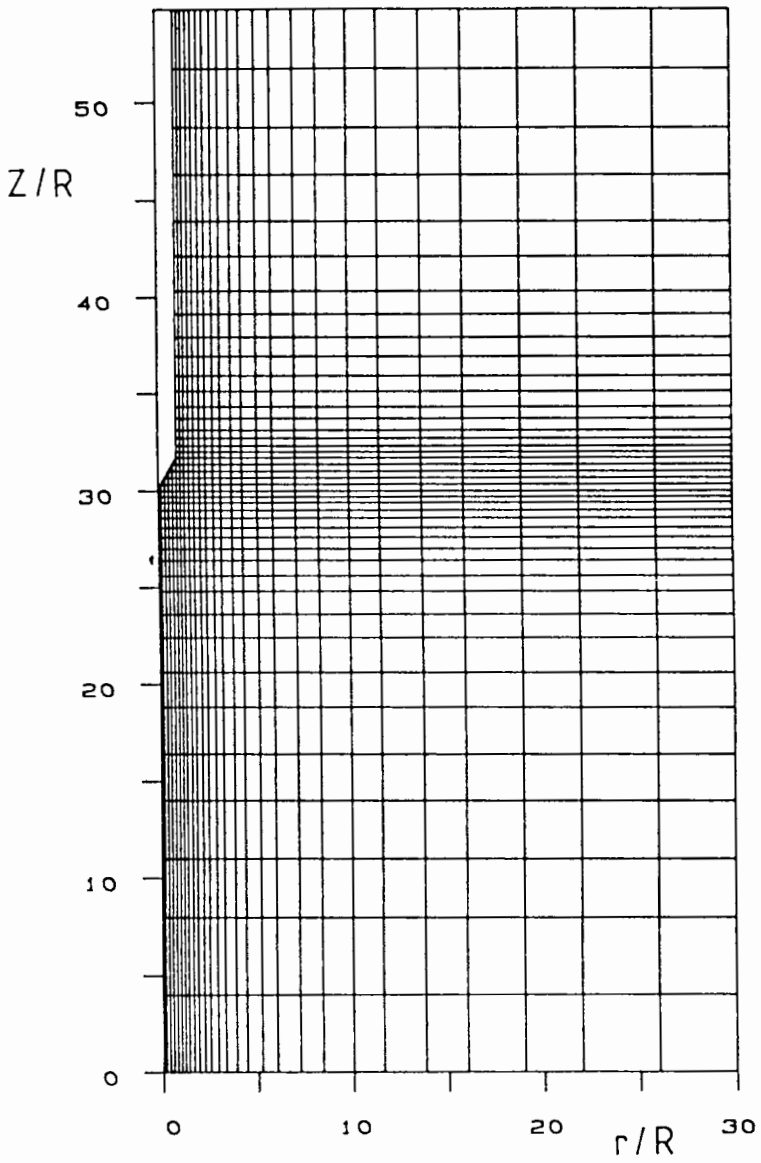

Figure 3.2: Finite Difference Mesh for Cone Penetration Problem

3.3.2 Overall Solution Procedure

The usual algorithm for the numerical solution of Fluid Dynamics problems expressed in vorticity-stream function form (Roache, 1976) has been used here. The main steps in the solution procedure are as follow:

(1) At the beginning of the solution procedure, the boundary values of ψ are calculated and the vorticity, ζ, at each node is initialised to zero. The Poisson equation governing the stream function is solved. This results in a set of stream function values, ψ_{ij}.

(2) Based on the stream function obtained in step 1, the vorticities generated at the boundaries are evaluated.

(3) The vorticity transport equation (3.12) which governs the convection and diffusion of the vorticity is then solved to obtain ζ at each internal nodal point.

(4) At the next time step, the stream function equation is solved subject to the new boundary values for ψ. The vorticity, ζ, computed at the previous time step is used as the source term.

(5) The computational cycle consisting of Steps (2) to (4) is repeated and the variation of ψ and ζ monitored. In a steady flow problem, the cycle of computation is continued until there are negligible changes in the flow variables in consecutive time steps.

3.3.3 The Vorticity Transport Equation

It is possible in a steady state computation to set the $\frac{\partial \zeta}{\partial t}$ term in the vorticity transport equation (3.12) to zero. However, this procedure presupposes the existence of a steady state solution which in fact may not exist at all. If a tight convergence criterion is adopted, the non-existence of a steady state solution will be revealed by the failure of the numerical process to converge. However, if the convergence criterion is not properly chosen, this procedure may lead to a solution which is in fact non-steady.

In this thesis, the time-dependent, transient approach has been used. This approach does not presume, a priori, the existence of a steady state. The solution is allowed to develop freely. If a steady state solution exists, it is revealed by negligible changes of the flow variables in consecutive time steps.

At each time step in the numerical procedure, the vorticity at the internal points of the flow field is updated using a finite difference form of the partial differential equation (3.12). This equation consists of two main parts which reflects the physical laws governing the problem. The portion of the equation involving terms of the form $u\frac{\partial \zeta}{\partial r}$ is called the convective component because it governs the convection of the vorticity in the flow. The second portion, which is pre-multiplied by the reciprocal of the Reynolds number, governs the diffusion of vorticity and is therefore called the diffusive component.

The numerical scheme used, discussed in detail below, is explicit in nature. The solution procedure is thus limited by an upper bound on the allowable time step size.

3.3.4 Finite Difference Representation

For the numerical algorithm to yield a correct solution, the finite difference equations must be consistent with the partial differential equations they are intended to represent. In other words, in the limit as δx, δy and δt approaches zero, the finite difference equation must reduce to the original partial differential equation. Consistency does not only imply the superficial similarity of the appearance but also the physical implications of the equation (Roache), and these include the conservation and transportation properties of the flow.

The numerical scheme adopted here makes use of two particular methods, namely the 'Second Upwind Differencing' and the Dufort-Frankel's substitution, which have been proven to be advantageous in Fluid Dynamics computations. The 'Second Upwind Differencing' method, also called the 'Donor-cell' method, has been used with success by a number of workers (e.g. Gillani & Swanson, 1976; Sobey, 1980). The application of this method ensures that the vorticity is convected only in the direction of flow (transportive property). Unlike in a conventional finite difference equation, velocities in the convective terms are computed at the mid-points between the current node and its neighbours. Backward or forward differencing is then used to represent the derivatives depending on whether the velocities are positive or negative respectively. The velocities used in the difference terms are those evaluated at intermediate points between nodes, while the vorticity values, ζ, remain those represented at the nodal points. If the velocities at the intermediate points are of the opposite signs, central differencing is used.

Dufort-Frankel's substitution is then applied. The purpose of this substitution is to prevent instabilities arising from the viscous vorticity transport terms. This is achieved by rendering the terms partially implicit. Following Gillani & Swanson, the value of $\zeta^{n}_{i,j}$ in both the advective and the diffusive terms are replaced by the average value ($\bar{\zeta}_{i,j}$) over the time steps (n-1) and (n+1). The values of ζ at neighbouring points continue to be represented at time step n. The resulting equation can be re-arranged to give an explicit expression for $\zeta^{n+1}_{i,j}$ in terms of $\zeta^{n-1}_{i,j}$ and ζ at neighbouring points at time level n. This yields:

$$\zeta^{n+1}_{i,j} = A_o\zeta^{n-1}_{i,j} + A_1\zeta^{n}_{i-1,j} + A_2\zeta^{n}_{i,j\ 1} + A_3\zeta^{n}_{i+1,j} + A_4\zeta^{n}_{i,j+1} \qquad (3.16)$$

where the constants A_i (i=0 to 4) are evaluated as shown in Appendix 3A.

3.3.5 Stream Function Equation

Using the time dependent approach, equation (3.15) must be solved at each time step subject to the appropriate boundary conditions. This equation is represented in finite difference form using central differences throughout. The resulting algebraic equation is re-arranged to give an explicit expression for $\psi'_{i,j}$, the value of stream function at the node (i,j) consistent with the stream function values at the neighbouring points:

$$\psi'_{i,j} = B_o r\zeta_{i,j} + B_1\psi_{i-1,j} + B_2\psi_{i,j-1} + B_3\psi_{i+1,j} + B_4\psi_{i,j+1} \qquad (3.17)$$

where B_i are evaluated as shown in Appendix 3A.

It should be noted that $\psi'_{i,j}$ does not necessarily represent the solution of the stream function at the node (i,j). This is because as the calculation proceeds through the mesh, the value of ψ at adjacent nodes will change. Nevertheless, if the procedure is carried out iteratively, the value at each point converges to the correct solution.

Expressed in this primitive form, ψ converges very slowly. Convergence can be speeded up by a procedure called Successive-Over-Relaxation (S.O.R.) first suggested by Southwell (1948). If $\psi^k_{i,j}$ represents the value of ψ after k^{th} iteration, the value of the ψ at the $(k+1)^{th}$ iteration is given by:

$$\psi^{k+1}_{i,j} = \psi^k_{i,j} + \Omega(\psi'_{i,j} - \psi^k_{i,j}) \qquad (3.18)$$

where $\psi'_{i,j}$ is as in equation (3.17) and Ω is a constant called the over-relaxation factor. In computing $\psi'_{i,j}$, the most up-to-date values of ψ at the neighbouring points are used. This means that for those nodes already

updated in the current iteration, values of ψ which correspond to the $(k+1)^{th}$ iteration step are used; and for those nodes yet to be updated, the values at the k^{th} iteration step are adopted instead.

In order to decide when to stop the iteration process, a suitable convergence criterion has to be chosen. The criterion used in this study is:

$$\frac{\Delta\psi_{rms}}{\psi_{max}} \leq \delta \qquad (3.19)$$

where $\Delta\psi_{rms}$ is the root-mean-square value of the change in ψ at all the nodes between two consecutive iterations, ψ_{max} is the maximum stream function value in the computation domain and δ is a small constant. A value of δ in the order of 10^{-6} (depending on the mesh) has been used in this study. Smaller values of δ were found to have very little effect on the solution but required substantially longer computing time.

The effect of varying the value of Ω on the rate of convergence has been studied by many workers (e.g. Frankel, 1950). But except for the simplest problem consisting of a rectangular domain with a uniform grid, no analytical solution for the optimum Ω value is available. Nevertheless, it has been well established that for $1<\Omega<2$, the S.O.R. procedure is unconditionally stable and convergent. Within this range an optimum value of Ω, which is dependent on the mesh used, always exists.

The effect of the Ω value on the number of iterations required for convergence under criterion (3.19) is shown in Figure 3.3. This result is based on a steady flow solution of Equation (3.15) using the mesh shown in Figure 3.2. The stream function at all nodes (except at the boundaries) and the vorticity were initially set to zero. In each case, Ω was set to 1 for the first iteration as it is known that this will speed up convergence

considerably. The graph in Figure 3.3 clearly shows an optimum Ω which results in convergence with the minimum number of iterations. The vorticity for a flow involving Newtonian fluid is generally not zero, but the Ω value derived by this method is still applicable because it is not very sensitive to the variation in ζ.

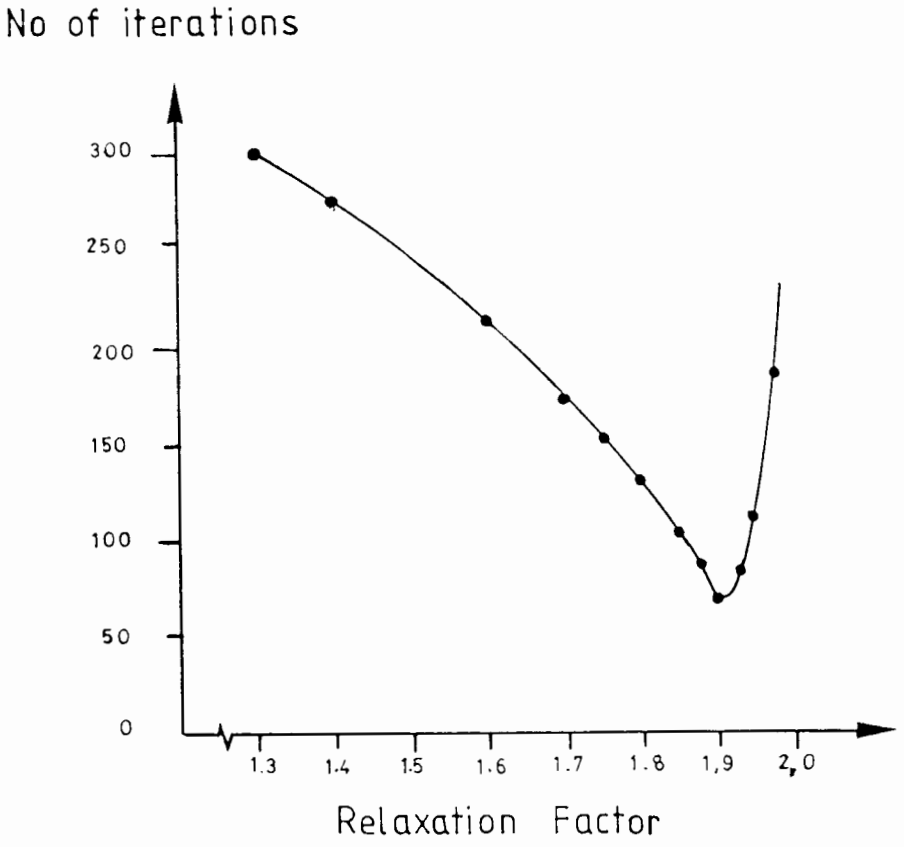

Figure 3.3: Determination of Over-Relaxation Factor, Ω

In a typical calculation, the values of ψ at a given time step are not initially zero but the converged solution from the previous time step. Since the changes in ψ from one time step to the next are generally small, the iteration process begins at each time step (except the first) with a set of ψ values which are very close to the converged solution. Consequently, the number of iterations required for the stream function equation to converge at each time step is very much less than that indicated in Figure 3.3.

3.4 Boundary Conditions

The solution to a set of differential equations such as (3.12) and (3.15) is determined primarily by the boundary conditions. In order to obtain a satisfactory solution, the boundary conditions must be properly specified. In addition, the prescribed values of the field variables at the boundary must be consistent with the physical laws governing the problem. Failure to satisfy these criteria always results in the divergence of the numerical procedure, or worse still, it may converge to a wrong solution (Roache, 1976).

3.4.1 Boundary Conditions for ψ

The boundary conditions for ψ appropriate to the present problem are set down below.

(1) Since the datum of the stream function is arbitrary, ψ on the axis is set to zero. Furthermore, the entire boundary ABCD (Figure 3.4) is a streamline by definition so ψ on the cone face BC and the shaft CD must also be zero.

(2) The far field boundary, EF, models the condition at infinity. The boundary condition can be specified by setting the velocity at EF to V_o, the uniform flow velocity:

$$\frac{1}{r}\frac{\partial \psi}{\partial r} = V_o \tag{3.21}$$

and in finite difference form, this is expressed as:

$$\psi_{m,j} = \psi_{m-1,j} + V_o r_m \Delta r_m \tag{3.22}$$

where m is the grid number of the extreme right hand boundary.

(3) Similarly, the upstream boundary (AF) models a uniform flow condition, so

$$\psi_{i,0} = \frac{V_o r_i^2}{2} \tag{3.23}$$

(4) At the downstream boundary, it is advantageous to constrain the flow as little as possible. This is achieved by requiring the flow to have attained a steady state condition with zero radial velocity. In finite difference form, this is expressed as:

$$\psi_{i,n} = \psi_{i,n-1} \tag{3.24}$$

where n is the grid number for the top boundary

3.4.2 Boundary Conditions for ζ

It should be emphasised that the boundary values of ζ (or its derivatives) must be consistent with the conditions prescribed for ψ. Contradictory boundary conditions for ψ and ζ would inevitably cause problems in the convergence of the numerical procedure. A suitable set of boundary conditions for ζ is described below.

(1) The symmetry condition on the axis (r=0) demands that $v_r=0$ and $\frac{\partial v_z}{\partial r}=0$ and so,

$$\zeta = \frac{\partial v_r}{\partial z} - \frac{\partial v_z}{\partial r} = 0 \tag{3.26}$$

(2) The far field and upstream boundaries model the conditions at infinity where the flow is uniform so ζ is set to zero.

(3) In the downstream boundary, we imposed the steady state condition and set

$$\zeta_{i,n} = \zeta_{i,n-1} \tag{3.27}$$

(4) For viscous fluid flow, the no-slip condition must be applied at the solid wall boundary, giving $v_z=0$. In addition, the penetrometer shaft is assumed to be impermeable, so $v_r=0$. Then ζ on the wall can be written as:

$$\zeta = \frac{\partial v_r}{\partial z} - \frac{\partial v_z}{\partial r} = -\frac{1}{r}\frac{\partial^2 \psi}{\partial r^2} \tag{3.28}$$

By using the Taylor's expansion of ψ at the node adjacent to the wall, it can be shown that the wall vorticity is,

$$\zeta = -\frac{2}{r}\left(\frac{\psi_{w+1} - \psi_w}{(\Delta r)^2}\right) \tag{3.29}$$

where: ψ_w = stream function on the wall

ψ_{w+1} = stream function adjacent to the wall

Δr = grid between the two nodes

The boundary value for ζ on the cone face can be derived in a similar manner.

If an inviscid solution is required, the boundary conditions for ζ should be altered to reflect the fact that the fluid slips at the solid boundary. The boundary value for the vorticity is then expressed as:

$$\zeta_w = \zeta_{w+1} \tag{3.30}$$

A summary of the boundary conditions for ψ and ζ are presented in Figure 3.4.

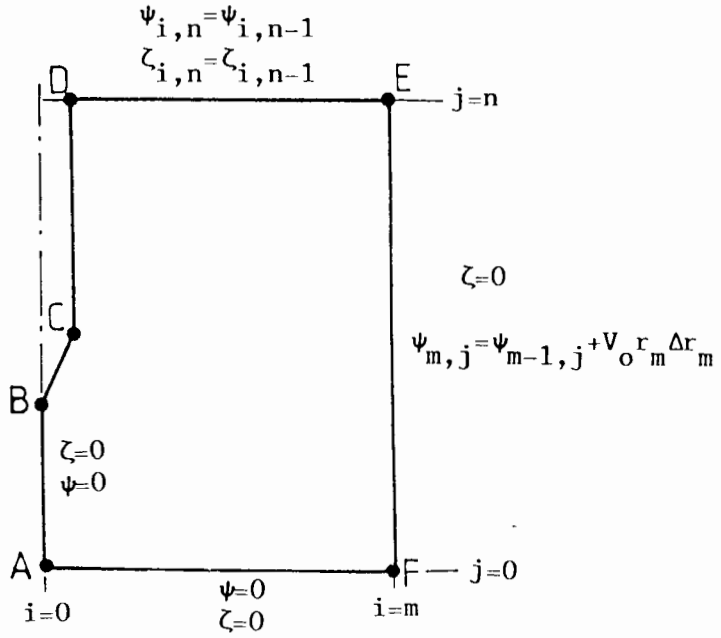

Figure 3.4: Boundary Conditions for ψ and ζ

3.5 Verification of the Computer Program

The accuracy and stability of the finite difference formulation described in this chapter is checked by using it to solve some simple flow problems. The object of this exercise is to ensure that the formulation is capable of giving a correct flow solution. Comparisons between the numerical results and published data will be restricted to primary flow variables such as the stream function. Although this parameter cannot be measured directly, it is usually amenable to flow visualization techniques. On this basis, three test cases have been selected:

1) Steady flow of a viscous, incompressible fluid in a circular conduit with a sudden expansion.

2) Steady flow of a viscous, incompressible fluid in a circular conduit with an abrupt contraction.

3) Steady flow around a circular disc placed normal to the direction of a uniform stream.

3.5.1 Steady Flow In a Circular Conduit with a Sudden Expansion

The flow in a conduit with a sudden expansion is characterized by a geometric condition that imposes separation even for very low Reynolds number. The geometry of the problem is illustrated in Figure 3.5a. Fully developed Poiseuille flows with parabolic velocity profiles are imposed on the upstream and downstream boundaries.

The numerical stream function solution for a flow with a Reynolds number, ($Re = \frac{V_o d}{\nu}$) of 35 is shown in Figure 3.5b. A re-circulation zone is visible downstream of the transition. This result is comparable with the experimental and computational results by Macagno & Hung (1967) which are shown in Figure 3.5c. The agreement between these solutions is exceptionally good. The locations of the point of re-attachment and the centre of re-circulation obtained from the two analyses are nearly identical. The vorticity contours are also very similar to the numerical result given by Macagno & Hung. This is remarkable considering that the computational results were obtained with different finite difference schemes. In addition, the use of a non-uniform mesh (as was used here) does not seem to have caused any loss of accuracy when compared to the computational results by Macagno & Hung which were based on a uniform grid system.

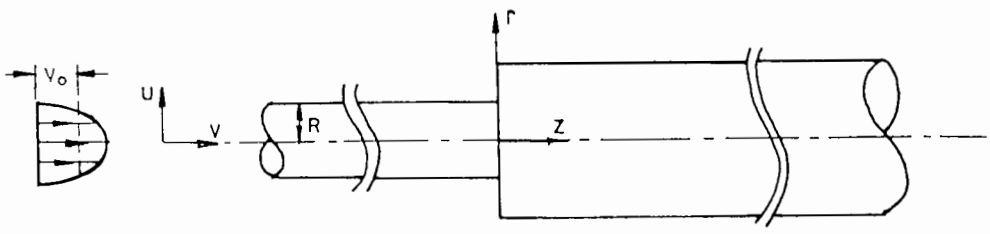

Figure 3.5a: Flow in a Circular Conduit with a Sudden Expansion

Definition Sketch

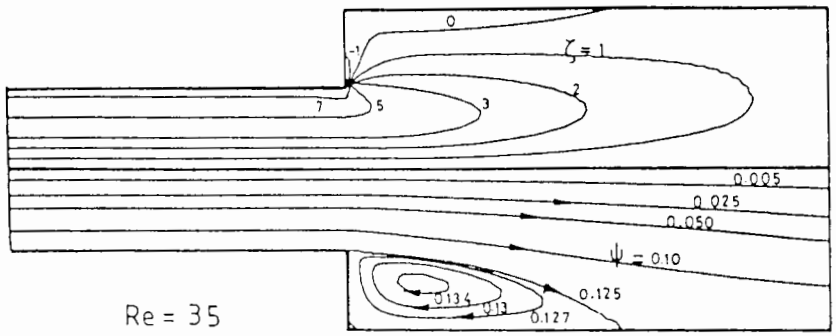

(b)

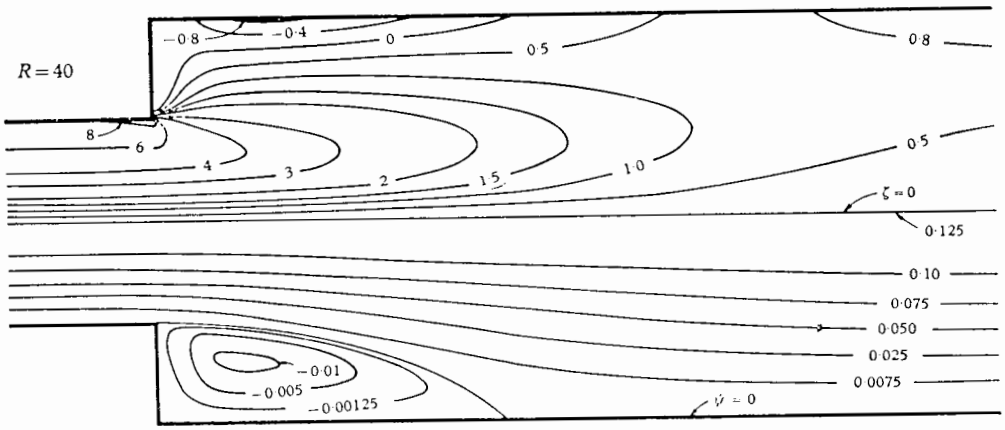

(c)

(d)

Figure 3.5: Flow in a Circular Conduit with a Sudden Expansion

3.5.2 Steady Flow in a Circular Conduit with a Sudden Contraction

The second test case consists of the same arrangement as in the previous problem but with the flow direction reversed. This flow configuration is more severe because the fluid is forced to flow towards a forward facing step. Hence, this test will provide a more rigorous test for the stability of the numerical procedure.

As far as the author is aware, no computational solution of this problem has been published even though a vast amount of literature on the equivalent two-dimensional flow problem is available. Dennis & Smith (1980) analysed a two-dimensional, symmetrically constricted channel flow and obtained a separation zone upstream of the transition. More recently, Mei & Plotkin (1986) analysed the same two-dimensional flow and obtained two zones of separated flow located just upstream and downstream of the constriction. Smith (1979) presented an analytical study of the axisymmetric flow in a pipe with a severe constriction and predicted the existence of two separation zones. Although this analytical result was based on the asymptotic theory involving very high Reynolds number, it is believed that it could be used as a qualitative check on the computed results.

The stream function contours for a Reynolds number of 100 computed by the numerical procedure described here is shown in Figure 3.6. Two zones of separation, as predicted by Smith, are clearly visible. Further confirmation of the accuracy of the numerical results could be obtained from the experimental flow data depicted in Figure 3.6c. (after Rouse, 1956). Good agreement between the experimental and numerical results regarding the shapes and the relative sizes of the two separation zones is apparent.

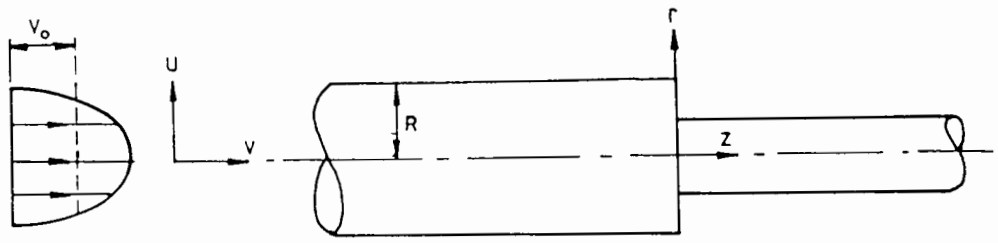

(a)

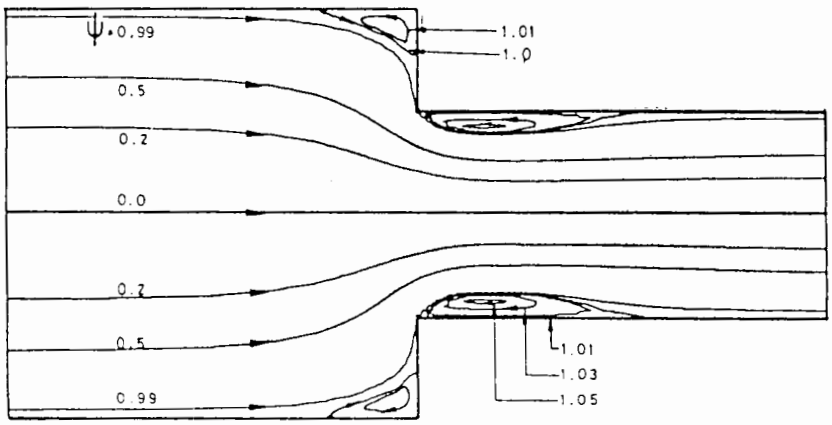

(b)

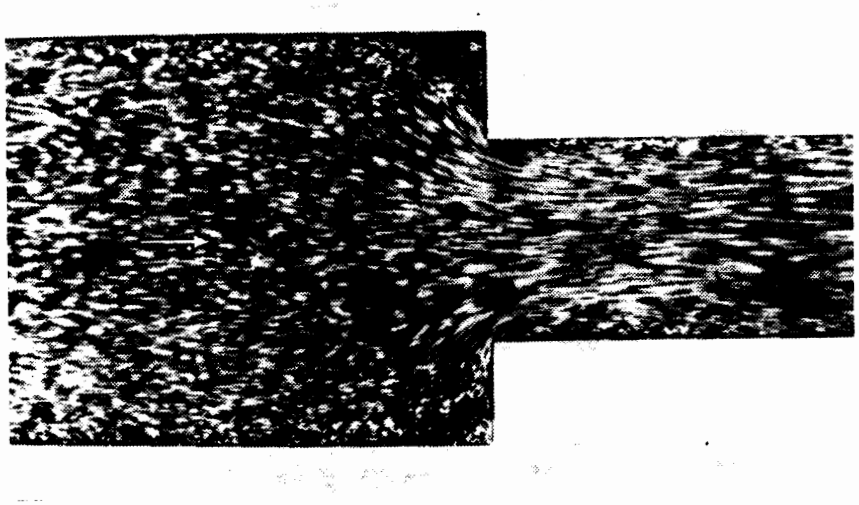

(c)

Figure 3.6: Flow in a Circular Conduit with a Sudden Contraction

3.5.3 Steady Flow around a Circular Disc

The two previous test cases involved flow systems with finite and well defined boundaries. These problems are generally classified as internal flows. The third test case has been chosen to verify the capability of the program for flow computation involving an infinite fluid domain.

The problem consists of a circular disc placed with its plane normal to the flow direction of a uniform stream. The configuration of the problem and the co-ordinate system is indicated in Figure 3.7a. The outer diameter of the disc is R and is bevelled at 45° at the edge. The disc is 0.1 R thick and it is attached on the backface to a cylindrical rod which has a radius 0.1 R.

The contours of the stream function computed for a flow with a Reynold's number of 5×10^4 are shown in Figure 3.7b. As far as the author is aware, no numerical solution for such a flow problem has been published even though numerous solutions have been presented for the equivalent two-dimensional flow around a flat plate. The flow around a circular disc is believed to exhibit similar features to the flow around a normal flat plate. The experimental result of such a two dimensional problem is shown in Figure 3.7c (after Prandtl & Tietjens, 1934). Similar features are observed in the re-circulation zone behind the circular disc. In addition, the average experimental stream function contours obtained by Smyth (1980) from a flow experiment using a Laser-Doppler method also confirmed the general flow pattern computed here.

These test problems have demonstrated that the numerical scheme adopted is suitable for general flow computations. The quality of the numerical results indicated that the boundary conditions have been prescribed

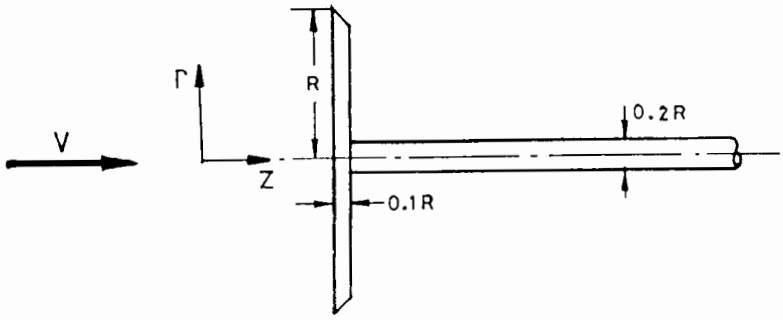

(a)

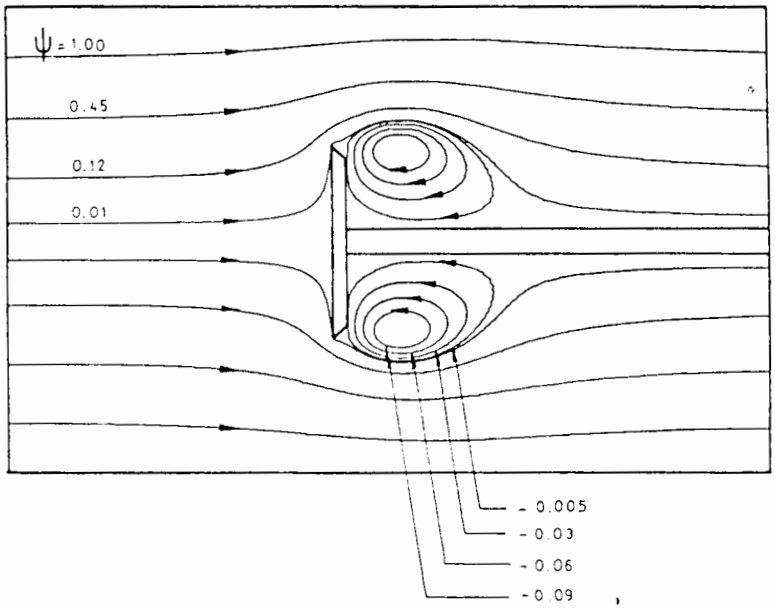

(b)

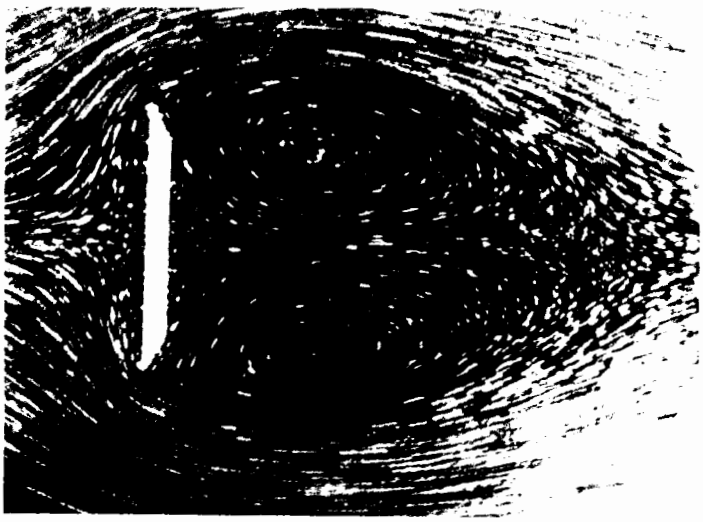

(c)

Figure 3.7: Flow Around a Circular Disc Placed Normal to the Stream

correctly and that the algorithm is numerically stable. It is therefore reasonable to assume that the numerical procedure formulated would provide a reliable initial flow solution for the cone penetration problem.

Appendix 3A: Derivation of Finite Difference Equations

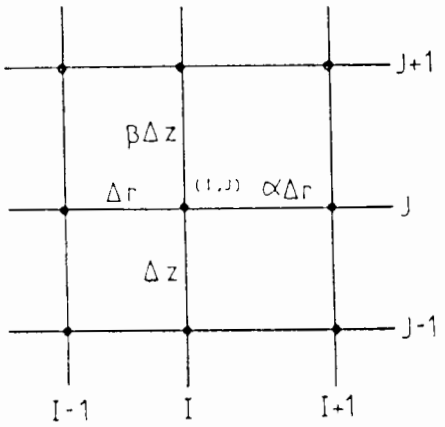

Figure 3A.1: Local Grid System

Consider a nodal point (i,j) with the local grid spacing as shown in Figure 3A.1. The partial derivative of a continuous, differentiable function F(r,z) at node (i,j) can be expressed in finite difference form using central differences as follow:

$$\frac{\partial F}{\partial r} = a_o F_{i,j} + a_1 F_{i-1,j} + a_2 F_{i+1,j} \qquad (3A.1)$$

$$\frac{\partial F}{\partial z} = b_o F_{i,j} + b_1 F_{i,j-1} + b_2 F_{i,j+1} \qquad (3A.2)$$

$$\frac{\partial^2 F}{\partial r^2} = c_o F_{i,j} + c_1 F_{i-1,j} + c_2 F_{i+1,j} \qquad (3A.3)$$

$$\frac{\partial^2 F}{\partial z^2} = d_o F_{i,j} + d_1 F_{i,j-1} + d_2 F_{i,j+1} \qquad (3A.4)$$

where the coefficients a_i, b_i, c_i, and d_i (i=0,1,2) are functions of the grid spacing between node (i,j) and the adjacent nodes. These are summarised in Table 3A.1.

Alternatively, the first order partial derivatives $\frac{\partial F}{\partial r}$ and $\frac{\partial F}{\partial z}$ can be expressed as forward or backward differences.

Using forward differences,

$$\frac{\partial F}{\partial r} = \frac{F_{i+1,j} - F_{i,j}}{\alpha \Delta r} \tag{3A.5}$$

$$\frac{\partial F}{\partial z} = \frac{F_{i,j+1} - F_{i,j}}{\beta \Delta z} \tag{3A.6}$$

and for backward differences,

$$\frac{\partial F}{\partial r} = \frac{F_{i,j} - F_{i-1,j}}{\Delta r} \tag{3A.7}$$

$$\frac{\partial F}{\partial z} = \frac{F_{i,j} - F_{i,j-1}}{\Delta z} \tag{3A.8}$$

i=	0	1	2
a_i	$\frac{\alpha - 1}{\alpha \Delta r}$	$\frac{-\alpha}{(1+\alpha)\Delta r}$	$\frac{1}{\alpha(1+\alpha)\Delta r}$
b_i	$\frac{\beta - 1}{\beta \Delta z}$	$\frac{-\beta}{(1+\beta)\Delta z}$	$\frac{1}{\beta(1+\beta)\Delta z}$
c_i	$\frac{-2}{\alpha(\Delta r)^2}$	$\frac{2}{(\alpha+1)(\Delta r)^2}$	$\frac{2}{\alpha(\alpha+1)(\Delta r)^2}$
d_i	$\frac{-2}{\beta(\Delta z)^2}$	$\frac{2}{(\beta+1)(\Delta z)^2}$	$\frac{2}{\beta(\beta+1)(\Delta z)^2}$

Table 3A.1: Finite Difference Coefficients

Finite Difference Form of the Vorticity Transport Equation

The vorticity transport equation (3.12) is transformed into a finite difference equation using forward differencing for time and central differencing for space. The 'Second Upwind Differencing' is then applied to the convective portion of the equation. This results in:

$$\frac{\zeta^{n+1}_{i,j} - \zeta^{n}_{i,j}}{\Delta t} = -\left[U(g_o\zeta^{n}_{i,j} + g_1\zeta^{n}_{i-1,j} + g_2\zeta^{n}_{i+1,j}) + V(h_o\zeta^{n}_{i,j} + h_1\zeta^{n}_{i,j-1} + h_2\zeta^{n}_{i,j+1}) - \frac{u_o}{r}\zeta_{i,j}\right] + \frac{1}{Re}\left[(c_1 + \frac{a_1}{r})\zeta^{n}_{i-1,j} + (c_2 + \frac{a_2}{r})\zeta^{n}_{i+1,j} + d_1\zeta^{n}_{i,j-1} + d_2\zeta^{n}_{i,j+1} + (c_o + \frac{a_o}{r} + d_o - \frac{1}{r^2})\zeta^{n}_{i,j}\right] \quad (3A.9)$$

where the coeffients a_i, b_i, c_i, and d_i are as shown in Table 3A.1 and the values of U , V, g_i and h_i are dependent on the sign of the velocities at intermediate points as described in section 3.2. The velocity at the intermediate points are evaluated as:

$$u_1 = \frac{1}{r}\frac{\psi_{i,j} - \psi_{i-1,j}}{\Delta r} \quad (3A.10)$$

$$u_2 = \frac{1}{r}\frac{\psi_{i+1,j} - \psi_{i,j}}{\alpha\Delta r} \quad (3A.11)$$

$$v_1 = \frac{1}{r}\frac{\psi_{i,j} - \psi_{i,j-1}}{\Delta z} \quad (3A.12)$$

$$v_2 = \frac{1}{r}\frac{\psi_{i,j+1} - \psi_{i,j}}{\beta\Delta z} \qquad (3A.13)$$

The velocity at the nodal point is denoted by u_o and v_o. The appropriate values of U, V, g_i and h_i to be substituted in equation (3A.9) are summarised in Table 3A.2.

	U	g_o	g_1	g_2
$u_1>0$ and $u_2>0$	u_1	$1/\Delta r$	$-1/\Delta r$	0
$u_1<0$ and $u_2<0$	u_2	$-1/\alpha\Delta r$	0	$1/\alpha\Delta r$
$u_1>0$ and $u_2<0$ or $u_1<0$ and $u_2>0$	u_o	$\frac{\alpha - 1}{\alpha\Delta r}$	$\frac{-\alpha}{(1+\alpha)\Delta r}$	$\frac{1}{\alpha(1+\alpha)\Delta r}$

Table 3A.2a: Coefficients for 'Second Upwind Differencing' method

	V	h_o	h_1	h_2
$v_1>0$ and $v_2\geq 0$	v_1	$1/\Delta z$	$-1/\Delta z$	0
$v_1\leq 0$ and $v_2<0$	v_2	$-1/\beta\Delta z$	0	$1/\beta\Delta z$
$v_1<0$ and $v_2>0$ or $v_1>0$ and $v_2>0$	v_o	$\frac{\beta - 1}{\beta\Delta z}$	$\frac{-\beta}{(1+\beta)\Delta z}$	$\frac{1}{\beta(1+\beta)\Delta z}$

Table 3A.2b: Coefficients for 'Second Upwind Differencing' method

Dufort-Frankel's substitution is then applied to the finite difference equation (3A.5) and $\zeta^n_{i,j}$ is substituted by:

$$\zeta^n_{i,j} = \frac{\zeta^{n+1}_{i,j} + \zeta^{n-1}_{i,j}}{2} \qquad (3A.14)$$

wherever it occurs in the equation. The resulting algebraic equation can be re-arranged to give:

$$\zeta^{n+1}_{i,j} = A_o\zeta^{n-1}_{i,j} + A_1\zeta^n_{i-1,j} + A_2\zeta^n_{i,j-1} + A_3\zeta^n_{i+1,j} + A_4\zeta^n_{i,j+1} \qquad (3A.15)$$

where: $$A_o = \frac{(1+D)}{(1-D)} \qquad (3A.16)$$

$$A_1 = \frac{2\Delta t\left((c_1 + a_1/r)/Re - Ug_1\right)}{(1-D)} \qquad (3A.17)$$

$$A_2 = \frac{2\Delta t\left((c_2 + a_2/r)/Re - Ug_2\right)}{(1-D)} \qquad (3A.18)$$

$$A_3 = \frac{2\Delta t(d_1/Re - Vh_1)}{(1-D)} \qquad (3A.19)$$

$$A_4 = \frac{2\Delta t(d_2/Re - Vh_2)}{(1-D)} \qquad (3A.20)$$

and $$D = \Delta t\left[(c_o + d_o + \frac{a_o}{r} - \frac{1}{r^2})/Re - Ug_o - Vh_o + \frac{u_o}{r}\right] \qquad (3A.21)$$

Finite Difference Form of the Stream Function Equation

Using the finite difference coefficients as shown in Table A.1, the stream function equation (3.15) can be transformed into the following finite difference form:

$$c_o\psi_{i,j} + c_1\psi_{i-1,j} + c_2\psi_{i+1,j} + d_o\psi_{i,j} + d_1\psi_{i,j-1} + d_2\psi_{i,j+1}$$

$$- \frac{1}{r}(a_o\psi_{i,j} + a_1\psi_{i-1,j} + a_2\psi_{i+1,j}) = -r\zeta_{i,j} \qquad (3A.22)$$

Rearranging, we obtain:

$$\psi_{i,j} = B_o r\zeta_{i,j} + B_1\psi_{i-1,j} + B_2\psi_{i,j-1} + B_3\psi_{i+1,j} + B_4\psi_{i,j+1} \qquad (3A.23)$$

where: $$B_o = \frac{1}{(a_o/r - c_o - d_o)} \qquad (3A.24)$$

$$B_1 = B_o\,(c_1 - a_1/r) \qquad (3A.25)$$

$$B_2 = B_o d_1 \qquad (3A.26)$$

$$B_3 = B_o(c_2 \quad a_2/r) \qquad (3A.27)$$

$$B_4 = B_o d_2 \qquad (3A.28)$$

In the Successive-Over-Relaxation method, the stream function values used in equation (3A.23) are always the most up to date values. That is, if the computation sweeps in the direction of increasing i and increasing j, then at the k^{th} iteration,

$$\psi'_{i,j} = B_o r\zeta_{i,j} + B_1\psi^{k+1}_{i-1,j} + B_2\psi^{k+1}_{i,j-1} + B_3\psi^{k}_{i+1,j} + B_4\psi^{k}_{i,j+1} \qquad (3A.29)$$

Chapter 4

Computation of Stress and Strain

4.1 Introduction

In this chapter, the strain path analysis of the undrained, deep steady penetration of a cone penetrometer into soft clay is described. The strains in the soil are estimated from the velocity field of an inviscid fluid. A numerical integration scheme has been implemented for computing soil strains and stresses. This process requires the determination of the streamlines, and the stream function formulation is thus a particularly convenient way of specifying the initial flow field.

For an incompressible material, the mean normal stresses are governed solely by the equilibrium equations. Three different methods have been used to evaluate the mean normal stress and these result in quite different solutions. The implications of the difference in these mean pressure solutions are discussed.

4.2 Flow Solution

The successful implementation of the strain path method requires the estimation of the velocity field of the soil around the penetrometer. This is usually obtained by assuming that soil deforms without any shear resistance (i.e. corresponds to an inviscid fluid). Thus, the algorithm for flow computation formulated in Chapter 3 can be used to generate the required velocity estimate.

The mesh used in the flow computation is shown in Figure 3.2. The infinite soil mass is modelled by a finite computational domain represented by the rectangular finite difference grid system. The dimensions of this mesh have been checked to ensure that the boundaries are sufficiently far away from the penetrometer to model an infinite soil mass. The mesh used has

been found to be adequate and increasing the size of the mesh does not change the flow solution significantly.

The streamlines for the flow of an inviscid fluid around a penetrometer are shown in Figure 4.1. It may be noted that only those streamlines in the proximity of the penetrometer are distorted by a significant amount. As the distance from the penetrometer increases, the streamlines become almost parallel to the axis.

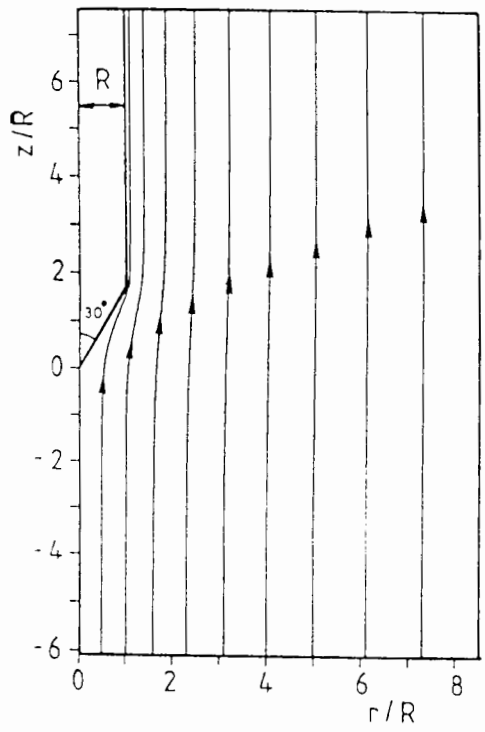

Figure 4.1: Inviscid Flow Field around a Cone Penetrometer

4.3 Strain Computations

In order to determine the soil strains associated with deep penetration problem, the natural strain increment tensor defined in chapter 2 must be evaluated along the paths taken by the soil elements during cone penetration. The computational procedure can be divided into two parts. The first stage involves the determination of the streamline profiles which, in a steady

state condition, represent the location of soil elements at different time. The second stage deals with the evaluation of the soil strain at different locations along these streamlines.

4.3.1 Determination of Streamline Profile

In a finite difference scheme, the strain in the soil is represented by discrete values at the nodes. In order to calculate these nodal strain values, the streamline that passes through each node must be found. Whilst it is theoretically possible to determine the complete profile of the streamline associated with each node, this is computationally inefficient. An alternative procedure, which requires only the determination of a streamline segment between two horizontal grid lines and an interpolation of the soil strain in the radial direction, has been used in this thesis. Substantial saving in computation effort is achieved by adopting such a procedure.

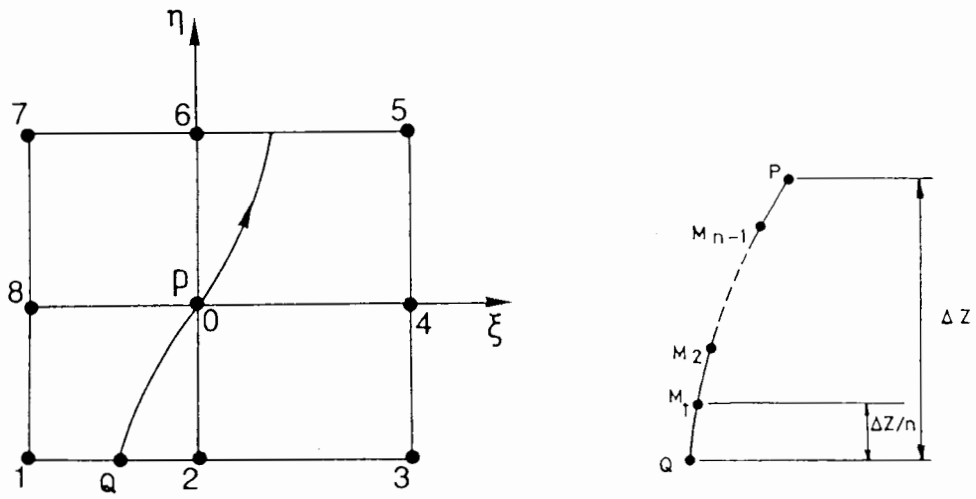

Figure 4.2: Determination of Streamline Profile

Consider an interior node P at the intersection of the vertical grid line I and the horizontal grid line J (Figure 4.2). The streamline that

passes through P is uniquely defined by ψ_o, the stream function value at P. Since the initial flow field does not have any re-circulation zone, this streamline must intersect the grid line below at some point, say Q. If the grid spacing is sufficiently small, the streamline segment between the two horizontal grids can be approximated by a straight line, PQ. However, due to the finite size of the grid spacings and the curvature of the streamline, this approximation generally does not provide the required degree of accuracy. In order to obtain an accurate solution, it is necessary to determine the curved streamline segment more exactly.

The shape of the short streamline segment is governed primarily by the local variation of ψ. For the purpose of this calculation, a 9-node local mesh system centred on P has been selected and the flow field around P is assumed to be completely determined by the 9 discrete nodal ψ values. The spatial variation of ψ locally is approximated by a Lagrangian interpolating polynomial in terms of the local co-ordinates (ξ, η):

$$\psi = a_0 + a_1\xi + a_2\eta + a_3\xi^2 + a_4\xi\eta + a_5\eta^2 + a_6\xi^2\eta + a_7\xi\eta^2 + a_8\xi^2\eta^2 \qquad (4.1)$$

where a_i are constant interpolation coefficients. By substituting the nodal co-ordinates and ψ values into equation (4.1), a set of 9 simultaneous equations in the unknown a_i is obtained:

$$[M]\ \{\underset{\sim}{a}\} = \{\underset{\sim}{\psi}\} \qquad (4.2)$$

where: $\{\underset{\sim}{a}\} = \begin{bmatrix} a_0 \\ a_1 \\ \vdots \\ a_8 \end{bmatrix}$ (4.3) ; $\{\underset{\sim}{\psi}\} = \begin{bmatrix} \psi_0 \\ \psi_1 \\ \vdots \\ \psi_8 \end{bmatrix}$ (4.4)

and

$$[M] = \begin{bmatrix} 1 & \xi_o & \eta_o & \xi_o^2 & \xi_o\eta_o & \eta_o^2 & \xi_o^2\eta_o & \xi_o\eta_o^2 & \xi_o^2\eta_o^2 \\ 1 & \xi_1 & \eta_1 & \xi_1^2 & \xi_1\eta_1^2 & \eta_1^2 & \xi_1^2\eta_1 & \xi_1\eta_1^2 & \xi_1^2\eta_1^2 \\ \cdot & & & & & & & & \\ \cdot & & & & & & & & \\ \cdot & & & & & & & & \\ \cdot & & & & & & & & \\ \cdot & & & & & & & & \\ 1 & \xi_8 & \eta_8 & \xi_8^2 & \xi_8\eta_8 & \eta_8^2 & \xi_8^2\eta_8 & \xi_8\eta_8^2 & \xi_8^2\eta_8^2 \end{bmatrix} \qquad (4.5)$$

Since the elements of the matrix [M] and the vector $\{\psi\}$ are known, a_i can be determined. The equation for the streamline that passes through P is obtained by setting $\psi=\psi_o$ in equation (4.1). This is used to obtain a series of points along the curved streamline segment for the purpose of integrating the stress strain equations.

4.3.2 Strain Rate Definitions

By adopting an Eulerian description, the components of the strain rate vector in an orthogonal Cartesian frame of reference are defined in terms of the velocity gradients:

$$\dot{\varepsilon}_{ij} = \frac{1}{2}\left[\frac{\partial v_i}{\partial x_j} + \frac{\partial v_j}{\partial x_i}\right] \qquad (4.6)$$

Substituting for the velocity components in the above definitions using equations (3.13) and (3.14), the strain rates can be are expressed in terms of ψ as:

$$\dot{\varepsilon}_{rr} = -\frac{1}{r}\frac{\partial^2\psi}{\partial r\partial z} + \frac{1}{r^2}\frac{\partial\psi}{\partial z} \qquad (4.7)$$

$$\dot{\varepsilon}_{zz} = \frac{1}{r}\frac{\partial^2\psi}{\partial r\partial z} \qquad (4.8)$$

$$\dot{\varepsilon}_{\theta\theta} = -\frac{1}{r^2}\frac{\partial\psi}{\partial z} \tag{4.9}$$

$$\dot{\gamma}_{rz} = -\frac{1}{r}\frac{\partial^2\psi}{\partial z^2} + \frac{1}{r}\frac{\partial^2\psi}{\partial r^2} - \frac{1}{r^2}\frac{\partial\psi}{\partial r} \tag{4.10}$$

The strain components which correspond to these strain rate definitions are as shown in Figure 4.3. The three normal strain rates as expressed in equations (4.7) to (4.9) sum to zero, so the incompressibility condition is automatically satisfied. If the strain rate at any nodal point is required, it can be evaluated from the known ψ values at the nodes by standard finite differences. The strain rates at locations other than the nodes are evaluated from the interpolation function for ψ (equation 4.1).

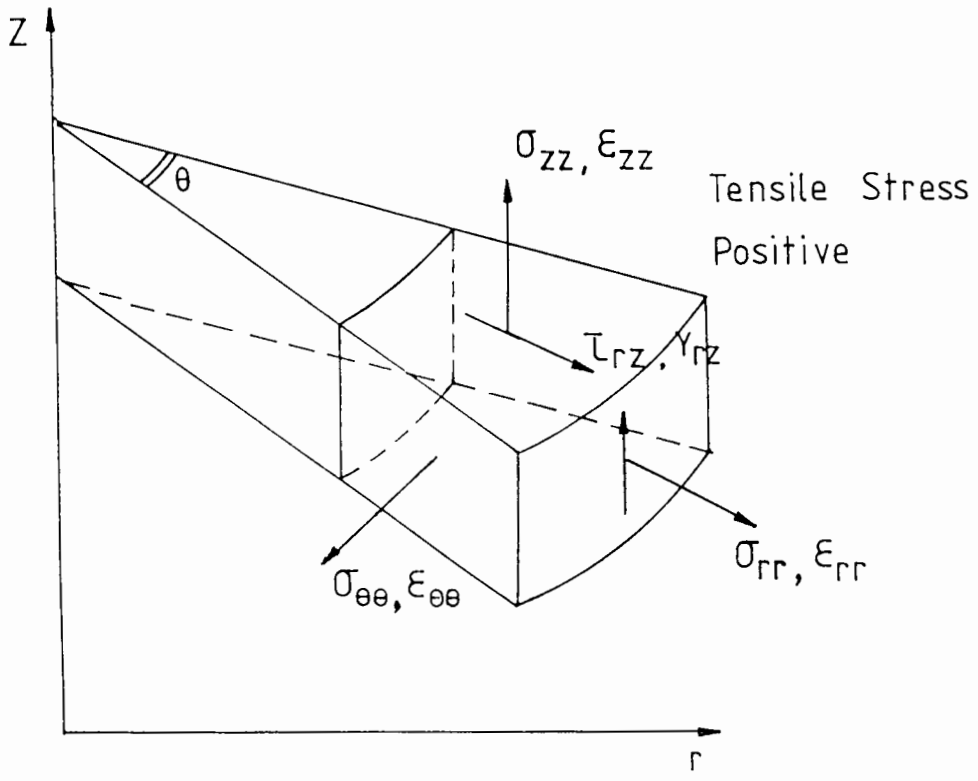

Figure 4.3: Stress and Strain Definitions in Axisymmetry

The transformation from the global to local co-ordinate systems involves merely a translation. Hence, the partial derivatives with respect

to (r, z) are similar to the partial derivatives with respect to (ξ, η), and the strain rate components can be evaluated from equation (4.1) as:

$$\dot{\varepsilon}_{rr} = \frac{1}{r^2}\left[a_2 + a_4(\xi - \eta) + 2a_5\eta + a_6\xi(\xi - 2r) + 2a_7\eta(\xi - \eta) + 2a_8\xi\eta(\xi - 2r)\right] \quad (4.11)$$

$$\dot{\varepsilon}_{zz} = \frac{1}{r}\left[a_4 + 2a_6\xi + 2a_7\eta + 4a_8\xi\eta\right] \quad (4.12)$$

$$\dot{\varepsilon}_{\theta\theta} = -\frac{1}{r^2}\left[a_2 + a_4\xi + 2a_5\eta + a_6\xi^2 + 2a_7\eta\xi + 2a_8\xi^2\eta\right] \quad (4.13)$$

$$\dot{\gamma}_{rz} = \frac{1}{r^2}\left[2(a_3 + a_6\eta)(r - \xi) - a_4\eta - 2a_5 r - a_7(2r\xi + \eta^2) - 2a_8\xi(r\xi + \eta^2)\right] \quad (4.14)$$

where r is the radial distance of the point in the global co-ordinate system.

4.3.3 Integration of Strain Rate Equations

The integration of the strain rate equations along streamline is facilitated by approximating the curved streamline segment by n linear sections as illustrated in Figure (4.2). By subdividing the streamline segment between the two horizontal grids into n equal vertical intervals, the co-ordinate η_i of the end points of each linear section will be known. The other co-ordinate component ξ_i can be calculated by substituting η_i into the streamline equation (4.1).

The strain increment between O and P is evaluated incrementally by the equation:

$$d\varepsilon_{ij} = \sum_{k=1}^{n} \left(\dot{\varepsilon}_{ij} \frac{dz}{v_z} \right)_k \tag{4.15}$$

The strain rates, $\dot{\varepsilon}_{ij}$, and the vertical velocity component, v_z, are evaluated at the mid-points of the n straight line sections. The natural strain tensor at P can then be calculated as:

$$(\varepsilon_{ij})_p = (\varepsilon_{ij})_q + d\varepsilon_{ij} \tag{4.16}$$

where $(\varepsilon_{ij})_q$, the soil strain at Q, is interpolated by fitting a parabolic curve over the strain values at the three nodes on the lower grid line. (Figure 4.2). The strain, ε_{ij}, at the inflow boundary (J=0) is assumed to be zero and derivation of the strain field begins at the horizontal grid level J=1. The values of ε_{ij} at all the nodes on each horizontal grid line are computed using the procedure described above before proceeding to the next grid line. By sweeping the computation in the direction of increasing J, an estimate of the strain field will be obtained.

4.4 Stress Computations

In a steady state condition, soil elements which are initially located at a fixed radial distance from the axis of penetration are subjected to the same strain history, and hence the same stress path. Therefore, by evaluating the stress changes along a streamline, an estimate of the stress state around the penetrometer can be obtained.

The stress path of a soil element can, in principle, be evaluated from the strain history in various ways. One possibility is to carry out laboratory tests in which strain paths similar to those predicted are imposed and the stress changes observed. The stress-strain curves obtained can then

be used to determine the stresses at different strain values. However, the strain paths which exist in a penetration test are very complicated, and in general cannot be duplicated in the laboratory. In an analytical study, it is usually more convenient to describe the stress-strain behaviour of soil by some constitutive model. This latter approach has been adopted and the choice of soil model is described below.

4.4.1 Constitutive Relationship for Clay

Extremely high strain rates and strains are induced in the soil during cone penetration. In addition, as illustrated by the simple pile problem, significant stress and strain reversals can also occur. In order to model accurately the soil behaviour due to cone penetration, the constitutive relationship selected should be able to account for all these features. Such a comprehensive constitutive model is not currently available and some idealised model has to be adopted.

In this thesis, a simple and yet relevant constitutive relationship has been chosen and the soil was modelled as an elastic-perfectly plastic material obeying the von Mises yield criterion. This simple model has been deliberately chosen so that the analytical procedure was not obscured by undue mathematical complexity. Such complications could not have been avoided if a more sophisticated constitutive law had been adopted.

The von Mises yield criterion is formulated in terms of deviatoric stresses and the yield function can be written as:

$$F = s_r(s_r + s_z) + s_z^2 + \tau_{rz}^2 - \frac{4}{3}c_u^2 \qquad (4.17)$$

where c_u is the shear strength in undrained triaxial compression and the deviatoric stress components are defined as:

$$s_r = \sigma_{rr} + p \tag{4.18}$$

$$s_z = \sigma_{zz} + p \tag{4.19}$$

$$s_\theta = \sigma_{\theta\theta} + p \tag{4.20}$$

where: $$p = -\frac{(\sigma_{rr} + \sigma_{zz} + \sigma_{\theta\theta})}{3} \tag{4.21}$$

A tension positive convention has been adopted and the stress components are as shown in Figure 4.3.

In the elastic range, the new stresses due to a small strain increment are given by:

$$s_r = s_{ro} + 2G\Delta e_r \tag{4.22}$$

$$s_z = s_{zo} + 2G\Delta e_z \tag{4.23}$$

$$s_\theta = s_{\theta o} + 2G\Delta e_\theta = (s_r + s_z) \tag{4.24}$$

$$\tau_{rz} = \tau_o + G\Delta\gamma_{rz} \tag{4.25}$$

where G is the shear modulus; s_{ro}, s_{zo} ,$s_{\theta o}$ and τ_o are the deviatoric stresses at the start of the calculation step and Δe_r, Δe_z and Δe_θ are the increments of deviatoric strains which are defined as:

$$e_r = \varepsilon_{rr} - \frac{v}{3} \tag{4.26}$$

$$e_z = \varepsilon_{zz} - \frac{v}{3} \tag{4.27}$$

$$e_\theta = \varepsilon_{\theta\theta} - \frac{v}{3} \tag{4.28}$$

where: $$v = \varepsilon_{rr} + \varepsilon_{zz} + \varepsilon_{\theta\theta} \tag{4.29}$$

In an undrained analysis, the volumetric strain v is equal to zero, so the deviatoric and the natural strain increments have the same numerical values.

4.4.2 von Mises Plasticity

In the plastic regime, the total strain rate can be decomposed into an elastic component and a plastic component:

$$\dot{\varepsilon}_{ij} = \dot{\varepsilon}^{e}_{ij} + \dot{\varepsilon}^{p}_{ij} \tag{4.30}$$

By adopting an associated flow rule for the plastic flow, the plastic strain rate for the case of no work hardening can be written as:

$$\dot{\varepsilon}^{p}_{ij} = \lambda \frac{\partial F}{\partial \sigma_{ij}} \tag{4.31}$$

where λ is a scalar multiplier. The elastic strain rate is related to the stress rate by the equation:

$$\dot{\varepsilon}^{e}_{ij} = \frac{\overset{\nabla}{s}_{ij}}{2G} \tag{4.32}$$

Since the strain rate solution is based on an inviscid flow field, the rotation term, ω, is identically zero. Hence, the Jaumann stress rate, $\overset{\nabla}{\sigma}_{ij}$, is equivalent to the Cauchy stress rate, $\dot{\sigma}_{ij}$.

Substituting equations (4.31) and (4.32) into (4.30), the stress rate and the strain rate are governed by three differential equations:

$$\dot{s}_{r} = 2G\dot{\varepsilon}_{rr} + 12G\lambda s_{r} \tag{4.33}$$

$$\dot{s}_{z} = 2G\dot{\varepsilon}_{zz} + 12G\lambda s_{z} \tag{4.34}$$

$$\dot{\tau}_{rz} = G\dot{\gamma}_{rz} + 12G\lambda\tau_{rz} \tag{4.35}$$

Equations (4.33) to (4.35) belong to a class of differential equations which can be solved analytically by the integration factor technique when the strain rates are constant with time. Applying the appropriate initial conditions, the deviatoric stress components which correspond to a small strain increment are given by the following equations (Booker, 1984):

$$s_r = (2Ge_r\Phi + s_{ro})/\Psi \tag{4.36}$$

$$s_z = (2Ge_z\Phi + s_{zo})/\Psi \tag{4.37}$$

$$\tau_{rz} = (G\gamma_{rz}\Phi + \tau_o)/\Psi \tag{4.38}$$

where:

$$\Phi = \frac{\alpha}{\beta}\left[\sinh(\frac{\beta}{\alpha}t) + \chi\cosh(\frac{\beta}{\alpha}t) - \chi\right] \tag{4.39}$$

$$\Psi = \chi\sinh(\frac{\beta}{\alpha}t) + \cosh(\frac{\beta}{\alpha}t) \tag{4.40}$$

$$\alpha = \frac{2c_u}{\sqrt{3}} \tag{4.41}$$

$$\beta^2 = 4G^2\left(\Delta e_r^2 + \Delta e_r\Delta e_z + \Delta e_z^2 + \frac{\Delta\gamma_{rz}^2}{4}\right) \tag{4.42}$$

$$\chi = \frac{G}{\alpha\beta}\left(s_{ro}(2\Delta e_r + \Delta e_z) + s_{zo}(\Delta e_r + 2\Delta e_z) + \tau_o\Delta\gamma_{rz}\right) \tag{4.43}$$

The above expressions are only applicable to a straight strain path, so the calculation was performed using small strain increments.

4.4.3 Deviatoric Stress Update Calculations

As with other field parameters described in this analysis, soil stresses are represented by discrete values at the nodes. Thus, the stress calculation follows an analogous procedure as the strain path computation. The stress changes due to small strain increments are evaluated using the constitutive equations derived in the previous section. Regardless of the initial stress state, the stress increment is first assumed to be purely

elastic. If the updated stress state violates the yield criterion, the calculation is repeated using the appropriate plastic stress update equations. This procedure has the advantage that any elastic unloading that might take place will be detected and accounted for.

As the calculation proceeds along a streamline, an element of soil which is initially elastic may become plastic during a strain increment. In such a case, the fraction of the strain increment which just brought the soil to yield is computed by combining the yield function and the elastic stress update equations. The remaining fraction of the strain increment is assumed to be purely plastic and the stress update calculation is performed using the relevant equations.

4.4.4 Stress Interpolations

The incremental stress update procedure described above requires that the stress state before the application of a strain increment is known. For example, in order to evaluate the stresses at P (Figure 4.2), the stresses at Q must be computed. It is clear therefore that some form of stress interpolation is necessary.

There is no unique way by which stress interpolation should be carried out and many different possibilities exist. In this study, the interpolation of deviatoric stresses was achieved via the equivalent Lode's parameters (Figure 4.4). The deviatoric stresses are related to the Lode's parameters (c, ζ and ϕ) by the equations:

$$s_r = \frac{4}{3} c \cos\zeta \sin(\phi + \frac{\pi}{6}) \qquad (4.44)$$

$$s_\theta = \frac{4}{3} c \cos\zeta \sin(\phi - \frac{\pi}{6}) \qquad (4.45)$$

$$s_z = \frac{4}{3}c \cos\zeta \sin\phi \tag{4.46}$$

$$\tau_{rz} = \frac{2}{\sqrt{3}}c \sin\zeta \tag{4.47}$$

where: $$c = s_r(s_r + s_z) + s_z^2 + \tau_{rz}^2 \tag{4.48}$$

Note that the value of c is constrained by the von Mises yield function (4.17) and will always be less than or equal to c_u, the undrained shear strength. The parameter c is equal to c_u when the stress state is plastic. For an elastic stress state, c is less than c_u. The value of c at Q is obtained by linear interpolation between the adjacent nodal values. The parameters ζ and ϕ associated with the stresses at the nodes on the bottom grid line are evaluated using equations (4.44) to (4.47). These nodal parameters are fitted with a second order interpolation function from which the value at Q is computed. The use of the above technique avoids the interpolation of an elastic stress state from two plastic states.

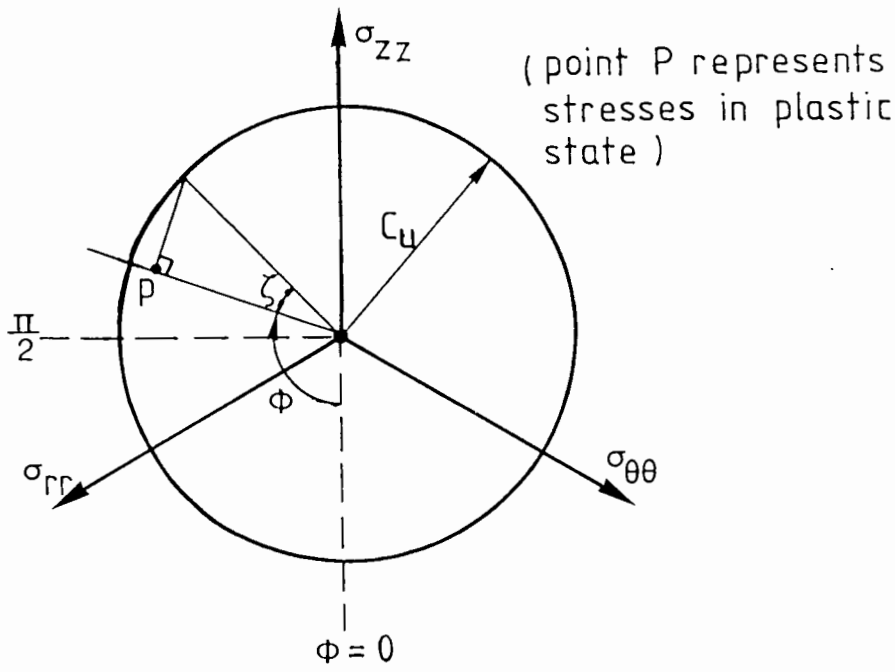

Figure 4.4: Equivalent Lode's Parameters

4.5 Calculation of the Octahedral Normal Stress

The octahedral normal stresses during undrained penetration, in which the soil behaves as an incompressible material, are governed by the equilibrium equations. For an axially symmetric problem formulated in a cylindrical co-ordinate system, these equations are given by:

$$-\frac{\partial p}{\partial r} + \frac{\partial s_r}{\partial r} + \frac{\partial \tau_{rz}}{\partial z} + \frac{s_r - s_\theta}{r} = 0 \qquad (4.49)$$

$$-\frac{\partial p}{\partial z} + \frac{\partial s_z}{\partial z} + \frac{\partial \tau_{rz}}{\partial r} + \frac{\tau_{rz}}{r} = 0 \qquad (4.50)$$

in the radial and axial directions respectively. The mean normal pressure p is a field parameter so for a stress field which is sufficiently smooth, the spatial variation of p is given by:

$$dp = \frac{\partial p}{\partial r}dr + \frac{\partial p}{\partial z}dz \qquad (4.51)$$

where dr and dz are small displacements in the direction of the co-ordinate axes. It is possible to calculate p if the boundary conditions and the distribution of s_r, s_z, s_θ and τ_{rz} are known. Two particularly convenient integration paths can be identified from Equation (4.51). One of these corresponds to the horizontal grid line for which dz = 0. Along this line, the mean pressure p is given by:

$$p = p_o + \int \frac{\partial p}{\partial r}\, dr \qquad (4.52)$$

where p_o is the in-situ mean pressure at a point very far away from the cone where the effect of penetration can be considered to be negligible. Alternatively, p can be evaluated by integrating equation (4.51) along a vertical grid line for which dr = 0:

$$p = p_o + \int \frac{\partial p}{\partial z}\, dz \tag{4.53}$$

In general the above procedures will result in different values of p, unless the deviatoric stress distribution is correct. Furthermore, for a sufficiently smooth stress field with no stress discontinuities, the equilibrium condition also requires that p satisfies the Poisson equation:

$$\frac{\partial^2 p}{\partial r^2} + \frac{1}{r}\frac{\partial p}{\partial r} + \frac{\partial^2 p}{\partial z^2} = g \tag{4.54}$$

where: $$g = \frac{\partial^2 s_r}{\partial r^2} + \frac{\partial^2 s_z}{\partial z^2} + 2\left(\frac{\partial^2 \tau_{rz}}{\partial r \partial z} + \frac{1}{r}\frac{\partial \tau_{rz}}{\partial z} + \frac{1}{r}\frac{\partial s_r}{\partial r}\right) - \frac{1}{r}\frac{\partial s_\theta}{\partial r} \tag{4.55}$$

Equation (4.54) is obtained by differentiating equation (4.49) and (4.50) with respect to r and z respectively and adding. The source term g can be evaluated from the known deviatoric stresses.

4.5.1 Integration along Radial Grid Lines

When p is computed using equation (4.52), the calculation procedure begins at a point on the right hand boundary and proceeds in the direction of decreasing r (Figure 4.5a). The mean pressure at an internal node is given by:

$$p_{i,j} = p_{i+1,j} - \left(\frac{\partial p}{\partial r}\right)_M \Delta r_i \tag{4.56}$$

where Δr_i is the grid interval between nodes (i,j) and (i+1,j) and M is a point midway between the nodes. The mean pressure at the boundary is taken to be the in-situ value, p_o. The term $\frac{\partial p}{\partial r}$ is evaluated from the known deviatoric stresses using standard finite differences. By repeating the calculation procedure at every horizontal line, a mean pressure solution which satisfies the equilibrium equation in the radial direction is obtained.

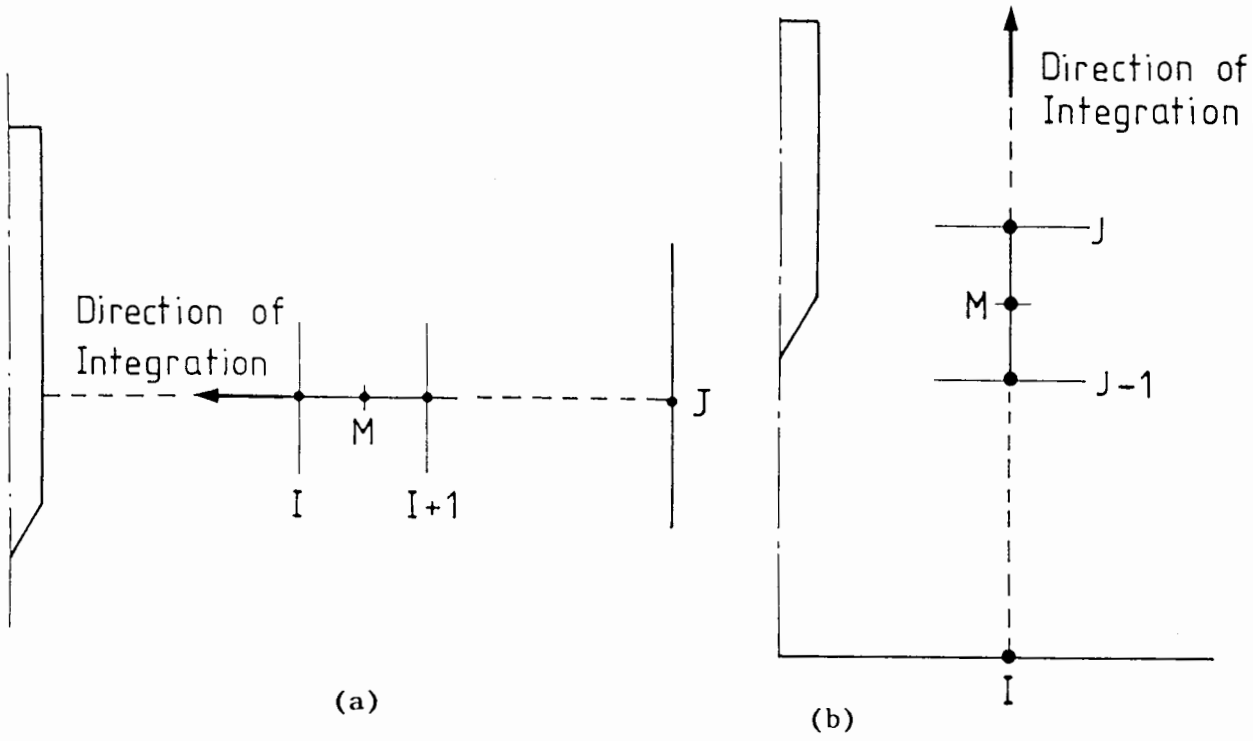

Figure 4.5: Integration Paths - (a) Radial Grid Lines, (b) Axial Grid Lines

4.5.2 Integration along Axial Grid Lines

If equation (4.53) is used to compute p, a procedure similar to that described in section (4.5.1) can be adopted. The integration path is shown in Figure 4.5b. At any node (i, j) along the vertical grid line, I, the mean pressure is given by:

$$p_{i,j} = p_{i,j-1} + \left(\frac{\partial p}{\partial z}\right)_M \Delta z_j \qquad (4.57)$$

where $\left(\frac{\partial p}{\partial z}\right)$ is evaluated at the mid point between nodes (i,j-1) and (i,j) and Δz_j is the grid spacing between the two nodes.

Special attention was given to the calculation of the $\frac{\partial \tau_{rz}}{\partial r}$ and $\frac{\tau_{rz}}{r}$ terms on the axis where r = 0. In the vicinity of the axis, the shear stress component, τ_{rz}, can be considered to be an odd function of r and can therefore be expressed in the form:

$$\tau_{rz} = ar^3 + br \tag{4.58}$$

By adopting a second order finite difference scheme, the derivative $\frac{\partial \tau_{rz}}{\partial r}$ and the quotient, $\frac{\tau_{rz}}{r}$, on the axis are expressed as:

$$\frac{\partial \tau_{rz}}{\partial r} = \frac{\tau_{rz}}{r} = \frac{\tau_1 r_2^3 - \tau_2 r_1^3}{r_1 r_2^3 - r_2 r_1^3} \tag{4.59}$$

where r_1 and r_2 are the radial distances of the two nodes closest to the axis and τ_1 and τ_2 are the corresponding nodal shear stresses.

4.5.3 Solution of the Poisson Equation for Mean Pressure

The Poisson equation for mean pressure (4.54) is an elliptic equation and can be solved by the numerical scheme developed in Chapter 3 for solving the stream function equation. The boundary conditions, however, are different and merit some detailed consideration.

At the upstream and far field boundaries, the mean pressure is specified as p_o. On the axis, symmetry condition requires that $\frac{\partial p}{\partial r} = 0$. At the downstream boundary, a steady state condition is imposed and the boundary condition is specified as:

$$\frac{\partial p}{\partial z} = 0 \tag{4.60}$$

The most important boundary by far is the soil-penetrometer interface. It is not appropriate to prescribe the value of p on this boundary since this is not known a priori. One possibility is to specify a Neumann type condition such as:

$$\frac{\partial p}{\partial r} = \mu \tag{4.61}$$

where μ was computed from the deviatoric stresses using equation (4.49). The implementation of this boundary condition requires special consideration because its incorporation in the S.O.R. scheme is not straightforward. At first sight, one possible solution scheme is to evaluate the values of p at the interior nodes as:

$$p_{i,j}^{k+1} = p_{i,j}^{k} + \frac{\Omega}{F_o}\left[F_1 p_{i-1,j}^{k+1} + F_2 p_{i,j-1}^{k+1} + F_3 p_{i,j+1}^{k} + F_4 p_{i+1,j}^{k} - F_o p_{i,j}^{k} - g\right] \tag{4.62}$$

and the pressure on the boundary is evaluated as:

$$p_B^{k+1} = p_{B+1}^{k+1} - \frac{\partial p}{\partial r}\Delta r \tag{4.63}$$

The superscript in these equations represents the iteration number, the subscript B denotes the boundary nodes and B+1 refers to the interior nodes adjacent to the bounday. The coefficients F_o to F_4 are finite difference coefficients as described in Appendix 3A.

Although plausible, this method has been tested in Fluid Dynamics (Roache, 1976) and was found not to converge to a solution. Miyakoda (1962) recommended that the derivative boundary condition should be incorporated directly into the S.O.R. difference scheme at the interior nodes adjacent to the boundary. Using this scheme, the pressures at these nodes are expressed as:

$$p_{i,j}^{k+1} = p_{i,j}^{k} + \frac{\Omega}{F_o}\left[F_1 (p_{i,j}^{k+1} - \frac{\partial p}{\partial r}\Delta r) + F_2 p_{i,j-1}^{k+1} + F_3 p_{i,j+1}^{k} + F_4 p_{i+1,j}^{k} - F_o p_{i,j}^{k} - g\right] \tag{4.64}$$

Note that the value of p at the boundary has been replaced by the expression in equation (4.63). This equation can be re-arranged to give an explicit expression for $p_{i,j}^{k+1}$ in terms of p at neighbouring nodes. The resulting equation is used in the S.O.R. scheme for all nodes adjacent to the soil-penetrometer boundary. When convergence is reached, p on the boundary is evaluated from equation (4.63). This procedure has been implemented successfully and the numerical scheme was found to be unconditionally stable.

4.6 Deviatoric Stresses

The numerical procedure described in this Chapter has been implemented for the analysis of the cone penetration problem. The soil was assumed to have a rigidity index of 100 and the initial vertical and horizontal stresses were assumed to be zero (Any initial isotropic stresses would appear purely as additive terms to the results).

The contours of the deviatoric stresses around the cone penetrometer are shown in Figure 4.6. Far behind the cone tip, the variation of the deviatoric stresses are predominantly in the radial direction and changes in the axial direction are negligible. This result appeared to provide some justification for using cylindrical cavity expansion to approximate the stress state around the shaft (Randolph et al., 1979). However, in the region around the tip, the deviatoric stresses are two-dimensional in nature and the stress distribution is very different from that obtained in a one-dimensional cavity expansion approach.

Very high stress gradients exist in the vicinity of the tip as indicated by the closely packed contour lines. These high stress gradients are also observed in the shear stress distribution. Adjacent to the cone

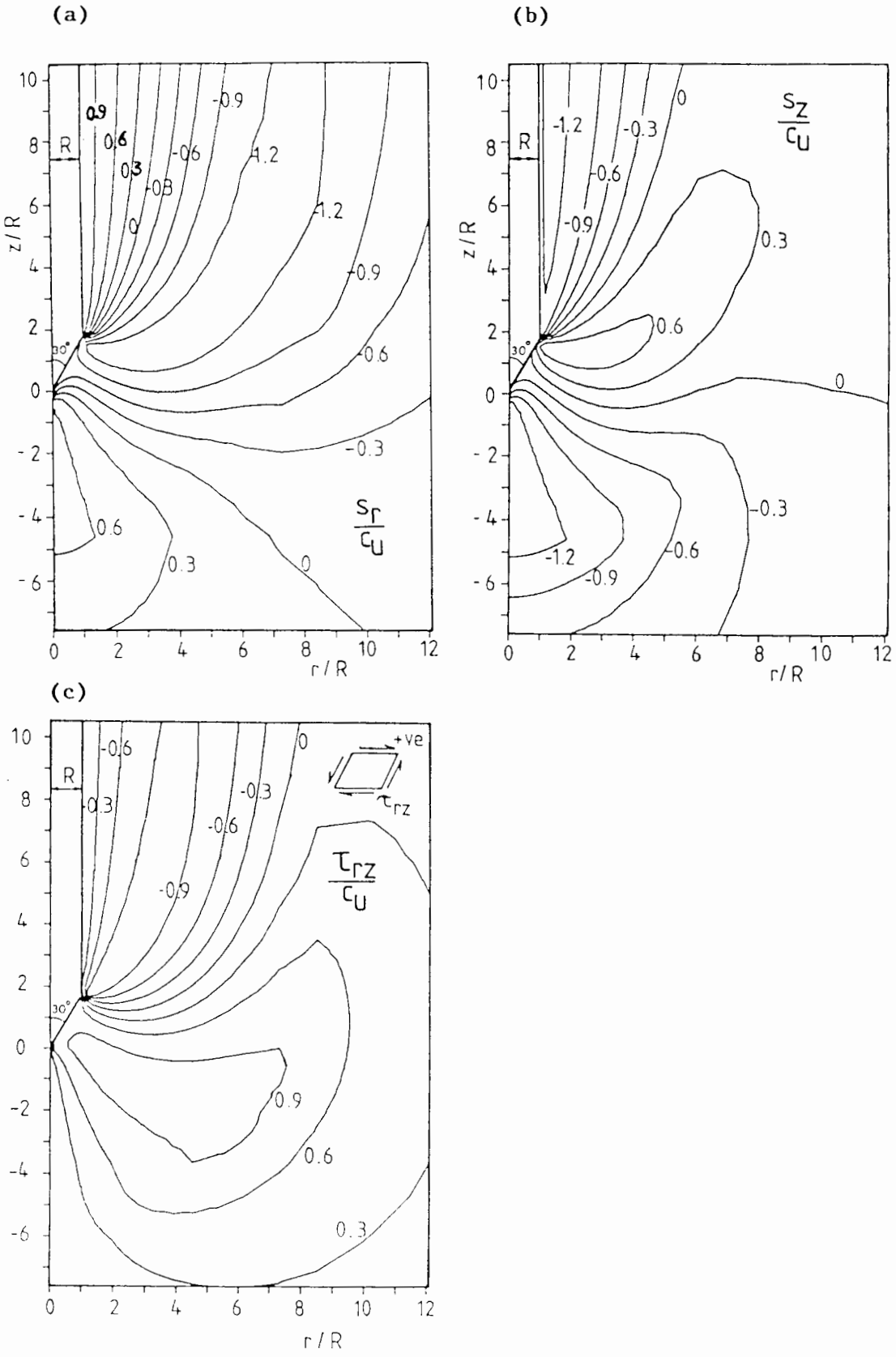

Figure 4.6: Contours of Deviatoric Stresses around a 60° Cone Penetrometer

shoulder, the shear stress changes very rapidly. However, due to the singularity associated with the sharp cone shoulder, it is difficult to draw any firm conclusion from these deviatoric stress distributions.

4.7 Mean Pressure Solution

The mean normal pressure has been computed using the methods described in Section 4.5. The results obtained are presented in Figure 4.7. The mean pressures obtained by integrating along the radial and axial lines are denoted by p_r and p_z respectively and p_p is derived from the Poisson equation. These solutions are found to differ significantly from each other.

The p_z contours show that a region of soil adjacent to the shaft is subjected to negative pressure (i.e. less than the initial in-situ value) which becomes progressively more negative as z increases. This result is

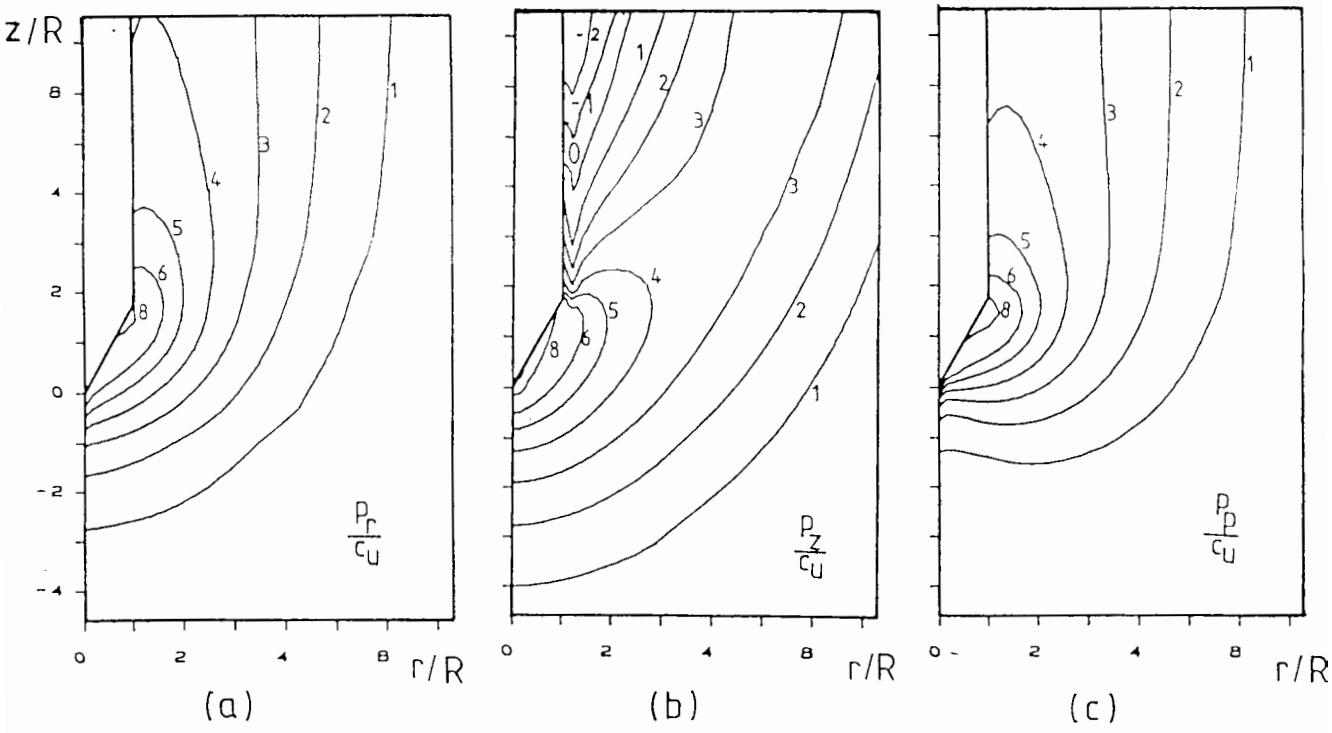

Figure 4.7: Mean Pressure Solutions around a 60° Cone Penetrometer Evaluated by 3 Different Methods

unrealistic and may be due to the errors associated with the shear stresses, τ_{rz}. The effect of errors in τ_{rz} on p_z can be studied by an analysis of the equilibrium equation (4.50) which is reproduced here for ease of reference.

$$\frac{\partial p}{\partial z} = \frac{\partial s_z}{\partial z} + \frac{\partial \tau_{rz}}{\partial r} + \frac{\tau_{rz}}{r} \qquad (4.50)$$

The above equation shows that the mean pressure variation in the axial direction is governed by the gradients of s_z and τ_{rz}. At a point far behind the cone tip, $\frac{\partial s_z}{\partial z}$ is very small (Figure 4.6b) and can be neglected. Thus, $\frac{\partial p}{\partial z}$ is entirely dependent on the shear stress distribution. From the shear stress contours, it is observed that $\frac{\partial \tau_{rz}}{\partial r}$ and $\frac{\tau_{rz}}{r}$ are negative in the region adjacent to the shaft and so $\frac{\partial p}{\partial z}$ is always negative. For such a deviatoric stress distribution, integration along axial lines will invariably lead to a solution for p_z which decreases indefinitely behind the tip. When the shaft of the penetrometer is smooth, it can be shown that a 'steady state' solution for p_z (in which $\frac{\partial p_z}{\partial z}$ is zero far behind the tip) is possible only if τ_{rz} vanishes far behind the tip.

The effect of the errors in τ_{rz} on p_r can be analysed from the equilibrium equation in the radial direction, which is reproduced below:

$$\frac{\partial p}{\partial r} = \frac{\partial s_r}{\partial r} + \frac{\partial \tau_{rz}}{\partial z} + \frac{s_r - s_\theta}{r} \qquad (4.49)$$

The shear stresses affect p_r through the term $\frac{\partial \tau_{rz}}{\partial z}$. At a point far from the tip, the computed value of $\frac{\partial \tau_{rz}}{\partial z}$ is very small and the influence of τ_{rz} on p_r is negligible. Therefore, p_r is less sensitive to the errors in τ_{rz}. In addition, the regions where the stresses are associated with high

uncertainties are located at the end of the integration path so their effects will be more localised.

The solution based on the Poisson equation, p_p, appears to support this argument. The Poisson equation was derived from the two equilibrium equations and can be considered to satisfy each one approximately. The source term, g, in this equation contains the terms $\frac{\partial^2 \tau_{rz}}{\partial r \partial z}$ and $\frac{\partial \tau_{rz}}{\partial z}$ which are small far behind the tip. Thus, the errors in τ_{rz} are likely to have only minor impact on p_p. This is partially confirmed by the similarity between p_r and p_p adjacent to the shaft.

Despite the differences in the mean pressure solutions, the variations of p along the cone face obtained from these three methods are quite similar. The values of the tip resistance computed using any of these solutions differ by not more than 10%. This degree of accuracy is sufficient for most practical applications. The strain path method can therefore be relied upon to give a good estimate of the tip resistance due to cone penetration.

The dependence of the mean normal pressure on the integration paths implies that the computed deviatoric stresses are not correct. Although it has been suggested that τ_{rz} is the stress component most likely to be in error, the accuracy of the other deviatoric stresses is more difficult to assess. It is believed that the approximate deviatoric stresses can be used to obtain an improved estimate for the velocity field. Several methods of correction based on this approach have been attempted and these are presented in the next chapter.

Chapter 5

Equilibrium Considerations

5.1 Introduction

The stresses calculated using the strain path method do not satisfy the equilibrium equations fully. This failure is reflected in the dependence of the octahedral mean stress on the integration path. Since the stress solution is only approximately correct, it is useful to estimate the amount of error in the computed results. This is particularly important if the results are to be used as a basis for interpreting test data.

In the following sections the quality of the stress solution from the strain path method is assessed, and regions where high uncertainties exist are identified. A measure of the amount of departure from the unknown exact solution is defined and the possible sources of approximation discussed. Three possible equilibrium correction methods have been attempted and these will be discussed in some detail in this chapter.

5.2 Estimating the Errors in the Stress Solution

In continuum mechanics, any set of internal stresses can be forced to satisfy the equilibrium equations provided that an appropriate body force field is assumed to be acting on the body. Thus, the deviatoric stresses obtained by the strain path method could be considered to be correct if a set of fictitious body forces was assumed to be present. In such a case, the equilibrium equations can be written as:

$$\frac{\partial p}{\partial r} + \frac{\partial s_r}{\partial r} + \frac{\partial \tau_{rz}}{\partial z} + \frac{s_r - s_\theta}{r} + F_r = 0 \qquad (5.1)$$

$$\frac{\partial p}{\partial z} + \frac{\partial s_z}{\partial z} + \frac{\partial \tau_{rz}}{\partial r} + \frac{\tau_{rz}}{r} + F_z = 0 \qquad (5.2)$$

in which F_r and F_z are the body forces in the radial and axial directions respectively. The deviatoric stresses in these equations are known and this leaves p, F_r and F_z as variables. With two equations and three unknowns, it is possible to obtain an infinite combination of p, F_r and F_z which will satisfy equations (5.1) and (5.2). Furthermore, if an estimate for any of these unknown quantities is available, then the remaining two can be evaluated from the equilibrium equations.

In Section 4.5, p has been evaluated using three different methods by implicitly assuming that the deviatoric stresses are correct. The mean pressure solutions obtained by integrating along radial lines, p_r, and by solving the Poisson equation, p_p, are found to be quite similar. These two solutions are considered to be reasonably accurate and so can be used to estimate the fictitious body forces required to maintain equilibrium. Since p_r was evaluated by implicitly assuming that F_r is zero, then only F_z need to be found if p_r is adopted as the mean pressure. The normalised contours of F_z evaluated by substituting p_r for p in equation (5.2) are plotted in Figure 5.1. Two regions where F_z is appreciably large can be identified. These are located in the vicinity of the cone shoulder and the cone tip. The magnitude of the fictitious body forces indicates that the errors in the deviatoric stresses are quite appreciable. Elsewhere, F_z is found to be generally small and the equilibrium condition is satisfied approximately.

As an alternative way of assessing the accuracy of the strain path results, the difference in the mean normal pressure solutions obtained from different integration paths can be computed. This pressure difference when expressed as a fraction of the mean pressure provides a useful indication of the accuracy of the stress solution. From Figure 4.7, it is observed that below the cone shoulder, the three pressure solutions are quite similar.

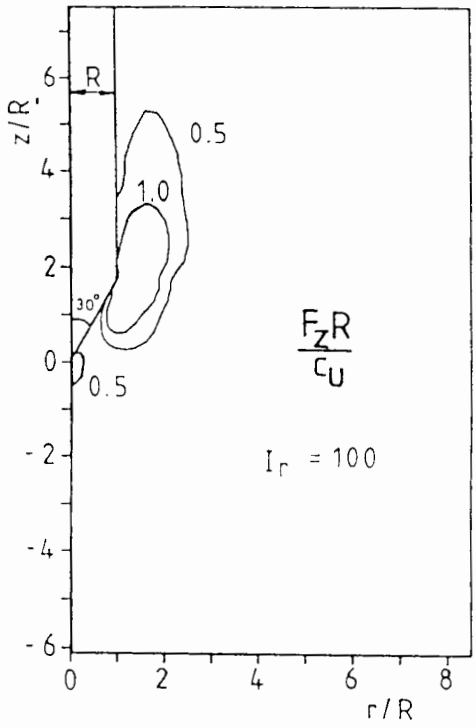

Figure 5.1: Out-of-Balance Body Forces, F_z

Good agreement between p_r and p_p is also apparent above this level. The strain path method can therefore be considered to be capable of giving a good estimate of the stress state in most regions around the penetrometer with the exception of the locations around the cone tip and the cone shoulder.

5.3 Equilibrium Correction Methods

The failure of the stresses computed by the strain path method to satisfy the equilibrium condition is mainly due to the approximate nature of the assumed velocity field. In order to improve the solution, it is necessary to obtain a better estimate of the soil velocities. Three different iterative procedures which made use of the approximate deviatoric stresses to correct the initial velocity field have been tried. The formulations of these iterative procedures are presented in the following sections.

5.3.1 Newton-Raphson Correction Scheme

In this section, a correction procedure which is based on the Newton-Raphson iterative principle is suggested. The algorithm involves carrying out numerical experiments in which the initial stream function at each nodal point is perturbed by a small amount. The effect of each perturbation on the magnitude of an error measure is calculated. The changes in the error measure are then used to obtain an estimate of the change in the stream function which is required in order to satisfy equilibrium.

Error Measure

By differentiating the radial and axial equilibrium equations with respect to z and r respectively and subtracting, the mean normal pressure in the two equilibrium equations can be eliminated. For a set of stresses which are in equilibrium, this results in:

$$\frac{\partial}{\partial z}\left[\frac{\partial s_r}{\partial r} + \frac{\partial \tau_{rz}}{\partial z} + \frac{s_r - s_\theta}{r}\right] - \frac{\partial}{\partial r}\left[\frac{\partial s_z}{\partial z} + \frac{\partial \tau_{rz}}{\partial r} + \frac{\tau_{rz}}{r}\right] = 0 \qquad (5.3)$$

Since the strain path solution is only approximate, the expression on the left hand side of equation (5.3) would generally be non-zero. This quantity, which will be denoted by H, provides a measure of the error in the stress solution.

Numerical Algorithms

The main steps of the Newton-Raphson procedure can be summarized as follows:

Step 1: Based on an initial stream function estimate, the deviatoric stresses are calculated using the strain path method. The error measure, H_o, which corresponds to the initial stress solution is

evaluated at each node using the left hand side expression of Equation (5.3)

Step 2: The initial stream function at a node N is perturbed by a small amount. The new stresses which correspond to the perturbed stream function field are evaluated by the strain path procedure.

Step 3: The error measure associated with the new stress field is computed. This is denoted by H_1. The 'partial derivatives' of the error measure at node M due to a perturbation, $\delta\psi_n$, at node N is evaluated as:

$$\chi_{m,n} = \frac{(H_1 - H_o)_m}{\delta\psi_n} \qquad (5.4)$$

The stream function at the perturbed node is then restored to its original value.

Step 4: By repeating the perturbation process at every node, a matrix equation can be set up.

$$|\chi| \{\Delta\psi\} = \{H_o\} \qquad (5.5)$$

Each element in the matrix $|\chi|$ is analogous to the derivative f'(x) in the standard one-dimensional Newton-Raphson equation. Since this matrix and the initial error $\{H_o\}$ are known, the required change in stream function $\{\Delta\psi\}$ can be evaluated from equation (5.5)

Step 5: The stream function field is up-dated as:

$$\{\psi\}^{k+1} = \{\psi\}^k + \{\Delta\psi\}^k \qquad (5.6)$$

where k is the iteration number.

Step 6: The stresses which correspond to the updated stream function field are re-evaluated using the strain path method.

The cycle of computation from Step (2) to Step (6) is repeated until the errors of equilibrium, represented by H, is acceptably small.

Test Cases:

The numerical procedure described above has been tested with a hypothetical problem involving a uniform flow of soil down a smooth walled tube. An arbitrary, non-uniform initial velocity field was assumed for the soil. The changes in soil stresses due to this assumed velocity field and the relevant boundary conditions were evaluated using the strain path procedures. The error measure, H, which corresponds to this non-uniform velocity field was in general non-zero. The Newton-Raphson scheme was then applied to obtain an up-dated velocity field.

This verification exercise revealed that the range of applicability of this correction procedure is very limited. When the soil stresses due to an assumed strain field lie entirely within the elastic range, the Newton-Raphson method results in very rapid convergence to the correct solution. This is illustrated in Figure 5.2. The non-uniform initial velocity estimate

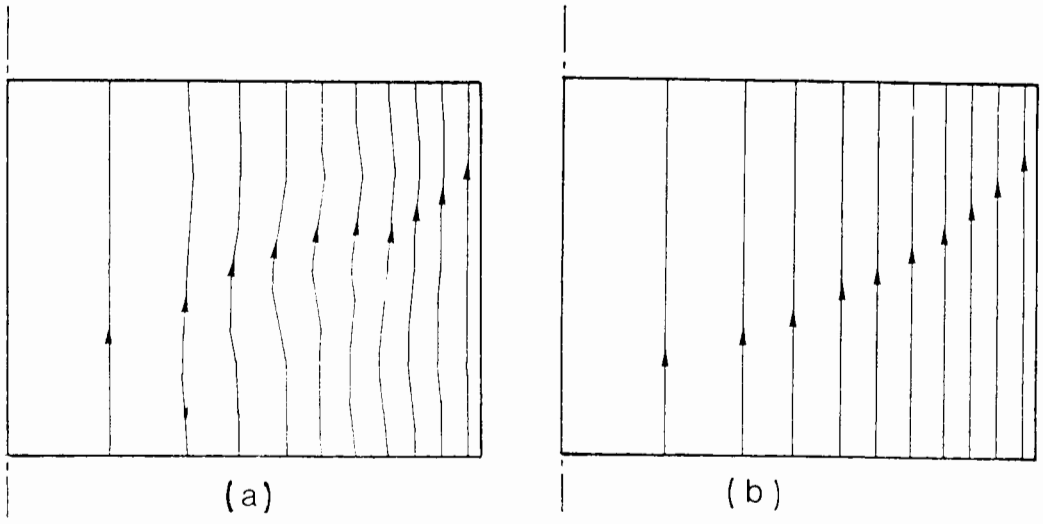

Figure 5.2: Streamlines (a) Before and (b) After Applying the Newon-Raphson Correction Scheme

is represented by the irregular streamline pattern in Figure 5.2a. The correct uniform velocity, represented by the streamline contours in Figure 5.2b, was obtained after two iterations.

However, the algorithm failed to converge to a solution when plastic deformations occurred. This suggests that the corrective scheme can only work for a system of linear equations and cannot be used when non-linearities such as soil plasticity are involved. Since plastic deformation is an essential feature of the cone penetration problem, the proposed method cannot provide the desired correction.

5.3.2 Pseudo-Dynamic Correction Method

The second correction method which has been attempted is based on an unsteady flow approach. Consider a soil element subjected to a set of stresses which are not in static equilibrium. Under the action of these stresses, the soil element will experience an acceleration governed by the equation:

$$-\frac{\partial \bar{p}}{\partial \bar{r}} + \frac{\partial \bar{s}_r}{\partial \bar{r}} + \frac{\partial \bar{\tau}_{rz}}{\partial \bar{z}} + \frac{\bar{s}_r - \bar{s}_\theta}{\bar{r}} = \bar{\rho}\left[\frac{\partial \bar{v}_r}{\partial \bar{t}} + \bar{v}_r \frac{\partial \bar{v}_r}{\partial \bar{r}} + \bar{v}_z \frac{\partial \bar{v}_r}{\partial \bar{z}}\right] \tag{5.7}$$

$$-\frac{\partial \bar{p}}{\partial \bar{z}} + \frac{\partial \bar{s}_z}{\partial \bar{z}} + \frac{\partial \bar{\tau}_{rz}}{\partial \bar{r}} + \frac{\bar{\tau}_{rz}}{\bar{r}} = \bar{\rho}\left[\frac{\partial \bar{v}_z}{\partial \bar{t}} + \bar{v}_r \frac{\partial \bar{v}_z}{\partial \bar{r}} + \bar{v}_z \frac{\partial \bar{v}_z}{\partial \bar{z}}\right] \tag{5.8}$$

where $\bar{\rho}$ is the density of the soil, $\bar{v}_r$ and $\bar{v}_z$ the velocity components in the radial and axial directions and $\bar{t}$ is the time. The bar in the two equations emphasises that the quantities have dimensions and these can be normalised as follow:

$$(s_{ij},\ p) = \frac{(\bar{s}_{ij},\ \bar{p})}{\bar{c}_u} \tag{5.9}$$

$$(r,\ z) = \frac{(\bar{r},\ \bar{z})}{\bar{R}} \tag{5.10}$$

$$(v_r,\ v_z) = \frac{(\bar{v}_r,\ \bar{v}_z)}{\bar{V}_o} \tag{5.11}$$

$$t = \frac{\bar{V}_o^2 \bar{t}}{\bar{R}} \tag{5.12}$$

By substituting these normalised quantities into (5.7) and (5.8) and eliminating $\bar{p}$ from the two equations gives:

$$\frac{\bar{c}_u}{\bar{\rho}\bar{V}_o} H = \frac{\partial}{\partial t}\left[\frac{\partial v_r}{\partial z} - \frac{\partial v_z}{\partial r}\right] + \frac{\partial}{\partial z}\left[v_r \frac{\partial v_r}{\partial r} + v_z \frac{\partial v_r}{\partial z}\right] - \frac{\partial}{\partial r}\left[v_r \frac{\partial v_z}{\partial r} + v_z \frac{\partial v_z}{\partial z}\right] \tag{5.13}$$

The rotation rate of the soil element is defined as:

$$\zeta = \frac{\partial v_r}{\partial z} - \frac{\partial v_z}{\partial r} \tag{5.14}$$

Substituting (5.14) into (5.13) results in:

$$\frac{\partial \zeta}{\partial t} = Q_e H - \left[v_r \frac{\partial \zeta}{\partial r} + v_z \frac{\partial \zeta}{\partial z} - \frac{v_r \zeta}{r}\right] \tag{5.15}$$

where:
$$Q_e = \frac{\bar{c}_u}{\bar{\rho}\ \bar{V}_o^2} \tag{5.16}$$

In addition, substituting for v_r and v_z in terms of ψ in equation 5.14 gives:

$$\zeta = -\frac{1}{r}\frac{\partial^2 \psi}{\partial r^2} - \frac{1}{r}\frac{\partial^2 \psi}{\partial z^2} + \frac{1}{r^2}\frac{\partial \psi}{\partial r} \tag{5.17}$$

Equation (5.15) is analogous to the vorticity transport equation with ($Q_e H$) replacing the vorticity diffusion terms. Equation (5.17) is identical to the stream function equation derived in Section 3.3.

In a viscous fluid flow, the shear stresses are directly related to the local velocity gradient. However, no such simple relationship exist for the 'flow' of an elasto-plastic material. The constitutive laws governing soil behaviour are much more complex and the stresses are related not only to the local velocity gradients (or strain rates) but are also dependent on the previous stress path. Nevertheless, it is hypothesized that the loose link that exists between the stresses and strain rates may be used to provide a means of correcting the initial velocity estimate.

Much insight into the stress strain behaviour of soil due to cone penetration can be gained by a detailed examination of equation (5.15). If the soil is assumed to have an undrained shear strength of 50 kPa and a density of 1800 kg/m^3, then for a standard penetration speed of 2 cm/sec, the dimensionless time factor, Q_e, is approximately equal to 7×10^4. As a first approximation, the bracketed terms in equation (5.15) can be neglected giving:

$$\frac{\partial \zeta}{\partial t} = Q_e H \tag{5.18}$$

Equations (5.17) and (5.18) can be solved by adopting a numerical procedure similar to that used in fluid flow computations. The solution algorithm proposed is outlined below.

Step 1: Equation (5.18) is expressed in a finite difference form and ζ is evaluated as:

$$\zeta^{k+1} = \zeta^{k} + Q_e H \Delta t \tag{5.19}$$

In order to ensure convergence of the numerical procedure, a very small time step, Δt, must be used.

Step 2: The boundary value of ζ is evaluated from the current stream function field.

Step 3: Equation (5.17) is solved by the S.O.R. scheme to obtain the stream function ψ. In this calculation, the updated ζ values are used in the source term.

Step 4: The stresses which correspond to the new stream function field are evaluated using the strain path method.

Step 5: The error measure, H, associated with the new stress field is evaluated.

The computation cycle from Steps (1) to (5) is repeated until H is acceptably small. Except for the first iteration, the most recent value of H is used in Step (1) to compute the new ζ values.

The major uncertainty in the implementation of this correction scheme concerns the calculation of the boundary ζ values from ψ. Due to the complexity of soil behaviour at the penetrometer-soil interface, it is not clear how this should be performed. A slip wall boundary condition which models an inviscid fluid flow has been applied in this thesis. However, this makes no distinction between soil and fluid behaviour and so is not strictly correct.

The error measure, H, represents a quantity which tends to alter the deformation pattern in the soil mass. Equation (5.18) expresses this fact by

indicating that H changes the rotation rates of the soil elements. Although this parameter is useful for quantifying the equilibrium imbalance, it is difficult to ascertain what magnitude of H represents an acceptable solution. This is not a major obstacle if H is used merely as an indicator for comparing the relative quality of various solutions. A reduction in H is an unambiguous signal of an improved solution and it will thus be a useful parameter for checking the performance of the numerical scheme.

Test Cases

The algorithm formulated above was used to solve the hypothetical test problem discussed in the previous section. The pseudo-dynamic method was found to be more stable than the Newton-Raphson procedure. It could approximate the exact solution quite closely even when plastic stresses were involved. The stream function field before and after the application of this correction procedure is very similar to that shown in Figure 5.2 and is not repeated here.

This algorithm has also been tested with the cone penetration problem. In this case, the overall progress of the correction procedure is monitored by a global error measure which is defined as:

$$E_r = \left(\frac{1}{n} \sum_{1}^{n} H^2 \right)^{1/2} \tag{5.25}$$

A reduction of 10 to 20 per cent in E_r is obtained when the algorithm is applied to the cone penetration problem. However, the correction procedure has very little effect on the errors in a small region around the cone shoulder where H is at a maximum. The failure of the scheme to eliminate completely the stress error is probably due to the inadequate treatment of

the penetrometer boundary, and partly due to the complexity introduced by the singularities at the cone tip and the cone shoulder. A detailed analysis of the shoulder in particular is necessary if the correction procedure is to be implemented successfully. Due to the limited scope of the present study, this has not been attempted here.

5.3.3 Finite Element Correction Method

It has been shown in Section 5.1 that the out-of-balance deviatoric stresses can be forced to obey the equilibrium equations if a set of fictitious body forces is present. In other words, the streamlines evaluated for an inviscid fluid flow would be the correct trajectories of the soil elements only if the fictitious body forces are present. If these body forces are removed, the soil elements will follow slightly different paths and a different streamline pattern is obtained.

In a correct solution, the fictitious body forces are identically equal to zero if the self weight of the soil is neglected. Therefore, there is a possibility of using the fictitious body forces computed to improve the initial velocity estimate. One possible solution scheme is described below. It should be emphasised that the proposed algorithm is based largely on heuristic argument and hence is not mathematically rigorous.

Consider a soil element which moves along a streamline with stream function ψ_e under the action of the deviatoric stresses and a set of fictitious body forces. At a point very far from the penetrometer, the stresses are close to the in-situ values and the equilibrium condition is satisfied fully. The fictitious body forces at any other location along the streamline can be cancelled by imposing an equal and opposite set of body forces. Under the action of these imposed loads, the soil elements along the

streamline would be displaced from their initial locations (Figure 5.3). The amount of displacement due to the imposed load can be evaluated by a numerical procedure such as the finite element method. The locus of the displaced soil element is assumed to represent a new streamline which retains the original stream function value ψ_e. This is a reasonable assumption since the value of ψ associated with any streamline is determined by its initial location far ahead of the penetrometer.

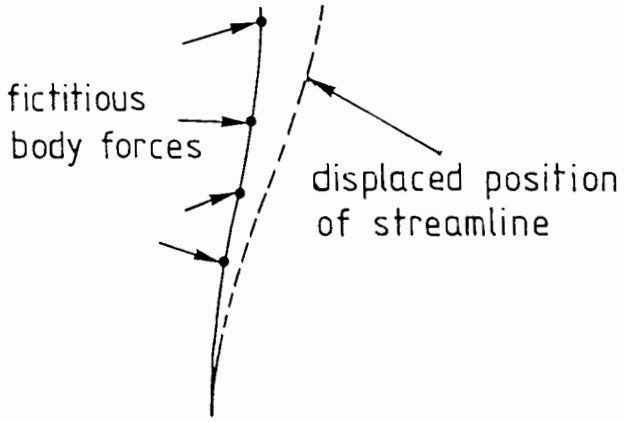

Figure 5.3: Displacement of Soil Elements Along Streamlines Due to Imposed Body Forces

The new streamline profiles obtained by the above procedure represent a new stream function (or velocity) field. The stresses which correspond to this new velocity estimates can be computed by the strain path method. In general, the updated stresses will not satisfy the equilibrium equations completely, so a new set of fictitious body forces is obtained. If the correction procedure has been performed correctly, the magnitude of these new fictitious body forces will be smaller. This process can then be repeated iteratively until the body forces are sufficiently small everywhere.

Preliminary studies using this correction method have not met with much success. One major difficulty with this iterative procedure was due to the

different numerical schemes which had been used in the strain path analysis and the corrective displacement calculations. The strain path method was formulated in finite differences and the field variables were represented at the grid points. The deformation analysis due to the imposed body forces, on the other hand, was performed with a finite element method in which stresses and strains were represented at the Gauss points. In general, the grid points and the Gauss points did not coincide and some form of interpolation was therefore necessary. The inevitable errors associated with the interpolation process rendered it extremely difficult to implement this algorithm accurately.

It is possible that the problem associated with interpolation may be alleviated by adopting a single numerical procedure, say the finite element method, for both the strain path analysis and the displacement calculations. This analysis is beyond the scope of the present study and has not been pursued further.

5.4 Summary

In this chapter, attempts have been made to utilised the approximate stresses based on an initial velocity field to obtain a better solution. Three different correction schemes have been investigated. The proposed iterative finite element method has not been implemented successfully. This is mainly due to the large amount of interpolation and data transfer required between the finite difference and finite element meshes. It is suggested that this corrective scheme is potentially useful if the problem of interpolation is eliminated by adopting a single numerical formulation for the overall analysis.

It has been found that the proposed Newton-Raphson scheme is applicable when the soil behaviour is linear (i.e. purely elastic). When non-linearities such as soil plasticity are included, this iterative scheme fails to converge to a solution. The pseudo-dynamic method improved the solution even when non-linearities are involved, but the errors of equilibrium imbalance cannot be eliminated completely. The failure of this algorithm can be attributed to inadequate treatment of the soil-penetrometer interface. In addition, detailed analyses of the singularities at the shoulder and the tip may also be necessary if an exact solution is to be found.

Chapter 6

Stress and Strain in the Soil due to Cone Penetration

6.1 Introduction

A series of parametric studies on the cone penetration problem has been carried out. Various combinations of soil properties, initial stress states and cone geometries were studied. An inviscid flow solution was used to approximate the strain field of soil. The stresses computed are only approximate because the equilibrium equations are not completely satisfied throughout the whole soil mass. However, the solution in most regions are of reasonable accuracy, except in the vicinity of the cone shoulder and (to a lesser extent) the cone tip, where appreciable errors exist. In this chapter, the total stresses are computed by adopting p_r as the mean pressure solution.

The results evaluated using the strain path method are compared extensively with the predictions based on cavity expansion theory, which is currently the state-of-the-art approach in deep penetration problems. It is shown that under certain circumstances, cavity expansion theory and the strain path method give rise to nearly identical solutions. But in general, the results obtained from these two approaches are rather different.

6.2 Effect of Cone Geometry

The simple pile problem discussed in Chapter 2 is attractive because it is amenable to analytical solution. However, if this solution is to be adopted for interpreting cone penetration data, the influence of the tip geometry must be thoroughly investigated. This is because the tip of a simple pile is very different from that of conventional cone penetrometers. In this section, the effect of tip geometry is studied by comparing the strain and stress paths of soil elements due to the penetration of penetrometers with different apex angles. The deviatoric stresses and

strains computed are plotted in the stress space defined by S_i and the strain space defined by E_i respectively.

Figure 6.1 shows the strain paths of soil elements located in the far field of a penetrometer tipped with a 60° cone. For all practical purposes, these strain paths are identical to those at comparable normalised distances due to simple pile penetration (Figure 2.4). The residual values of the deviatoric strains E_1 and E_3 at the downstream boundary are due mainly to the finite size of the mesh used in the numerical computations and do not imply differences in the two solutions.

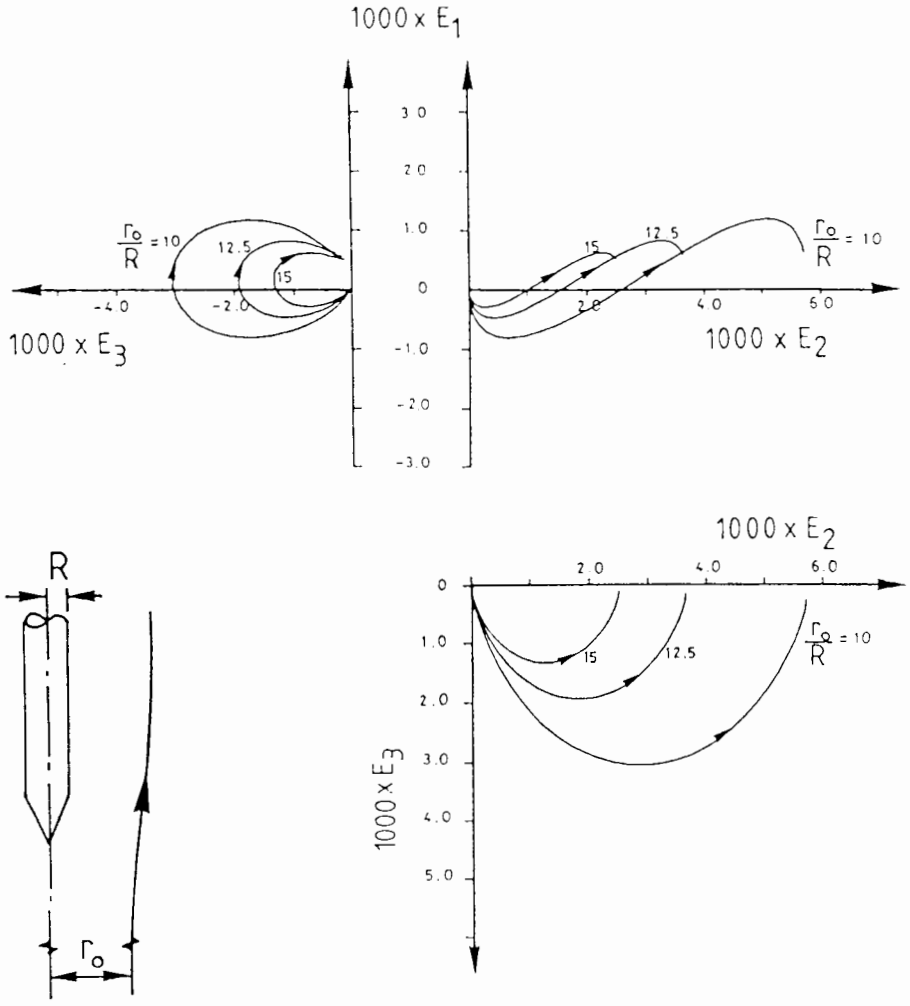

Figure 6.1: Strain Paths in the Far Field of a 60° Cone Penetrometer

In the far field, where the stresses lie entirely within the elastic range, the deviatoric stresses S_i are proportional to the deviatoric strains E_i (equation (2.30)). Therefore, the shapes of the stress paths at comparable radial distances are similar to those of the strain paths. In addition, these stress paths are also similar to those in the simple pile problem. Two important conclusion can be drawn from this result. The obvious deduction is that the far field conditions in the soil are not sensitive to the actual shape of the tip (an example of St Venant's principle). The second conclusion concerns the accuracy of the numerical scheme. In the simple pile problem, the equation of the streamline is known, and the stress path can be determined to any required degree of accuracy by refining the calculation steps. The good agreement between the numerical results and the analytical solutions for the simple pile problem is therefore an indication of the accuracy of the numerical scheme.

Different results, however, were obtained for the near field stresses. The stress paths of two soil elements originally located at normalised distances, $(\frac{r_o}{R})$, of 0.5 and 1.0 from the axis of the penetrometer are plotted in Figure 6.2. These stress paths are significantly different from those in the simple pile solution described in Chapter 2. Due to the finite size of the grid spacings and the extremely high strains that exist in the near field, some discretization errors are inevitable in the numerical solution. This, however, could not explain the large difference observed and the discrepancy must be due to the different tip geometries.

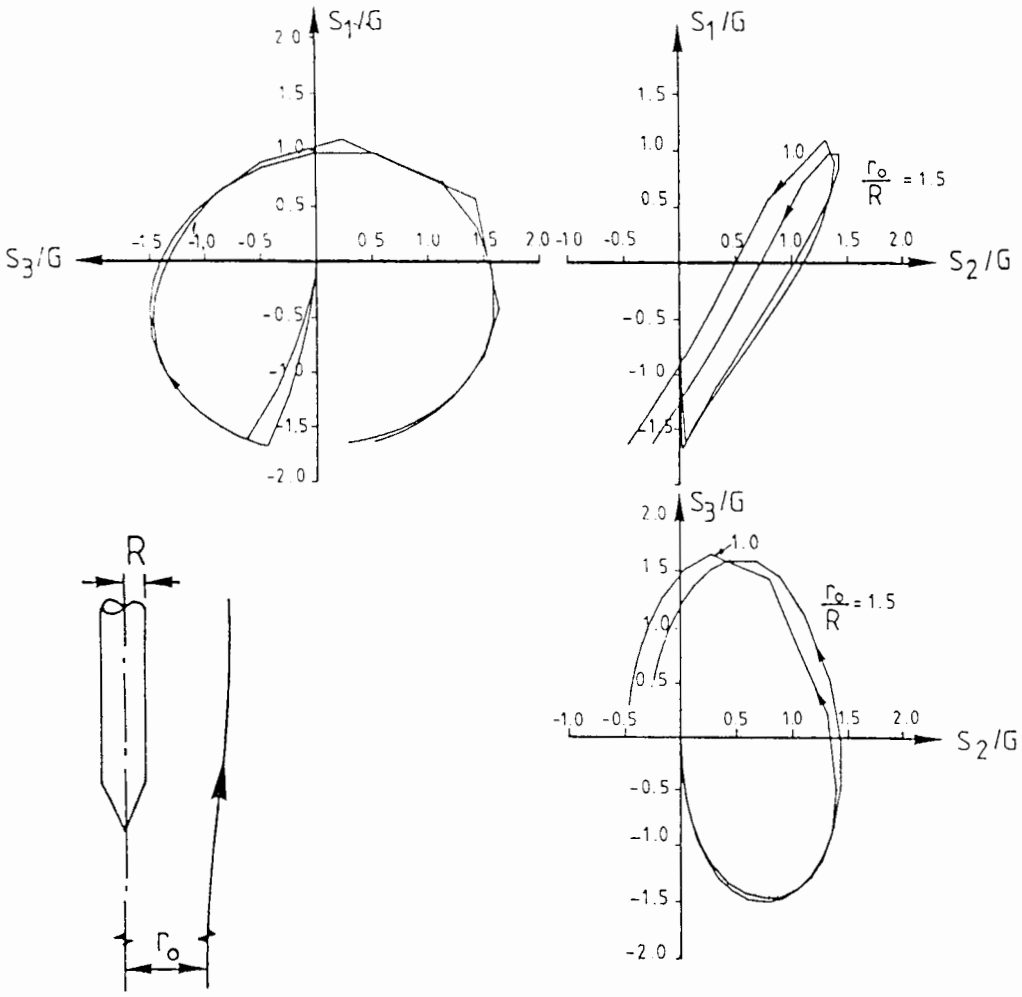

Figure 6.2: Stress Paths in the Near Field of a 60° Cone Penetrometer

In order to gain a better understanding of the effect of tip geometry, penetration analyses of penetrometers with different apex angles were carried out. The near field strain paths of soil elements initially located at a radial distance of 1.0 R from the axis are shown in Figure 6.3. Regardless of the cone angles, the values of E_2 (which corresponds to the strain mode in a pressuremeter test) at the level of the cone shoulder are nearly similar. The main features that distinguish these strain paths are the amount of deviatoric shear strain E_3 and the deviatoric axial strain E_1. Increasing the cone angle increases the E_1 and E_3 strain components quite significantly.

For the 10° sharp cone, E_1 and E_3 are relatively small. The projection of the strain path on the E_1-E_2 plane is nearly parallel to the E_2-axis, and thus closely resembles that due to the expansion of a cylindrical cavity. A major proportion of the soil strain caused by the penetration of a 10° cone occurs when the soil is between the tip and shoulder elevations. In contrast, for larger cone angles, the soil on reaching the tip elevation has already been subjected to a significant level of straining and this is mainly due to the E_1 and E_3 components.

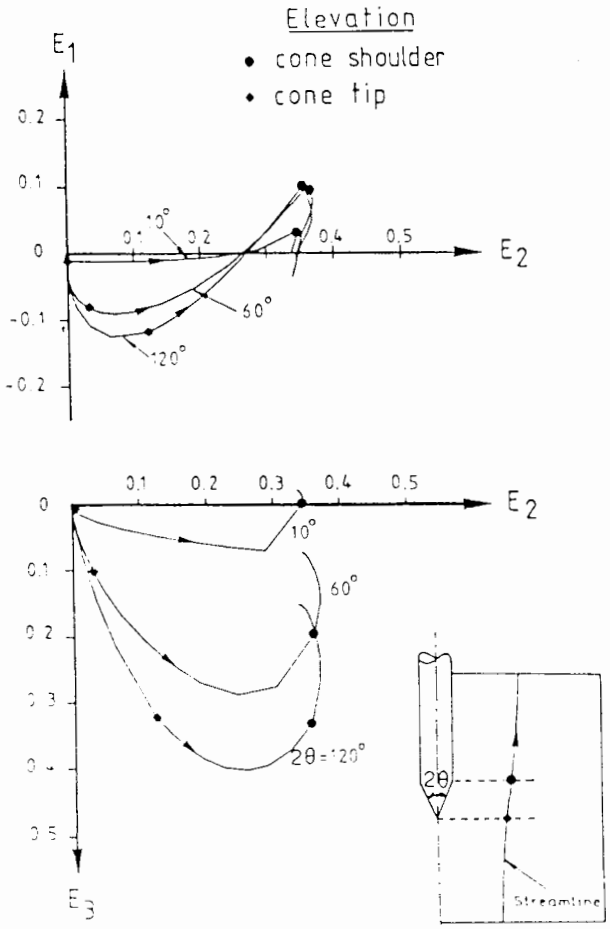

Figure 6.3: Strain Paths Due to Penetrometers with Different Apex Angles

A good indication of the soil deformations due to cone penetration can be obtained from the velocities of the soil elements around the penetrometer, and these are plotted in Figure 6.4. The scale for the velocity vectors are

kept constant in all the plots. The soil velocities are found to be higher around penetrometers with larger apex angles. In the 10^{o} cone, soil was displaced mainly in the radial direction with very little axial movement. For the blunter cones, the deformation fields are more complex involving large radial and axial movements.

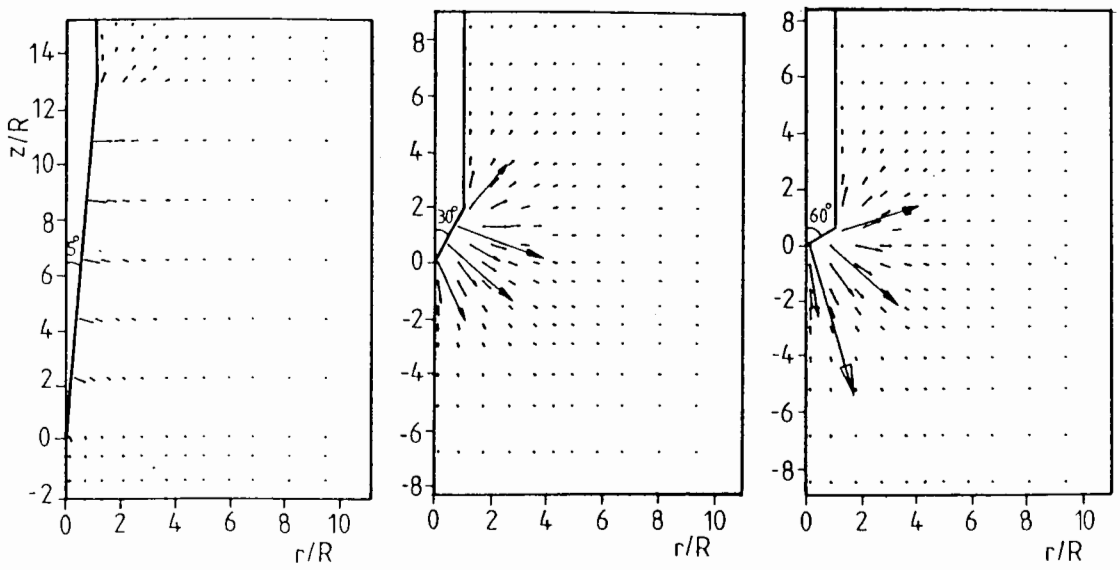

Figure 6.4: Velocity Field around Penetrometers with Different Apex Angles

6.3 Stress and Strain around a 10^{o} Cone Penetrometer

Norbury and Wheeler (1987) presented an analysis of the penetration of an infinite cone with very small apex angle. They report that the leading order terms of the analytical solution for such a body is identical to the cylindrical cavity expansion solution. It is thus reasonable to assume that cylindrical cavity expansion theory can provide a good estimate of the soil stresses around a penetrometer with a very small apex angle.

The strain contours due to the penetration of a 10^{o} cone are shown in Figure 6.5. Ahead of the cone tip, a small zone of soil is subjected to

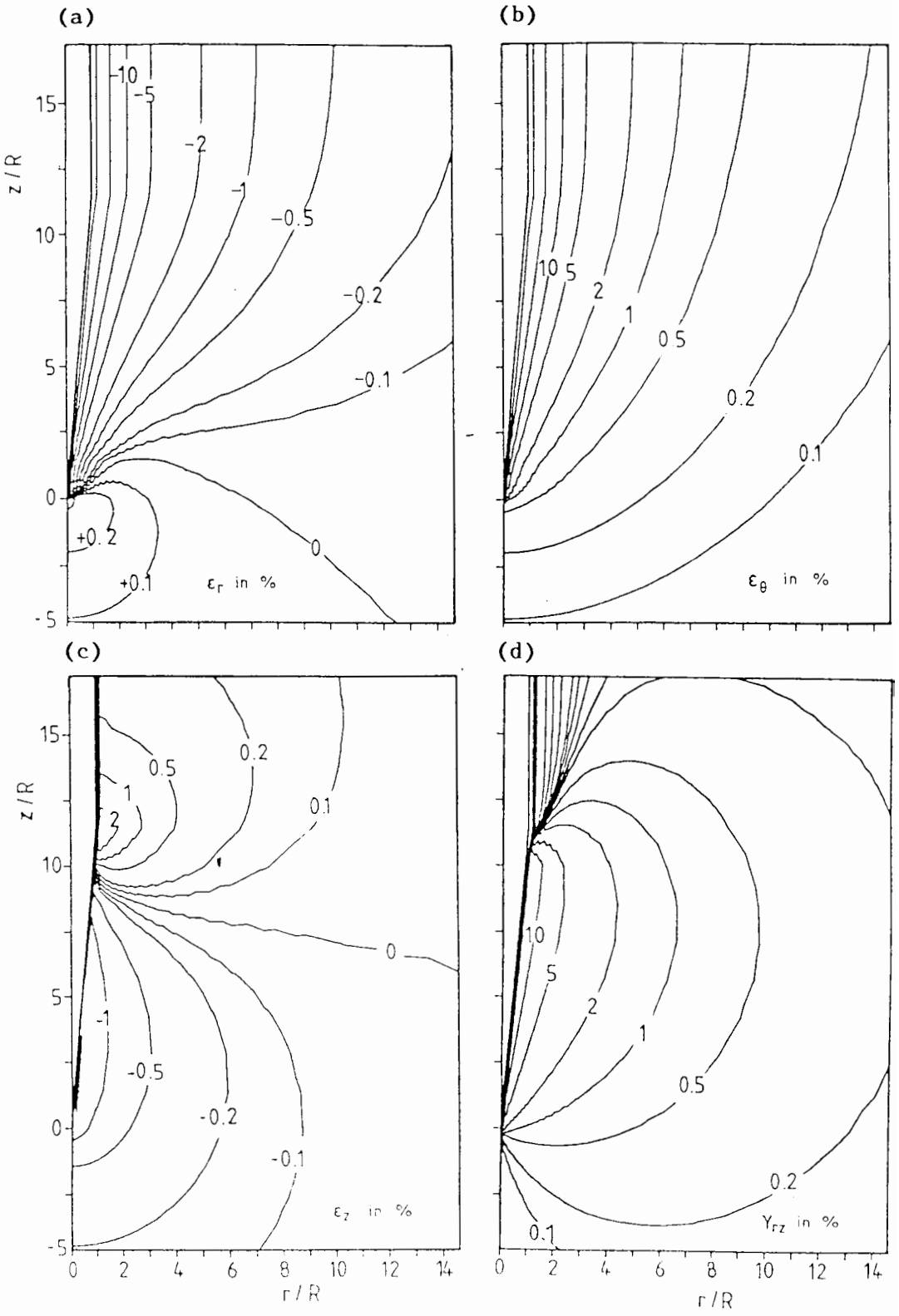

Figure 6.5: Strain Contours around a 10° Cone Penetrometer

tensile radial strains. Above the tip elevation, ε_{rr} is purely compressive and the contours adjacent to the shaft are parallel to the axis of penetration. The magnitudes of soil strains above the shoulder level are broadly comparable to those derived from cylindrical cavity expansion theory.

In addition to the radial and hoop strain components, the strain path method also predicts finite axial and shear strains. Approximately below the cone shoulder level, the axial strain is purely compressive, and above it purely tensile. This reversal in the direction of strain would not occur in a slender body problem due to the infinite length of the body and the absence of a sharp corner. This suggests that the slender body theory is strictly not applicable to a penetrometer which has a more complicated geometry.

The stresses due to the penetration of a 10° cone penetrometer are shown in Figure 6.6. The solution is based on a soil with a rigidity index of 100 and an isotropic initial stress state. At the cone-soil interface, soil stresses increase with the radius of the conical section, reaching a maximum at the cone shoulder. Above the cone shoulder, the normal stress components decrease quite rapidly to reach a steady value some distance from the shoulder. The stress contours far behind the tip are parallel to the shaft, suggesting that a steady state condition has been reached.

In order to compare the results obtained from the strain path analysis with the predictions by cavity expansion theory, the variations of the stresses with radial distance have been plotted in Figure 6.7. The soil stresses shown are for a plane mid-way between the tip and shoulder. The analytical solution for the expansion of a cylindrical cavity from zero radius (Sagaseta, 1984) is shown as dotted lines. Good agreement between the two solutions is obtained for a zone of soil within a radius of $3\ R_c$ from

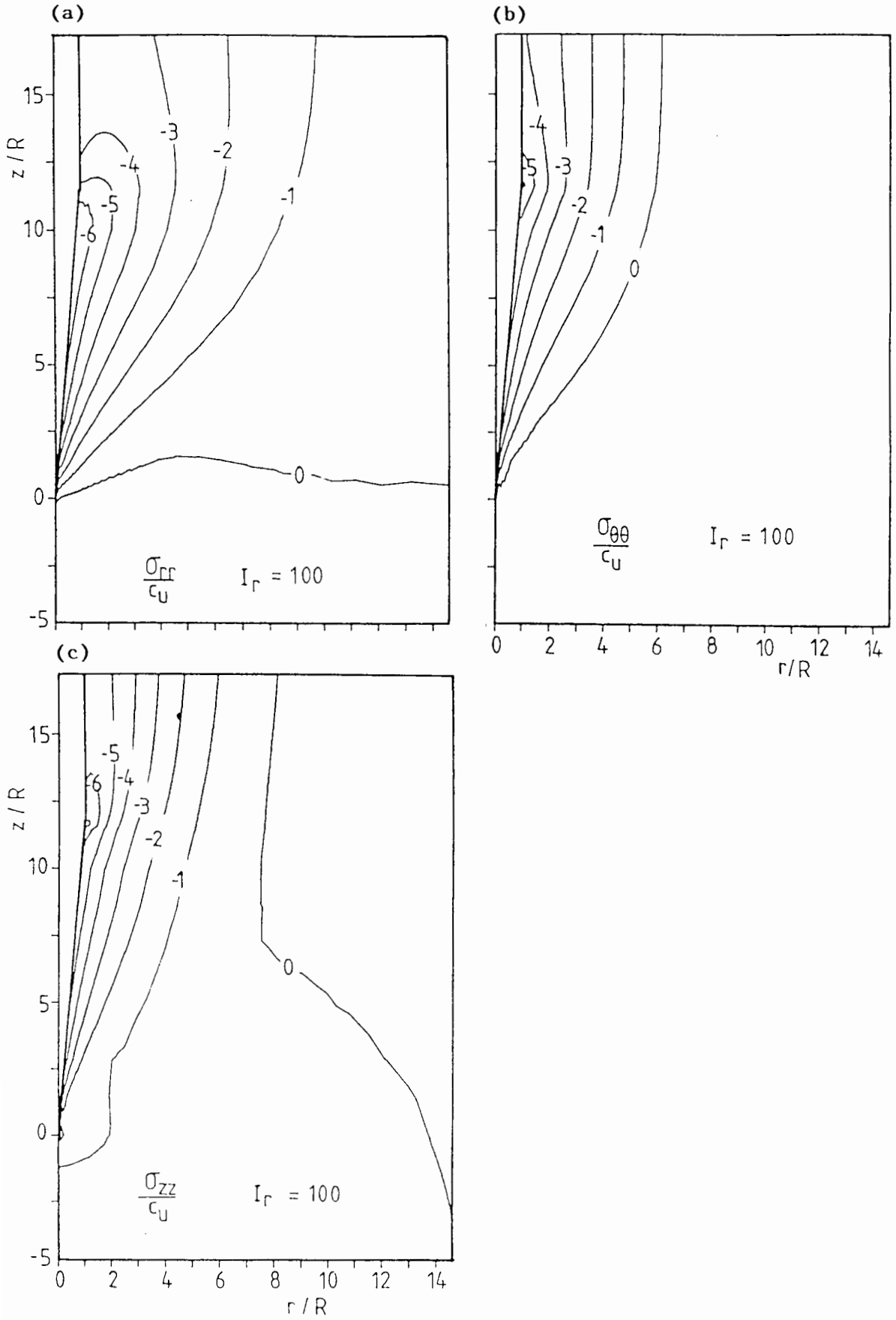

Figure 6.6: Stress Contours around a 10° Cone Penetrometer

the axis, where R_c is the radius of the conical section (or final cavity radius). Further from the cone face, the radial stresses still agree very closely but significant differences are observed in the axial and hoop stress components. In addition, the strain path method results in finite shear stresses, in constrast to cavity expansion theory which predicts that τ_{rz} is zero. The differences in $\sigma_{\theta\theta}$ and σ_{zz} computed by these approaches appear to be directly related to the magnitude of the shear stress. These differences are large at the locations where τ_{rz} is of appreciable magnitude, and vice versa.

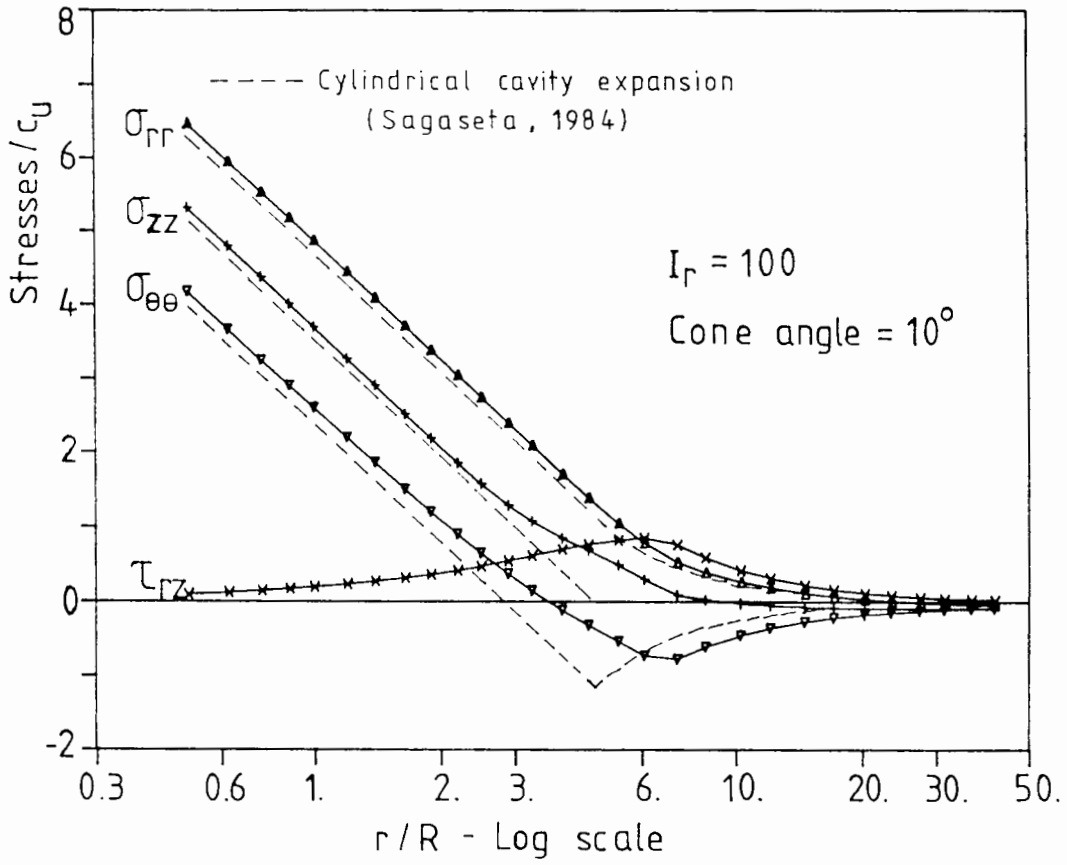

Figure 6.7: Stress Variation on a Horizontal Plane at the Mid-Cone

The variations of σ_{rr} on various levels of the conical section are plotted in Figure 6.8. As the cone shoulder is approached, the magnitude of σ_{rr} close to the cone falls below the value predicted by cylindrical cavity expansion theory. It is apparent that the change in the trend of stress

variation from the strain path analysis can be directly attributed to the abrupt change in the cone geometry at the shoulder. Far from the cone shoulder, the predicted agreement between a slender cone and cylindrical cavity expansion has been reproduced quite satisfactorily.

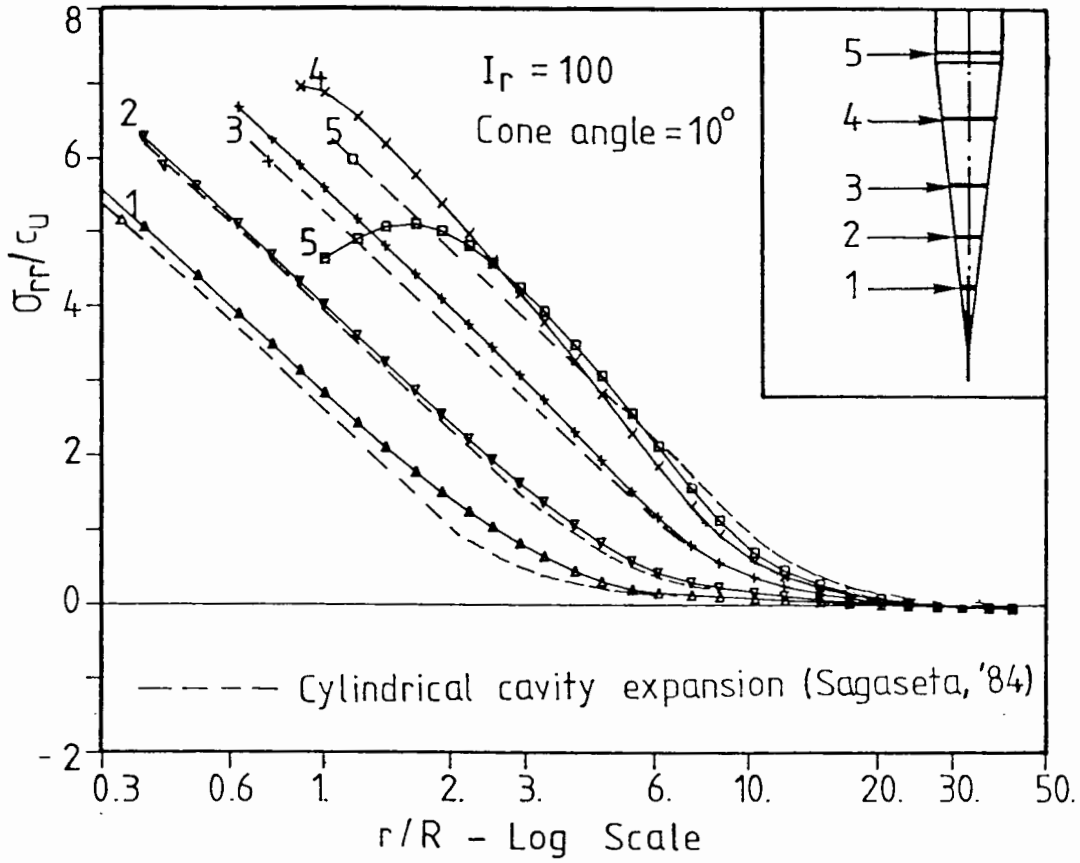

Figure 6.8: Variation of σ_{rr} with Radial Distance on the Conical Section of a 10° Cone Penetrometer

6.4 Stress and Strain around a Standard 60° Cone Penetrometer

In this section, the stresses and strains in the soil around a 60° cone calculated by the strain path method are described. The initial soil velocities based on the inviscid flow solution were partially corrected for equilibrium imbalance by the iterative pseudo-dynamic scheme.

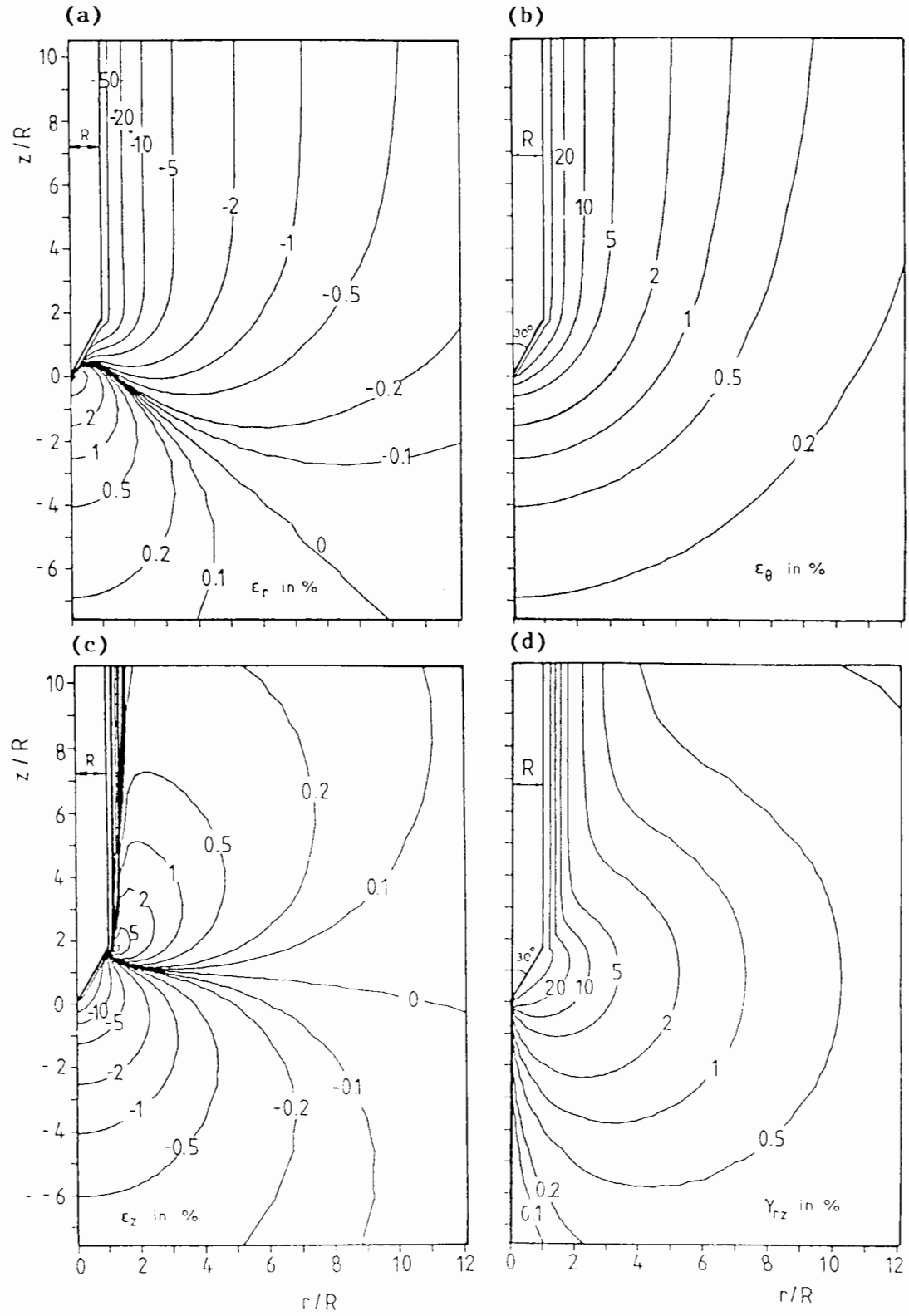

Figure 6.9: Strain Contours around a 60° Cone Penetrometer

The strain field which corresponds to this initial velocity estimate is shown in Figure 6.9. Beneath the tip, tensile radial strain is again observed in a small zone of soil. Beyond this zone, ε_{rr} is everywhere compressive. Far behind the tip, the strain contours are approximately parallel to the axis of the penetrometer and the variations of $\varepsilon_{\theta\theta}$ and ε_{rr} with radial distance are comparable to the solutions based on cylindrical cavity expansion theory.

The contours of the axial and shear strains are shown in Figures 6.9c and 6.9d respectively. The cone shoulder once again marks an important transition in the axial strain direction. Below the shoulder level, ε_{zz} is compressive, and above this level ε_{zz} is entirely tensile. A good indication of the level of straining in the soil is provided by the octahedral shear strain, γ_{oct}, and this is plotted in Figure 6.10. The zone of maximum shear straining was located just adjacent to the penetrometer, and the strain

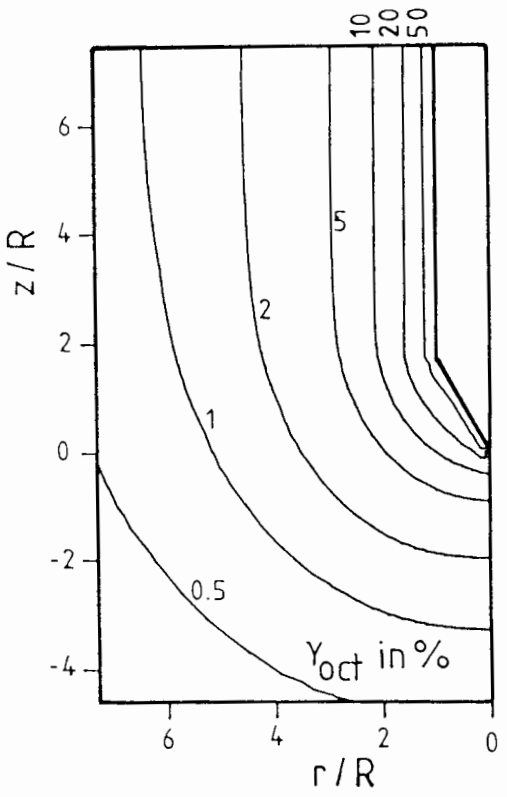

Figure 6.10: Octahedral Strain Contours around a 60° Cone Penetrometer

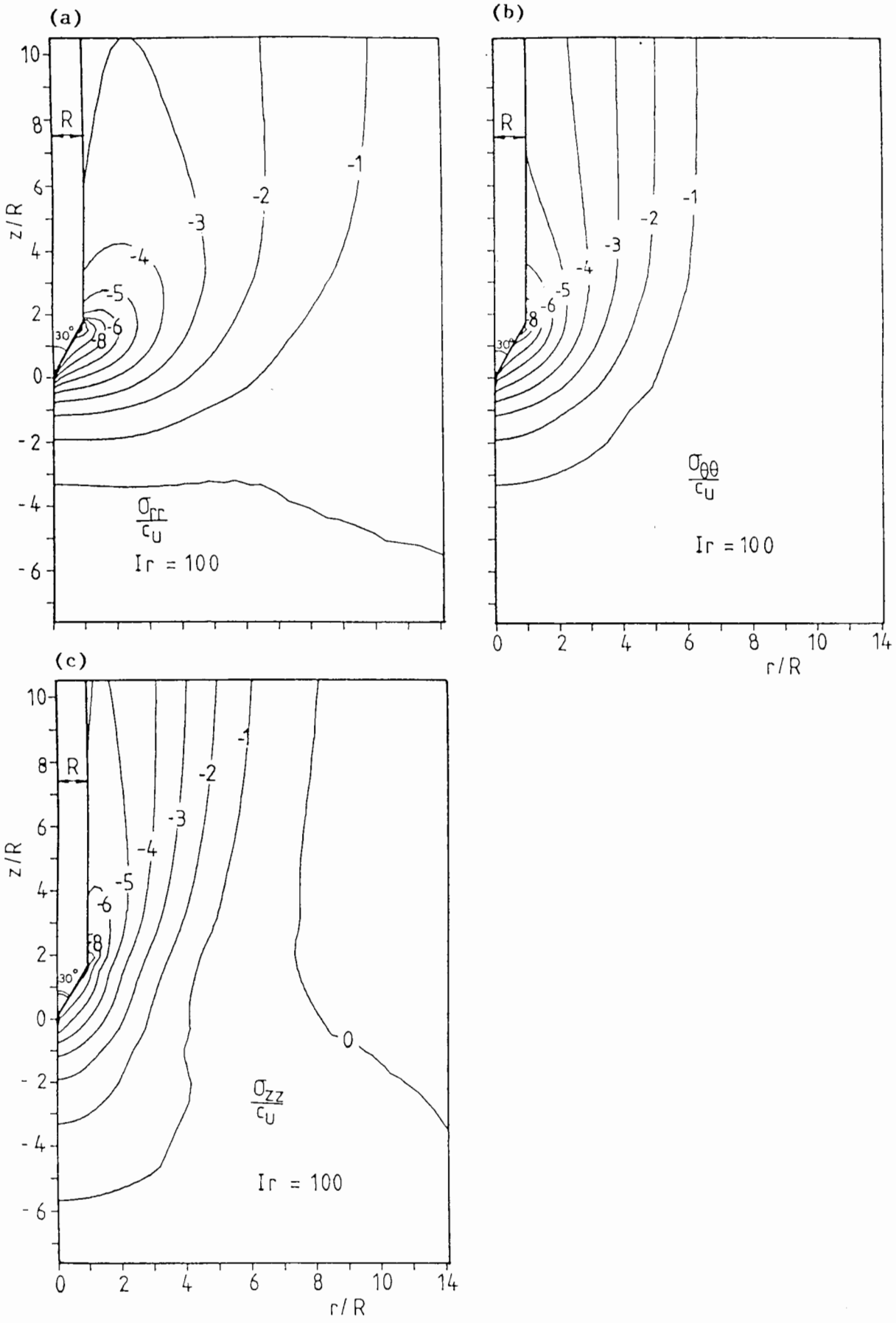

Figure 6.11: Stress Contours around a 60° Cone Penetrometer

magnitudes are found to be very much higher than those normally encountered in conventional laboratory tests.

The stresses which correspond to the assumed strain field for a soil with a rigidity index of 100 are shown in Figure 6.11. The initial stresses in the soil were assumed to be zero. High stress intensities are observed around the cone face. The stresses are at a maximum in a region just below the cone shoulder. Above the shoulder level, the normal stresses drop off rapidly over a distance of about 5 R to reach a steady value. The stress contours far behind the cone tip are parallel to the shaft indicating that a steady stress state has been reached.

Figure 6.12 shows the stress variation on a level mid-way between the

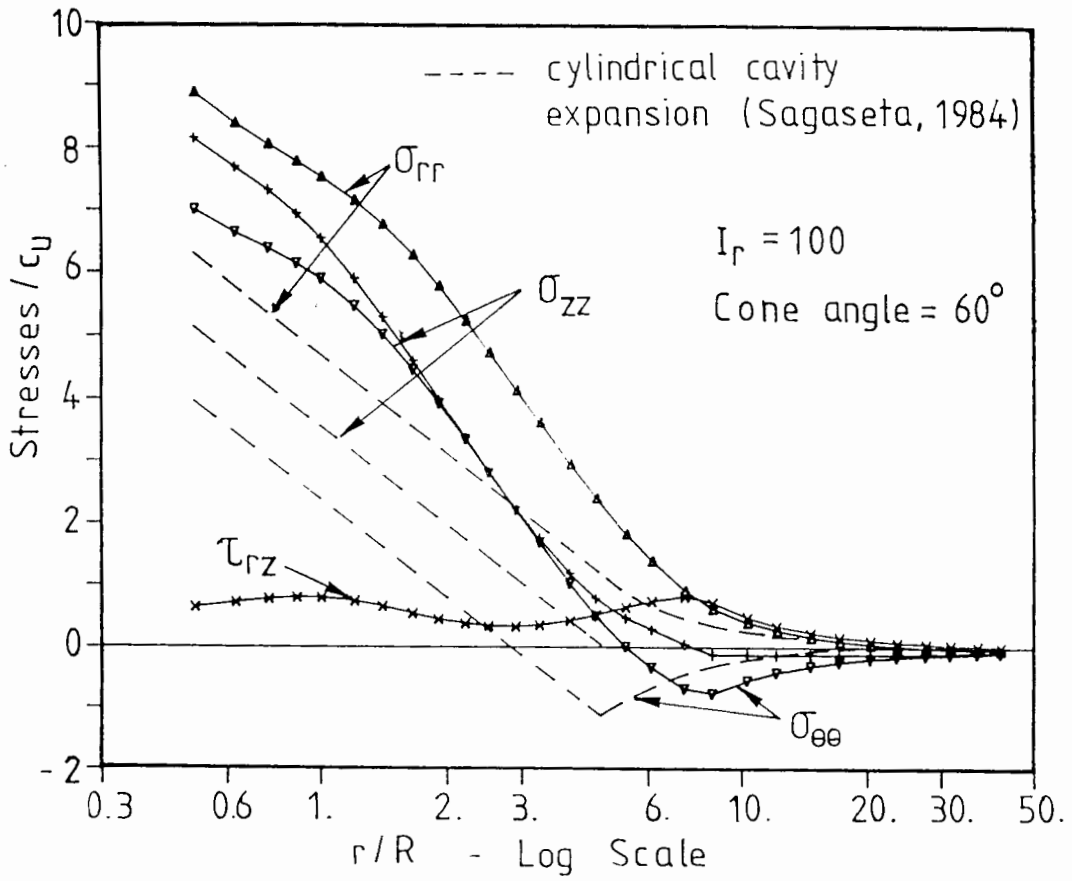

Figure 6.12: Stress Variation on a Horizontal Plane Mid-way between the Shoulder and Tip of a 60° Cone Penetrometer

tip and the shoulder. Close to the cone, the total stress components are higher than those predicted by cylindrical cavity expansion theory. The variations of the stresses with radial distance derived from these two methods also differ significantly. It has often been assumed that cylindrical cavity expansion theory can be used to provide an estimate of soil stresses around the shaft far from the tip. This, however, is not supported by the results from strain path analysis which shows a significantly different distribution (Figure 6.13). The radial stress σ_{rr} adjacent to the shaft is smaller than σ_{zz} and $\sigma_{\theta\theta}$, in contrast to the stress distribution at the cone face region where σ_{rr} is the largest stress component.

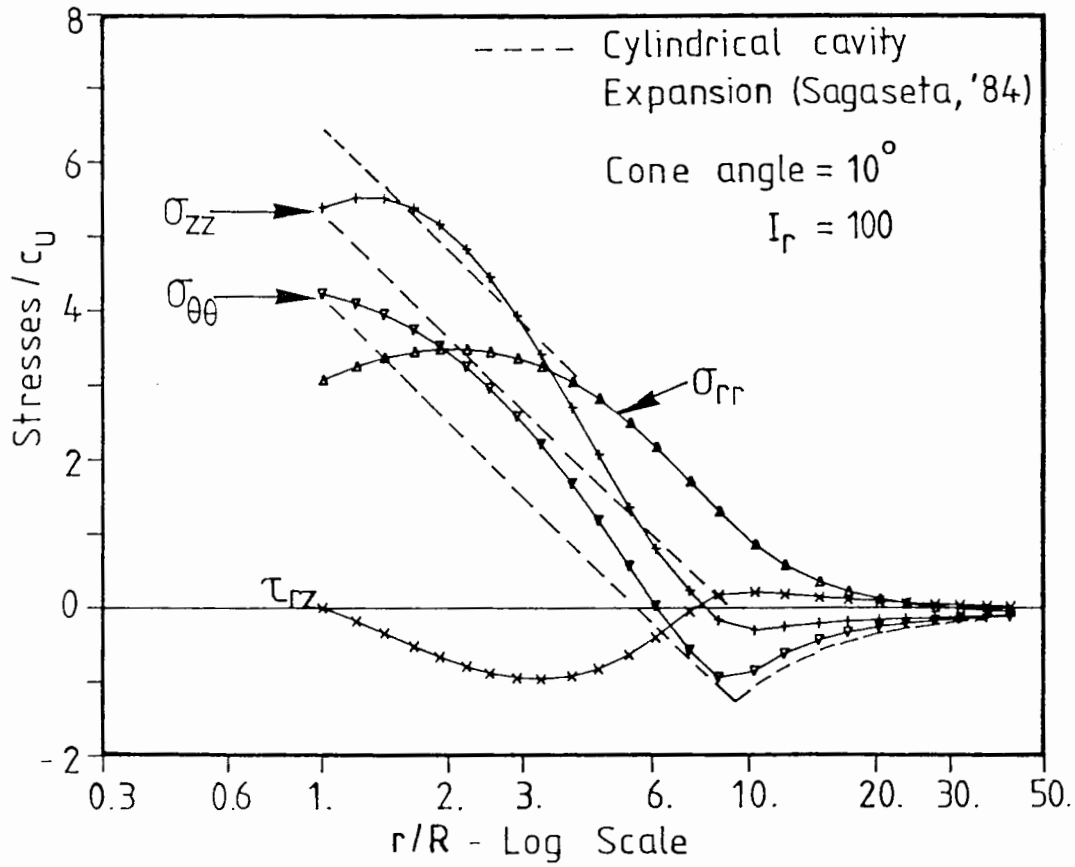

Figure 6.13: Stress Variation on a Horizontal 20 R above the Tip

The variation of the stress components along a vertical grid line is illustrated in Figure 6.14. The rapid reduction in the normal stresses when the soil emerges from the shoulder level is clearly evident and this is accompanied by a reversal in the shear stress component, τ_{rz}. Changes in the relative magnitudes of the stress components are indicative of rotations of the principal stress axes. This result has important implications on the interpretation of penetration test data because the rotations of principal stress axes is known to have a significant influence on the stress-strain behaviour of soil.

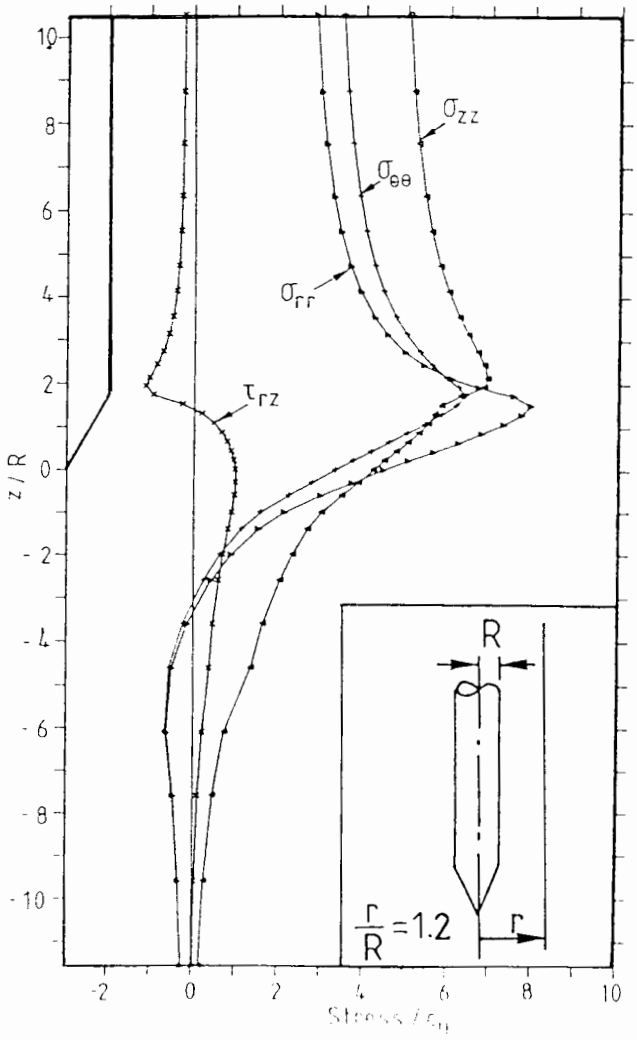

Figure 6.14: Stress Variation along a Vertical Grid Line

6.5 Failure Zone due to Cone Penetration

A useful indicator of the deformation mechanism around a penetrometer can be obtained from an analysis of the failure zone, which is defined as a region in which the soil is deforming plastically. The failure zones around penetrometers with cone angles of 10°, 60° and 120° in a soil with a rigidity index of 100 are plotted in Figure 6.15. The cone angle is found to have an appreciable effect on the extent of yielded soil around the tip. Above the shoulder level, however, the zones of the plastically deformed soil are unaffected by the apex angles.

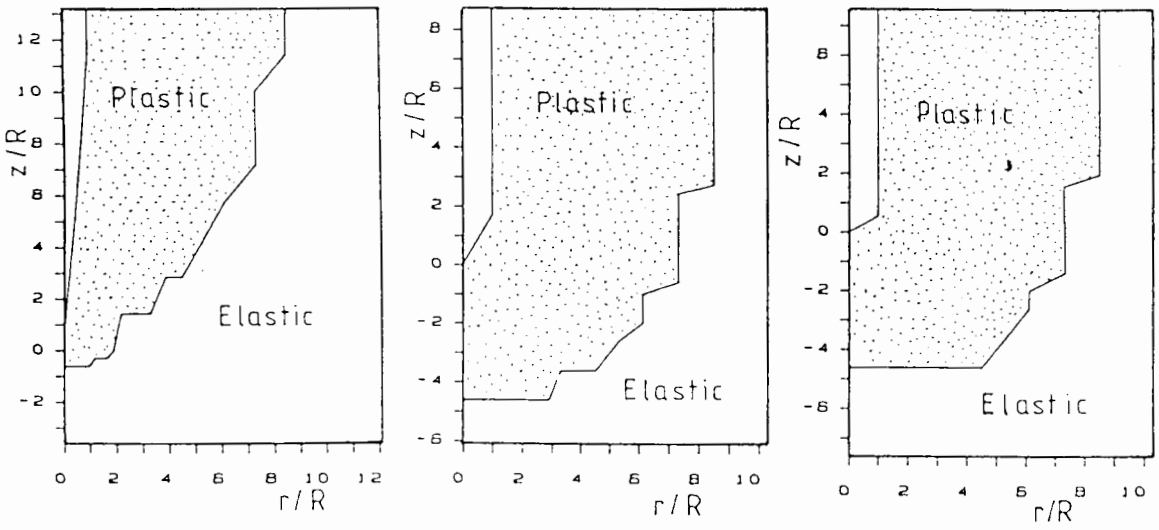

Figure 6.15: Failure Zones around Cone Penetrometers

The failure zone around a penetrometer is most conveniently described by the elasto-plastic boundary which divides the soil into two regions in which the soil is deforming either plastically or elastically. In the cone penetration problem, the size of the failure zone is characterised by two parameters R_p and Z_p. The radial distance of the elasto-plastic boundary from the axis of the penetrometer, at a large distance above the tip, is denoted by R_p. The distance of this boundary from the cone tip, measured

along the axis of penetration, is represented by Z_p. The values of these two parameters for different values of I_r are shown in Figure 6.16.

The normalised plastic radius, R_p/R, is found to be independent of the cone angle but is significantly affected by changes in I_r. As I_r increases, the zone of yielded soil around the cone also increases. The radius of the elasto-plastic boundary in the expansion of either a cylindrical or a spherical cavity from zero radius in an infinite medium, normalised by the current cavity radius, is shown in the diagram for comparison. The variation of R_p with I_r is very similar to that predicted by the expansion of a cylindrical cavity although the normalised plastic radius from strain path analysis was slightly smaller.

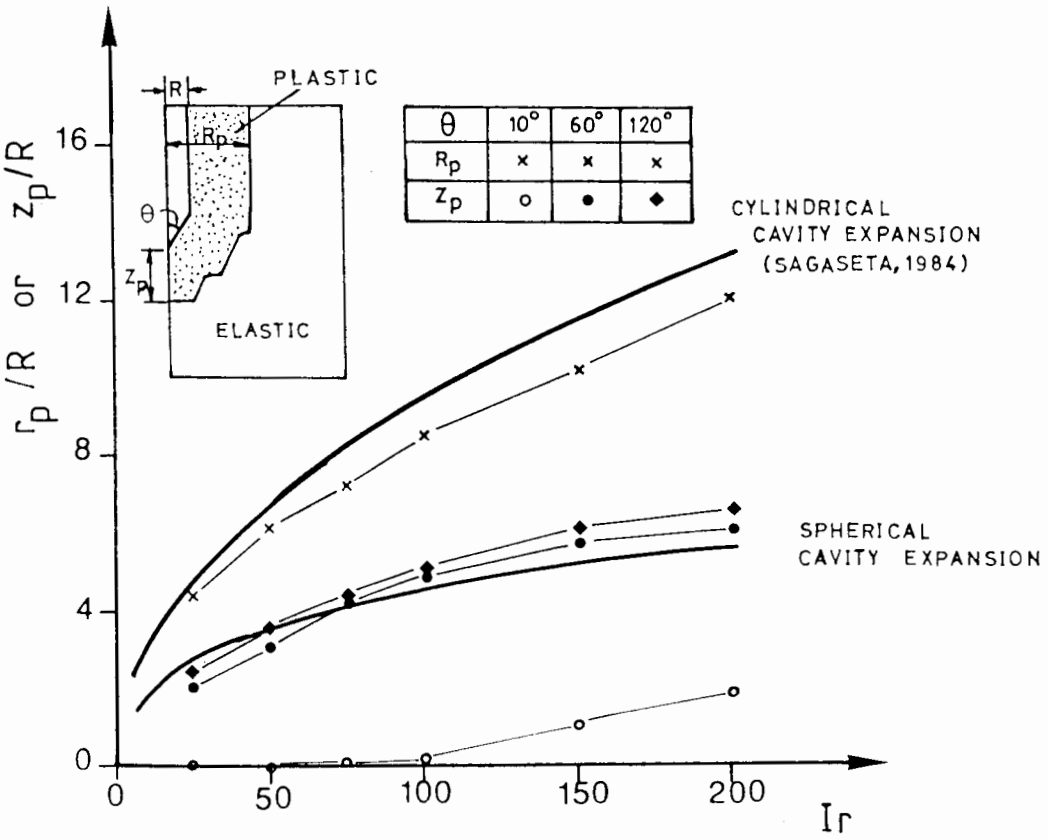

Figure 6.16: Variations of R_p and Z_p with I_r

The values of Z_p due to the penetration of 60° and 120° cones are comparable to the spherical cavity expansion solution. This apparent similarity is mainly due to the datum from which Z_p is being measured. It is obviously convenient to use the cone tip as a reference datum, but it is more difficult to justify that this point corresponds logically to the centre of the spherical cavity from which the theoretical solution is based. Hence, the good agreement between the two solutions for the range of I_r studied is partially fortuitious.

A more interesting trend is observed in the case of a 10° penetrometer. The computed Z_p is found to be very different from the cavity expansion solution. For I_r values less than about 100, the elasto-plastic boundary is coincident with the cone tip. This means that the soil surrounding the cone tip can be divided into an elastic zone and a plastic zone. Similar result has also been obtained analytically by Sagaseta (1984) who studied the problem around the tip of an infinite cone. Sagaseta reported that the soil around the tip can be in one of the two possible stress states. In case I, the entire zone of soil surrounding the tip is in a plastic state. However,

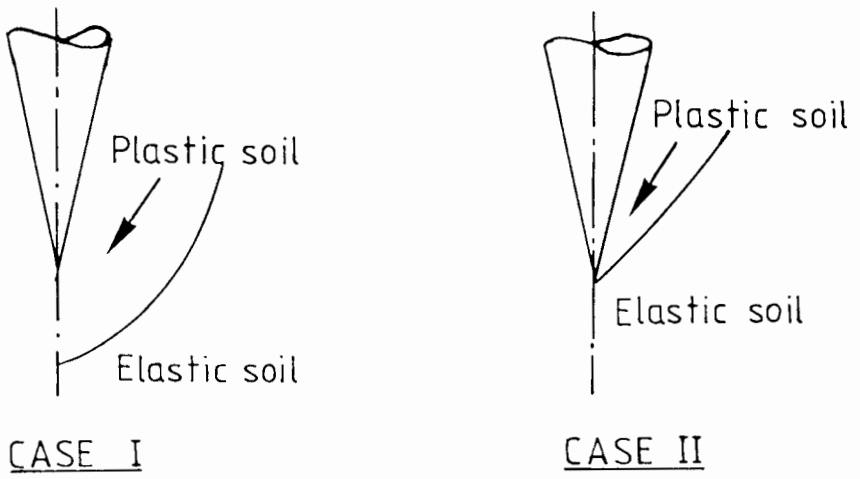

Figure 6.17: Possible Soil States Due to the Penetration of an Infinite Cone

for certain combinations of I_r and cone angle, both plastic and elastic states can exist around the tip and this is classified as case II. These two possible situations are illustrated in Figure 6.17.

For a 10° cone, the analytical result predicts that the transition from case I to case II occurs at an I_r of approximately 200. This is much higher than the numerical result obtained from the strain path approach. The discrepancy in the solutions may be caused by discretization error due to the finite mesh size. It is possible that the agreement between the numerical and the analytical results could be improved by adopting a finer mesh for the strain path analysis. It is nevertheless significant that the trend of the theoretical prediction has been successfully reproduced in a numerical calculation for this is an indication that the solution algorithm has been formulated correctly.

6.6 Tip Resistance

The tip resistance derived from a cone penetration test is defined as the average pressure acting on the cone during steady penetration. This is one of the most important quantities obtained from the CPT and is widely used in empirical correlations to determine the undrained shear strength of cohesive soil.

By definition, the tip resistance can be evaluated from the equation:

$$q_c = \frac{\int \left(P_n \sin(\theta) + P_t \cos(\theta)\right) \, dA}{\int \sin(\theta) \, dA} \qquad (6.1)$$

where: P_n = Component of soil stress normal to cone face

P_t = Component of soil stress tangential to cone face

dA = infinitesimal cone face area

The normal and tangential stress components are evaluated from the soil stresses by a simple Mohr circle construction.

In the strain path method as implemented here, it is not possible to control the roughness on the cone face. However, P_t obtained from the analysis is approximately equal to zero, so the calculated tip resistance is relevant for a smooth cone. In general, the deviatoric stresses in the soil adjacent to a rough cone face are different from those computed here. Nevertheless, the roughness on the cone face is not expected to change the mean pressure in the soil significantly and it is possible to estimate the tip resistance of a rough cone by the following approximate relationship:

$$(q_c)_{rough} = (q_c)_{smooth} + \tau_f \cot(\theta) \qquad (6.2)$$

where τ_f is the mobilised friction on the cone face.

6.6.1 Effect of Rigidity Index on Tip Resistance

A series of analyses have been performed to investigate the effect of the rigidity index of soil on cone resistance. The initial stresses in the soil were assumed to be zero and a standard 60° cone was used in the analysis. The cone resistance is evaluated from the computed stress state using equation (6.1). The results of these analyses are shown in Figure 6.18. The cone resistance, q_c, normalised by the undrained shear strength, c_u, is found to increase with the rigidity index of soil. For comparison, the limit pressures required to expand a spherical cavity and a cylindrical cavity have also been plotted in the same figure. It is observed that q_c

broadly exhibits the same trend of variation as the two cavity expansion limit pressures but the magnitude of q_c is significantly higher. In addition, for a 60° cone, spherical rather than cylindrical cavity expansion provides a closer approximation to the tip resistance.

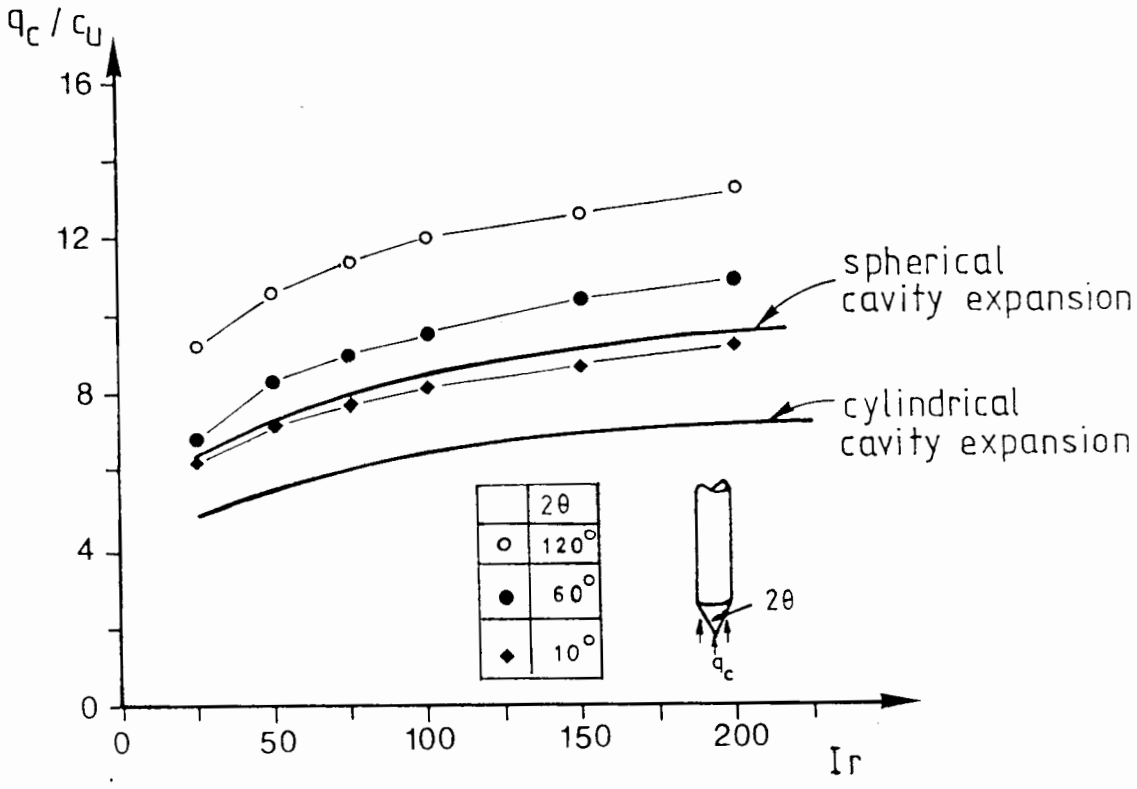

Figure 6.18: Variation of q_c with I_r

The effect of cone angle on tip resistance was investigated by repeating the above analysis for cone angles of 10° and 120°. The trend of variation of q_c with I_r for each of these two cone angles is similar to that for a 60° cone. For a particular value of I_r, the magnitude of q_c is also dependent on the cone angle. The greater the cone angle, the greater is the computed q_c. It is also interesting to note that although the stresses around the 10° cone are similar to the prediction based on cylindrical cavity expansion theory, the value of q_c is considerably higher than the corresponding limit pressure.

Experimental evidence suggests that cavity expansion theories generally under-predict the cone resistance. The value of q_c evaluated by the strain path method is higher than the cavity expansion limit pressure and can, in this sense, be considered to provide a better estimate.

6.7 Effect of Anisotropic Initial Stresses

The results that have been presented so far are based on an initial stress state which is identically zero. For the deviatoric soil model adopted, yielding of soil is independent of the mean pressure. Hence, these results are applicable to the situation where the initial stress state is isotropic, but non-zero. The in-situ stress value will appear as an additive term to the solution derived from zero initial stresses.

In a natural clay deposit, the horizontal stress is generally different from the vertical stress. Anisotropy in the initial stresses could have a significant influence on the stress changes in the soil due to cone penetration and this is investigated in this section. The analyses were performed with a standard penetrometer having an apex angle of 60° and the soil was assumed to have a rigidity index of 100.

Initially, two arbitrary stress conditions were considered. The lateral and vertical in-situ stresses are as follows:

Case A: $\frac{\sigma_{ho}}{c_u} = 2.0$ and $\frac{\sigma_{vo}}{c_u} = 3.5$ (6.3)

and

Case B: $\frac{\sigma_{ho}}{c_u} = 3.5$ and $\frac{\sigma_{vo}}{c_u} = 2.0$ (6.4)

The results obtained from the strain path method are presented as stress contours in Figure 6.19 and 6.20 for cases A and B respectively. The distributions of the radial stresses in the two cases are generally similar. Significant differences, however, are observed in the axial and hoop stress distributions. Despite the higher in-situ vertical stress in Case A, the final value of σ_{zz} around the cone in Case B is considerably higher. This higher axial stress value is duly reflected in the cone resistance, q_c, which has a value of 11.6 c_u for case A and 13.1 c_u for case B.

Conventionally, the correlation between q_c and c_u is expressed by the equation:

$$N_k = \frac{q_c - \sigma_{vo}}{c_u} \tag{6.5}$$

The N_k factors computed for the two initial stress states A and B are found to be 8.1 and 11.1 respectively. The N_k factor for a soil with the same rigidity index but an isotropic initial stress state is about 9.6. These results show that the initial stress condition has a considerable effect on the computed N_k factor.

In order to establish in greater detail the effect of the initial stress conditions on the N_k factor, the analysis has been repeated for other combinations of σ_{ho} and σ_{vo}. For this purpose, the initial stress state was characterised by a dimensionless factor, Δ, which is defined as:

$$\Delta = \frac{\sigma_{vo} - \sigma_{ho}}{2c_u} \tag{6.6}$$

Using this factor, all possible combinations of horizontal and vertical stresses are covered in the range of $-1<\Delta<1$.

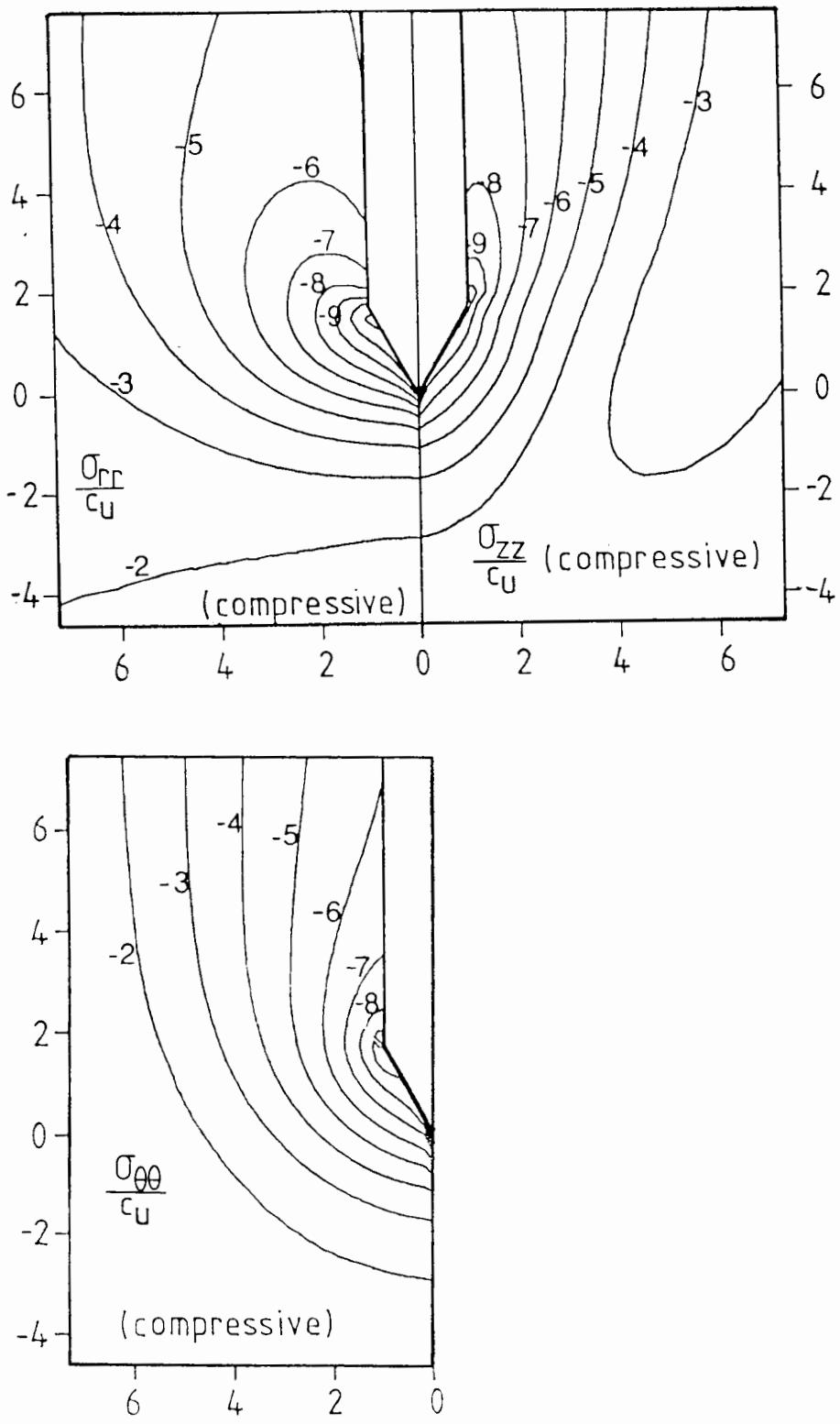

Figure 6.19: Stress Contours due to Cone Penetration

$$\frac{\sigma_{ho}}{c_u} = 2.0, \quad \frac{\sigma_{vo}}{c_u} = 3.5$$

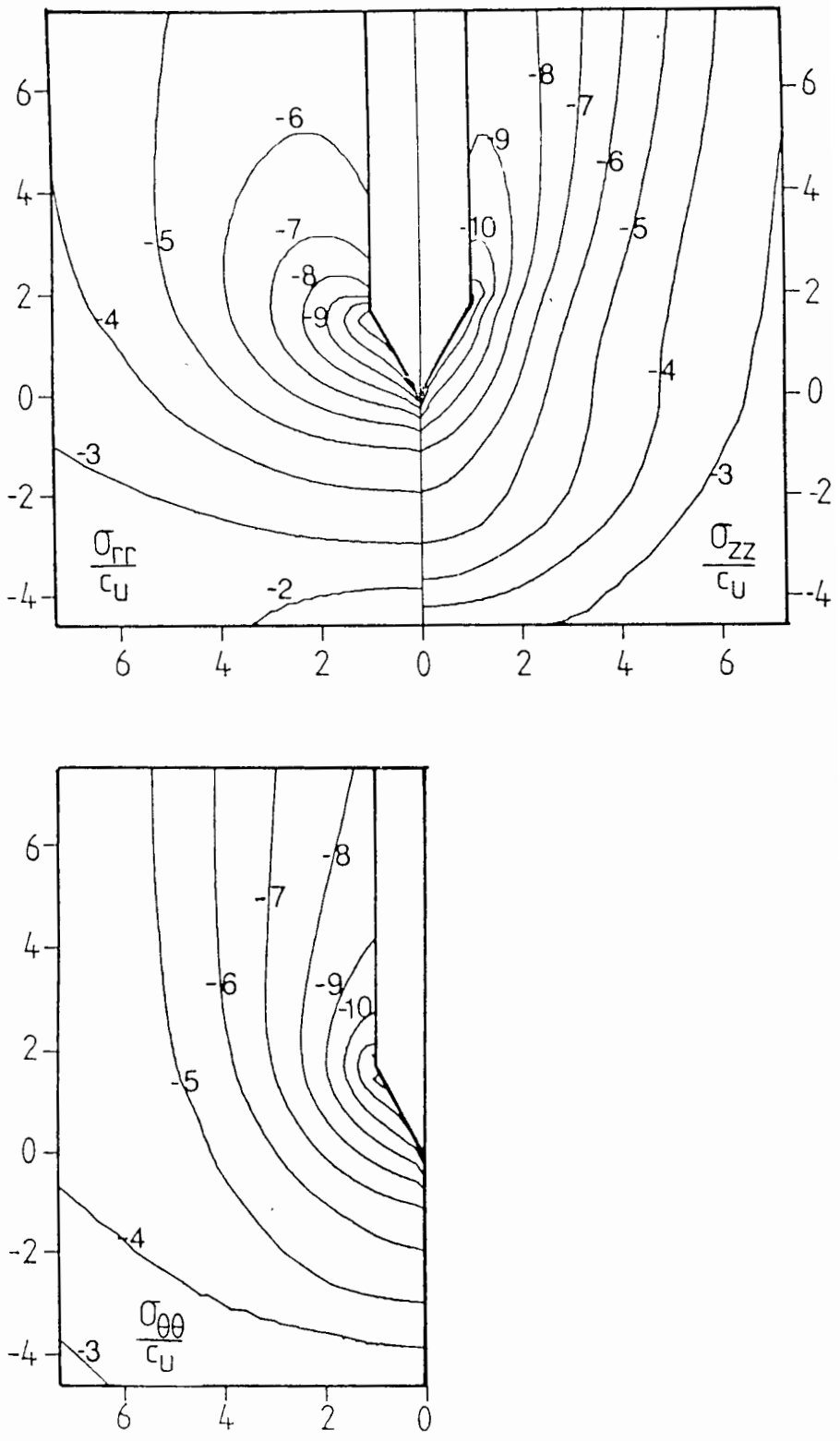

Figure 6.20: Stress Contours due to Cone Penetration

$$\frac{\sigma_{ho}}{c_u} = 3.5, \quad \frac{\sigma_{vo}}{c_u} = 2.0$$

The variation of the computed N_k with the normalised initial stress factor Δ is plotted as shown in Figure 6.21. The variation of N_k with Δ can be approximated very closely by a straight line. The gradient of this line is found to be approximately -2. This result indicates that q_c is almost independent of σ_{vo} and is affected mainly by the changes in σ_{ho}. Futhermore, it suggests that if the cone factor is re-defined in terms of σ_{ho}, then an almost unique value can be obtained.

$$N_h = \frac{q_c - \sigma_{ho}}{c_u} \tag{6.7}$$

This N_h factor can be considered to be more appropriate for correlation with soil properties because it is independent of the initial stress state. Unfortunately, an accurate determination of the in-situ lateral stress in the soil is extremely difficult to achieve. The N_k factor must therefore be retained for correlation purposes. When N_k is used for interpreting CPT data, due consideration should be given to the effect of stress conditions in the ground on the tip resistance.

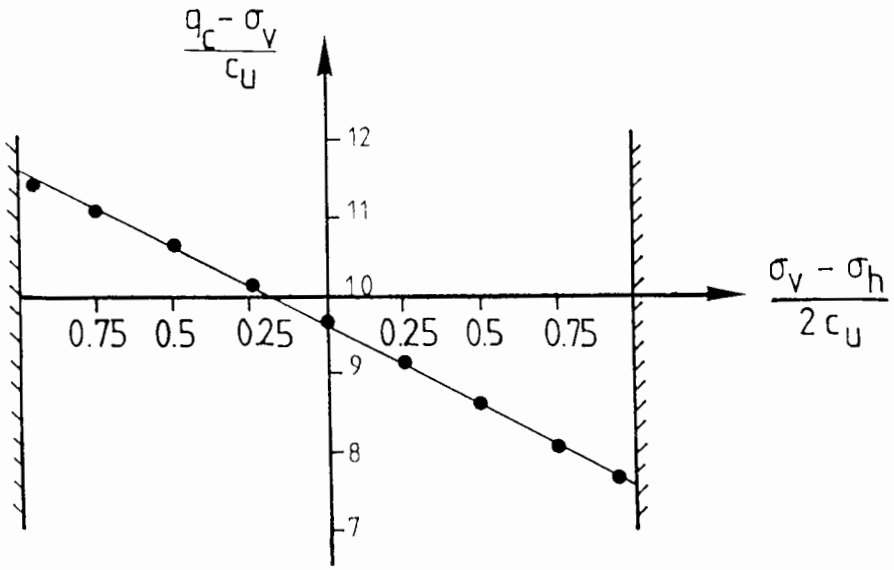

Figure 6.21: Variation of N_k with Δ

6.8 Cone Factor as Evaluated by the Strain Path Method

When the N_k factor evaluated by the strain path method is plotted against the logarithm of I_r, a straight line relationship is obtained. If the effect of the initial stress anisotropy and cone roughness are taken into consideration, the N_k factor for a 60° cone can be expressed approximately as:

$$N_k = 0.4 + 2\ln(I_r) - 2\Delta + 2\alpha \tag{6.8}$$

where α is the roughness coefficient of the cone face and is defined as:

$$\alpha = \frac{\sqrt{3}\tau_f}{2c_u} \tag{6.9}$$

For a perfectly rough cone, $\alpha = 1$ and for a perfectly smooth cone, $\alpha = 0$.

The term 2Δ in equation (6.8) accounts for the effect of the anisotropic initial stresses. The influence of cone roughness is catered for approximately by the term 2α. For extreme combinations of soil condition and cone roughness, the value of N_k may range from 6.2 to 16.8 as illustrated in Table 6.1. This range of values is quite consistent with the N_k factors obtained in both field and laboratory tests.

I_r	Δ	α	N_k
50	1	0	6.2
500	-1	1	16.8

Table 6.1: N_k Values for Two Combinations of I_r, Δ and α

6.9 Summary

The suitability of the strain path method as an approximate solution procedure has been validated by the analysis of a penetrometer with a sharp 10^{o} conical tip. Slender body theory predicted that the stresses around a very slender infinite cone can be approximated by the expansion of a cylindrical cavity. This result has been reproduced quite satisfactorily by the numerical procedure formulated in this thesis.

The cone angle has a significant effect on the deformation mechanism around the penetrometer tip. This is reflected in the shapes of the failure zones around penetrometers with different apex angles. The size of the failure zone is also affected significantly by the rigidity index of soil, and increasing I_r increases the extent of soil around the penetrometer which deformed plastically. The stresses and strains in the far field of the penetrometer are not significantly affected by the cone geometry. In the near field, however, the cone angle has a major effect on the stresses and strains in the soil. Larger cone angles are found to result in greater cone resistance.

The value of q_c computed from the strain path method is dependent on the rigidity index of the soil. The variation of q_c with I_r is broadly similar in trend to that predicted by cavity expansion theory. The magnitude of q_c, however, is higher than the limit pressure for either cylindrical or spherical cavity expansion.

The cone factor is significantly affected by in-situ stress state. This influence is mainly due to the dependence of the cone resistance on the horizontal stress. When the cone factor is expressed in terms of σ_{ho}, an almost unique value which is independent of the stress state can be obtained.

Chapter 7

Formulation of Finite Element Analysis

7.1 Specific Considerations for the Finite Element Formulation

The rate of penetration for a standard CPT in clay is generally considered to be sufficiently fast to give rise to undrained conditions. In such conditions, the clay behaves as an incompressible material and this feature must be included in the finite element formulation.

The rigidity index of natural clay is typically in the range of 30 to 500. For low values of I_r, a displacement controlled finite element analysis may have to be carried out for a large displacement before the limit load condition is reached. These large displacements and therefore large strains features of the problem must be taken into account in the formulation of the finite element equations in order to obtain a correct solution. When large displacements and large soil rotations are involved, the choice of the stress rate definition also merits special consideration.

7.2 Description of Kinematics

For a body subjected to infinitesimal deformation, it is always possible to define strain in a unique way. This is not true when the deformations are large, since a variety of co-ordinate systems may be used which will inevitably result in different strain definitions. In continuum mechanics, the deformation of a body subjected to large displacements is usually described by either a Lagrangian or an Eulerian reference system.

Consider a body subjected to large displacements as illustrated in Figure 7.1. At a given time t_o, the position of a typical material point, P_o, in the deforming body is described by the co-ordinate vector, $\underset{\sim}{a}_i$,

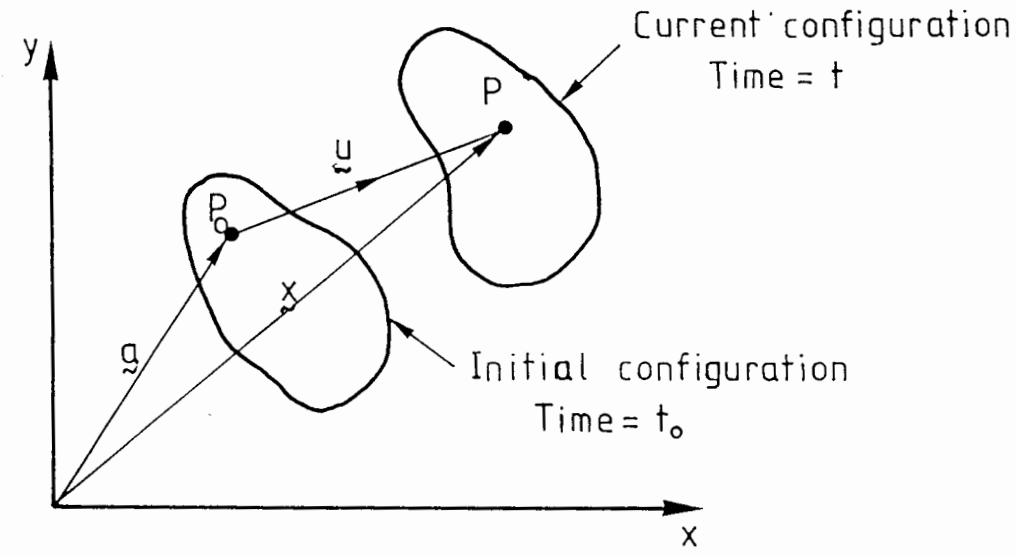

Figure 7.1: Large Displacement Deformations

relative to some fixed reference frame. At time t, the same material point has moved to position P which is described by the global vector, $\underset{\sim}{x}_i$, in the same reference frame.

In the Lagrangian description, the co-ordinate vector $\underset{\sim}{x}_i$ is related to $\underset{\sim}{a}_i$, in an equation of the form:

$$\underset{\sim}{x}_i = x(\underset{\sim}{a}_i, t) \tag{7.1}$$

and the deformations are described in terms of a strain measure:

$$E_{ij} = \frac{1}{2}\left[\frac{\partial x_k}{\partial a_i} \cdot \frac{\partial x_k}{\partial a_j} - \delta_{ij}\right] \tag{7.2}$$

where: δ_{ij} is the Kronecker delta

In the Eulerian description, the velocity of a material point, $\dot{\underset{\sim}{x}}_i$, in the current configuration is considered to be related to the co-ordinates of the material point $\underset{\sim}{x}_i$ and the time t in the form:

$$\dot{\underset{\sim}{x}}_i = \dot{x}(\underset{\sim}{x}_i, t) \tag{7.3}$$

The deformation of the material is described by the rate of deformation tensor defined as:

$$d_{ij} = \frac{\partial \dot{x}_i}{\partial x_j} \tag{7.4}$$

When the deformation is infinitesimally small, these two descriptions yield the same results. When the deformation is finite, the different kinematic descriptions give rise to different strain definitions, so clear distinction must be made between the two systems.

These two kinematical descriptions have both been used in finite element analysis of large strain problems (Hibbitt et al., 1970; Carter et al., 1977; Osias & Swedlow, 1974). The choice of a kinematical description is arbitrary and is influenced to a large extent by the material behaviour that is being modelled. The kinematical equations in an Eulerian description are well suited to the analysis of material for which the constitutive laws are conveniently expressed in terms of stress and strain rates, as is often the case in Soil Mechanics. The Eulerian description has also been widely used in fluid flow analysis where the deformation is described in terms of the velocity field in a fixed reference frame, and was adopted in the flow computation described in Chapter 3. To preserve the consistency in approach, the Eulerian description has been adopted in the formulation of the finite element equations.

7.3 Objective Stress Rate

One of the major considerations in continuum mechanics is the selection of a suitable definition of stress rate for use in the constitutive equations. In a consistent mathematical formulation, the stress rate adopted should satisfy the condition of being objective. This condition requires that the stress rate vanishes under a rigid body motion.

This definition of objectivity is not sufficiently restrictive to provide a unique definition of stress rate (Prager, 1961). As a result, several definitions have been proposed (Jaumann, 1911; Truesdell, 1953 Oldroyd, 1950). Amongst these, the Jaumann definition has been most commonly used in large strain finite element analysis. This popularity is mainly due to the desirable feature that the vanishing of this stress rate implies stationary behaviour of the stress invariants (Prager). The Jaumann definition is adopted in the present study and the stress rate is given by:

$$\overset{\nabla}{\sigma}_{ij} = \dot{\sigma}_{ij} - \dot{\sigma}_{ik}\omega_{jk} - \dot{\sigma}_{jk}\omega_{ik} \qquad (7.5)$$

7.4 Incompressibility

It is well known that the analysis of incompressible materials using the finite element method based on the conventional displacement formulation often gives rise to severe numerical difficulties. Nagtegaal et al. (1974) have shown that this is due to the excessive number of kinematic constraints imposed on the incremental displacement field by the incompressibility condition. Since many of the elasto-plastic constitutive relationships used in Soil Mechanics require that the incompressibility condition is satisfied throughout the material, the effect of incompressibility on the results of computation will have important practical implications.

The detrimental effects of the incompressibility condition can be divided into two main categories. Firstly, in a calculation in which the material stresses are of primary importance, the effect of incompressibility is to produce large oscillations in the stresses across an element (Naylor, 1974). Secondly, in a collapse load calculation where the limit load is sought, the excessive kinematic constraints imposed by the incompressibility conditions often result in an over-stiff response. In such cases, it is not uncommon for the finite element results to over-estimate the limit load, and in extreme cases may even indicate no limit load when one is known to exist (Sloan, 1981).

Several methods have been proposed to overcome the detrimental effect of incompressibility. One of the earliest approach involved the so called 'reduced-integration' technique. This method uses a lower order numerical integration scheme than that required for exact integration to evaluate the stiffness matrix. The use of an 8-noded quadrilateral with a 4-point Gauss rule is a common example (Naylor, 1974). Several modified forms of the 'reduced integration' technique have also been used. Nagtegaal et al. (1974) proposed an approach in which the volumetric strain rates and the velocities are admitted as independent variables and different geometric expansions are used for each of these variables. This method is described as 'selective integration' by Malkus and Hughes (1978).

A particularly comprehensive analysis of the problems associated with limit load calculation involving incompressibility has been given by Nagtegaal et al. (1974). Having identified the effect of incompressibility constraints, they proposed a criterion which must be satisfied if the finite element analysis is to yield a satisfactory solution. This criterion, which is based on a limiting mesh consisting of an infinite number of elements of identical type, requires that the number of degree of freedom in an element

must be greater than the number of constraints imposed by the incompressibility condition. Sloan & Randolph (1982) show that the criterion proposed by Nagtegaal et al. can be satisfied by the use of higher order elements. This hypothesis was verified by Sloan (1981) who performed a series of small strain collapse load calculations using triangular elements.

As an extension to the analysis for the limiting mesh, Sloan & Randolph also analysed the necessary conditions for a mesh consisting of a finite number of elements to be suitable for collapse load calculations. This analysis has shown that the suitability of any finite element mesh is governed by a factor, k. This factor is defined as the ratio of the number of degrees of freedom to constraints per element derived from a mesh with an infinite number of elements. When k is greater than unity, most meshes generated will be suitable for limit load calculations. The reverse is true when k is less than unity. When k is equal to unity, it has been demonstrated that at least half of the boundary degrees of freedom must be left unrestrained in order to satisfy the criterion.

The philosophy of the last approach has been adopted in the finite element calculation described in this thesis. The formulation is based on the 15-node cubic strain triangle which is the lowest order element for which the necessary criterion given by Sloan & Randolph holds.

7.5 Formulation of Finite Element Equations

In an Eulerian description, the instantaneous rate of deformation may be described by the velocity gradients as:

$$\dot{\varepsilon}_{rr} = \frac{\partial v_r}{\partial r} \tag{7.6}$$

$$\dot{\varepsilon}_{zz} = \frac{\partial v_z}{\partial z} \tag{7.7}$$

$$\dot{\varepsilon}_{\theta\theta} = \frac{v_r}{r} \tag{7.8}$$

$$\dot{\gamma}_{rz} = \frac{\partial v_r}{\partial z} + \frac{\partial v_z}{\partial r} \tag{7.9}$$

$$\omega = \frac{1}{2}\left[\frac{\partial v_r}{\partial z} - \frac{\partial v_z}{\partial r}\right] \tag{7.10}$$

where v_r and v_z are the velocity components in the r and z directions respectively. The corresponding Jaumann stress rates are:

$$\overset{\nabla}{\sigma}_{rr} = \dot{\sigma}_{rr} - 2\omega\tau_{rz} \tag{7.11}$$

$$\overset{\nabla}{\sigma}_{zz} = \dot{\sigma}_{zz} + 2\omega\tau_{rz} \tag{7.12}$$

$$\overset{\nabla}{\sigma}_{\theta\theta} = \dot{\sigma}_{\theta\theta} \tag{7.13}$$

$$\overset{\nabla}{\tau}_{rz} = \dot{\tau}_{rz} + \omega(\sigma_{rr} - \sigma_{zz}) \tag{7.14}$$

The superior dot denotes the time derivative with respect to the fixed Cartesian axes.

7.5.1 Element Stiffness Matrix

The formulation of the element stiffness matrix is based on the iso-parametric concept (Zienkiewicz, 1979). The conventional small displacement formulation is modified to include the effects of rotation and geometrical distortion. In the derivation of the finite element equations, the nodal global co-ordinates of a point in the element is (x,y), and this corresponds to the co-ordinates (α,β) in the fixed reference frame.

The global co-ordinates of a typical point in an element, $\underset{\sim}{x}$, are related to the vector of nodal global co-ordinates, $\underset{\sim}{X}$, by

$$\underset{\sim}{x} = [N]\ \underset{\sim}{X} \tag{7.15}$$

where, [N], the matrix of shape functions, is a function of the local co-ordinates (α,β). Using the iso-parametric concept, the velocity, $\dot{\underset{\sim}{x}}$, of a typical point is related to the nodal velocity, $\dot{\underset{\sim}{X}}$, by a similar equation,

$$\dot{\underset{\sim}{x}} = [N]\ \dot{\underset{\sim}{X}} \tag{7.16}$$

The strain rate vector is defined as:

$$\dot{\underset{\sim}{\varepsilon}} = \begin{pmatrix} \dot{\varepsilon}_{rr} \\ \dot{\varepsilon}_{zz} \\ \dot{\varepsilon}_{\theta\theta} \\ \dot{\gamma}_{rz} \\ \omega \end{pmatrix} \tag{7.17}$$

$$= [L]\ [N]\ \dot{\underset{\sim}{X}} \tag{7.18}$$

$$= [B]\ \dot{\underset{\sim}{X}} \tag{7.19}$$

where [L] is the operator matrix:

$$[L] = \begin{bmatrix} \frac{\partial}{\partial r} & 0 \\ 0 & \frac{\partial}{\partial z} \\ \frac{1}{r} & 0 \\ \frac{\partial}{\partial z} & \frac{\partial}{\partial r} \\ \frac{\partial}{\partial z} & -\frac{\partial}{\partial r} \end{bmatrix} \tag{7.20}$$

This strain rate vector also includes the rotation rate and this has been found to be a convenient way of dealing with the Jaumann terms in the stress rate definition (Carter et al., 1977; Burd, 1986).

The stress rate vector, $\dot{\underset{\sim}{\sigma}}$, which is energetically conjugate to $\dot{\underset{\sim}{\varepsilon}}$,is

$$\dot{\underset{\sim}{\sigma}} = \begin{bmatrix} \dot{\sigma}_{rr} \\ \dot{\sigma}_{zz} \\ \dot{\sigma}_{\theta\theta} \\ \dot{\tau}_{rz} \\ 0 \end{bmatrix} \tag{7.21}$$

The total strain rate can be decomposed into two parts,

$$\dot{\underset{\sim}{\varepsilon}} = \dot{\underset{\sim}{\varepsilon}}^{e} + \dot{\underset{\sim}{\varepsilon}}^{p} \tag{7.22}$$

where $\dot{\underset{\sim}{\varepsilon}}^{e}$ is the elastic component, and $\dot{\underset{\sim}{\varepsilon}}^{p}$, the plastic component. The elastic strain rate is related to the Jaumann stress rate, $\overset{\nabla}{\underset{\sim}{\sigma}}$, through Hooke's Law:

$$\overset{\nabla}{\underset{\sim}{\sigma}} = [D]^{e} \dot{\underset{\sim}{\varepsilon}}^{e} \tag{7.23}$$

where $[D]^{e}$ is a matrix of elastic constants. In axisymmetry, $[D]^{e}$ for an isotropic material is given by:

$$[D]^{e} = \begin{bmatrix} K + \frac{4G}{3} & K - \frac{2G}{3} & K - \frac{2G}{3} & 0 & 0 \\ K - \frac{2G}{3} & K + \frac{4G}{3} & K - \frac{2G}{3} & 0 & 0 \\ K - \frac{2G}{3} & K - \frac{2G}{3} & K + \frac{4G}{3} & 0 & 0 \\ 0 & 0 & 0 & G & 0 \\ 0 & 0 & 0 & 0 & 0 \end{bmatrix} \tag{7.24}$$

where K and G are the elastic moduli of the material.

The plastic strain rates are derived from the plastic potential $g(\underset{\sim}{\sigma})$ based on the normality condition,

$$\dot{\underset{\sim}{\varepsilon}}^{p} = \lambda \underset{\sim}{b} \tag{7.25}$$

where:
$$\underset{\sim}{b} = \frac{\partial g}{\partial \underset{\sim}{\sigma}} \tag{7.26}$$

and λ is a scalar multiplier which must be positive in order to satisfy the requirement that plastic work done is always positive.

If the yield function is given by $f(\underset{\sim}{\sigma}) = 0$, then on plastic yielding, the stress state will stay on the yield surface, thus:

$$\underset{\sim}{a}^{T} \overset{\nabla}{\underset{\sim}{\sigma}} = 0 \tag{7.27}$$

where:
$$\underset{\sim}{a} = \frac{\partial f}{\partial \underset{\sim}{\sigma}} \tag{7.28}$$

Substituting equations (7.22), (7.23) and (7.25) into the above expression gives:

$$\lambda = \frac{\underset{\sim}{a}^{T} [D]^{e} \dot{\underset{\sim}{\varepsilon}}}{\underset{\sim}{a}^{T} [D]^{e} \underset{\sim}{b}} \tag{7.29}$$

This expression can be substituted in equation (7.22) to obtain a relationship between the Jaumann stress rate and the total strain rate:

$$\overset{\nabla}{\underset{\sim}{\sigma}} = [D]^{ep} \dot{\underset{\sim}{\varepsilon}} \tag{7.30}$$

where: $$[D]^{ep} = \left[[D]^{e} + [D]^{p}\right] \tag{7.31}$$

and $$[D]^{p} = - \frac{[D]^{e} \underset{\sim}{b} \underset{\sim}{a}^{T} [D]^{e}}{\underset{\sim}{a}^{T} [D]^{e} \underset{\sim}{b}} \tag{7.32}$$

The matrix $[D]^{p}$ is applicable whenever the stress state of a material point is plastic. If the stress state lies inside the yield surface, $[D]^{p}$ is set to zero.

The Jaumann stress rate equation can be expressed as:

$$\overset{\nabla}{\underset{\sim}{\sigma}} = \dot{\underset{\sim}{\sigma}} - [R] \dot{\underset{\sim}{\varepsilon}} \tag{7.33}$$

where: $$[R] = \begin{bmatrix} 0 & 0 & 0 & 0 & \tau_{rz} \\ 0 & 0 & 0 & 0 & -\tau_{rz} \\ 0 & 0 & 0 & 0 & 0 \\ 0 & 0 & 0 & 0 & \frac{\sigma_{zz} - \sigma_{rr}}{2} \\ 0 & 0 & 0 & 0 & 0 \end{bmatrix} \tag{7.34}$$

Combining equations (7.30) and (7.33), we obtain an equation which relates the Cauchy stress rate to the total strain rate:

$$\dot{\underset{\sim}{\sigma}} = \left[[D]^{ep} + [R]\right] \dot{\underset{\sim}{\varepsilon}} \tag{7.35}$$

By the virtual work principle, a set of equivalent nodal forces, $\underset{\sim}{P}$, which is consistent with the internal stresses in an element is given by:

$$\underset{\sim}{P} = \int [B]^{T} \underset{\sim}{\sigma} \, dV \tag{7.36}$$

Equation (7.36) can be transformed using the reference co-ordinates (α,β) into:

$$\underset{\sim}{P} = \iint [B]^T \underset{\sim}{\sigma}\, 2\pi r \det[J]\, d\alpha\, d\beta \tag{7.37}$$

where [J] is the Jacobian of transformation from global to local co-ordinates. This equation may be differentiated with respect to time, as described by Burd (1986), to give a rate equation:

$$\dot{\underset{\sim}{P}} = \iint [B]^T \dot{\underset{\sim}{\sigma}}\, 2\pi r \det[J]\, d\alpha\, d\beta + \iint \dot{\left([B]^T 2\pi r \det[J]\right)}\, \underset{\sim}{\sigma}\, d\alpha\, d\beta \tag{7.38}$$

$$\dot{\underset{\sim}{P}} = \iint 2\pi r [B]^T \left([D]^{ep} + [R]\right)[B]\, \dot{\underset{\sim}{X}} \det[J]\, d\alpha\, d\beta + \iint [C]\, \dot{\underset{\sim}{X}}\, d\alpha\, d\beta \tag{7.39}$$

The matrix [C], called the distortion rate maxtrix, is evaluated by expanding the second integrand in equation (7.38) and re-grouping the relevant terms. The elements of the matrix [C] for a 15-node cubic strain triangle are given in Appendix 7A.

7.6 Constitutive Relationship

The soil is assumed to behave as an elastic-perfectly plastic bi-linear material with constant moduli. In the plastic regime, the material behaviour is governed by the von Mises yield criterion as described in Chapter 4. An associated flow rule was adopted for describing the plastic deformation, so

$$g(\underset{\sim}{\sigma}) = f(\underset{\sim}{\sigma}) \tag{7.40}$$

For such a constitutive model, the plastic material matrix $[D]^p$ is given by:

$$[D]^p = -\frac{3G}{4c_u^2}\begin{bmatrix} (s_r)^2 & s_r s_z & s_r s_\theta & s_r \tau_{rz} & 0 \\ s_z s_r & (s_z)^2 & s_z s_\theta & s_z \tau_{rz} & 0 \\ s_\theta s_r & s_\theta s_z & (s_\theta)^2 & s_\theta \tau_{rz} & 0 \\ \tau_{rz} s_r & \tau_{rz} s_z & \tau_{rz} s_\theta & (\tau_{rz})^2 & 0 \\ 0 & 0 & 0 & 0 & 0 \end{bmatrix} \qquad (7.41)$$

where s_r, s_θ and s_z are the deviatoric stresses.

7.7 Strain Rate Calculations

The basic finite element equations are solved by an incremental approach using small load steps. At each calculation step, the Gauss point stresses are evaluated by integrating equation (7.35) and this requires the determination of the strain rate at each Gauss point.

Since the incremental approach adopted consists of evaluating the primary variables at discrete intervals, information regarding how these variables change during the interval is not available. In order to compute the strain rates, it is necessary to make some assumptions concerning the variation of the velocities or the strain rates during the load increment. Houlsby (as described by Burd, 1986) assumes that the strain rates are constant and derives a set of closed form solutions for the strain rates in a plane strain formulation. Carter et al. (1977) adopted an averaging procedure for all time dependent variables in an axisymmetric analysis and the mean values of these quantities during a load step are used in the calculation. In this thesis, the strain rate calculation as described by Carter et al. is adopted.

7.8 Stress Update Calculations

At each increment, the Gauss point stresses are updated using the appropriate constitutive law. At the beginning of each calculation step, the stresses at each Gauss point can either be in an elastic state or a plastic state. In the present formulation, all stress increments are first assumed to be purely elastic regardless of the initial stress states. If the updated stress state violates the yield criterion, then the calculation is repeated using the appropriate constitutive equations. This has been found to be successful for dealing with the possibility of elastic unloading (Davies et al., 1974).

7.8.1 Elastic Behaviour Including Jaumann Terms

The deviatoric Jaumann stress rates can be written as:

$$\overset{\nabla}{s}_r = \dot{s}_r - 2\omega\tau_{rz} \tag{7.42}$$

$$\overset{\nabla}{s}_z = \dot{s}_z + 2\omega\tau_{rz} \tag{7.43}$$

$$\overset{\nabla}{\tau}_{rz} = \dot{\tau}_{rz} + \omega(\dot{s}_r \quad \dot{s}_z) \tag{7.44}$$

For a purely elastic behaviour, the mean pressure at the end of the load increment is:

$$p = p_o + K\Delta v \tag{7.45}$$

where Δv is the volumetric strain increment and p_o is the mean pressure at the start of the load increment. The deviatoric Jaumann stress rates are related to the deviatoric strain rates by the following relationships:

$$\overset{\nabla}{s}_r = 2G\dot{e}_r \tag{7.46}$$

$$\overset{\nabla}{s}_z = 2G\dot{e}_z \tag{7.47}$$

$$\overset{\nabla}{\tau}_{rz} = G\dot{\gamma}_{rz} \tag{7.48}$$

where $\dot{e}_r$ and $\dot{e}_z$ are the deviatoric strain rates as defined in Chapter 4. Substituting the above expressions into the deviatoric Jaumann stress rate equations results in three differential equations which relate the deviatoric stresses to the deviatoric strain rates. From these equations, the updated elastic stresses can be evaluated as (Houlsby, 1986):

$$s_a = 2G\dot{e}_a t + s_{ao} \tag{7.49}$$

$$s_b = s_{bo}\cos(2\omega t) + 2G\dot{e}_b\left(\frac{\sin(2\omega\tau t)}{2\omega}\right) + 2\tau_o\sin(2\omega t) + 2G\dot{\gamma}_{rz}t\left(\frac{1 - \cos(2\omega t)}{2\omega}\right) \tag{7.50}$$

$$\tau_{rz} = \tau_o\cos(2\omega t) + G\dot{\gamma}_{rz}\left(\frac{\sin(2\omega t)}{2\omega}\right) - \frac{1}{2}s_{bo}\sin(2\omega t) - G\dot{e}_b\left(\frac{1 - \cos(2\omega t)}{2\omega}\right) \tag{7.51}$$

where:

$$s_a = s_r + s_z \qquad s_b = s_r - s_z \tag{7.52}$$

$$\dot{e}_a = \dot{e}_r + \dot{e}_z \qquad \dot{e}_b = \dot{e}_r \quad \dot{e}_z \tag{7.53}$$

and s_{ao}, s_{bo} and τ_o are the values at the start of the calculation step. Evaluation of equations (7.50) and (7.51) with small ω values could lead to significant errors. To overcome this problem, the equations are expressed in a Taylor's series expansion retaining only the first order rotation terms when ω is small:

$$s_b = s_{bo} + 2G\dot{e}_b t + 4\tau_o\omega t + 2G\dot{\gamma}_{rz}\omega t^2 \tag{7.54}$$

$$\tau_{rz} = \tau_o + G\dot{\gamma}_{rz}t - s_{bo}\omega t - G\dot{e}_b\omega t^2 \tag{7.55}$$

7.8.2 von Mises Plasticity Including Jaumann Terms

If the rotation rate, ω, is very small, it can usually be dropped from the stress rate equations without any significant effect. The analytical solutions relating stress increments to small strain increments derived in Chapter 4 would then be applicable for the stress update calculation in the plastic range.

In general, however, the rotation effect must be taken into account in order to provide a consistent description of material behaviour. When the rotation rates are included in the stress rate equations, it is necessary to solve for the plastic stresses numerically. In this thesis, a Runge-Kutta scheme described by Sloan (1984) has been adopted for stress update calculations when the stresses at the Gauss point become plastic. By adopting such a scheme, it is possible to control the accuracy of the stress solution by varying the number of sub-increments in each load step.

7.8.3 Calculation of Yield Surface Intersection

For the case when the material becomes plastic during the load step, it is necessary to determine the fraction of the increment which is elastic. This can be found by combining the equations for the elastic stresses with the von Mises yield function. The time at which intersection with the yield surface occurs is then given by:

$$A_1 t^2 + A_2 t + A_3 \frac{(1 - \cos(2\omega t))}{\omega^2} + A_4 \frac{\sin(2\omega t)}{\omega} + A_5 = 0 \qquad (7.56)$$

where:
$$A_1 = 12G^2 \dot{e}_a^2 \qquad (7.57)$$

$$A_2 = 12G s_{ao} \dot{e}_a \qquad (7.58)$$

$$A_3 = 2\omega G(2\tau_o \dot{e}_b - s_{bo}\dot{\gamma}_{rz}) + 2G^2(\dot{\gamma}_{rz} + \dot{e}_b^2) \tag{7.59}$$

$$A_4 = 2G(2\tau_o \dot{\gamma}_{rz} + s_{bo}\dot{e}_b) \tag{7.60}$$

$$A_5 = 4(s_{ro}^2 + s_{ro}s_{zo} + s_{zo}^2 + \tau_o^2 - \frac{4}{3}c_u^2) \tag{7.61}$$

Equation (7.56) can be solved by the Newton-Raphson iterative scheme with the initial estimate of t given by:

$$t_o = \frac{F_b}{F_b - F_a} \tag{7.62}$$

where: F_a = yield function at the start of the calculation step.

F_b = yield function at the end of the load step assuming a purely elastic response.

7.8.4 Yield Surface Correction

When the plastic stresses are evaluated numerically, there is a possibility that the final stress state may lie outside the yield surface. The error associated with such a violation of the yield criterion is cumulative and the offending stress state must be corrected back to the yield surface.

There is no unique way by which yield surface correction should be performed and the choice of a correction algorithm is largely arbitrary. In this thesis, yield surface corrections are carried out by keeping the direction of the principal stresses fixed (Carter et al., 1977), and the stresses are corrected along a path normal to the yield surface (Figure 7.2). The corrected stresses, σ_i^c, are given by:

$$\sigma_i^c = \frac{\sigma_i + (\Omega - 1)p}{\Omega} ; \qquad i=1, 2, 3 \tag{7.63}$$

where: $$\Omega = \frac{(\sigma_1-\sigma_3)^2 + (\sigma_3-\sigma_1)^2 + (\sigma_1-\sigma_2)^2}{8c_u^2} \qquad (7.64)$$

σ_i = uncorrected principal stresses.

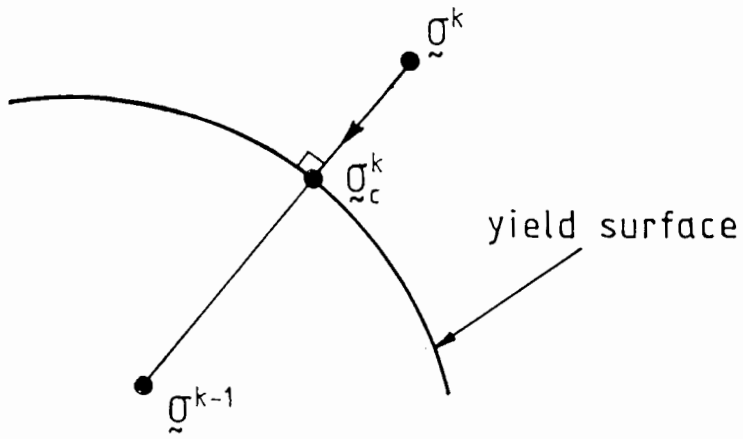

Figure 7.2: Yield Surface Correction

7.9 Solution Scheme

In a finite element analysis where material or geometric non-linearities are present, it is important that an appropriate algorithm is chosen for solving the resulting non-linear equations. This is usually achieved by an incremental procedure. Within each increment, it is important to ensure that the equilibrium equations are approximately satisfied. Many different approaches have been proposed and these can be divided into two main categories.

The first category uses an approach generally called the Euler scheme. In the simplest algorithm, the exact solution is approximated by a series of straight lines. Each of these straight line segments has a gradient equal to that of the exact curve at the start of a load increment. More refined variants of this approach have also been used sucessfully. Carter et al.

(1977) modified the basic scheme by using the slope of the exact curve at the mid-point of the increment. Another variation employs the stiffness at the start of the load increment but provides a correction procedure for the out-of-balance nodal forces at the next increment (Hofmeister et al., 1971; Sloan, 1981).

The second category is based on the Newton-Raphson iterative principle. In these schemes, the exact solution which corresponds to a load increment is approximated by a series of iterations (Figure 7.3). Different methods have been used to evaluate the stiffness matrix in each iteration. In a 'true' Newton-Raphson scheme, the stiffness matrix which corresponds to the updated stress state is evaluated at each iteration. This can lead to excessive computing time because of the need to evaluate and invert the stiffness matrix for each iteration. Nayak & Zienkiewicz (1972) described an

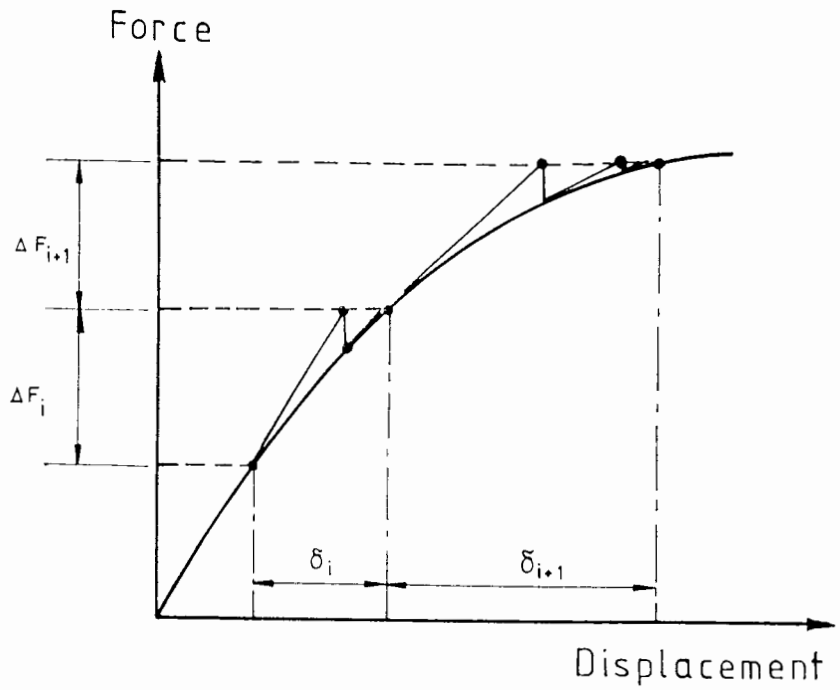

Figure 7.3: Newton-Rahpson's Solution Scheme

alternative procedure called the 'initial stress' method in which the stiffness matrix calculated at the start of the increment is used for all the iterations within an increment.

In this thesis, the modified Euler scheme described by Sloan (1981) is adopted. This algorithm has been shown to be efficient and numerically stable in a series of collapse load calculations by Sloan. A high degree of accuracy can be obtained provided that small increments are used. The application of this method is illustrated in Figure 7.4 for a problem with a single degree-of-freedom.

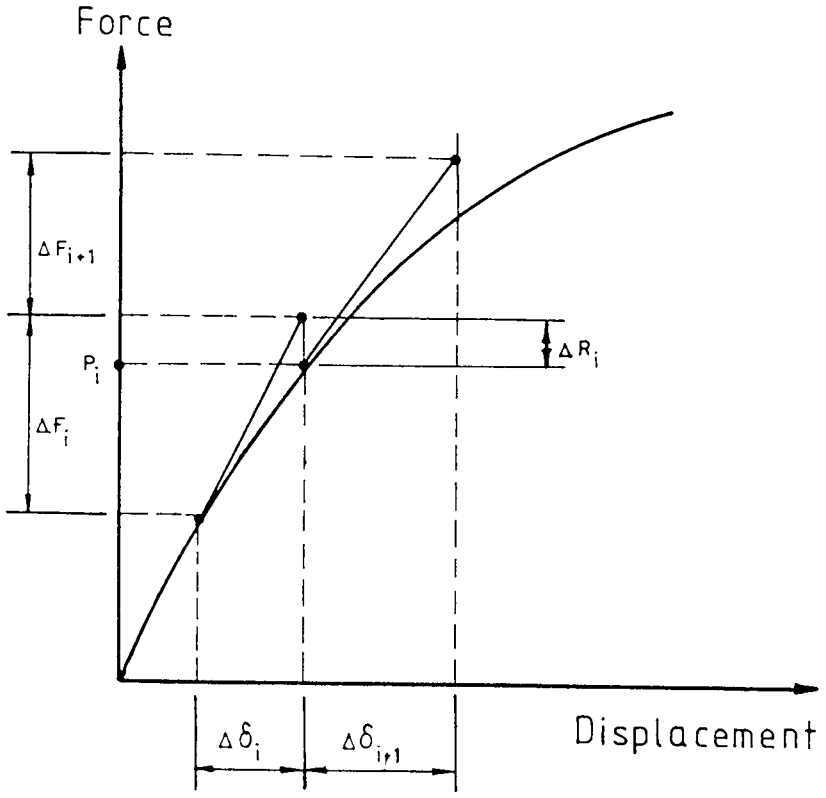

Figure 7.4: Modified Euler Scheme

The general finite element equation can be written as:

$$\underset{\sim}{F} = [K] \underset{\sim}{\delta} \tag{7.65}$$

where $\underset{\sim}{F}$ is the imposed nodal load. At the start of the k^{th} iteration, equation (7.65) is solved using the stiffness matrix based on the initial stresses to give a set of nodal displacement $\underset{\sim}{\delta}$. The Gauss point stresses within the element are updated using the method as described in section 7.3. The nodal forces which are consistent with the internal Gauss point stresses and the updated geometry are calculated using the virtual work equation:

$$\underset{\sim}{P} = \int [B]^T \underset{\sim}{\sigma} \, dV \tag{7.66}$$

The nodal force vector, $\underset{\sim}{P}$, evaluated from equation (7.66) is generally different from the applied nodal load, $\underset{\sim}{F}$. The difference between these two quantities is the out-of-balance nodal forces, ΔR. During the subsequent calculation step, ΔR is added to the load increment to obtain a better approximation to the exact non-linear response.

7.10 Calculation of Consistent Nodal Forces

In a finite element analysis, load application is effected through concentrated loads acting at the nodes. When body forces and surface tractions are involved, these must be transformed into an equivalent nodal load vector.

7.10.1 Body Forces

Consider an element which is subjected to a body force vector, $\underset{\sim}{F}_b$. Under an arbitrary displacement, denoted by a nodal displacement vector $\underset{\sim}{\delta}$, the work done by the body forces is given by:

$$W = \int \underset{\sim}{\delta} \, [N]^T \, \underset{\sim}{F}_b \, dV \tag{7.67}$$

By the virtual work principle, the equivalent nodal force vector, $\underset{\sim}{P}_b$, is given by the equation:

$$\underset{\sim}{P}_b = \iint [N]^T F_b \, 2\pi r \, \det[J] \, d\alpha \, d\beta \tag{7.68}$$

7.10.2 Distributed Boundary Tractions

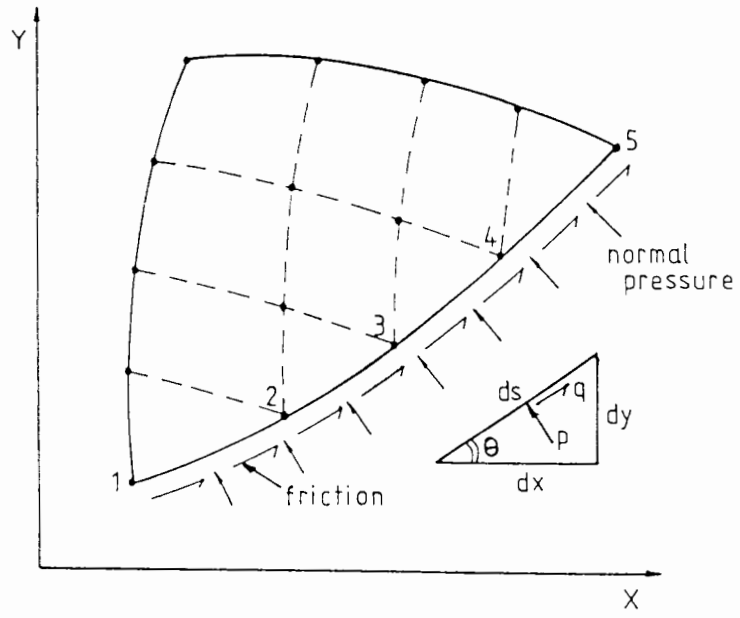

Figure 7.5: Distributed Boundary Tractions

Figure 7.5 shows a distributed force, $\underset{\sim}{T}$, acting on one of the edges of an element. For an infinitesimal section along the loaded boundary, dS, inclined at an angle θ to the positive r axis, the surface traction can be resolved into two concentrated forces , f_r and f_z, in the direction of the co-ordinate axes:

$$f_r = q \, dS \cos(\theta) - p \, dS \sin(\theta) \tag{7.69}$$

$$f_z = q \, dS \sin(\theta) + p \, dS \cos(\theta) \tag{7.70}$$

where p and q are the normal and tangential components of **T** acting on dS. By the virtual work principle, the equivalent nodal load vector, $\underset{\sim}{P}_t$, can be shown to be:

$$\underset{\sim}{P}_t = \int [N]^T \underset{\sim}{Q} \, d\xi \tag{7.71}$$

where:

$$\underset{\sim}{Q} = \begin{bmatrix} q \dfrac{\partial r}{\partial \xi} - p \dfrac{\partial z}{\partial \xi} \\ \\ q \dfrac{\partial z}{\partial \xi} + p \dfrac{\partial r}{\partial \xi} \end{bmatrix} \tag{7.72}$$

Appendix 7A: Finite Element Equations for a 15-node Triangular Element

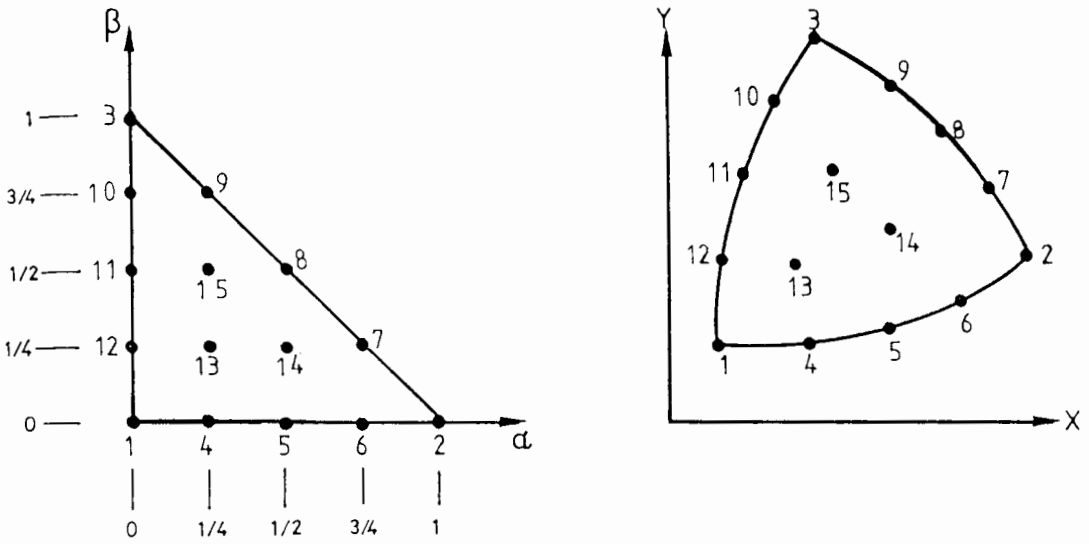

Figure 7A.1: Element Transformation

Consider the iso-parametric mapping for a 15-node triangular element (Figure 7A.1). The vectors of global co-ordinates and displacement of a point within the element are given by:

$$\underset{\sim}{x} = \begin{bmatrix} r \\ z \end{bmatrix} \qquad \underset{\sim}{u} = \begin{bmatrix} u \\ v \end{bmatrix} \tag{7A.1}$$

The vectors of nodal global co-ordinates and nodal displacements are:

$$\underset{\sim}{X} = \begin{bmatrix} r_1 \\ z_1 \\ r_2 \\ z_2 \\ \cdot \\ \cdot \\ \cdot \\ \cdot \\ r_{15} \\ z_{15} \end{bmatrix} \qquad \underset{\sim}{\delta} = \begin{bmatrix} u_1 \\ v_1 \\ u_2 \\ v_2 \\ \cdot \\ \cdot \\ \cdot \\ \cdot \\ u_{15} \\ v_{15} \end{bmatrix} \tag{7A.2}$$

where the subscript refers to the element node number. Using the iso-parametric concept, the global co-ordinates and displacement of a point within the element are related to the nodal values by the equation:

$$\underset{\sim}{x} = [N]\underset{\sim}{X} \qquad \text{and} \qquad \underset{\sim}{u} = [N]\underset{\sim}{\delta} \tag{7A.3}$$

The shape function matrix [N] is of the form:

$$[N] = \begin{bmatrix} N_1 & 0 & N_2 & 0 & N_3 & 0 & \cdots & 0 & N_{15} & 0 \\ 0 & N_1 & 0 & N_2 & 0 & N_3 & \cdots & N_{14} & 0 & N_{15} \end{bmatrix} \tag{7A.4}$$

where: $N_1 = \frac{32}{3}\,\gamma(\gamma - \frac{1}{4})(\gamma - \frac{1}{2})(\gamma - \frac{3}{4})$

$N_2 = \frac{32}{3}\,\alpha(\alpha - \frac{1}{4})(\alpha - \frac{1}{2})(\alpha - \frac{3}{4})$

$N_3 = \frac{32}{3}\,\beta(\beta - \frac{1}{4})(\beta - \frac{1}{2})(\beta - \frac{3}{4})$

$N_4 = \frac{128}{3}\,(\alpha)(\gamma)(\gamma - \frac{1}{4})(\gamma - \frac{1}{2})$

$N_5 = 64\,(\alpha)(\gamma)(\alpha - \frac{1}{4})(\gamma - \frac{1}{4})$

$N_6 = \frac{128}{3}\,(\alpha)(\gamma)(\alpha - \frac{1}{4})(\alpha - \frac{1}{2})$

$N_7 = \frac{128}{3}\,(\alpha)(\beta)(\alpha - \frac{1}{4})(\alpha - \frac{1}{2})$

$N_8 = 64\,(\alpha)(\beta)(\alpha - \frac{1}{4})(\beta - \frac{1}{4})$

$N_9 = \frac{128}{3}\,(\alpha)(\beta)(\beta - \frac{1}{4})(\beta - \frac{1}{2})$

$N_{10} = \frac{128}{3}\,(\beta)(\gamma)(\beta - \frac{1}{4})(\beta - \frac{1}{2})$

$N_{11} = 64\,(\beta)(\gamma)(\beta - \frac{1}{4})(\gamma - \frac{1}{4})$

$$N_{12} = \frac{128}{3}(\beta)(\gamma)(\gamma - \frac{1}{4})(\gamma - \frac{1}{2})$$

$$N_{13} = 128\ (\alpha)(\beta)(\gamma)(\gamma - \frac{1}{4})$$

$$N_{14} = 128\ (\alpha)(\beta)(\gamma)(\alpha - \frac{1}{4})$$

$$N_{15} = 128\ (\alpha)(\beta)(\gamma)(\beta - \frac{1}{4})$$

The [B] matrix is of the form:

$$[B] = \begin{bmatrix} \frac{\partial N_1}{\partial r} & 0 & \frac{\partial N_2}{\partial r} & \cdots & \frac{\partial N_{15}}{\partial r} & 0 \\ 0 & \frac{\partial N_1}{\partial z} & 0 & \cdots & 0 & \frac{\partial N_{15}}{\partial z} \\ \frac{N_1}{r} & 0 & \frac{N_2}{r} & 0 \cdots & \frac{N_{15}}{r} & 0 \\ \frac{\partial N_1}{\partial z} & \frac{\partial N_1}{\partial r} & \cdots & & \frac{\partial N_{15}}{\partial r} & \frac{\partial N_{15}}{\partial z} \\ \frac{\partial N_1}{\partial z} & -\frac{\partial N_1}{\partial r} & \cdots & & \frac{\partial N_{15}}{\partial r} & -\frac{\partial N_{15}}{\partial z} \end{bmatrix} \qquad (7A.5)$$

and

$$\frac{\partial N_i}{\partial r} = \frac{1}{\det[J]}\left[\frac{\partial N_i}{\partial \alpha}\ \Sigma\left(\frac{\partial N_i}{\partial \beta}\ z_i\right) - \frac{\partial N_i}{\partial \beta}\ \Sigma\left(\frac{\partial N_i}{\partial \alpha}\ z_i\right)\right] \qquad (7A.6)$$

$$\frac{\partial N_i}{\partial z} = \frac{1}{\det[J]}\left[\frac{\partial N_i}{\partial \beta}\ \Sigma\left(\frac{\partial N_i}{\partial \alpha}\ r_i\right) - \frac{\partial N_i}{\partial \alpha}\ \Sigma\left(\frac{\partial N_i}{\partial \beta}\ r_i\right)\right] \qquad (7A.7)$$

where det[J] is the determinant of the transformation matrix from the global to the reference co-ordinate systems:

$$[J] = \begin{bmatrix} \frac{\partial r}{\partial \alpha} & \frac{\partial z}{\partial \alpha} \\ \frac{\partial r}{\partial \beta} & \frac{\partial z}{\partial \beta} \end{bmatrix} \qquad (7A.8)$$

The large displacement formulation used in this thesis account for the distortion of the element by a distortion rate matrix [C]:

$$[C] = \begin{bmatrix} C_{1,1} & C_{1,2} & C_{1,3} & \cdots & C_{1,30} \\ C_{2,1} & C_{2,2} & C_{2,3} & & C_{2,30} \\ \vdots & & & & \\ C_{29,1} & & & & \\ C_{30,1} & C_{30,2} & C_{30,3} & \cdots & C_{30,30} \end{bmatrix} \tag{7A.9}$$

Where:
$$C_{2i-1,\,2j-1} = -r\tau_{rz}\det[J_{ij}] + \left[\sigma_{rr}\frac{\partial N_i}{\partial z} + \tau_{rz}\frac{\partial N_i}{\partial z}\right]\det[J]\,N_j + N_i\sigma_{rr}\left[\frac{\partial z}{\partial \beta}\frac{\partial N_j}{\partial \alpha} - \frac{\partial z}{\partial \alpha}\frac{\partial N_j}{\partial \beta}\right] \tag{7A.10}$$

$$C_{2i-1,\,2j} = r\sigma_{rr}\det[J_{ij}] + N_i\sigma_{\theta\theta}\left[\frac{\partial r}{\partial \alpha}\frac{\partial N_j}{\partial \beta} - \frac{\partial r}{\partial \beta}\frac{\partial N_j}{\partial \alpha}\right] \tag{7A.11}$$

$$C_{2i,\,2j-1} = -r\sigma_{zz}\det[J_{ij}] + \left[\tau_{rz}\frac{\partial N_i}{\partial z} + \sigma_{zz}\frac{\partial N_i}{\partial z}\right]\det[J]\,N_j \tag{7A.12}$$

$$C_{2i,\,2j} = r\tau_{rz}\det[J_{ij}] \tag{7A.13}$$

and
$$\det[J_{ij}] = \begin{bmatrix} \frac{\partial N_i}{\partial \alpha} & \frac{\partial N_j}{\partial \alpha} \\ \frac{\partial N_i}{\partial \beta} & \frac{\partial N_j}{\partial \beta} \end{bmatrix} \tag{7A.14}$$

Chapter 8

Finite Element Analysis of the Cone Penetration Test

8.1 Verification of Finite Element Formulation

It is essential in any numerical analysis that the formulation and solution algorithm are checked against bench mark problems with known solutions. This is especially important in the present study where the finite element equations are formulated to take account of large displacements, for which problems with exact solutions are rare. Since the finite element formulation described here is used mainly for the determination of limit loads and stress distributions in the soil, the formulation has been comprehensively tested for its suitability for these types of calculations. The verification process was achieved by solving three problems which have known solutions.

8.1.1 Expansion of a Thick-Walled Cylinder

The effect of incompressibility on the quality of the computed stresses was investigated by the analysis of a small strain thick cylinder problem. The problem consisted of a thick-walled cylinder, with inner radius a and outer radius b, subjected to an internal pressure p. For a cylinder made of a material which obeys the Tresca yield criterion, a closed form solution for the stresses has been obtained by Hill (1951).

Two separate analyses have been carried out. In one of these, the capability of the formulation for stress calculation involving incompressibility was studied. In order to isolate possible errors due to the non-linear solution algorithm, a material with infinite strength has been assumed so as to ensure a purely linear elastic response. The infinite cylinder was modelled by a mesh consisting of four 15-node triangular elements. The prescribed boundary conditions are as shown in Figure 8.1. A Poisson's ratio of 0.49 was used to approximate the incompressible material

behaviour. The expansion of the cylinder was modelled by prescribing a radial displacement of 0.003 times the internal radius to the inner boundary.

The computed stresses are normalised by the Young's modulus E and plotted in Figure 8.1. The analytical solutions by Hill are shown as continuous lines. It is observed that the finite element results approximate closely the analytical solutions for the perfectly incompressible case even though a Poisson's ratio of 0.49 instead of 0.5 has been used in the calculation.

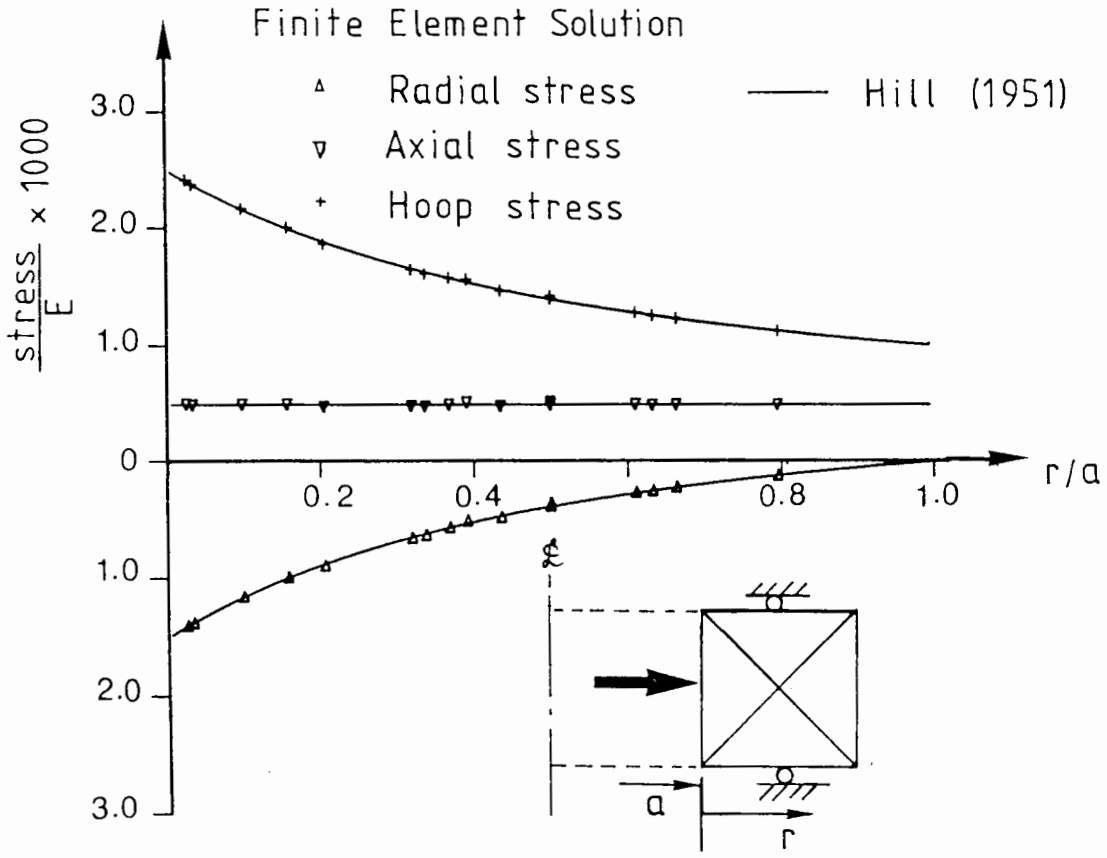

Figure 8.1: Expansion of Thick-Walled Cylinder - Stresses

The objective of the second analysis is to investigate the capability of the finite element program for limit load calculations. The mesh used in the first analysis has been retained. The material behaviour was described by a rigidity index of 100 and a Poisson's ratio of 0.49. A radial

displacement, δ, of 5% of the inner radius was prescribed at the inner boundary.

The load-displacement curve from this analysis is shown in Figure 8.2. The cavity pressure, p, is normalised by the shear strength in undrained triaxial compression c_u. A limiting value for p is clearly defined in the finite element results. For all practical purposes, this limit pressure is identical to the analytical solution by Hill (1951). The factor $\frac{2}{\sqrt{3}}$ accounts for the different yield criteria which were used in Hill's analysis and the finite element calculation.

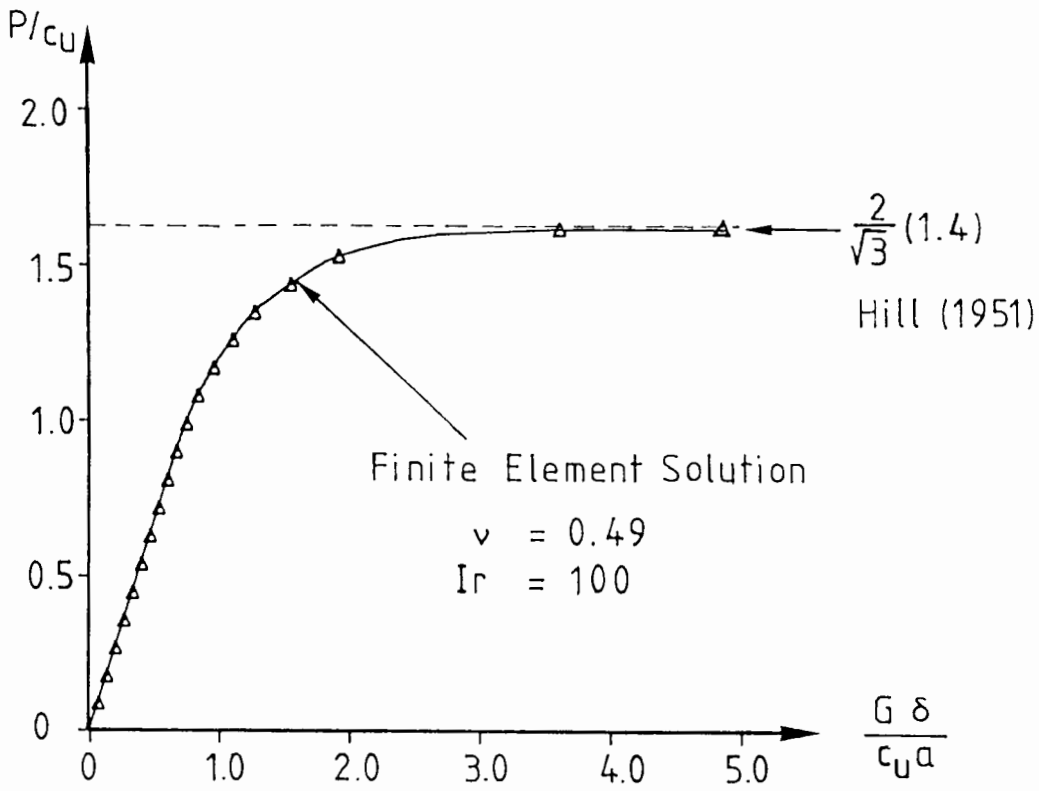

Figure 8.2: Expansion of a Thick-Walled Cylinder - Limit Pressure

8.1.2 Cylindrical Cavity Expansion in an Infinite Medium

The expansion of a cylindrical cavity in an infinite medium is a rare example of a problem involving large displacements which has a closed form

solution. For the case of a von Mises material, an analytical solution has been obtained by Sagaseta (1984). This problem thus provide a useful test for the large displacement formulation discussed in this chapter.

The mesh used in the finite element calculation is necessarily finite. Burd (1986) shows that if b is the outer radius of the mesh, it is possible to simulate correctly the material behaviour of the infinite medium within a radius b from the axis by the addition of a compensating layer to the outer perimeter of the mesh. If the thickness of this correction layer is b, then the material properties are given as:

$$E^* = \frac{5}{12} E \quad \text{and} \quad \nu^* = 0.25 \tag{8.1}$$

where E is the Young's modulus of the continuum and E^* and ν^* are the Young's modulus and Poisson's ratio of the compensating layer.

The mesh used for the finite element calculation is depicted in Figure 8.3a. The soil was assumed to have a rigidity index of 100, and a Poisson's ratio of 0.49 was used to approximate the incompressibility condition. The initial cavity radius was expanded by a factor of four.

The stresses in the vicinity of the expanded cavity are plotted in Figure 8.3b. A good match between the stresses computed by the finite element method and the analytical solution has been obtained. Close to the cavity wall, the numerical results are slightly lower than the analytical solutions. These small deviations can be due to the smaller Poisson's ratio and the finite discretization of the soil in the finite element calculation. Otherwise, the agreement is surprisingly good.

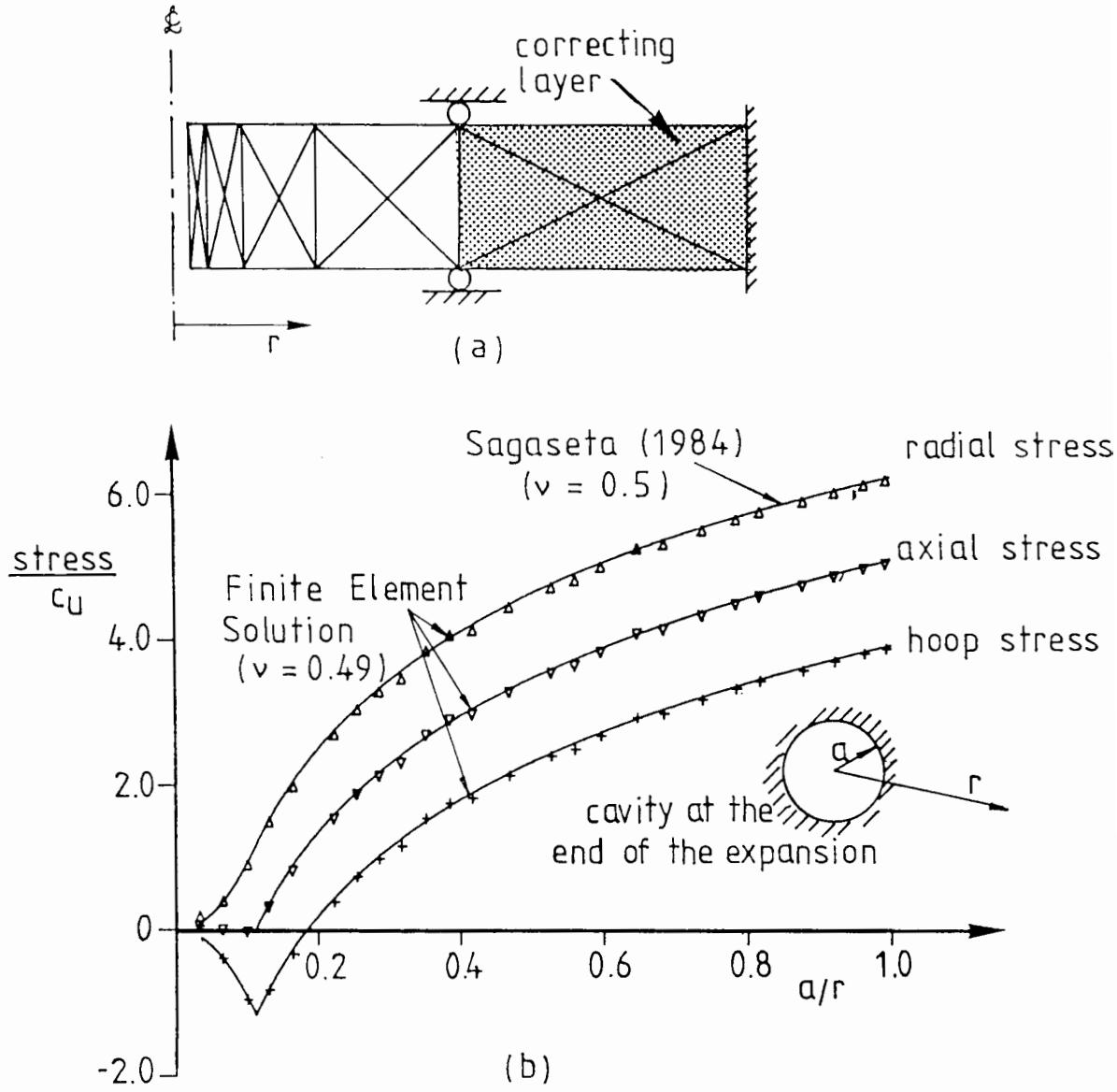

Figure 8.3: Finite Element Analysis of an Infinite Cavity Expansion

(a) Finite Element Mesh (b) Stress Changes

8.1.3 Collapse Load Analysis of a Rough Rigid Circular Footing

Finite element calculations have a well known tendency to over-estimate collapse loads and in severe cases to show no limit load at all, even though one is known to exist (Toh & Sloan, 1980). Since the analysis of a cone penetrometer is basically a collapse load problem, it is necessary to check that the proposed formulation is suitable for this type of computations. The collapse load calculation of a thick cylinder described in

the previous section is not a sufficiently rigorous test because it is essentially a one-dimensional problem. Therefore, a two dimensional collapse load calculation for a circular footing has been selected.

The mesh which has been used in the calculation is shown in Figure 8.4a. The semi-infinite soil mass is modelled by a square mesh with each side equal to 10B, where B is the radius of the footing. Around the edge of the footing, a refined mesh system has been adopted to cater for the high stress gradients expected in this region. The soil was assumed to be an elasto-plastic von Mises material with a rigidity index of 100 and a Poisson's ratio of 0.49.

A uniform vertical displacement was prescribed to the footing base and horizontal movement of the nodes in contact with the footing is prevented to simulate a perfectly rough, rigid footing. Two sets of calculations with different stress rate definitions were performed. In the first series, the effect of soil rotations in the Jaumann stress rate definition was neglected, while the complete Jaumann equation was used in the second series of analyses.

Figure 8.4b shows the load-displacement response of the footing. When the rotation rates are not included, the finite element analysis yields a collapse load of $6.78c_u$. This is comparable to the value of $\frac{2}{\sqrt{3}}(6.04c_u)$ which is an estimate of the collapse load value for a rigid-plastic von Mises material. The theoretical estimate is obtained by multiplying the solution for a Tresca material ($6.04c_u$) obtained by slip line theory by the factor $\frac{2}{\sqrt{3}}$.

No well defined collapse load was observed when the full Jaumann stress definition was used. The pressure on the footing base after a displacement of 0.125B continues to increase with further displacement increment, albeit

at a much reduced rate. Similar behaviour has also been observed in the finite element analyses of smooth flexible footings by Carter et al. (1977). At a footing displacement of 0.1B, the footing pressure calculated using the full Jaumann stress rate equation exceeds the corresponding solution which ignored the Jaumann terms by about $1.0c_u$. The difference between these two solutions remains unexplained.

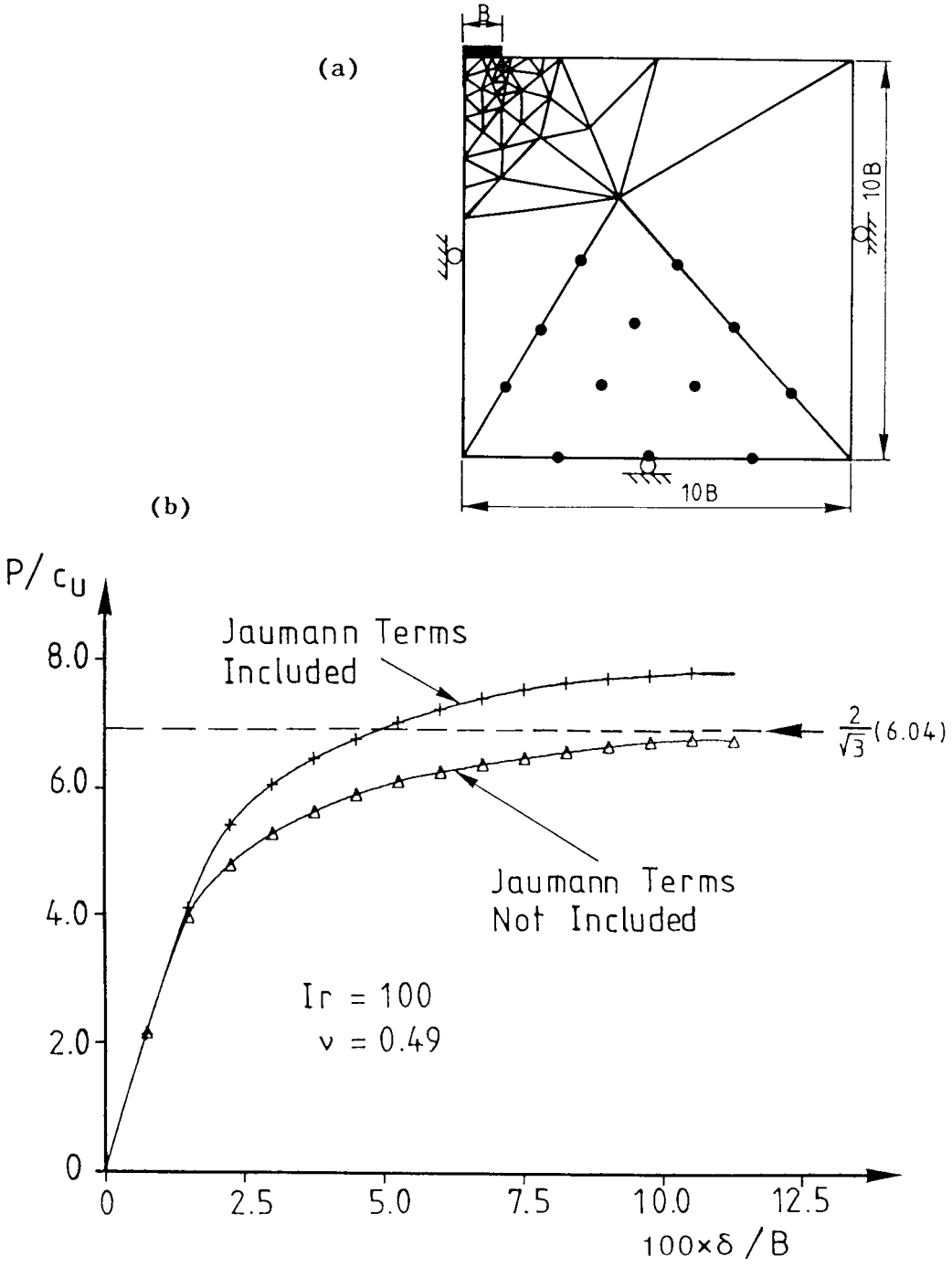

Figure 8.4: Collapse Load Analysis of a Rough Rigid Circular Footing

(a) Finite Element Mesh (b) Load Displacement Curves

In a deformation analysis involving finite displacements such as the cone penetration problem, large soil rotations around the tip are expected. Therefore, a consistent analysis should take this into account by adopting an objective definition for the stress rate. This is achieved in the present study by using Jaumann's definition.

8.2 Finite Element Modelling of the Cone Penetration Test

In this section, a finite element analysis of the cone penetration problem is described. The penetrometer was assumed to be installed deep in the ground either by previous penetration or by placing it in a pre-formed hole. These different modes of placement were modelled by adopting different initial stresses in the soil prior to loading the penetrometer. The stresses derived from the strain path method were used when modelling a penetrometer which had been pushed into place. When modelling a penetrometer which has been placed in a pre-formed hole, an undisturbed in-situ stress state was assumed. This latter analysis is carried out for comparison with the work of De Borst & Vermeer, and to assess the importance of the stresses set up during penetration.

A series of parametric studies has been carried out. The parameters investigated include the Poisson's ratio, the rigidity index and the in-situ stress state of the soil. The effect of shaft roughness has also been considered. A mesh which consists of 81 15-node triangular elements (Figure 8.5) was used in all the finite element calculations. The layout of the mesh was chosen with due consideration of the likely stress distribution around the cone penetrometer. A good estimate of this stress distribution is provided by the strain path analysis. In regions of high stress gradients, the density of the elements was increased. The overall dimension of the mesh

was designed to be similar to the finite difference mesh shown in Figure 3.2. This facilitates the transfer of stress data between the two meshes when the stresses computed by strain path method are used as the initial stress state for the incremental finite element calculations (section 8.8).

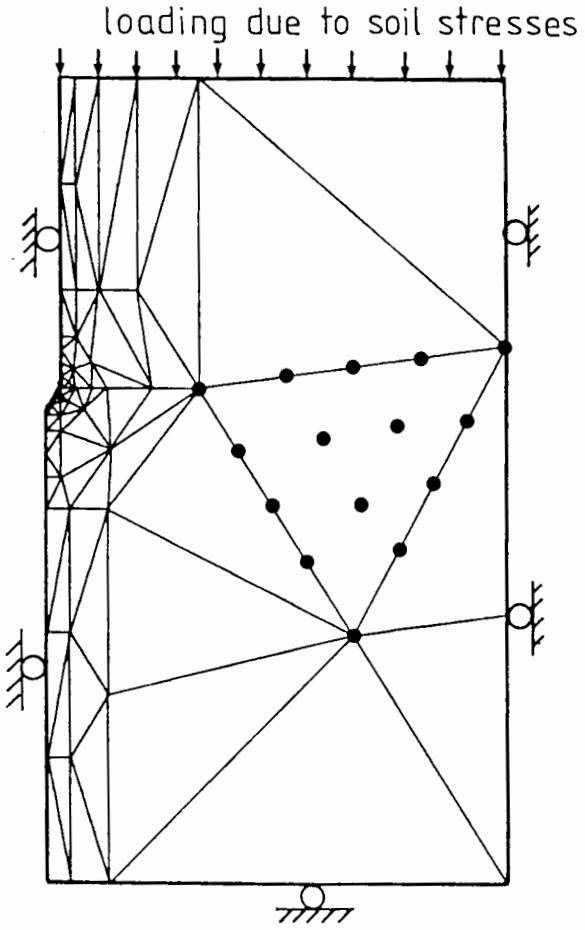

Figure 8.5: Finite Element Mesh for Cone Penetration Analysis

In the finite element analysis, the cone penetration process was modelled by prescribing incremental displacements to the penetrometer. For a rough shaft, vertical displacements were prescribed on all the nodes on the penetrometer-soil interface and radial movement of these nodes was prevented. When modelling a smooth shaft, vertical displacements were prescribed only for the nodes on the cone face but lateral movement was again prevented, the

nodes on the shaft were free to slide in the vertical direction. Hence, in both of these analyses, the cone face was assumed to be perfectly rough.

For the range of I_r generally associated with clay, the imposed vertical displacement has to be sufficiently large to achieve a collapse load or 'failure' condition. If the cone face is to be modelled as smooth, the interface nodes should be allowed to slide freely along the inclined surface. When such a node reaches the cone shoulder, the restraint conditions must be changed. This requirement increases the complexity of the solution procedure considerably. The complication caused by the changing boundary conditions can be avoided by assuming that the cone face is perfectly rough.

8.3 Effect of Poisson's Ratio

The elastic compressibility of a material is governed by the Poisson's ratio, ν. For a perfectly incompressible material, ν is equal to 0.5. However, this value could not be implemented directly in the finite element method and the incompressible material behaviour is usually approximated by adopting a value very close to 0.5. In order to investigate the effect of ν on the load-displacement characteristics of a cone penetrometer, finite element calculations with three different values of ν have been performed. The soil was assumed to have a rigidity index of 100 and the initial stresses were assumed to be zero. The calculations were carried out by prescribing a vertical displacement of 0.2 R on a penetrometer with a smooth shaft.

The results of the finite element analyses are shown in Figure 8.6. At a cone displacement of 0.1 R, the pressure on the cone tip on each of the three cases has reached a constant value and further increase in displacement does not change it significantly. Increasing the Poisson's ratio resulted in a stiffer initial response and a greater limit pressure on the cone tip. The

pressure on the cone tip at the limit state condition has generally been assumed to be equivalent to the steady state cone penetration resistance. Hence, the results show that ν not only governs the elastic response, but it also affects the cone resistance computed by finite element method. It is therefore essential in modelling undrained soil behaviour that a value of ν very close to 0.5 is used to enforced the condition of zero volumetric strain. A value of ν equal to 0.49 has been shown to approximate the incompressibility condition quite satisfactorily in the infinite cavity expansion problem, so this was adopted in the finite element calculations described in the following sections.

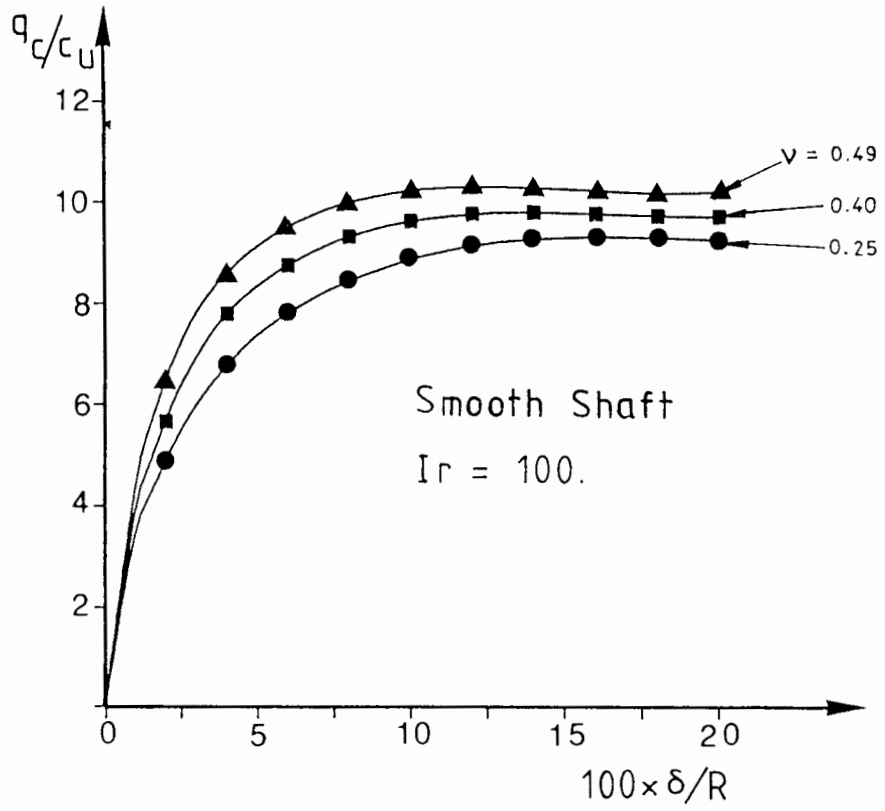

Figure 8.6: Effect of Poisson's Ratio on Cone Resistance

8.4 Stress Changes Due to Rough Cone Penetration

It has generally been accepted that the stresses evaluated by the finite element method are of acceptable accuracy even though the equilibrium conditions are not satisfied exactly at each material point. The quality of the stresses evaluated by the finite element program formulated here has been shown to be extremely high (section 8.2). It is reasonable to assume that the numerical results around the cone would be of comparable quality and can therefore be used to assess the accuracy of the stresses computed by the strain path method.

In order to study the effect of shaft roughness, finite element calculations have been carried out for penetrometers with smooth and rough shaft. The displacement vectors in the soil after an imposed displacement of 0.2 R are shown in Figure 8.7. The computed displacement fields below the tip in these cases are found to be quite similar. The effect of shaft friction is reflected in the large soil displacements adjacent to the rough shaft. In contrast, soil movements around the smooth shaft is very small, and the deformation field is mainly confined to a region around the cone face.

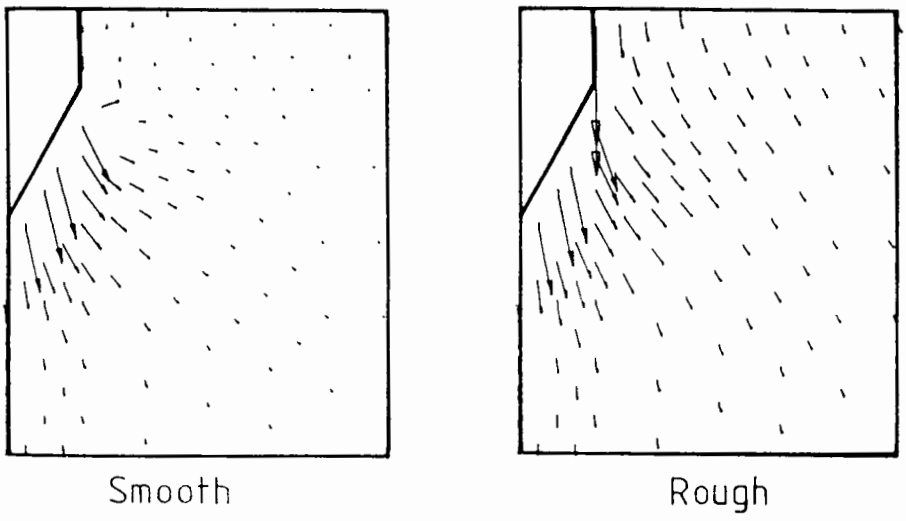

Figure 8.7: Displacement Field in Soil after a Cone Penetration of 0.2 R

The difference in the deformation patterns for the two extreme shaft conditions is reflected in the zone of yielded soil (Figure 8.8). For a penetrometer with a smooth shaft, the plastic zone is confined to the cone face region, whilst a thin annular zone of soil around the rough shaft is observed to have yielded as well.

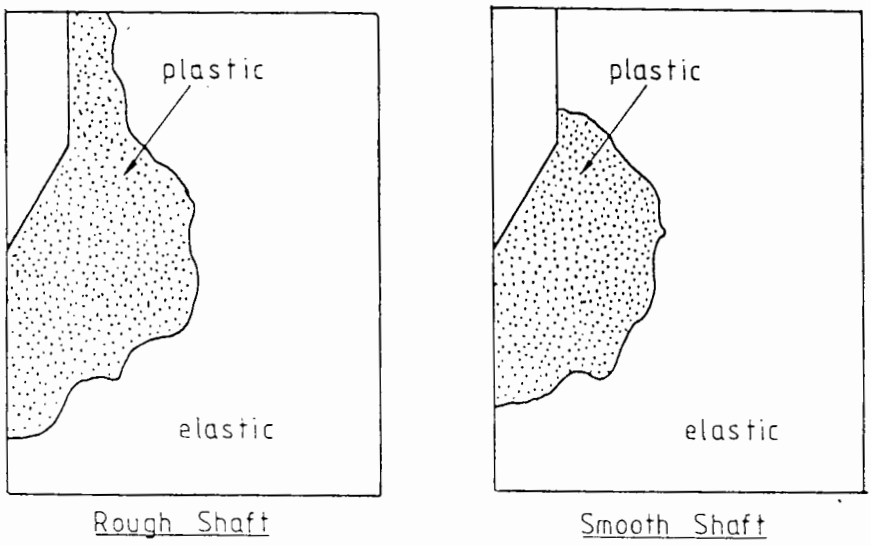

Figue 8.8: Failure Zone around Cone Penetrometers with different Shaft Roughness

The variations of the tip resistance with cone displacement for the two shaft conditions are shown in Figure 8.9. Shaft roughness is found to have a significant influence on the shape of the load-displacement curve. A 'softer' load-deformation response is observed for the penetrometer with a rough shaft. This is mainly due to the higher stresses generated in the soil around the shaft by interface friction, which leads to a larger cone displacement at comparable total load on the penetrometer. More significantly, however, the results suggest that the limit cone resistance is not very sensitive to shaft roughness. For a soil with an I_r of 100, the values of q_c for the two shaft conditions at a displacement of 0.2 R are

nearly identical. For an I_r value of 300, the difference in q_c at this displacement is found to be slightly greater.

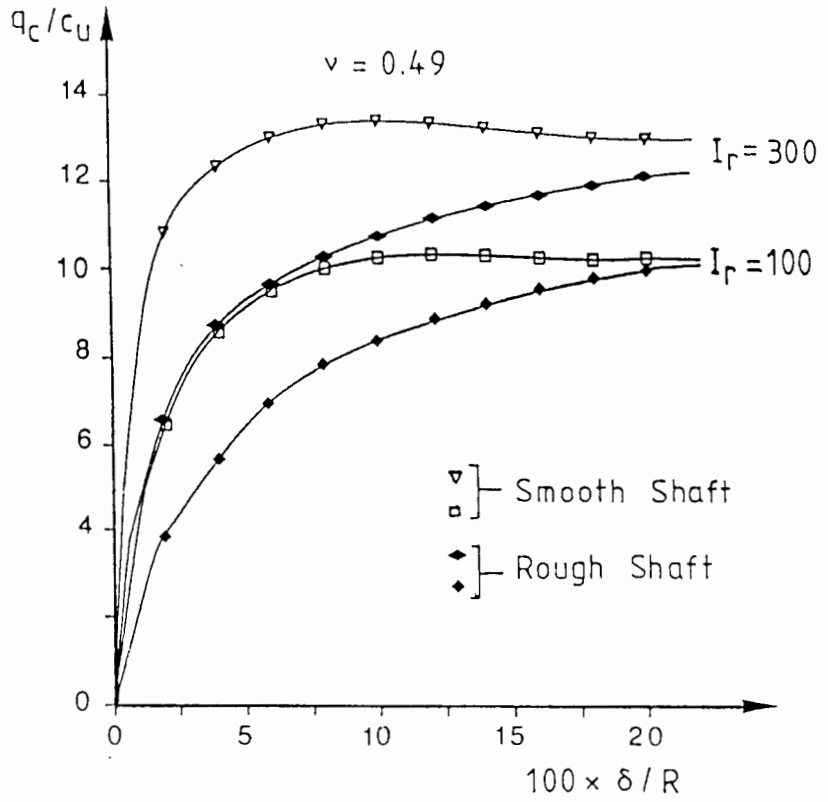

Figure 8.9: Effect of Shaft Roughness on Tip Resistance

The stress changes in the soil around a penetrometer after an imposed displacement of 0.2 R are shown in Figure 8.10. The shaded areas indicate regions where small stress oscillations render the contours irregular so that they cannot be shown in detail. Below the cone tip, the patterns of stress distributions for the two shaft conditions show broad similarities. The zone of soil subjected to significant stress changes are considerably greater when the shaft is rough. High stress gradients are observed around the cone shoulder, and the soil adjacent to the shaft is subjected to significant shear loading.

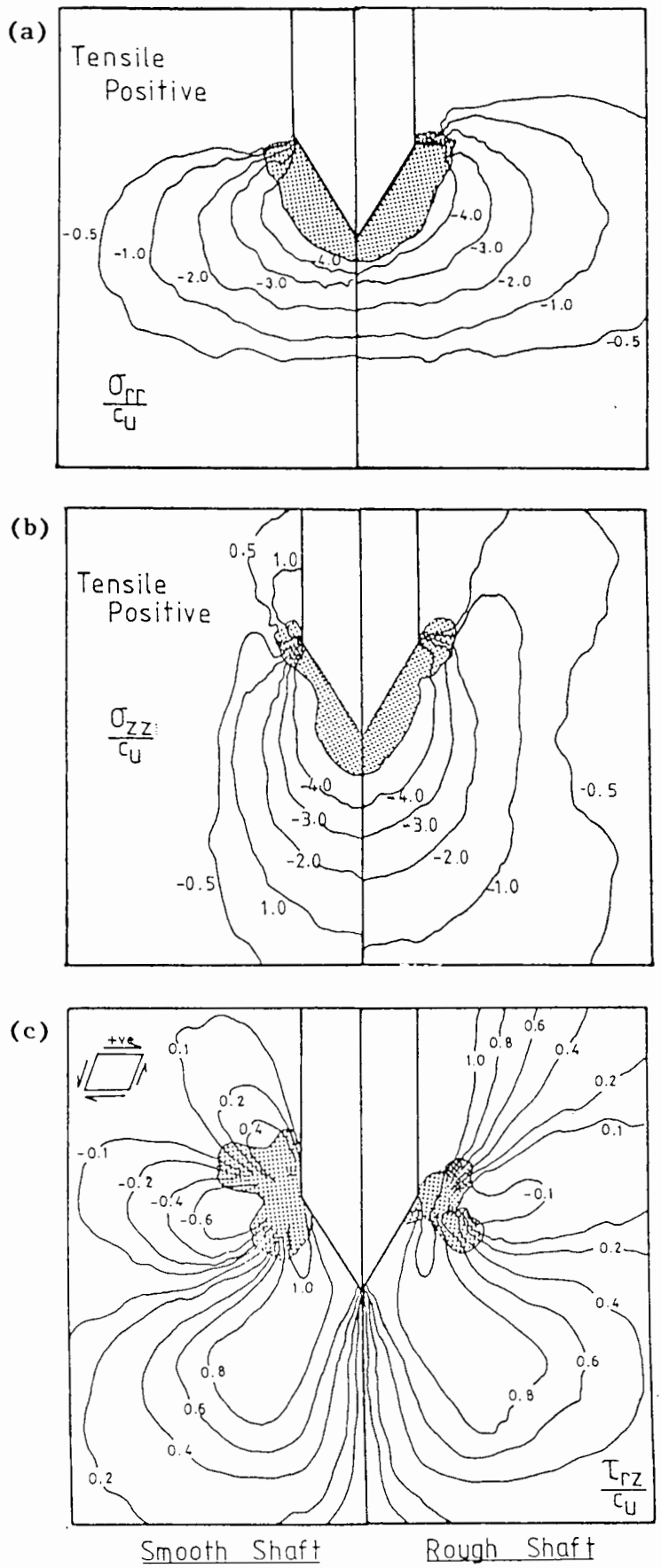

Figure 8.10: Stress Distributions around a 60° Cone Penetrometer

The stress changes around a smooth penetrometer shaft are generally very small. The soil just above the cone shoulder is subjected to tensile axial stress changes. These features may be due firstly to the way the penetration process was being modelled, and secondly by the extreme combination of a smooth shaft and a rough conical tip.

Despite the difference in approach, it is interesting to note that the stress distributions around the cone face obtained from finite element computations and the strain path method show striking similarities. The shear stress distribution below the shoulder level are also broadly in agreement with the strain path solution. These similarities partially confirmed the reliability of the strain path method as an approximate analytical tool. In addition, the uncertainty in the stresses around the cone shoulder, which has been observed in the strain path solution, is also present in the finite element analysis. This is an indication of the importance of a detailed analysis at this point.

The variations of the stress components with radial distance are plotted in Figure 8.11. Due to the nature of the discretization, it is not possible to show the stress variation on any particular horizontal plane. The data points shown in these plots correspond to the Gauss point stresses in a thin horizontal layer of soil with a thickness of 0.1 R, located mid-way between the tip and the shoulder levels (see inset of Figure 8.11a). The magnitudes of the axial and hoop stress components immediately adjacent to the cone are found to be considerably higher than those given by either the cavity expansion theories or strain path method. The scatter in the computed stresses for $\frac{r}{R} < 1.0$ is possibly due to the severe restraints prescribed on the cone face. For $\frac{r}{R} > 1.0$, the stresses in the plastic region vary almost linearly with $\log(\frac{r}{R})$. This feature has also been observed in the strain path solution.

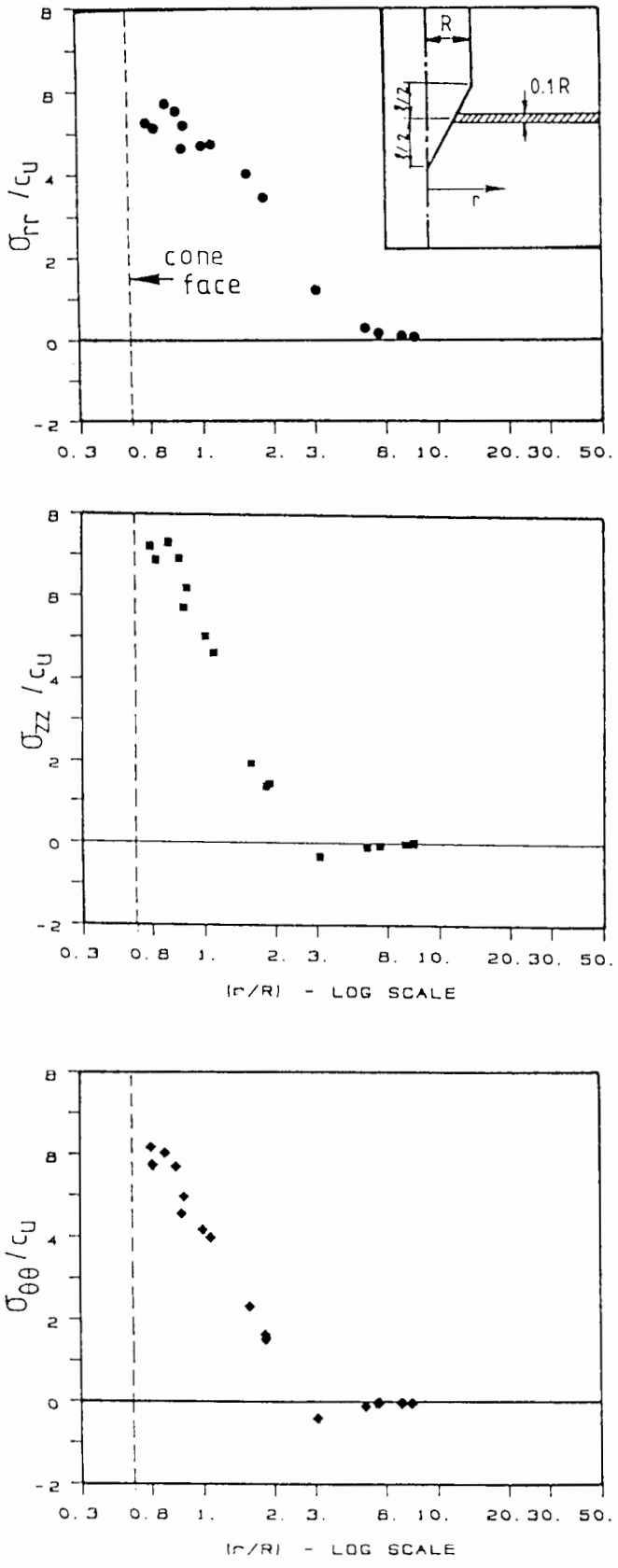

Figure 8.11: Variation of Stresses with Radial Distance

8.5 Effect of Rigidity Index on Cone Resistance

The results of the strain path analysis indicate that the rigidity index of soil has a significant effect on the computed tip resistance. A series of computations has been performed to investigate if the same trend exists in finite element calculations. The I_r values which have been analysed range from 30 to 500. A smooth penetrometer shaft was assumed in all the calculations and the soil stresses was initially set to zero.

The computed results are plotted in Figure 8.12, which shows the variation of tip resistance with penetrometer displacement. The limit state

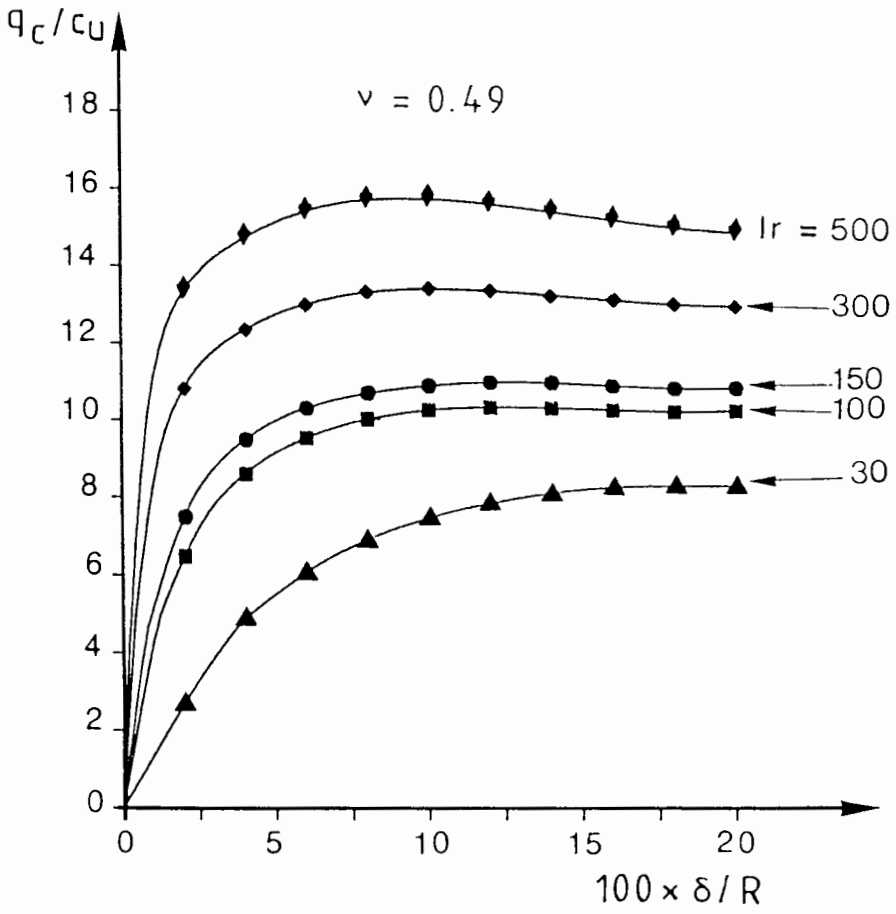

Figure 8.12: Effect of Rigidity Index on Cone Resistance

tip resistance at a cone displacement of 0.2 R exhibits the same general trend of variation as the results obtained from the strain path method. However, the magnitude of q_c derived from the finite element calculations is slightly higher. It should be noted that the finite element result were computed for a rough cone, whereas the cone face was assumed to be perfectly smooth in the strain path method.

8.6 Effect of In-situ Stress State

In the analyses considered so far, the initial stresses in the soil were assumed to be zero. The effect of different stress states on the cone resistance computed by the finite element method is investigated in this section. This is accomplished by prescribing various combinations of vertical and horizontal stresses as the initial conditions.

Figure 8.13 shows the finite element results based on four different isotropic initial stress states ($\sigma_{ho}=\sigma_{vo}$) in a soil which has a rigidity index of 100. At a displacement of 0.2 R, the limit load condition has been reached in each of the calculations. The values of the cone resistance at limit state were found, as expected, to differ by an amount which is equal to the difference in σ_{vo}. Therefore, if the results are expressed in terms of the normalised cone factor N_k, then a unique value is obtained. This suggests that q_c is not an appropriate quantity for correlating soil properties since it contains a component due to the stress level. The N_k factor is a preferred correlation parameter because it is independent of the stress level when the initial stress state is isotropic.

The effect of anisotropic initial stress state on the N_k value is investigated by varying the relative magnitude of σ_{ho} and σ_{vo}. The variations of N_k with cone displacement for three different initial stress

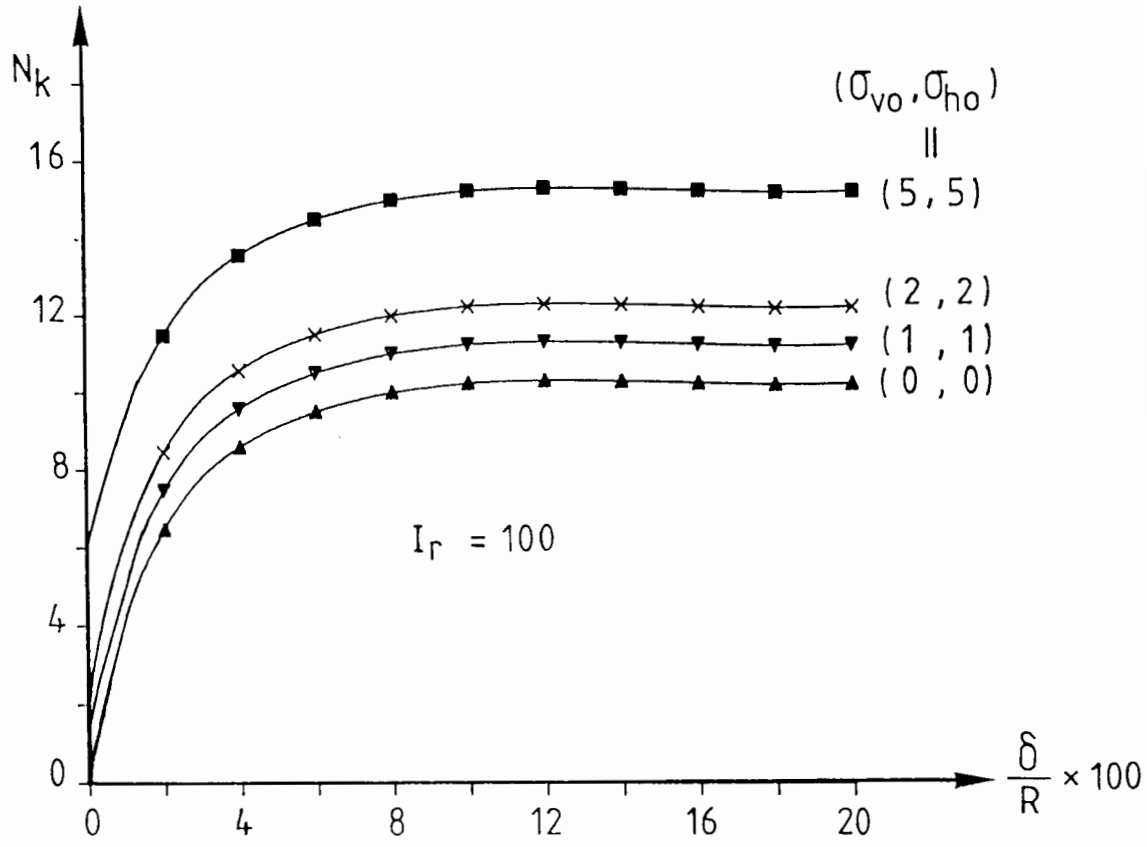

Figure 8.13: Effect of Stress Levels on Cone Resistance, q_c

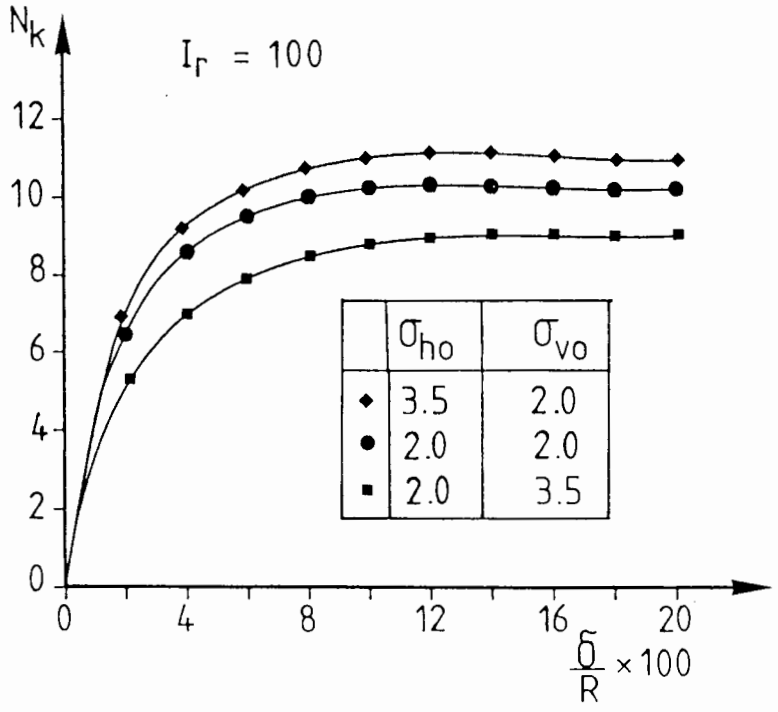

Figure 8.14: Effect of Stress Anisotropy on Cone Resistance, q_c

conditions are shown in Figure 8.14. The values of σ_{vo} and σ_{ho} are as indicated in the diagram. It is found that N_k increases when σ_{ho} is greater than σ_{vo}. Conversely, if σ_{ho} is less than σ_{vo}, a lower N_k value is obtained. This result confirms the general trend observed in the solution derived from the strain path method. The N_k values determined by the finite element method, however, are greater than those obtained from a strain path analysis.

8.7 Strain Path-Finite Element Analysis

The N_k factors evaluated by the incremental finite element analyses described so far are not representative of the steady state penetration resistance. The soil stresses at failure are different from those around a cone which is continually penetrating. A more realistic estimate of the cone factor could be obtained if the penetrometer is assumed to have been penetrated into place. An incremental displacement finite element analysis in this case would then model the phase in an actual CPT when penetration was resumed after a temporary interruption (e.g. for connecting the extension rods). Experimental evidence suggests that the cone resistance at this stage of the test is similar to the steady state value.

However, this type of analysis requires the knowledge of the stresses around the penetrometer which is in fact the solution being sought. To overcome this circular problem, a good, though inexact, estimate of the stress state can be obtained from the strain path method. Thus, for a given set of soil properties and in-situ stress conditions, the stresses around the penetrometer are computed via the procedure described in Chapter 4. This set of stresses is then used as the starting condition in the incremental finite element analysis. For want of a better term, this analytical procedure is called the strain path-finite element method (abbreviated as SPFEM).

Due to the different meshes used for the strain path and finite element calculations, the initial Gauss point stresses in the finite element mesh must be interpolated from the nodal values in the finite difference grid. A data transfer routine has been implemented and the errors introduced by the interpolation process were found to be minimal. However, the stresses obtained via the strain path method do not satisfy the equilibrium conditions completely and this should be corrected prior to the incremental finite element analysis. Based on the fictitious body forces concept described in Chapter 5, the errors of equilibrium were eliminated by an intermediate finite element calculation. The equilibrium correction calculation was accomplished by imposing a set of body forces, equal and opposite to the calculated fictitious body forces, on the soil mass.

The results of the strain path-finite element analysis are shown in Figure 8.15. A rigidity index of 100 was assumed for the soil and a Poisson's ratio of 0.49 was used in the finite element calculation to approximate the incompressibility condition. The in-situ soil stresses were assumed to be zero, so $\frac{q_c}{c_u}$ is exactly equivalent to N_k. The result of the finite element calculation for a penetrometer placed in a pre-formed hole in a soil with zero initial stresses (abbreviated as FEM), has also been plotted in the same diagram for comparison. Point A in Figure 8.15 corresponds to a stress state obtained directly from the strain path method without the intermediate finite element correction and so is not in equilibrium. Point B represents a corrected stress state after the fictitious body forces have been eliminated. Therefore, the curves in Figure 8.15 represent the numerical results for three different initial stress conditions.

It is observed that the curve from point B rises monotonically to reach a well-defined limit value. On the other hand, the curve from point A

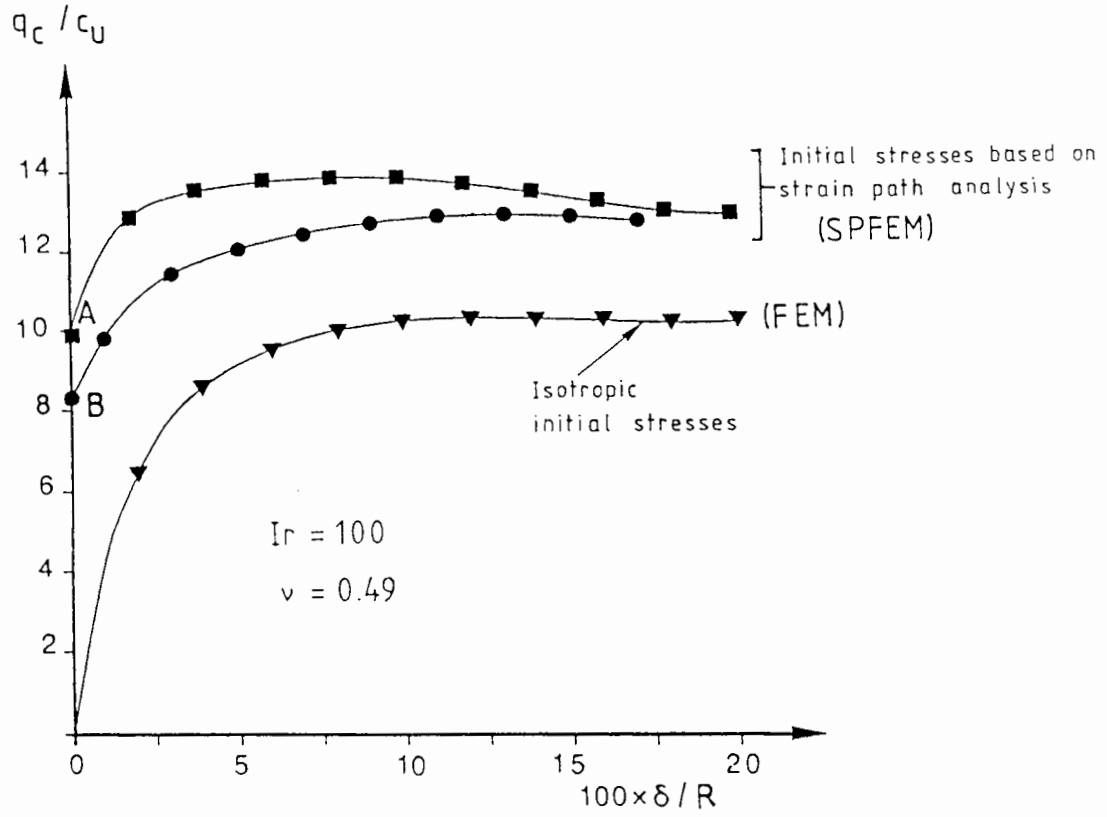

Figure 8.15: Variation of Cone Resistance with Cone Displacements from Strain Path-Finite Element Analysis

increases gradually to a peak before settling down to the same limit value. The peak in the second load-displacement curve cannot be due to strain softening because the adopted constitutive model does not provide for such material behaviour. It is possible that the shape of this curve is caused by the equilibrium errors in the Gauss point stresses which are quite significant initially. The difference between the curves therefore merely reflect the errors in the stresses at A. However, due to the equilibrium correction procedure inherent in the Modified Euler solution scheme, the out-of-balance stresses in case A are gradually corrected. Towards the final stages of the calculation (when the equilibrium correction has taken its full effect), the stresses are the same in both cases. As a result, the limiting cone resistances (evaluated from the internal soil stresses) will have the same numerical value.

The tip resistances computed from the strain path-finite element method is considerably higher than the corresponding results from the conventional finite element analysis. An increase of about 20% in the N_k factor has been obtained for a rigidity index of 100. The SPFEM result can be considered to provide a more realistic estimate because the initial stresses are more representative of the stress condition that actually exist around the cone penetrometer that has been continuosly penetrated into place.

8.7.1 Effect of Anisotropic Initial Stresses

The effect of anisotropic in-situ stresses on computed tip resistance has been analysed using the strain path-finite element method. The initial stresses obtained from the strain path method were corrected for equilibrium prior to the displacement controlled incremental finite element calculations. The results of these analyses are illustrated in Figure 8.16. The in-situ stress state is characterised by the stress factor, Δ. The values of N_k

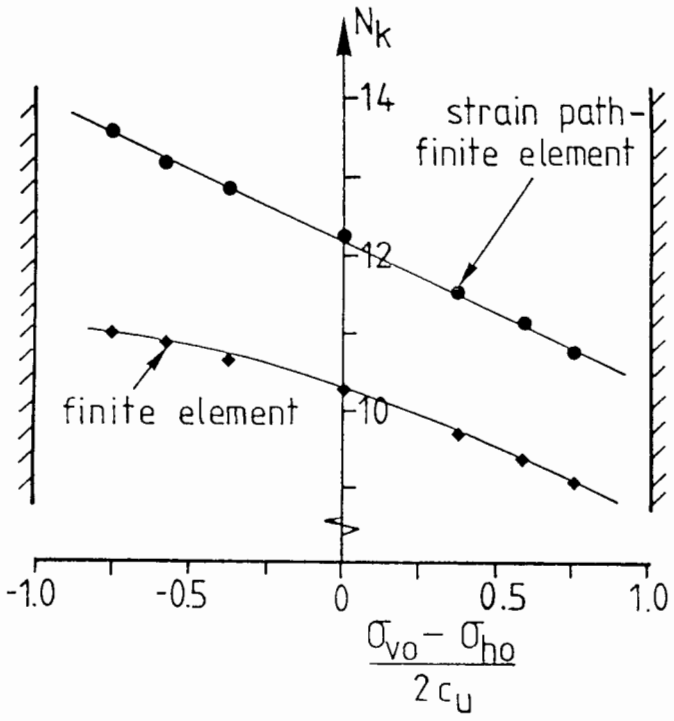

Figure 8.16: Variation of N_k with Stress Factor, Δ

obtained from the conventional finite element method (FEM) have also been plotted on the same figure.

The N_k factors evaluated by SPFEM for various combinations of σ_{ho} and σ_{vo} are found to be higher than the corresponding FEM results. It is also observed that changes in the stress factor, Δ, has a greater effect on the SPFEM solutions. This is indicated by the steeper gradient of the best straight line fit of the SPFEM results. The gradient of this line is approximately -2, indicating that N_k is dependent on σ_{ho}. Hence, an almost unique value would be obtained if the cone factor is defined in terms of σ_{ho}. The trend from the conventional FEM is less conclusive; it suggests that the N_k factor is affected by both σ_{ho} and σ_{vo}. Nevertheless, the results of these two analyses are consistent with the trend obtained from the strain path method which shows that increasing σ_{ho} increases the N_k factor.

8.7.2 Variation of N_k with I_r

The variation of the N_k factor with I_r computed by SPFEM for zero initial stress states is illustrated in Figure 8.17. The results obtained from the strain path analysis have been reproduced in the same diagram for comparison. The N_k factor evaluated by SPFEM is significantly higher than the strain path results. A rough cone solution (dotted line in Figure 8.17) is estimated from the strain path analysis using the approximate expression in equation (6.2). This is found to provide a better agreement with the SPFEM results.

The possible ranges of N_k due to anisotropic stress effect for two I_r values (100 and 500) are shown by vertical bars. The upper limit corresponds to a stress state characterised by $\Delta \simeq -1$, and the lower limit is relevant for $\Delta \simeq 1$. These results suggest that for any given I_r, it is more

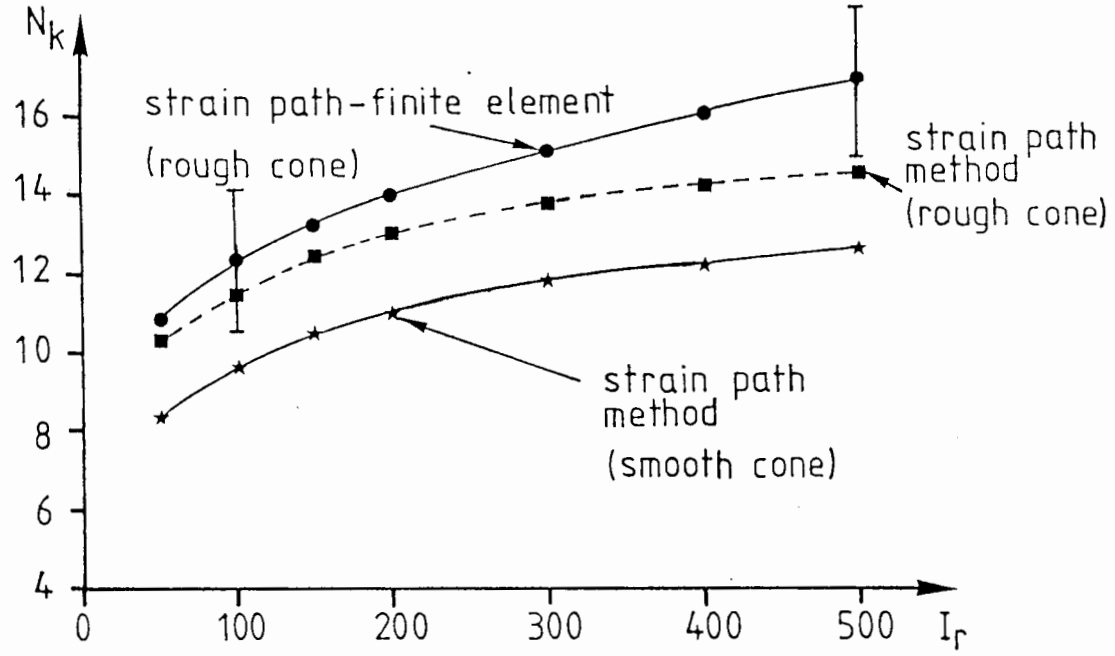

Figure 8.17: Variation of N_k with I_r as Evaluated from SPFEM and Strain Path Method

appropriate to express N_k as a range of values, rather than a discrete value. Such an expression helps to emphasise the dependence of N_k on the in-situ stress state. Based on the results of the strain path-finite element analyses, the following expression is suggested:

$$N_k = N_{ko} - 1.89\Delta \tag{8.1}$$

where N_{ko} is the cone factor evaluated for an isotropic initial stress state.

For the range of I_r values between 50 and 500, the effect of rigidity index may be expressed by the approximate expression:

$$N_{ko} = 0.19 + 2.64\ln(I_r) \tag{8.2}$$

The cone factors computed from equation (8.2) and those derived numerically are presented in Table 8.1. The maximum deviation between these two sets of values are found to be less than 3%.

I_r	$(N_{ko})_1$ from SPFEM	$(N_{ko})_2$ from Eq. (8.2)	$\frac{(N_{ko})_2}{(N_{ko})_1}$
50	10.69	10.52	0.98
100	12.26	12.35	1.01
150	13.25	13.42	1.01
200	14.03	14.18	1.01
300	15.11	15.25	1.01
400	16.10	16.01	0.99
500	16.98	16.60	0.98

Table 8.1: Comparison of the Cone Factors Derived from SPFEM and Those Computed Using Equation (8.2)

Equation (8.2) was derived for a perfectly rough cone. If an approximate correction for different cone face roughness similar to that discribed in Chapter 6 is made, then N_{ko} may be expressed as:

$$N_{ko} = 0.19 + 2.64\ln(I_r) - 2(1-\alpha) \qquad (8.3)$$

where α is the roughness coefficient of the cone face as defined in equation (6.9). Repeating the calculation for the two extreme combinations of soil conditions presented in Table 6.1 using equations (8.2) and (8.3), the values of N_k are found to be 6.6 and 18.5. This is illustrated in Table 8.2. These values are consistent with the range of N_k obtained from field and laboratory tests. Furthermore, it is believed that the SPFEM can provide a better estimate of N_k than the strain path method because the uncertainty due to the

equilibrium errors in soil stresses is less significant in the former approach.

I_r	Δ	α	N_k
50	1	0	6.6
500	-1	1	18.5

Table 8.1: N_k for Two Combinations of I_r, Δ and α

8.8 Summary

The finite element formulation described in Chapter 7 has been verified by the analysis of three problems with known solutions. Good agreements between the finite element results and the established solutions were obtained. The cone resistance computed by finite element methods shows the same variation with I_r as those evaluated by the strain path procedure. The tip resistance, q_c, was found to be dependent on the in-situ stresses as well as the soil properties. Correlation should therefore be effected through the dimensionless cone factor. For an isotropic in-situ stress state, the cone factor is independent of the initial stress level. However, N_k is affected quite significantly by stress anisotropy and this is mainly due to the lateral stress component.

Due to the influence of the stress states on N_k factors, the correct initial stress state must be prescribed for the soil around the penetrometer if the incremental finite element analysis is to give a reliable solution. The strain path-finite element method is considered to give the best estimate of N_k because the soil stresses provide the most realistic representation of the condition that actually exists around a penetrometer.

Chapter 9

Dissipation Analysis

9.1 Introduction

The development of the cone penetrometer with simultaneous measurements of pore pressure and tip resistance has greatly enhanced the piezocone as a soil profiling tool. When steady penetration is interrupted, the dissipation of the excess pore water pressures is controlled by the consolidation characteristics of the soil. Until very recently, no rational interpretation techniques were available to derive the consolidation parameters from dissipation test data. Levadoux & Baligh (1986) suggest an interpretation technique based on a linear consolidation analysis of the pore pressure around the cone. When applied to the dissipation records in Boston Blue clay, this technique has been found to give very consistent estimates for the consolidation coefficients.

In this chapter, a dissipation analysis of excess pore pressure around a piezocone is described. The initial pore water pressure distribution is evaluated by the strain path method. The effects of soil parameters and cone angle on the initial pressure distribution are addressed. The characteristics of the dissipation curves at various locations on the penetrometer are discussed and based on the results of these analyses, two techniques for interpreting dissipation test data are suggested.

9.2 Consolidation Theories

The consolidation characteristics of soil are conventionally defined by the coefficients of consolidation, c_h and c_v, which are related to the permeability and compressibility of the soil. The permeability, which governs fluid flow in the soil matrix, is principally a function of void ratio whereas the compressibility is a function of the current effective stress level as well as the past stress history (i.e. the overconsolidation

ratio, OCR). As the excess pore pressure dissipates, the effective stress in the soil increases and this is accompanied by a decrease in the void ratio. In general, these changes in the permeability and void ratio will cause the coefficient of consolidation to vary as dissipation proceeds.

This variation should be taken into account in a comprehensive consolidation analysis. In practice, however, non-linear consolidation solutions are very difficult to obtain and the few that have been attempted are limited to very simple geometry and simplified soil models (Small et al., 1976). Moreover, non-linear consolidation analyses are governed by many parameters and the results are not amenable to normalization. Such analyses are useful for predicting the response of a particular clay under particular conditions, but the results cannot be generalised for other clays or even the same clay under different conditions. A useful interpretation method, on the other hand, should provide sufficient generality so that it is applicable to a wide range of soils. Linear analysis, in which the coefficient of consolidation is assumed to be constant, permits normalization and hence is useful for interpretation purposes.

Linear consolidation analyses are usually treated by means of one of the two theories:

1) The Terzaghi-Rendulic uncoupled theory in which consolidation is assumed to take place without changes in total stress.

2) Biot's coupled consolidation theory in which the full interaction between soil skeleton and pore pressure is introduced.

One significant feature of the coupling between pore pressure and total stress changes is the Mandel-Cryer effect (Mandel, 1953; Cryer, 1963). This

effect causes for some cases an increase in pore pressure in the early stages of consolidation. This has been observed experimentally in the consolidation of a spherical sample of clay (Gibson et al., 1963). However, this effect decreases when the permeability of the loaded area decreases or when the drained Poisson's ratio of the material is greater. Sills (1975) shows that under certain conditions both theories lead to the same governing equations. Viggiani (1970) and Davies & Poulos (1970) show that in a wide range of practical problems, the Terzaghi-Rendulic theory predicts fairly well the dissipation-time relationship with the exception of the Mandel-Cryer effect. This effect is generally limited to the early stages of the consolidation process and is not significant at later times. Levadoux & Baligh (1980) have studied the dissipation around the cone using both the coupled and the uncoupled theories by a finite element formulation. The solutions from these analyses give quite similar results except at the cone tip where the Mandel-Cryer effect is observed.

In this thesis, the Terzaghi-Rendulic uncoupled theory has been chosen as the basis of dissipation analysis. The governing equation based on this theory is amenable to solution by the finite difference method, which is not true for Biot's coupled theory. Since the numerical schemes used in the evaluation of stresses and pore pressure are formulated in finite difference forms, this provides the desired continuity in the overall numerical approach and avoids undue interpolations. The same mesh which has been used in the determination of the stresses and strains can thus be utilised for dissipation analysis.

9.3 Mathematical Formulation

For an axisymmetric problem, the Terzaghi-Rendulic three dimensional consolidation equation is given by:

$$\frac{\partial \bar{u}}{\partial \bar{t}} = \bar{c}\left(\frac{\partial^2 \bar{u}}{\partial \bar{r}^2} + \frac{1}{\bar{r}}\frac{\partial \bar{u}}{\partial \bar{r}} + \frac{\partial^2 \bar{u}}{\partial \bar{z}^2}\right) \tag{9.1}$$

The bar denotes dimensioned quantities. In the derivation of equation (9.1), it is assumed that the soil is elastic, isotropic and homogeneous with a constant coefficient of consolidation, $\bar{c}$. By expressing the various quantities in normalised forms, equation (9.1) can be transformed into a dimensionless equation:

$$\frac{\partial U}{\partial T} = \frac{\partial^2 U}{\partial r^2} + \frac{1}{r}\frac{\partial U}{\partial r} + \frac{\partial^2 U}{\partial z^2} \tag{9.2}$$

where:

$$T = \frac{\bar{c}\,\bar{t}}{\bar{R}^2} \tag{9.3}$$

$$U = \frac{\bar{u}}{\bar{c}_u} \tag{9.4}$$

$$(r, z) = (\bar{r}, \bar{z})/\bar{R} \tag{9.5}$$

and $\bar{R}$ is the cone radius and $\bar{c}_u$ is the undrained shear strength. Equation (9.2) is a parabolic equation and can be solved for the value of U at any time T provided that:

(i) the values of U at all points are known at T=0, and

(ii) the values or the gradients of U at the boundaries are known for all T.

Equation (9.2) can be expressed in finite difference form using several approaches. One obvious possibility is to use an explicit method in which the time derivative is expressed in forward differences and the spatial derivatives are computed using central differences:

$$\frac{U_{i,j}^{k+1} - U_{i,j}^{k}}{\Delta T} = \delta_r^2(U_{i,j}^{k}) + \frac{1}{r}\delta_r(U_{i,j}^{k}) + \delta_z^2(U_{i,j}^{k}) \qquad (9.6)$$

where δ_r, δ_r^2 and δ_z^2 represent the central finite difference operators for $\frac{\partial}{\partial r}$, $\frac{\partial}{\partial^2 r}$ and $\frac{\partial}{\partial^2 z}$ respectively and $U_{i,j}^{k}$ is the pore pressure for node (i,j) at the k^{th} time level. Equation (9.6) can be rearranged to give an explicit expression of U at $(k+1)^{th}$ time level. The stability of this straightforward finite difference scheme is constrained by the requirement of a very small time step size and is generally not practicable.

Alternatively, the consolidation equation can be expressed using a general weighted implicit finite difference method giving:

$$\frac{U_{i,j}^{k+1} - U_{i,j}^{k}}{\Delta T} = \lambda\left[\delta_r^2 U_{i,j}^{k+1} + \frac{1}{r}\delta_r U_{i,j}^{k+1} + \delta_z^2 U_{i,j}^{k+1}\right]$$

$$+ (1-\lambda)\left[\delta_r^2 U_{i,j}^{k} + \frac{1}{r}\delta_r U_{i,j}^{k} + \delta_z^2 U_{i,j}^{k}\right] \qquad (9.7)$$

where: $$0 \leq \lambda \leq 1 \qquad (9.8)$$

Note that equation (9.6) is recovered when λ is set to zero in equation (9.7), and λ=1 gives a purely implicit scheme. If λ=1/2, equation (9.7) is known as the Crank-Nicholson formula. When this equation is applied to each node, a system of n simultaneous equations is obtained for the n unknown u^{k+1} at the nodes. These must be solved at each time increment. When n is very large, this implicit scheme is not viable due to the excessive amount of computing required.

It is desirable that the finite difference scheme selected should be unconditionally stable while at the same time avoids excessive computations. One such scheme is the Alternating-Direction-Implicit (A.D.I.) procedure

first suggested by Douglas (1951). The main feature of this method is a re-formulation of the implicit finite difference equation so that the matrix of simultaneous equations is tridiagonal. This is achieved by splitting a time step into two equal sub-increments. The derivatives in one co-ordinate direction are expressed using the Crank-Nicolson's implicit formula and the derivatives in the other direction is expressed using explicit finite differences:

$$\frac{U_{i,j}^{k+0.5} - U_{i,j}^{k}}{\Delta T/2} = \frac{1}{2}\delta_r^2(U_{i,j}^{k+0.5} + U_{i,j}^{k}) + \frac{1}{2r}\delta_r(U_{i,j}^{k+0.5} + U_{i,j}^{k}) + \delta_z^2 U_{i,j}^{k} \qquad (9.9)$$

For the second sub-increment, the forms of expressions for the spatial derivatives are switched and the finite difference equation is given by:

$$\frac{U_{i,j}^{k+1} - U_{i,j}^{k}}{\Delta T/2} = \delta_r^2 U_{i,j}^{k+0.5} + \frac{1}{r}\delta_r U_{i,j}^{k+0.5} + \frac{1}{2}\delta_z^2(U_{i,j}^{k+1} + U_{i,j}^{k+0.5}) \qquad (9.10)$$

Equations (9.9) and (9.10) when applied to each of the nodal points results in two tridiagonal systems which can be solved efficiently. It should be noted that only the solutions after a double sweep are of any significance because of the inherent bias in the solution after the first sub-increment.

The A.D.I. formulation is unconditionally stable and therefore provides extra flexibility in the choice of the time step size for optimising the solution procedure. At the beginning of the solution process, the high pore pressure gradients that exist near the cone make it necessary to use a very small time step so that the required degree of accuracy and resolution in the dissipation curve can be achieved. As dissipation continues, the pressure gradient becomes progressively more gentle so the time step size, ΔT, can be increased. The use of a variable ΔT helps to reduce the amount of calculation steps without unduly affecting the quality of the solution.

9.4 Boundary Conditions

The solution of the parabolic consolidation equation requires the boundary conditions to be specified for all time, T. The boundary conditions which are relevant to the dissipation analysis are considered in this section.

The bottom boundary has been chosen to be located sufficiently far away from the cone for the pore pressure effects to be negligible. The choice of the boundary condition here is not critical and the pore pressure can be assumed to be zero at all time, T. The same also applies to the far field boundary. The variation of pore pressure at the top boundary is essentially in the radial direction and the pore water movement is primarily in the same direction. Thus, it is appropriate to specify this as an impervious boundary. The shaft of the penetrometer is assumed to be impermeable and on the axis, symmetry condition requires that $\frac{\partial U}{\partial r} = 0$.

The cone face boundary was given special consideration because pore pressure measurement is usually taken around this region in most penetrometer design. Due to the high pore pressure gradients that exist here, any relaxation in the boundary conditions will have a significant effect on the computed dissipation curve. Therefore, a tight boundary condition which requires that the flow of water across the boundary is zero has been prescribed. By Darcy's law, this condition can be expressed as:

$$\int \frac{\partial U}{\partial \underset{\sim}{\mathbf{n}}} \, dS = 0 \qquad (9.12)$$

where dS is the infinitesimal length along the boundary and $\underset{\sim}{\mathbf{n}}$ is a unit vector normal to the cone face.

9.5 Factors Affecting Pore Pressure Dissipation

The rate of dissipation of excess pore water pressure in soil is influenced by a number of factors. For a soil with a constant coefficient of consolidation, it is primarily governed by the pore pressure gradients. This is in turn affected by the initial pore pressure distribution and the boundary conditions associated with a particular problem.

Levadoux & Baligh (1980) have carried out a series of parametric studies on a one-dimensional consolidation problem. The factors governing the rate of dissipation on a pile are investigated using a combination of pressure distributions and boundary conditions. These studies show that provided the drainage boundary is located beyond the zone of soil initially affected by excess pore pressure, it has negligible influence on the dissipation rate. The consolidation process is thus entirely determined by soil properties within the zone subjected to excess pore pressures.

In a realistic dissipation analysis, it is necessary to obtain an accurate estimate of the initial pressure distribution around the penetometer. Consolidation analyses based on arbitrary pore pressure distributions (Jones & Van Zyl, 1982; Tortensson, 1977) are of limited practical application because the assumed distribution is different from the actual condition that exists around the penetrometer. In this thesis, the pore pressures derived from the strain path method have been used for the dissipation analysis. The reliability of the computed result is verified by comparing with published experimental results.

9.6 Initial Pore Pressure Distribution

The mechanism of pore water pressure generation in soil is a complicated process which depends on the interaction between effective stress behaviour of the soil and the equilibrium equations. Skempton (1954) introduced an approximate expression which relates the excess pore pressure in a triaxial compression test to changes in the principal stresses:

$$\Delta u = B[\Delta\sigma_3 + A(\Delta\sigma_1 - \Delta\sigma_3)] \tag{9.13}$$

where A and B are pore pressure parameters. For a fully saturated soil, the parameter B is taken as unity and A is essentially a ratio of the change in pore pressure to change in the deviatoric stresses:

$$A = \frac{\Delta u - \Delta\sigma_3}{\Delta\sigma_1 - \Delta\sigma_3} \tag{9.14}$$

This equation is later refined by Henkel (1960) who proposed an equation of the form:

$$\Delta u = \Delta\sigma_{oct} + \alpha_f \Delta\tau_{oct} \tag{9.15}$$

where: $\Delta\sigma_{oct}$ = change in octahedral mean normal stress (9.16)

$\Delta\tau_{oct}$ = change in octahedral shear stress (9.17)

At failure, the parameter α_f is related to the Skempton's pore pressure parameter A_f by:

$$\alpha_f = \frac{1}{\sqrt{2}}(3A_f - 1) \tag{9.18}$$

Thus given the stress path of the soil specimen, the pore pressure in the plastic zone can be estimated if either A_f or α_f is known.

Based on the critical state concept, Wroth (1984) demonstrated that the excess pore pressure generated in undrained triaxial compression is dependent on the total stress path. This is illustrated in Figure 9.1. For a given soil subjected to two different total stress paths, different values of Δu are obtained. This shows that the excess pore pressure, Δu, is not a unique measure of soil behaviour. Wroth suggests that Δu is made up of two components, one of which (CD or CE) merely reflects the change in the mean normal pressure during the test. The other component, BC, is a property of the soil and can be correlated with other soil parameters.

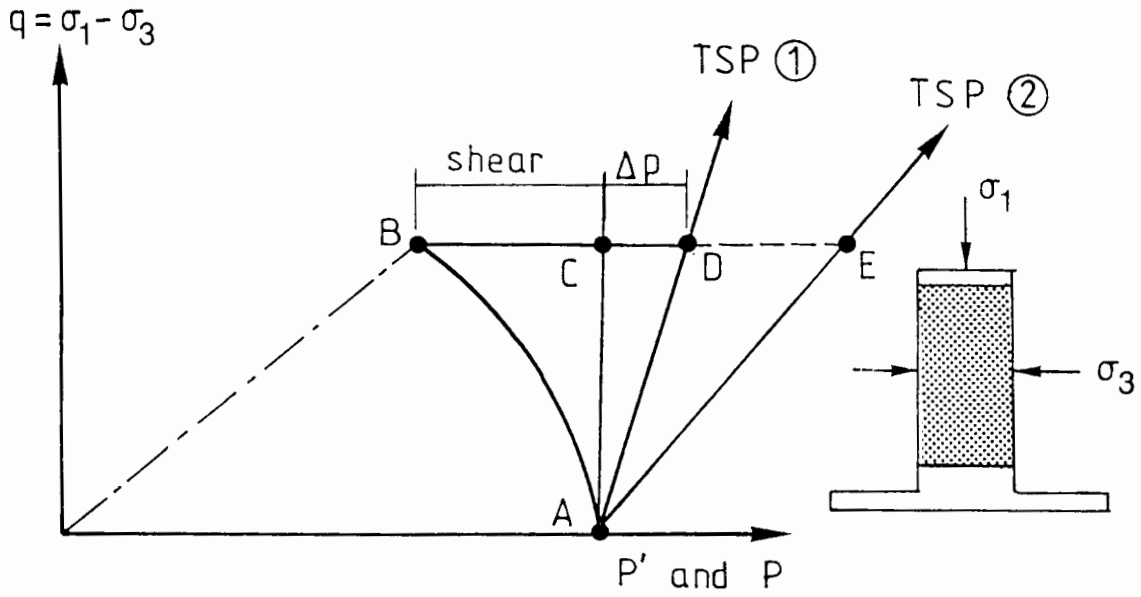

Figure 9.1: Interpretation of Excess Pore Pressure Observed in Undrained Triaxial Compression Tests (after Wroth, 1984)

This theoretical argument is reflected in Henkel's empirical pore pressure equation which, as well as identifying the component due to the change in mean pressure, suggests that the shear induced pore pressure component is a function of the change in octahedral shear stress. In view of the lack of any comprehensive pore pressure model, this empirical equation

has been used for evaluating the excess pore pressure due to cone penetration.

9.7 Pore Pressure Dissipation around a Cone Penetrometer

The contours of excess pore pressure computed using equation (9.15) with α_f equal to 1.0 is shown in Figure 9.2. This result was obtained for a soil with an I_r of 100, subjected to an isotropic initial stress state. It is observed that the pore pressure gradients at the tip of the penetrometer are extremely high. Maximum excess pore pressure is found on the cone face region just below the shoulder. Above the cone shoulder, the pore pressure drops off rapidly to a value of about $5.0c_u$. This value is slightly smaller than that predicted by the cylindrical expansion theory.

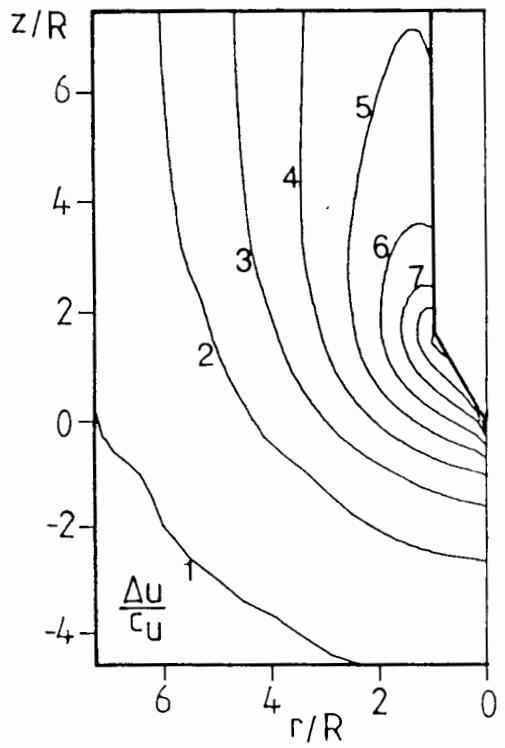

Figure 9.2: Excess Pore Pressure Distribution due to Cone Penetration

In order to ensure a meaningful dissipation analysis, the reliability of the predicted pore pressure distribution must be established by comparing with that determined experimentally. However, it is extremely difficult to measure the pore pressure in the soil accurately (Baligh & Levadoux, 1980). As a result, published data are rare. A good record of the pore pressure generated in the soil during deep penetration was obtained by Roy et al. (1981) who conducted a comprehensive in-situ pile test programme in the St. Alban clay. Prior to the pile tests, piezometers were installed at various radial distances from the intended axis of penetration and at various depths in the ground. The excess pore pressures generated during the installation of these piezometers were allowed to dissipate. Due to the large pile to piezometer diameter ratio, the piezometers are believed to provide a reliable measurement of the actual Δu generated in the soil during pile penetration.

The variations of $\frac{\Delta u}{\sigma'_p}$ with radial distance obtained from these tests are shown in Figure 9.3, where σ'_p is the maximum effective pre-consolidation

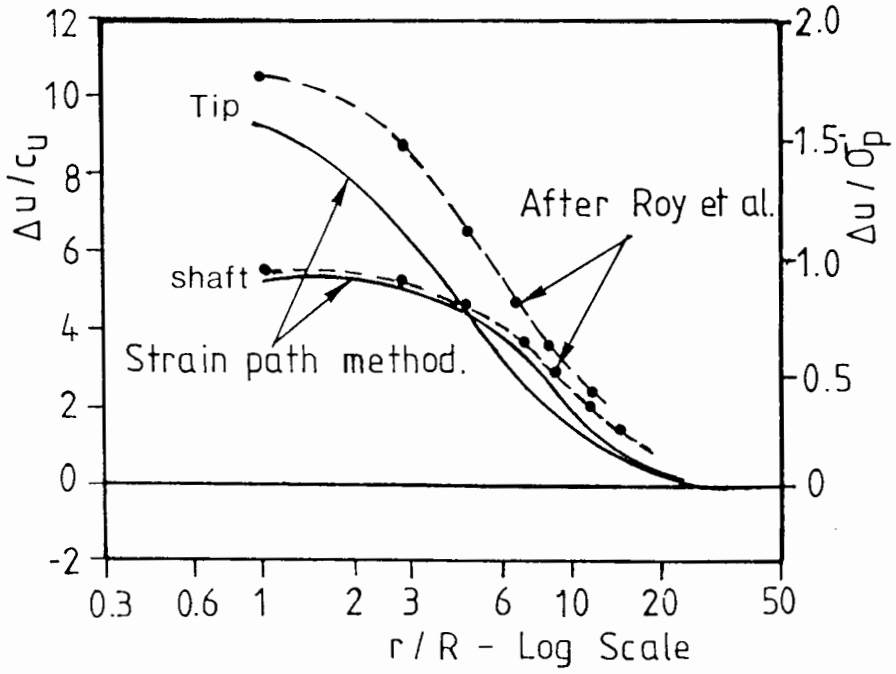

Figure 9.3: Variation of Excess Pore Pressure due to Deep Penetration

stress of the soil. The solid lines represent $\frac{\Delta u}{c_u}$ evaluated from strain path method for a rigidity index of 300, a value quoted by Roy et al. Excellent agreement was obtained for the measured and computed Δu around the shaft far from the pile tip. There is also a general agreement in the trend of variation even at the tip level, although the shape of the pile tip (flat-ended) is significantly different from a cone.

The change in the pore pressure measured by the piezometers during pile penetration is shown in Figure 9.4. The variation of the computed Δu along vertical grid lines, located at various radial distances from the cone axis, are shown in Figure 9.5. This latter plot is equivalent to an inverted version of Figure 9.4. The computed results are found to have captured the essential features of pore pressure changes in the soil due to pile penetration even though no direct quantitative comparison can be made. The major difference between the numerical result and the test data is the negative pore pressure measured before the pile tip reaches the piezometer level. Baligh (1980) suggests that this observed behaviour is probably caused by the soil-piezometer interaction as the soil is displaced by the pile.

These comparisons show that the normalised Δu distribution computed by the strain path method is capable of giving a reasonable estimate of the pore pressure surrounding a penetrometer. Therefore, a dissipation analysis based on this initial pore pressure regime can be expected to give a good approximation of the actual dissipation process.

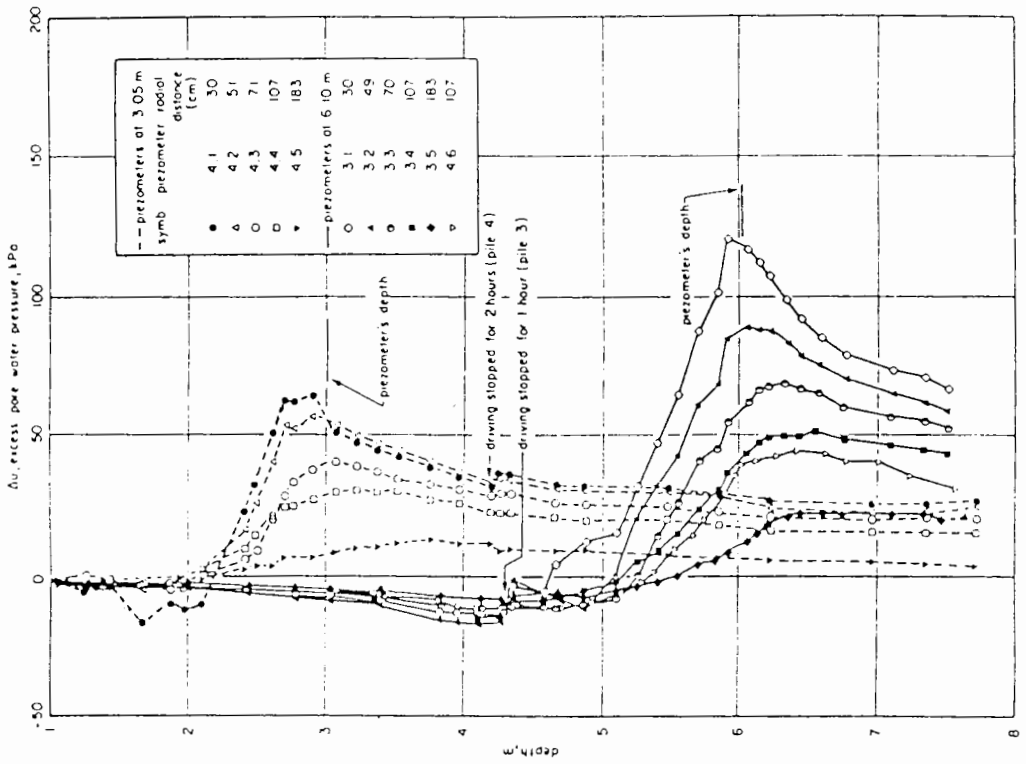

Figure 9.4: Excess Pore Pressure during Pile Penetration (after Roy et al., 1981)

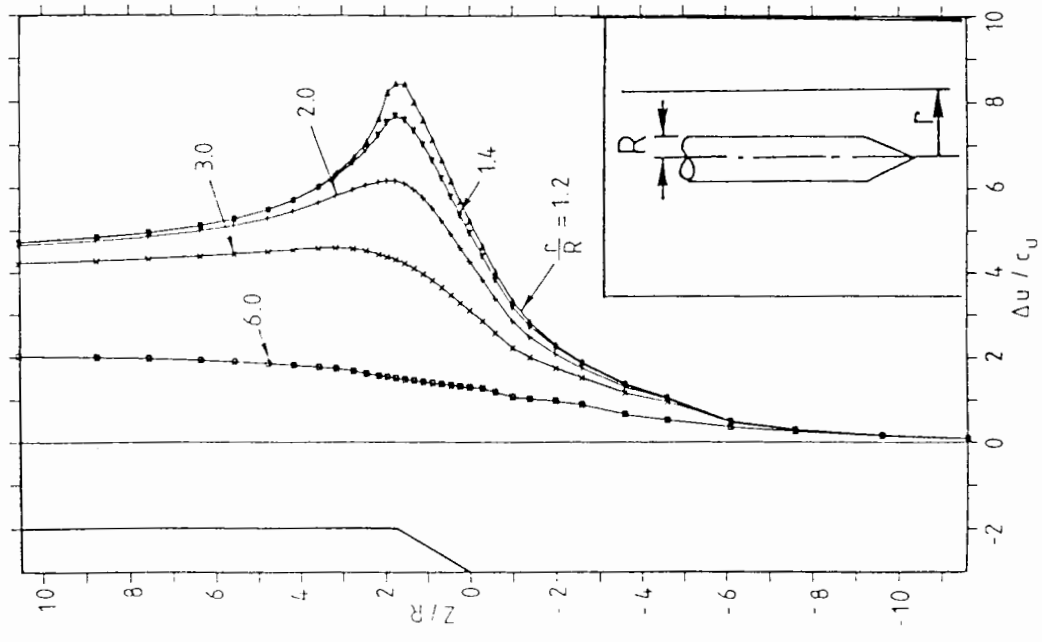

Figure 9.5: Variation of Excess Pore Pressure along Vertical Grid Lines

9.8 Results of Dissipation Analysis

A series of dissipation analyses using an A.D.I. formulation of the Terzaghi-Rendulic consolidation theory has been carried out. The soil was assumed to be subjected to zero initial stresses and has a rigidity index of 100. The excess pore pressure distributions at various stages of the dissipation process are shown in Figure 9.6. The excess pore pressure, Δu, at the cone face dissipates very rapidly. At T=1.0, Δu on the cone face has dropped by more than 50% and the zone of maximum Δu has moved to a point just above the shoulder. As dissipation continues, this zone is found to recede further up the shaft.

The dissipation process as measured by the penetrometer is most conveniently expressed as a pore pressure-time relationship. The dissipation curves monitored at six locations along the probe are shown in Figure 9.7. The normalised excess pore pressure, $\frac{\Delta u}{\Delta u_i}$, is plotted against the logarithm of T, where Δu_i is the initial pore pressure measured at each location. The rapid rates of dissipation at locations 1, 2 and 3 are apparent in this plot. The shape of the curve for location 1 is distinctly different from those measured at the other locations. This could be due to the unique location of the tip which allows dissipation to take place three dimensionally. The extremely high pressure gradient around the tip may also be a contributory factor.

Along the shaft, no significant dissipation is observed for T less than 0.5. In fact, a slight increase in pore pressure is detectable at the initial stages. This is due to the flow of water from the cone face region to the soil adjacent to the shaft, induced by the high pressure gradient that exists between these two locations.

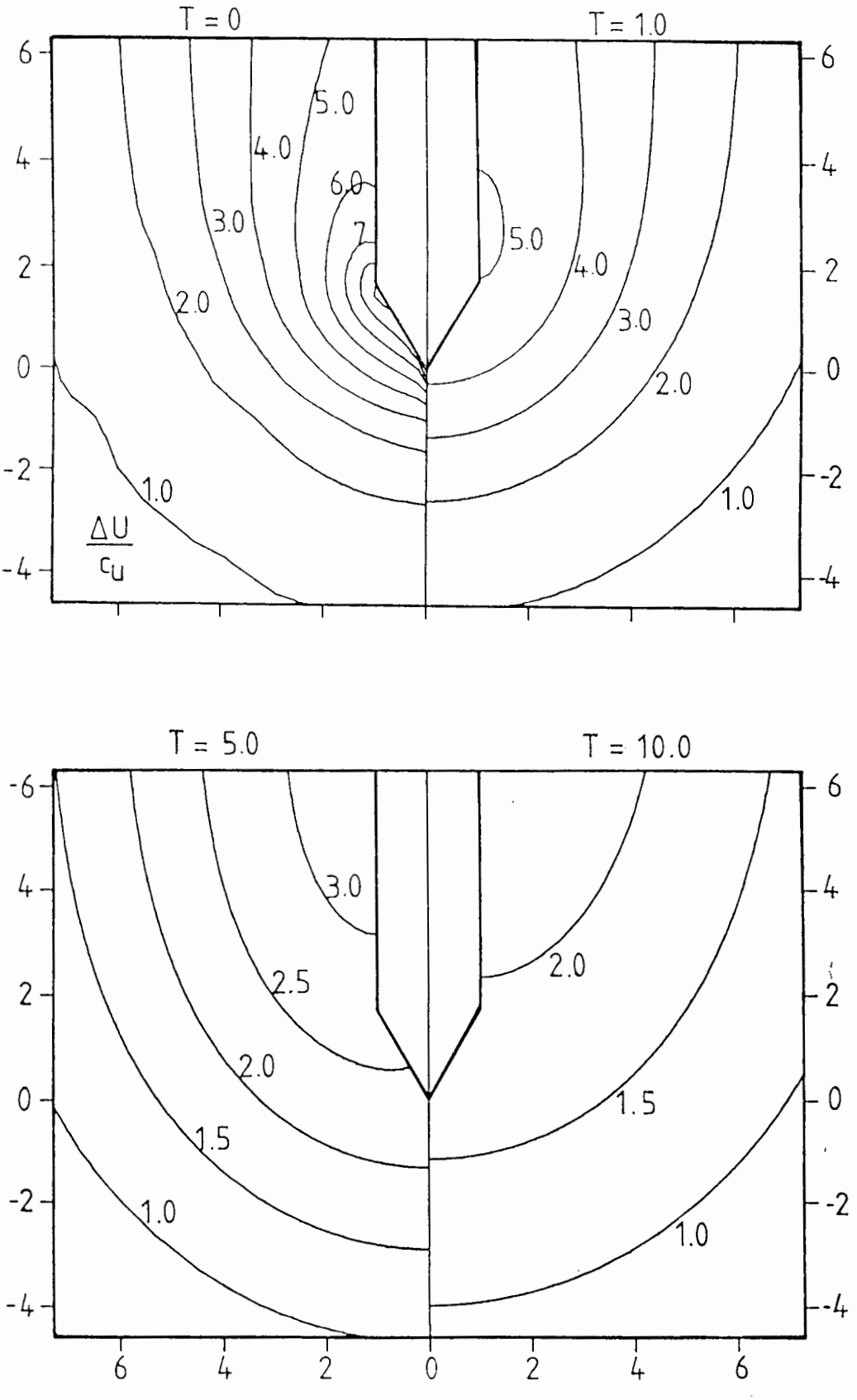

Figure 9.6: Pore Pressure Contours at Different Stages of Dissipation

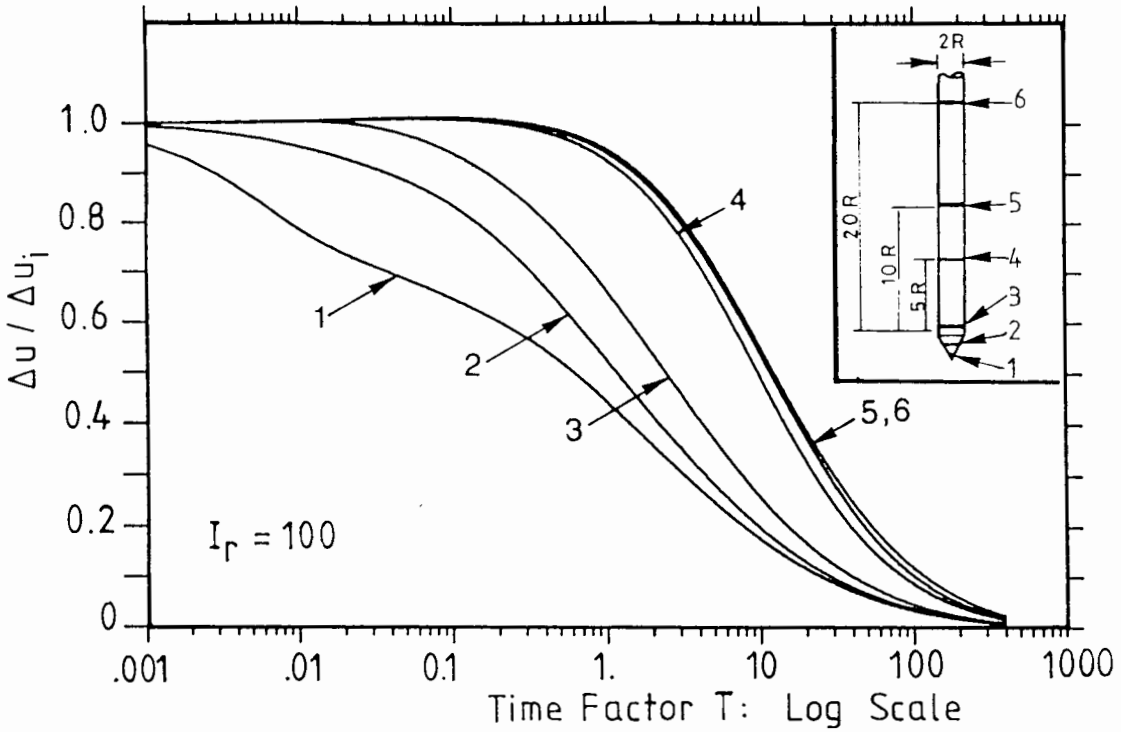

Figure 9.7: Dissipation Curves at Different Locations on a 60° Cone Penetrometer (I_r=100)

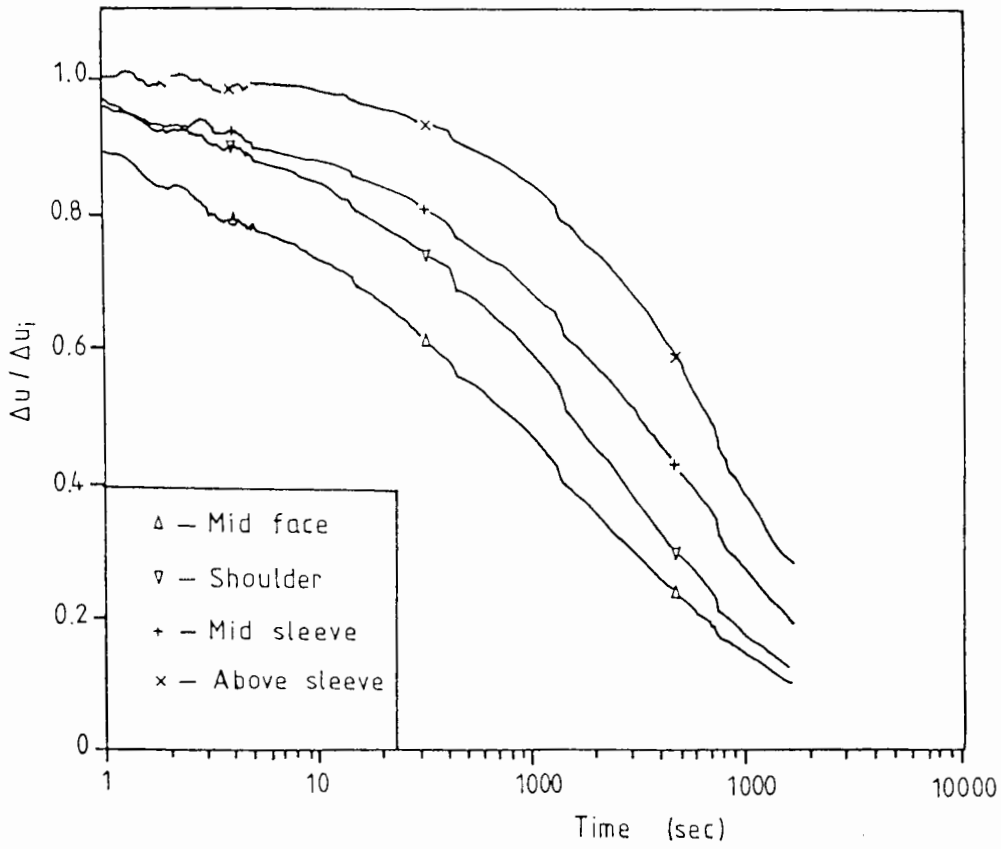

Figure 9.8: Dissipation Data in Re-constituted Kaolin (after May, 1987)

The experimental result obtained by May (1987) in re-constituted kaolin in a large calibration chamber is shown in Figure 9.8. The curves were obtained at four locations on the probe which correspond roughly to positions 2 to 5 in Figure 9.7. It is observed that the predicted dissipation curves broadly exhibit the same trend of variation as the experimental results. However, the difference in the rate of dissipation between positions 4 and 5 from the chamber test is greater than that evaluated numerically.

9.8.1 Effect of Anisotropic Consolidation Characteristics

The coefficient of consolidation has been assumed to be the same in all directions in the previous analysis. In a natural clay deposit, the consolidation coefficient in the horizontal direction is very often higher than that in the vertical direction. This anisotropy in the consolidation coefficients may have significant implications for the interpretation of experimental dissipation records.

The effect of anisotropy in consolidation characteristics on the rate of dissipation is investigated in this section. A c_v value which is equal to $0.1c_h$ has been chosen for the study. The initial excess pore pressure distribution is based on the same soil properties as in the previous analysis. The contours of Δu at different time, T, was shown in Figure 9.9. The dimensionless time factor, T, is defined in terms of c_h.

On comparing Figure 9.9 with Figure 9.7, it is observed that reducing c_v slows down the rate of dissipation on the cone face. This is clearly illustrated by the contour for $\frac{\Delta u}{\sigma_{iu}} = 0.5$. The impact of a smaller c_v on the dissipation rate measured on the shaft is less significant and the effect is not apparent until towards the end of the consolidation process.

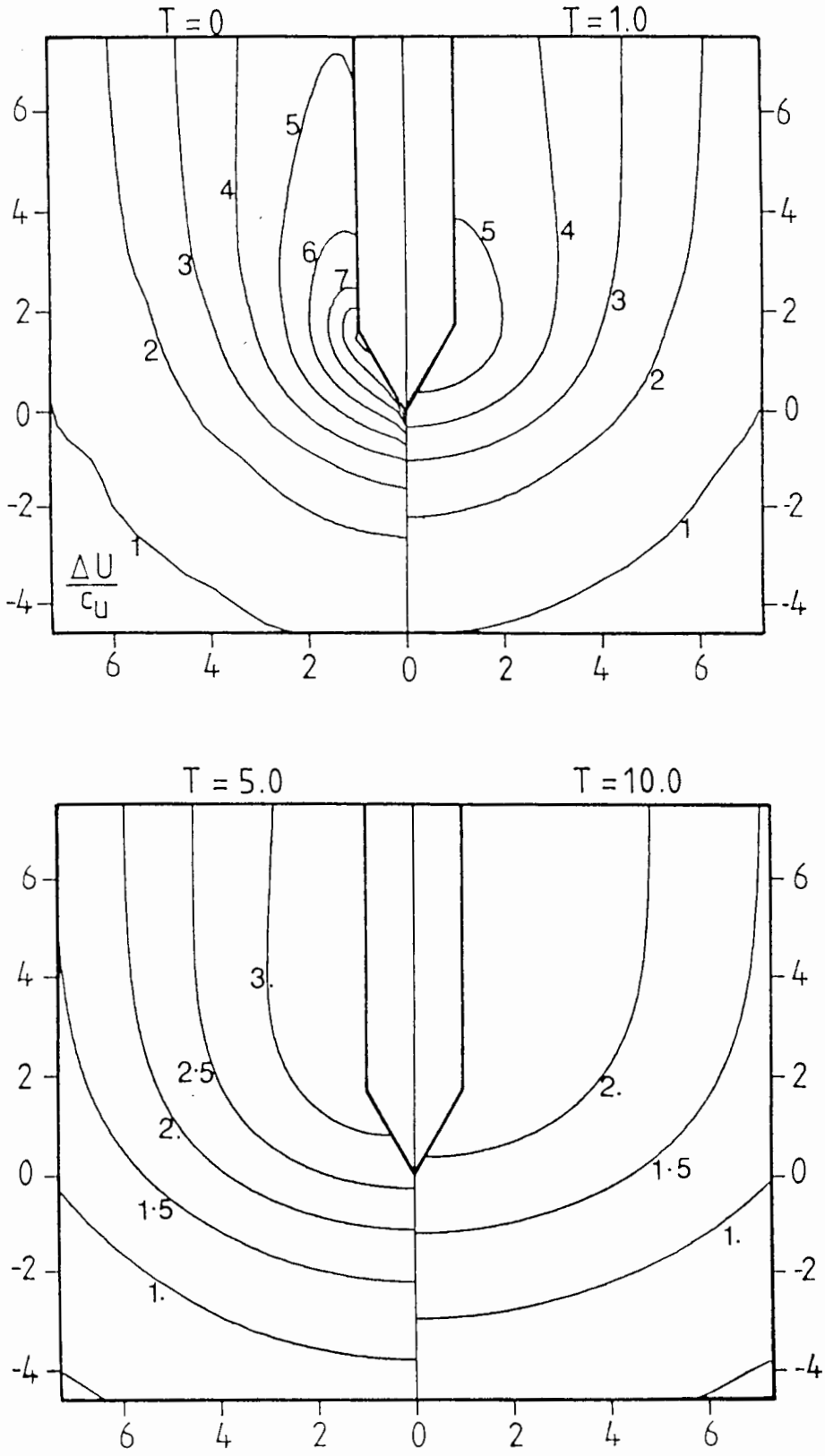

Figure 9.9: Contours of Δu at Different Stages of Dissipation ($c_v = 0.1c_h$)

The dissipation curves at six locations along the probe are plotted in Figure 9.10. For comparisons, the results for the isotropic case are superimposed on the same figure as dotted lines. It is observed that the rate of dissipation at a point slightly above the shoulder is speeded up at the initial stages. This apparently anomalous response can be readily explained by a careful examination of the pressure distribution at various stages of dissipation. Initially, the pore pressure in the region beneath the cone shoulder is very much higher than that which exists around the shaft. In a perfectly isotropic soil (i.e. $c_v=c_h$), the higher pressure gradient induces the pore fluid to flow from the cone face region towards the shaft, thus effectively delaying the dissipation process at the latter location. At larger T, the flow direction is reversed as the pore pressure Δu at the cone face drops below that adjacent to the shaft. When c_v is

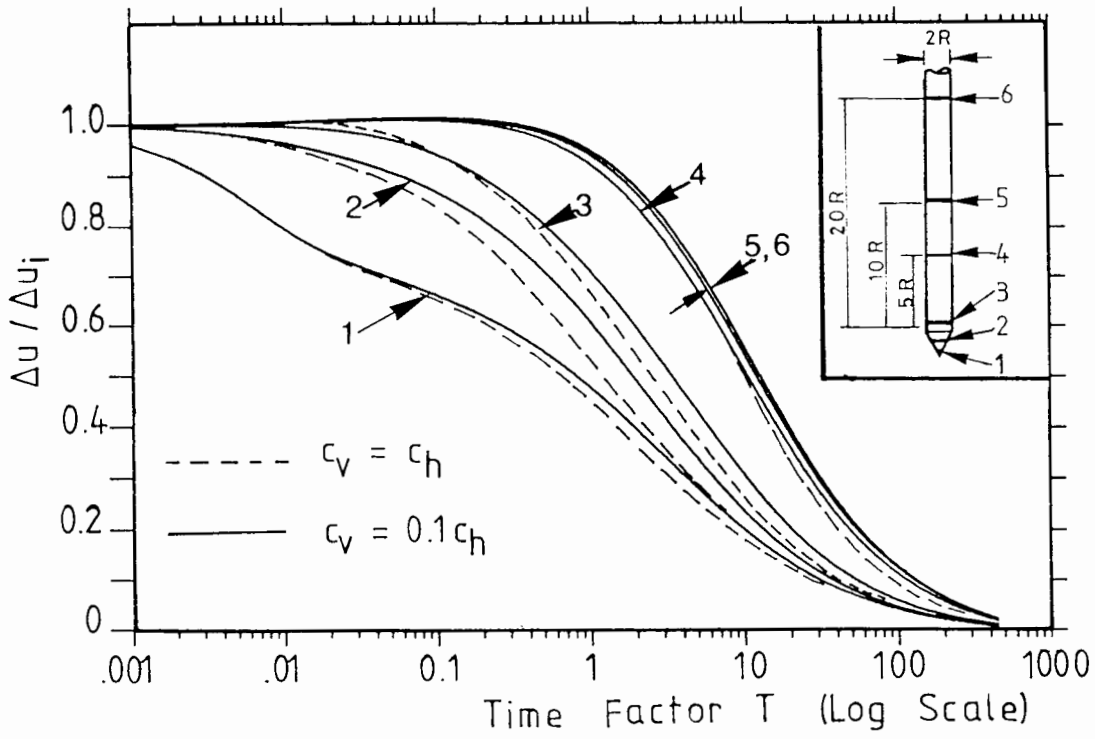

Figure 9.10: Effect of Anisotropic Consolidation Characteristics on the Rates of Dissipation

reduced, the movement of water in the vertical direction is impeded. Therefore, the net effect of a smaller c_v is to increase the rate of dissipation at a point just above the cone shoulder at the initial stages, and to reduce it towards the end of the dissipation process.

For positions 1 and 2, the smaller c_v causes an overall reduction in the dissipation rates as the flow in the axial direction is impeded. Far behind the tip, the initial Δu distribution dictates that dissipation takes place mainly in the radial direction. Thus, changes in c_v have very little impact on the rate of dissipation monitored at these locations at the initial stages. However, a hydraulic gradient gradually builds up in the axial direction as T increases. Reducing c_v again slows down the water movement in this direction and hence reduces the dissipation rate at later times.

In summary, it may be stated that the dissipation process around the conical tip is two-dimensional in nature, so the rate of dissipation is sensitive to changes in both c_v and c_h. However, the effect of c_v is relatively small and dissipation is primarily controlled by c_h. This is indicated by the small changes in the dissipation curves for the two cases studied when T is defined in terms of c_h. If alternatively c_v is used for the normalisation, significant differences are apparent.

9.8.2 Effect of I_r on the Rate of Dissipation

The magnitude of the excess pore pressure and the zone of yielded soil due to cone penetration will generally vary with I_r. As I_r increases, the extent of the failure zone as well as the magnitude of Δu both increase. For the constitutive model adopted, the failure zone also represents the extent of soil subjected to excess pore pressure. These changes in pore pressure distribution will in turn affect the rate of dissipation. Therefore, the

dissipation curves evaluated for an I_r of 100 (Figure 9.8) are not unique. This is apparent from the results evaluated for a soil with an I_r of 500 (Figure 9.11) which show that the time T taken to reached a given degree of dissipation has increased quite significantly. The shift in the dissipation curves due to changes in I_r can be attributed partially to the choice of R as a normalising quantity for T.

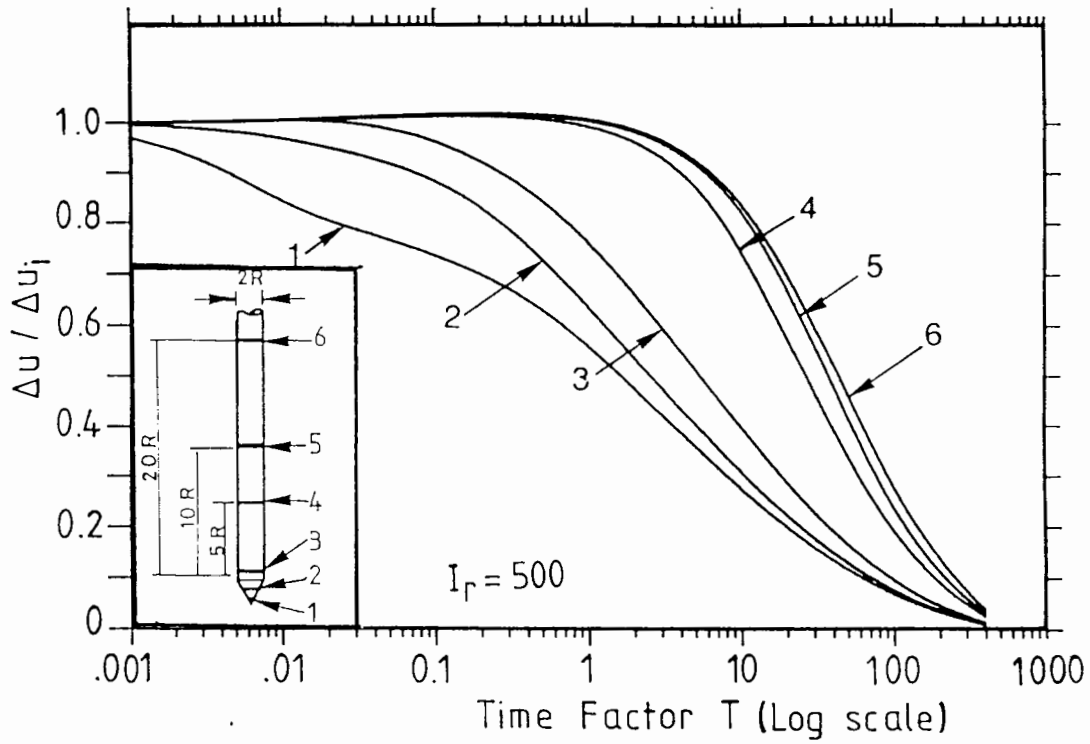

Figure 9.11: Dissipation Curves at Different Locations of a 60° Cone Penetrometer (I_r=500)

For a conventional consolidation test conducted in an oedometer, the length of the longest drainage path is used as the characteristic dimension in the definition of T. If this philosophy is adopted in the cone penetrometer problem, the time factor ought to be normalised by a parameter which characterised the zone of soil subjected to excess pore pressure. One such parameter is the plastic radius, R_p, as defined in Chapter 6. It has

been shown that a good estimate of R_p can be obtained from the cylindrical cavity expansion theory which gives $\frac{R_p}{R}$ equal to $\sqrt{I_r}$ approximately. Adopting R_p as the normalising quantity gives:

$$T = \frac{c_h t}{I_r R^2} \tag{9.21}$$

However, unlike an oedometer test, the contour for $\Delta u=0$ does not stay stationary during the entire dissipation process. In addition, the effect of the changes in the magnitude and gradient of the excess pore pressure due to different I_r has not been adequately accounted for in the defintion of T as expressed in equation (9.21). Increasing I_r increases both R_p and the excess pore pressure, Δu, which have opposing effects on the dissipation rate. Equation (9.21) would only be adequate if the pore pressure distribution normalised with respect to R_p was the same for different values of I_r. Unfortunately, this is not the case and the normalisation as expressed in equation (9.21) remains unsatisfactory.

In an attempt to account for the effect of I_r on the dissipation curves, a new time factor, T^* was defined:

$$T^* = \frac{c_h t}{(I_r)^n R^2} \tag{9.22}$$

where: $0 \leq n \leq 1$

Note that when n=0, the conventional definition of T is obtained and when n=1, equation (9.21) is recovered.

It has been found that a good normalisation of the dissipation curves for different I_r values can be achieved when n is set to $\frac{1}{2}$ in equation

(9.22). The dissipation data at four locations on the probe have been plotted against the logarithm of T^* (with $n=\frac{1}{2}$) in Figure 9.12. The trace in each plot consists of 7 curves with I_r ranging from 25 to 500. Except for an I_r value of 25, all the curves are found to lie within a very narrow band, especially for the piezometric element half way up the cone or at the cone shoulder. One possible explanation for the scatter at an I_r of 25 is the different dissipation pattern that exists around the cone for soil with such a low rigidity index.

The dissipation results have also been plotted against the square root of T^* in Figure 9.13. The dimensionless time factor is again defined with n equal to $\frac{1}{2}$. The scatter in the dissipation curves is found to be minimal. and a linear response is evident in the initial stages. The gradient of this initial tangent is useful for making an estimate of c_h from short dissipation records, as will be illustrated in a later section.

9.8.3 Interpretation of Dissipation Data from CPT

Two methods for deriving the consolidation coefficients from dissipation test data are suggested. These are based on the theoretical dissipation curves presented in the previous section and only differ in the scale chosen for T^*.

(A) Log-time Plot:

This technique is based on a curve matching principle. The test data are presented as a plot of $\frac{\Delta u}{\Delta u_i}$ against the logarithm of time, t. In order to obtain an estimate of the consolidation coefficient, the time taken to reach a certain degree of dissipation is matched with the corresponding theoretical time factor, T^*. It has been demonstrated that the rate of dissipation as measured by a piezocone is controlled mainly by the horizontal

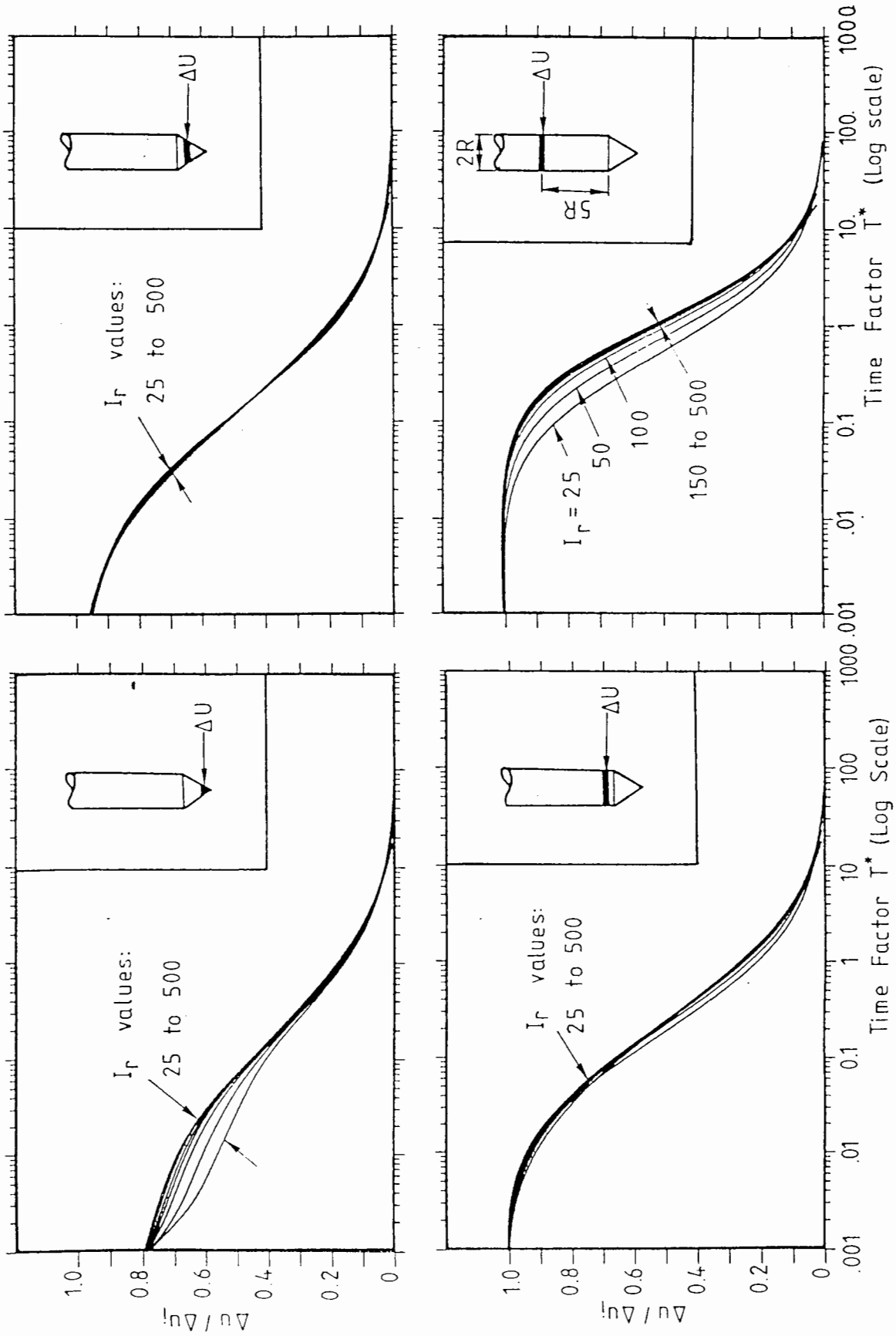

Figure 9.12: Normalised Dissipation Curves - Log-time Plot ($T^* = \frac{c_h t}{\sqrt{I_r} R^2}$)

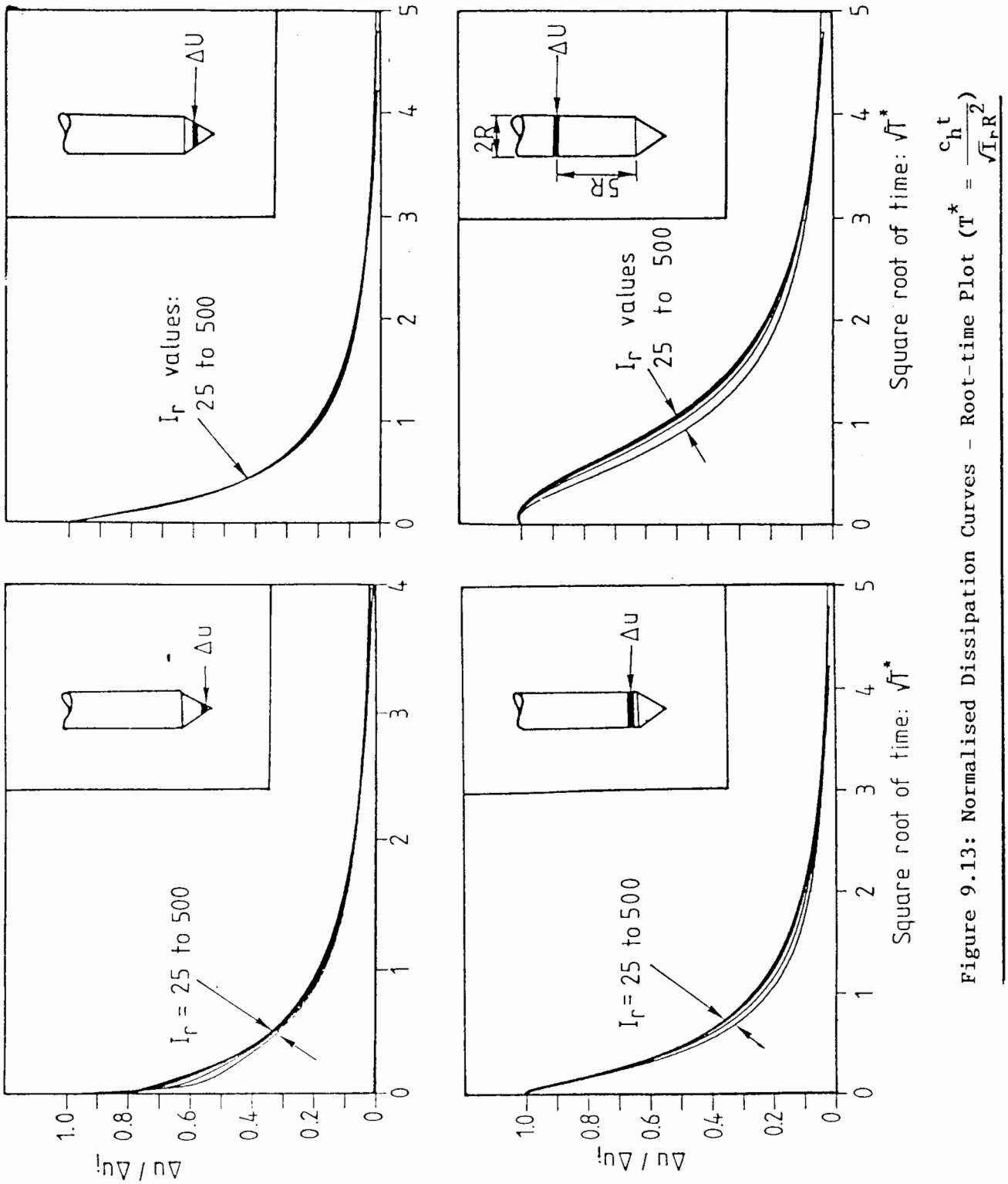

Figure 9.13: Normalised Dissipation Curves - Root-time Plot ($T^* = \frac{c_h t}{\sqrt{I_r R^2}}$)

consolidation coefficient. Hence, the value obtained from the test is a measure of c_h.

For example, if the time taken for 50% dissipation is t_{50}, then c_h can be evaluated from the equation:

$$c_h = \frac{T_{50}^* \; I_r^{1/2} \; R^2}{t_{50}} \tag{9.23}$$

Where R is the radius of the cone penetrometer and I_r is the rigidity index of soil. T_{50}^* can be extracted from Table 9.1 for the relevant location along the probe.

$\frac{\Delta u}{\Delta u_i}$ (in %)	Tip	Mid-face	Shoulder	Distance above Cone Shoulder	
				5R	10R
20.0	0.001	0.014	0.038	0.294	0.378
25.0	0.002	0.022	0.056	0.378	0.528
30.0	0.006	0.032	0.078	0.503	0.662
40.0	0.027	0.063	0.142	0.756	0.995
50.0	0.069	0.118	0.245	1.109	1.458
60.0	0.154	0.226	0.439	1.646	2.139
70.0	0.345	0.463	0.804	2.430	3.238
75.0	0.530	0.665	1.104	3.235	3.887
80.0	0.829	1.035	1.598	4.103	5.240

Table 9.1: Dimensionless Time Factor, T^*

The consistency of the prediction based on this interpretation technique can be checked by computing the value of $\frac{c_h}{\sqrt{I_r}}$ at various degrees of dissipation. Slight variations in the computed values of this ratio are inevitable partly because of the various idealizations adopted in the theoretical analysis, and partly due to the complexity of real soil behaviour. However, if the $\frac{c_h}{\sqrt{I_r}}$ ratios evaluated at various degrees of dissipation differ significantly, it is possible that the initial pore pressure distribution in the soil is different from that evaluated by the strain path method. In such cases, the recommended interpretion technique described herein would not then be applicable.

(B) Root-time Plot :

In a cone penetration test, it is usually possible to obtain a short dissipation record without incurring substantial extra cost. This can be achieved during the interuption in the penetration process for installing the extension rods. The short dissipation data obtained could provide a very valuable means of making an estimate of c_h. This is accomplished by plotting the test data against the square root of time. The initial dissipation process presented in this form can usually be approximated by a straight line. If the gradient of this linear section is m, then c_h is evaluated from the equation:

$$c_h = \left[\frac{m}{M} \right]^2 I_r^{1/2} R^2 \qquad (9.24)$$

where M is the gradient corresponding to the theoretical curve for the relevant location on the probe. The value of M derived from the numerical analysis is shown in Table 9.2.

	Cone Tip	Cone Face	Cone Shoulder	5R Above Shoulder
Gradient of Dissipation curve	1.30	1.63	1.15	0.62

Table 9.2: Gradient of Dissipation Curves, Root-Time Plot

9.9 Pore Pressure Correction for Cone Resistance

Due to the intrinsic design of the piezocone, the pore water pressure can exert a downward force on the 'exposed' surface area at the base of the cone (Figure 9.14), leading to a smaller measured cone resistance. Since the values of u and q_c in soft clay are often of the same order of magnitude, it is important that the measured q_c is corrected for pore pressure effect.

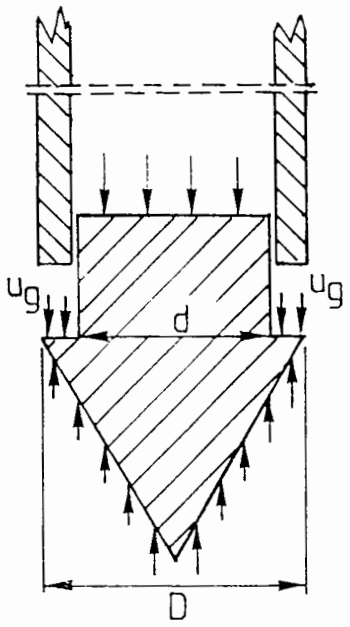

$$a = \left(\frac{d}{D}\right)^2$$

$$q_t = q_c + (1-a)u_g$$

Figure 9.14: Correction of Measured Cone Resistance for Pore Pressure Effect

This is essential if the measured values are to be compared with analytical results or when experimental data from various cone designs are to be correlated.

Referring to Figure 9.14, the total corrected cone resistance, denoted by q_t, is given by:

$$q_t = q_c + (1 - \frac{d^2}{D^2})u_g \qquad (9.25)$$

where u_g is the pore pressure acting at the gap behind the cone shoulder.

In most common penetrometer designs, the pore pressure is very often measured at some locations other than immediately behind the cone shoulder (in the cone design used by Zuidberg et al., for example). Thus, it is necessary to know the variation of pore pressure along the probe if a proper correction is to be made.

The variation of Δu along the penetrometer as computed by the strain path method is shown in Figure 9.15. The pore pressure has been normalised by Δu_{sh}, which is the excess pore pressure measured on the shaft a long way behind the tip. The experimental data obtained by May (1987) in reconstituted kaolin in a large calibration chamber has been plotted in the same figure. It is clear that the general trend of Δu variation along the probe is predicted quite reasonably by the strain path method. The computed results can therefore be used as a calibration curve for pore pressure variation. When the pore pressure at any point along the probe is known, the value of u_g can be scaled from the curve in Figure 9.23. It should be noted the results presented are for $I_r = 100$. The shape of the curve may change for different I_r values.

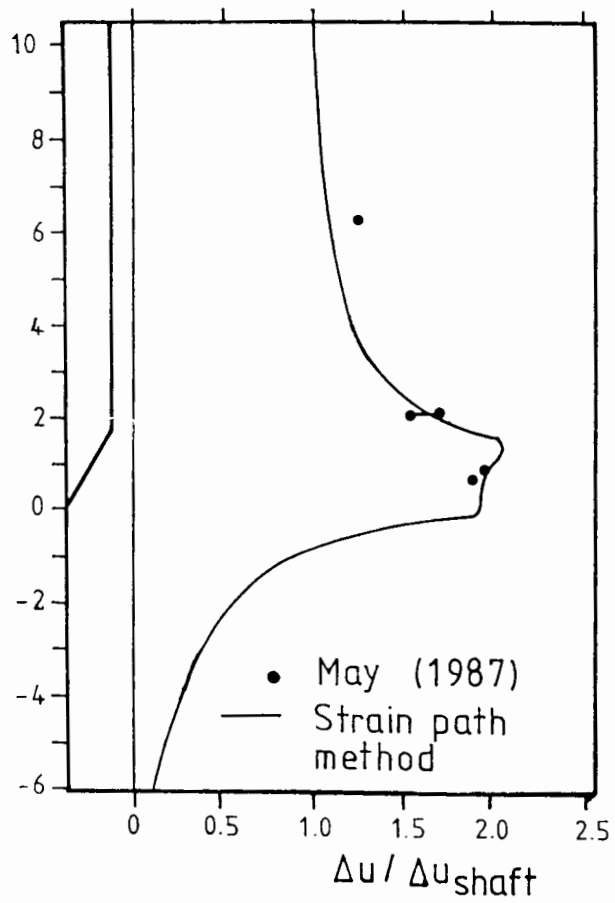

Figure 9.15: Normalised Pore Pressure Variation along a 60° Cone Penetrometer

9.10 Location of the Piezometric Element

In recent years, a standardised piezocone geometry has been widely adopted. In one crucial design aspect, however, much debate is still continuing. This concerns the siting of the piezometric element. Currently, the two most popular locations are at the cone face and just behind the cone shoulder. Various arguments have been put forward both for and against placing the piezometric element at either of these two locations.

The location behind the cone shoulder has been adopted by some workers (Campanella et al., 1982, Tavenas et al., 1982) because it is suggested that

Δu measured here can be used directly for correcting the cone resistance. It has also been reported that the filters located at this position are less susceptible to wear and tear. Wroth (1984), based on a consideration of soil behaviour, suggests that a higher proportion of the Δu measured behind the shoulder is due to shearing of soil, and is therefore more representative of soil behaviour. This consideration is important if the measured Δu is to be used for correlating with soil properties such as OCR. A recent study by Baligh (1986), however, suggests that the proportion of Δu on the shaft due to shearing is small compared to the change in mean normal pressure. Hence, the measured Δu may not be sufficiently sensitive to the changes in OCR.

From a theoretical standpoint, there are considerable difficulties in interpreting the pore pressure measured at the cone shoulder. Significant stress and strain reversals are observed in this region. Stress relaxation in the soil around this region also make it extremely difficult to provide a rational interpretation of the measured data.

A number of workers (De Ruiter, 1981; Zuidberg et al., 1982) have selected the cone face location for pore pressure measurement because Δu is at a maximum in this region. This contention is well supported by experimental data (Sugawara & Chikaraishi, 1982; Levadoux & Baligh, 1980). The numerical results obtained in the present study also show that maximum Δu occurs on the cone face. The higher magnitude helps in increasing the sensitivity of the measured data to changes in the soil. In addition, the rate of dissipation at this location is comparatively higher, thereby permitting a full dissipation curve to be obtained in a shorter time and helps in reducing the cost of site investigation.

Clearly, an ideal way of resolving this problem would be to have porous elements located at both the cone face and the shoulder. This design has in

fact been used in some research instruments (May, 1987). However, such a proposition may not be practical in a commercial cone and a compromise location has to be sought. Based on the results of the strain path analysis and taking into consideration the uncertainty associated with the solution around the cone shoulder, it is the author's opinion that the cone face would be the preferred location for placing the piezometric element.

Chapter 10

Concluding Remarks

10.1 Summary and Remarks

Experimental evidence suggests that soil deformation around a deep penetrometer is largely independent of soil properties and is determined primarily by the kinematic constraints on the problem. The strain path method capitalised on this observation to obtain a solution for the stress changes due to cone penetration via a rational and systematic procedure. This approach was adopted in the present study, and the quasi-static cone penetration process was modelled by soil flowing past a stationary cone. These two situations are exactly equivalent when the soil medium can be considered to be homogeneous and infinite in extent.

The velocities of soil particles around the penetrometer were approximated by the flow field of an inviscid fluid. It is clear that the choice of an inviscid flow field is arbitrary and since the algorithm for flow computation derived in this thesis is also applicable to viscous flow computation, an alternative flow field could have been used as an initial estimate. This has not been done principally because a viscous flow solution would require special treatment of the boundary layer and it is not clear how this should be implemented for soil. Furthermore, the viscous flow field is dependent on the Reynolds number, which introduces an additional arbitrary factor into the initial estimate. All these complications have been avoided by adopting the inviscid flow solution.

The results derived from the strain path method were compared, wherever possible, with other analytical solutions. It has been shown that the stresses around a slender body can be approximated closely by cylindrical cavity expansion theory (Norbury & Wheeler, 1987). This prediction has been reproduced quite satisfactorily by the strain path method for a penetrometer with a very sharp conical tip. However, for a 60° cone penetrometer, cavity

expansion theory has been shown to be no longer adequate because of the predominantly two-dimensional nature of soil behaviour around the penetrometer tip.

The stresses obtained from the strain path method are inexact because the velocity field was based on an idealization of soil behaviour. The approximate nature of the computation was revealed by the failure of the deviatoric stresses to satisfy the equilibrium equations. Consequently, the mean normal pressure was dependent on the path of integration. The impact of these simplifying assumptions on the computed stress field was found to be highly localised. The regions where the stresses are associated with appreciable uncertainties are located in the vicinity of the singular points in the penetrometer geometry. Elsewhere, a solution of reasonable quality, as indicated by the small deviations from the equilibrium condition, has been obtained.

It is clear that the velocity field in the region of high uncertainty should be modified if an improved solution is to be obtained. Three different methods, which utilise the approximate stress solution to derive an improve velocity estimate, have been attempted. None of these was successful in completely eliminating the errors.

A series of finite element calculations has also been carried out. Apart from being an independent analysis, the results of the finite element calculations can also be used to verify the reliability of the strain path solutions. A complete finite element analysis which simulate the actual penetration process is not currently feasible. However, it has generally been assumed that a incremental plastic finite element analysis could provide a useful approximation to the solution of the penetration problem, and such a procedure has been adopted in this thesis.

Extensive comparisons were made between the strain path solutions and the finite element results. Despite the difference in the analytical approaches, the stress fields in the soil around the cone face evaluated by these two methods are comparable. The stress contours exhibit similar features even though the magnitudes of the stresses differ slightly. Part of this difference can be directly attributed to the roughness of the cone face, which was assumed to be perfectly rough in the finite element calculations. Far behind the penetrometer tip, the finite element calculations show very small stress changes in the soil around the shaft, due mainly to the way the penetration was modelled numerically. A more realistic solution requires that a displacement in the order of a few cone radii be applied in the incremental finite element calculations. This is not a practicable proposition because of the prohibitive computing time required.

The uncertainties in the stresses around the shoulder were observed in both types of analyses. In the finite element computation, this uncertainty was reflected by the considerable scatter in the Gauss point stresses around the cone shoulder. While it may be possible to reduce the scatter by using a finer mesh system around the cone shoulder, it is not clear that the errors could be completely eliminated by this process alone.

The conventional finite element analysis is strictly a small displacement failure calculation and does not take into account the fact that the cone is continually penetrating. As a result, the computed stress field is not truly representative of the soil stresses around a steadily moving penetrometer. In order to make a more accurate estimate of the steady state cone resistance, a series of strain path-finite element analyses (SPFEM) were carried out. The solution procedure consisted of estimating the steady state stresses from the strain path method, this was then used as the initial condition for the subsequent incremental finite element analysis. The tip

resistances evaluated by this method were significantly higher than the results obtained from conventional finite element calculations based on an 'undisturbed' in-situ stress condition.

Anisotropy in the in-situ stress state has been found to have a significant influence on the N_k factors obtained from the strain path method and SPFEM analysis. When the in-situ horizontal stresses were higher than the vertical stresses, greater N_k factors were obtained. The changes in the value of N_k due to anisotropy in the initial stresses could be significantly reduced if it was defined in terms of σ_{ho}. The cone factor defined in this way is less sensitive to the in-situ stresses and would be a preferred parameter for correlating soil properties. Unfortunately, an accurate measurement of σ_{ho} is extremely difficult to achieve in practice, so N_k should be retained for interpretation purposes. Proper adjustment could then be made in this parameter to account for the effect of stress anisotropy. For example, in a highly over-consolidated soil deposit, σ_{ho} is usually higher than σ_{vo} so N_k should be adjusted upwards.

The N_k values obtained from the finite element analysis and the strain path method were found to exhibit nearly the same trend of variation with I_r. A best estimate of N_k from the analyses carried out is:

$$N_k = 0.19 + 2.64\ln(I_r) \quad 1.89\Delta \quad 2(1-\alpha) \qquad (10.1)$$

The last term in equation (10.1) is an approximate correction to account for the different roughness condition on the cone face.

On the whole, the strain path method has been found to be capable of giving an overall solution which is of the same order of accuracy as the finite element method. In fact, the strain path method was found to yield a

more realistic steady state solution than the conventional finite element analysis. The advantage of the former procedure can be better appreciated when the cost of computation is taken into consideration. On a DEC Vax11/780 computer, a calculation based on the strain path method on the average required about 2 minutes of CPU time. The average finite element analysis performed in this thesis, on the other hand, required about 4.5 CPU hours.

The normalised pore pressure distribution derived from the strain path method using Henkel's pore pressure equation was found to show good qualitative agreement with field and laboratory test data. A dissipation analysis based on such a pore pressure distribution could therefore be expected to give a fair representation of the actual consolidation process around the cone.

The dissipation analysis, based on Terzaghi's three dimensional uncoupled consolidation theory, was formulated in finite difference form using the Alternating-Direction-Implicit method. This formulation is unconditionally stable and permits the use of a variable time step to optimize the solution procedure. The normalised dissipation curves at different locations on the penetrometer derived from these analyses are comparable to those obtained from dissipation tests conducted in a large calibration chamber. In addition, the analyses showed that the rate of dissipation is affected significantly by the rigidity index of the soil. A dimensionless time factor was proposed to take account of this effect.

Two interpretation techniques based on the computed normalised dissipation curves were suggested. In the first technique which was based on a curve matching principle, the dissipation data are plotted against the logarithm of time. The time taken to reach a certain degree of dissipation (expressed in the relevant normalised form) is equated to the theoretical

time factor T^*, from which an estimate of c_h could be made. When only a short dissipation record is available, a useful estimate of c_h can be obtained by plotting the dissipation data against the square root of time. The parameter c_h is estimated by equating the initial tangents of the experimental and theoretical dissipation curves.

An important feature of this research has been to reveal the importance of the parameter I_r. Therefore, in order to use the interpretation techniques suggested in this thesis, the rigidity index of the soils must be known. Since the piezocone is not a suitable device for stiffness measurement, separate tests may be needed to determine the value of I_r. This is unavoidable if a rational and consistent interpretation of the CPT data is to be achieved, principally because the tip resistance and pore pressure generated during cone penetration are affected significantly by I_r. Moreover, current developments in new testing equipment such as the pressuremeter-cone (Houlsby, 1986) may enable a measure of the soil stiffness to be obtained in a penetration test. The additional information acquired will undoubtedly enhance the rational interpretations of cone penetration data.

10.2 Future Research

In the analyses described in the thesis, a number of simplifying assumptions have been introduced. These were made in order to clarify the solution procedure and to avoid unnecessary complications in the formulation. Due to the idealization of the problem, some important aspects of soil behaviour have inevitably been neglected, and this in turn renders the solution less representative of the real problem. One of the major assumptions made was in the choice of constitutive relationship in which the clay was modelled as an elastic-perfectly plastic von Mises material. This

constitutive assumption is clearly unrealistic. The high strain level in the soil during cone penetration raised question about the reliability of the stress calculation based on such a simplified model. In addition, it has been known that clay behaviour is strain rate dependent so the extremely high strain rates encountered during cone penetration should be taken into account in any future studies. The analysis would also benefit if additional features of real soil behaviour such as strain softening and hardening could be included in the constitutive model.

An important area of future research is the development of a correction procedure which is capable of completely eliminating the errors due to equilibrium imbalance. It is the author's belief that the pseudo-dynamic method outlined in Chapter 5 may provide the basis for such a scheme. However, in order to improve the performance of this method, two particular aspects of the scheme require special attention. Firstly, a proper treatment of the soil-penetrometer interface must be found. Secondly, a detailed analysis of soil behaviour around the points of singularity in the penetrometer geometry may also be necessary. A solution for the cone tip is already available (Sagaseta, 1985), so a similar analysis for the shoulder would be required. Preliminary studies suggest that it is the inadequate treatment of these two aspects of the problem that prevented the complete elimination of errors in the stress solution. It is highly probable that progress along these lines would aid the development of a successful iterative correction scheme.

REFERENCE

Al-Awkati, Z. (1977) "The Effects of Shape, Roughness and Size on the Bearing Capacity of Deep Bases" Post-Doctoral Research Rept., Univ. Florida.

Allersma, H.J.B. (1982) "Photoelastic Investigation of the Stress Distribution During Penetration" ESOPT II, Amsterdam

ASTM (1977) "Standard Method for Deep, Quasi-Static, Cone and Friction-Cone Penetration Tests of Soil" American Society for testing Materials, Standard D3441

Baligh, M.M. (1986a) "Undrained Deep Penetration, I: Shear Stresses" Geotechnique Vol. 36, No. 4

Baligh, M.M. (1986b) "Undrained Deep Penetration, II: Pore Pressure" Geotechnique Vol. 36, No. 4

Baligh, M.M. (1985) "Strain Path Method" J. Geotech. Engg., ASCE Vol. 111, No. 9

Baligh, M.M. (1975) "Theory of Deep Site Static Cone Penetration Resistance" Publication No. R75-56 Dept. of Civil Engg., M.I.T.

Baligh, M.M., Azzouz, A.S., Wizza, A.Z.E., Martin, R.T. and Morrison, M.J. (1981) "The Piezocone Penetrometer" ASCE Conf. Cone Penetration Testing and Experience, St. Louis.

Baligh, M.M. and Levadoux, J.N. (1980) "Pore Pressure Dissipation after Cone Penetration" Publication No R80-11 Dept. of Civil Engg. M.I.T.

Baligh, M.M. and Levadoux, J.N. (1986) "Consolidation after Undrained Piezocone Penetration, II: Interpretation" J. Geotech. Engg., ASCE Vol. 112, No. 7

Baligh, M.M and Vivatrat, V. (1979) "In-situ Measurements in a Marine Clay" 2nd. Int. Conf. on Behaviour of off-shore Struct., London.

Baligh, M.M., Vivatrat, V. and Ladd, C.C. (1980) "Cone Penetration in Soil Profiling" J. Geotech. Engg., ASCE, Vol. 106 GT4.

Batchelor, G.K. (1967) "An Introduction to Fluid Dynamics" Cambridge Univ. Press

Battaglio, M., Jamiolkowski M., Lancellotta R. and Maniscalco R. (1981) "Piezometer Probe Tests in Cohesive Deposits" Proc. ASCE Conf. Cone Penetration Testing and Experience, St. Louis.

Begemann, H.K.S. (1965) "The Friction Jacket as an Aid in Determining the Soil Profile" Proc. 6th ICSMFE, Montreal, Vol. 1.

Begemann, H.K.S. (1963) "The Use of Static Cone Penetrometers in Holland" New Zealand Engineering Vol. 18 No. 2.

Begemann, H.K.S. (1953) "Improved Method of Determining Resistance to Adhesion by Sounding Through a Loose Sleeve Placed Behind the Cone." Proc 3rd. ICSMFE, Zurich Vol. 1.

Bjerrum, L. and Johannessen, I.J. (1960) "Pore Pressures Resulting From Driving Piles in Soft Clay" Conf. on Pore Pressure and Suction in Soil, Sydney.

Biot, M.A. (1941) 'General Theory of Three Dimensional Consolidation.' J. Appl. Phys., Vol. 12.

Bishop, A.W., Hill, R. and Mott, N.F. (1945) "The Theory of Indentation and Hardness Tests" Proc. Phy. Soc. London, Vol. 57 No. 3

Booker, J.R. (1984) Personal Communication

Burd, H.J. (1986) "A Large Displacement Finite Element Analysis of a Reinforced Unpaved Road" D.Phil. Thesis, Oxford University

Butterfield, R. and Bannerjee, P.K. (1970) "The effect of Pore Water Pressure on the Ultimate Bearing Capacity of Driven Piles" Proc. 2nd. South East Asian Regional Conf. Soil Mech. Fdns. Engg.

Campanella, R.G., Gillespie, D.G. and Robertson, P.K. (1982) "Pore Pressures During Cone Penetration Testing" ESOPT II, Amsterdam

Campanella, R.G., Robertson, P.K. and Gillespie, D.G. (1981) "In-situ Testing in Saturated Silt (Drained or Undrained?)" 34th Canadian Geotech. Conf.

Campanella, R.G., Robertson, P.K., Gillespie, D.G. and Grieg, J. (1985) "Recent Developments in In-situ Testing of Soils" 11th. ICSMFE, San Francisco Vol. 2

Carter, J.P. (1977) "Finite Deformation Theory and its Application to Elastoplastic Soils" Ph.D. Thesis, Univ. of Sydney, Australia

Carter, J.P., Booker, J.R. and Davis, E.H. (1977) "Finite Deformation of an Elasto-Plastic Soil" Int. J. Num. Analyt. Meth. Geomech. Vol. 1(4)

Carter, J.P., Randolph, M.F. and Wroth, C.P. (1979) "Stress and Pore Pressure Changes in Clay During and After the Expansion of a Cylindrical Cavity" Int. J. Num. Analyt. Meth. in Geomech., Vol. 3

Cook, R.D. (1981) "Concepts and Applications of Finite Element Analysis" John Wiley & Sons, New York

Cox, A.D., Eason, G. and Hopkins, H.G. (1961) "Axially Symmetric Plastic Deformations in Soils" Phil. Trans. Roy. Soc. Ser. A Vol. 254

Cryer, C.W. (1963) "A Comparison of The Three Dimensional Consolidation Theories of Biot and Terzaghi." Quart. J. Mech. and Appl. Maths. Vol. 16, Part 4

Davis, E.H. and Poulos, H.G. (1970) "Discussion of 'An Analysis of Consolidation Theories' by R.L. Schiffman, A.T.F. Chen and J.C. Jordan' " J. Soil Mech. Fdns. Div., ASCE Vol. 96 No. SM1.

Davis, E.H., Ring, G.J. and Booker, J.R. (1974) "The Significance of the Rate of Plastic Work in Elasto-Plastic Analysis" Proc. Int. Conf. on Finite Element Meth. in Engg., Sydney, Australia

Delft Laboratory of Soil Mechanics (1936) "The Predetermination of the Required Length and the Prediction of the Toe Resistance of Piles" 1st ICSMFE, Cambridge, Mass.

De Beer, E. (1977) "Static Cone Penetration Testing in Clay and Loam" Sondeer Symposium, Utrecht.

De Borst (1982) "Calculation of Collapse Loads Using Higher Order Elements" Proc. IUTAM Symp. on Deformation and Failure of Granular Materials, Rotterdam

De Borst, R. and Vermeer, P.A. (1984) "Possibilities and Limitation of Finite Element for Limit Analysis" Geotechnique Vol. 34, No. 2

Dennis, S.C.R. and Smith, F.T. (1980) "Steady Flow Through a Channel with a Symmetrical Constriction in the Form of a Step" Proc. Roy. Soc. London, Ser. A, Vol. 372

De Ruiter, J. (1982) "The Static Cone Penetration Test - State of the Art Report" ESOPT II ,Amsterdam.

De Ruiter, J. (1981) "Current Penetrometer Practice" Proc. ASCE Conf. on Penetration Testings and Experience, St Louis, Missouri

De Ruiter, J. (1971) "Electric Penetrometer for Site Investigations" J. Soil Mech. Fdns. Div., ASCE Vol. 97 SM2

Douglas, J. (1961) "Survey of Numerical Methods for Parabolic Differential Equations" Advances in Computers, Vol. 2, Academic Press, New York

Durgunoglu, H.T. and Mitchell, J.K. (1974) "Influence of Penetrometers on Static Penetration Resistance" ESOPT I Stockholm Vol. 2:2

Frankel, S.P. (1950) Math. Tabl. Nat. Res. Coun., Washington 4, 65

Gibson, R.E. and Anderson, W.F. (1961) "In Situ Measurement of Soil Properties with the Pressuremeter" Civil Engg. and Public Works Review Vol. 56

Gibson, R.E., Knight, K. and Taylor, P.W. (1963) "A Critical Experiment to Examine Theories of Three Dimensional Consolidation" Proc. ECSMFE, Wiesbaden, Germany, Vol.1.

Gillani, N.V. and Swanson, W.M. (1976) "Time-Dependent Laminar Flow Through a Spherical Cavity" J. Fluid Mech., Vol. 78

Henkel, D.J. and Wade, N.H. (1966) "Plane Strain Tests on a Saturated Remoulded Clay" J. Soil Mech Fdns. Div., ASCE Vol. 92 SM6

Hill, R. (1951) 'The Mathematical Theory of Plasticity' Clarendon Press, Oxford

Hofmeister, L.D., Greenbaum, A., and Evenson, D.A. (1971) "Large Strain, Elasto-Plastic Finite Element Analysis" AIAA J., Vol. 9, No. 7

Houlsby, G.H. (1986) Private Communication

Houlsby, G.T. and Wroth, C.P. "Determination of Undrained Strength By Cone Penetration Tests" ESOPT II, Amsterdam.

ISSMFE (1977) "Report of the Sub-Committee on Standardization of Penetration Testing in Europe", 9th ICSMFE, Tokyo.

Janbu, N. and Senneset, K. (1974) "Effective Stress Interpretation of In-situ Penetration Tests" ESOPT I Stockholm Vol. 2:2

Jones, G.A. and Rust, E. (1982) "Piezometer Penetration Testing - CUPT" ESOPT II, Amsterdam.

Jones, G.A. and van Zyl, D.J.A. (1981) "The Piezometer Probe - a Useful Investigation Tool" Proc. 10th. ICSMFE, Stockholm.

Kay, J.N. and Parry, R.H.G. (1982) "Screw Plate Tests in a Stiff Clay" Ground Engineering Vol. 15 No. 6.

Koizumi, Y. and Ito, K. (1967) "Field Tests with Regard to Pile Driving and Bearing Capacity of Piled Foundarions" Soils and Foundations, Japan, Vol. 7 No. 3

Koumoto, T. and Kaku, K. (1982) "Three Dimensional Analysis of Static Cone Penetration into Clay" ESOPT II, Amsterdam.

Lacasse, S., Jamiolkowski, M., Lancellotta, R. and Lunne, T. (1981) "In-situ Characteristics of Two Norwegian clays" Proc. 10th ICSMFE, Stockholm.

Lacasse, S. and Lunne, T. (1982) "Penetration Tests in Two Norwegian Clays" ESOPT II, Amsterdam.

Ladanyi, B. (1963) "Expansion of a Cavity in a Saturated Clay Medium" J. Soil Mech. Fdns. Engg. Div., ASCE Vol. 89, SM4.

Ledoux, J.L., Menard J. and Soulard P. "The Penetro-gammadensimeter" ESOPT II, Amsterdam

Lee, E.H. and McMeeking, R.M. (1980) "Concerning Elastic and Plastic Components of Deformation" Int. J. Sol. Struct. Vol 16(1)

Levadoux,J.N. and Baligh, M.M. (1986) "Consolidation After Undrained Piezocone Penetration, I: Prediction" J. Geotech. Engg., ASCE, Vol. 112, No. 7

Levadoux J.N. and Baligh M.M. (1980) "Pore Pressures During Cone Penetration in Clays" Publication R80-15, Dept. of Civil Engg., M.I.T.

Lo, K.Y. and Stermac, A.G. (1965) "Induced Pore Pressures During Pile Driving Operations" 6th. ICSMFE, Montreal.

Macagno, E.O. and Hung, T.K. (1967) "Computational and Experimental Study of a Captive Annular Eddy" J. Fluid Mech. Vol. 28 Part 1

Malkus, D.S. and Hughes, T.J.R. (1978) "Mixed Finite Element Methods, Reduced and Selective Integration Techniques: A Unification of Concepts" Comp. Meth. Appl. Mech. Engg. Vol. 15

Mandel, J. (1953) "Consolidation des Sols (Etude Mathematique)" Geotechnique, Vol. 3

May, R.E. (1987) "A Study of the Piezocone Penetrometer in Normally Consolidated Clay" D.Phil Thesis, Oxford University.

McMeeking, R.M. and Rice, J.R. (1975) "Finite Element Formulation for Problems of Large Elastic-Plastic Deformation" Int. J. Sol. Struct. Vol. 11(5)

Mei, R.W. and Plotkin, A. (1986) "Naview-Stokes Solutions for Laminar Incompressible Flows in a Forward Facing Step Geometries" AIAA J. Vol. 24 No. 7

Meyerhof, G.G. (1951) "The Ultimate Bearing Capacity of Wedge-shaped Foundations" Geotechnique, Vol. 2, No. 3

Meyerhof, G.G. (1961) "The Ultimate Bearing Capacity of Wedge-shaped Foundations" Proc. 5th ICSMFE, Paris, Vol. 2

Muromachi, T. (1974) "Experimental Study on Application of Static Cone Penetrometer to Subsurface Investigation of Weak Cohesive Soils" ESOPT I Stockholm, Vol 2:2

Nagtegaal, J.C., Parks, D.M. and Rice, R.R. (1974) "On Numerically Accurate Finite Element Solutions in the Fully Plastic Range" Comp. Meth. Appl. Mech. Engg. Vol. 4

Nayak, G.C. and Zienkiewizc, O.C. (1972) "Elasto-Plastic Stress Analysis: A Generalization for Various Constitutive Laws Including Strain Softening" Int. J. Num. Meth. Engg. Vol. 5

Naylor, D.J. (1974) "Stresses in Nearly Incompressible Materials by Finite Elements with Application to the Calculation of Excess Pore Pressure" Int. J. Num. Meth. Engg. Vol. 8

Norbury, J. and Wheeler, A.A. (1987) "On the Penetration of an Elastic-Plastic Material by a Slender Body" to appear in Quart. J. Mech. Appl. Math.

Oldroyd, J.G. (1950) "On the Formulation of Rheological Equations of State" Proc. Roy. Soc. London, Ser. A Vol. 200

Osias, J.R. and Swedlow, J.L. (1974) "Finite Elasto-Plastic Deformation I - Theory and Numerical Examples" Int. J. Sol. Struct. Vol. 10(3)

Plantema, G. (1948) "Construction and Method of Operating of a New Sounding Method" Proc. 2nd ICSMFE, Rotterdam.

Prager, W. (1961) "An Elementary Discussion of Definitions of Stress Rate" Quart. J. Appl. Math. Vol. 18

Prandtl, L. (1921) "Eindringungsfestigkeit und Festigkeit von Schneiden" Z. Angew. Math. Mech. Vol. 1(15)

Prandtl, L. and Tietjens, O.G. (1934) "Fundamentals of Hydro- and Aerodynamics" McGraw-Hill, New York

Randolph, M.F., Carter, J.P. and Wroth, C.P. (1979) "Driven Piles in Clay; the Effects of Installation and Subsequent Consolidation" Geotechnique Vol. 29 No. 4.

Randolph, M.F., Steenfelt, J.S. and Wroth, C.P. (1979) "The Effect of Pile Design for Driven Piles" Proc. 7th. ECSMFE Brighton, England

Randolph, M.F. and Wroth, C.P. (1979) "An Analytical Solution for The Consolidation Around a Driven Pile" Int. J. Num. Analyt. Meth. in Geomech. Vol. 3.

Rendulic, L. (1936) "Poreziffer und Poren Wasserdruck in Tonen" Bauingeneur, Vol 17, pp 559-564

Roache P.J. (1976) "Computational Fluid Mechanics" Hermosa, Alburquerque

Rourk, T.L. (1961) "Model Studies of a Pile Failure Surface in a Cohesive Soil" Master's Thesis, Dept. of Civil Engg. Georgia Inst. Tech., Atlanta

Rouse, H. (1959) "Advanced Mechanics of Fluid" John Wiley & Sons, New York

Roy M., Blanchet R., Tavenas, F. and La Rochelle, P. (1981) "Behaviour of a Sensitive Clay During Pile Driving" Can. Geotech. J. Vol. 108.

Roy, M., Tremblay, M., Tavenas, F. and La Rochelle, P. (1982a) "Development of Pore Pressures in Quasi-Static Penetration Tests in Sensitive Clay" Can. Geotech. J. Vol. 109.

Roy M., Michand D., Tavenas, F., Leroueil, S. and La Rochelle, P. (1974) "The Interpretation of Static Cone Penetration Tests in Sensitive Clays" ESOPT I, Stockholm Vol. 2:2.

Sagaseta, C. (1984) Private communication.

Sanglerat, G. (1979) "The Penetrometer and Soil Exploration" 2nd Ed. Elsevier

Schmertmann, J.H. (1974a) "Penetration Pore Pressure Effects on Quasi-Static Cone Bearing q_c' ESOPT I, Stockholm, VOL. 2:2

Schmertmann, J.H. (1974b) "Pore Pressures that Produce Non-conservative q_c Data" - Discussion, ESOPT I, Stockholm.

Senneset, K., Janbu, N. and Svano, G. (1982) "Strength and Deformation Parameters from Cone Penetration Tests" ESOPT II, Amsterdam.

Sills, G.C. (1975) "Some Conditions Under Which Biot's Equation of Consolidation Reduced to Terzaghi's Equation" Geotechnique, Vol. 25, No. 1

Skempton, A.W. (1954) "The Pore Pressure Coefficients A and B" Geotechnique Vol. 4, No. 1.

Skempton, A.W. (1951) "The Bearing Capacity of Clays" Building Research Congress, London, Vol. 1.

Sloan, S.W. (1981) "Numerical Analysis of Incompressible and Plastic Solids Using Finite Elements" D.Phil. Thesis, University of Cambridge

Sloan, S.W. (1984) "Substepping Schemes for the Numerical Integration of Elasto-Plastic Stress-Strain Relations" Report No. 003.12.84, Dept.

of Civil Engg and Surveying, Univ. of Newcastle, New South Wales, Australia

Sloan, S.W. and Randolph, M.f. (1982) "Numerical Prediction of Collapse Loads Using Finite Element Methods" Int. J. Num. Analyt. Meth. Geomech. Vol. 6

Small, J.C., Booker, J.R. and Davis, E.H. (1976) "Elasto-Plasto Consolidation of Soil" Int. J. of Sol. Struct. Vol. 12(1)

Smith, F.T. (1979) "The Separating Flow Through a Severely Constricted Symmetric Tube" J. Fluid Mech., Vol. 90

Smyth, R. (1979) "Turbulent Flow Over a Disk Normal to a Wall" J. Fluid Engg., Trans. ASME Vol. 101

Sobey, I.J. (1980) "On Flow Through Furrowed Channels, Part I: Calculated Flow Patterns" J. Fluid Mech., Vol. 96

Soderberg, L.O. (1962) "Consolidation Theory Applied to Foundation Pile-Time Effects" Geotechnique Vol. 12 No. 2.

Southwell, R.V. (1948) "Relaxation Methods in Theoretical Physics" Clarendon Press, Oxford

Sugawara, N. and Chikaraishi, M. (1982) "On Estimation of ϕ' for Normally Consolidated Mine Tailings Using the Pore Pressure Cone Penetrometers" ESOPT II, Amsterdam.

Szechy, K. (1968) "Deformation Around and Below Driven and Vibrated Test Tubes" Acta Technica Acad. Sci., Hungary, Vol 62

Tavenas, F. and Leroueil, S. (1979) "Clay Behaviour and the Selection of Design Parameters" Proc. 7th ECSMFE, Brighton.

Tavenas, F. Leroueil, S. and Roy, M. (1982) "The Piezocone Test in Clays - Use and Limitations" ESOPT II, Amsterdam.

Terzaghi, K. (1923) "Die Berechnung der Durchlassigheitsziffer des Tones aus dem Verlaug der Hydrodynamischen Spanrungsercheinungen" Akademie der Wissenchafen in Win, Sitzungsberichte Mathematish Naturwissenschaftliche Klass, Part IIa, Vol. 132 No. 3/4

Terzaghi K. (1943) "Theorectical Soil Mechanics" John Wiley & Sons, New York.

Terzaghi, K. and Peck, R. (1967) "Soil Mechanics in Engineering Practice" John Wiley & Sons, New York

Toh, C.T. and Sloan, S.W. (1980) "Finite Element Analysis of Isotropic and Anisotropic Cohesive Soils with a View to Correctly Predicting Impending Collapse" Int. J. Num. Analyt. Meth. Geomech. Vol. 4

Toolan, F.E. (1980) "Discussion on 'The Importance of Stress History of Cohesive Soils and Penetration Test' by Thorburn et al." Structural Engineer, Vol. 60A, No. 6

Torstensson B-A. (1982) "A Combined Pore Pressure and Point Resistance Probe" ESOPT II, Amsterdam.

Torstensson B-A. (1978) "The Pore Pressure Probe" Proc. Geoteknikkdagen, Tapir Forlag, Oslo.

Torstensson B-A. (1975) "Pore Pressure Sounding Instrument" Proc. ASCE Conf. In-Situ Measurement of Soil Properties, Raleigh.

Tringale, P.T. and Mitchell J.K. (1982) "An Acoustic Cone Penetrometer for Site Investigation" ESOPT II, Amsterdam

Truesdell, C. (1953) 'The Mechanical Foundations of Elasticity and Fluid Dynamics' J. Rat. Mechs. Analys. Vol. 2(3)

Tumay, M.T., Bogges, R.L. and Acar, Y. (1981) "Subsurface Investigation with Piezocone Penetrometer" Proc. ASCE Conf. on Penetration Testings and Experience, St Louis, Missouri

Vesic, A.S. (1963) "Bearing Capacity of Deep Foundations on Sand" Stresses in Soils and Layered Systems, Can. Highway Research Board No. 39

Vesic A.S. (1972) "Expansion of Cavities in Infinite Soil Mass" J. Soil Mech. Fdns. Div., ASCE, Vol. 98, SM3.

Viggiani, C. (1970) "Discussion of 'An Analysis of Consolidation Theories' by Schiffman, R.L., Chen, A.T.F. and Jordan, J.C." J. Soil Mech. Fdns. Div., ASCE, Vol. 96, SM1

Wizza A.E.Z., Martin R.T. and Garlanger J.E. (1975) "The piezometer probe" ASCE Conf. In-situ Measurement of Soil Properties, Raleigh.

Wroth C.P. (1984) "The interpretation of In-situ soil tests" 24th. Rankine Lecture, Geotechnique Vol. 34, No. 4.

Yamada, Y., Yoshimura, N. and Sakurai, T.(1968) "Plastic Stress-Strain Matrix and its Application for the Solution of Elastic-Plastic Problems by the Finite Element Method" Int. J. Mech. Sci., Vol. 10

Zienkiewicz, O.C. (1977) "The Finite Element Method" McGraw-Hill, London

Zuidberg H.M., Schaap L.H.J. and Beringen F.L. (1982) "A Penetrometer for Simultaneously Measuring of Cone Resistance, Sleeve Friction and Dynamic Pore Pressure" ESOPT II, Amsterdam.